SUBSONIC AND TRANSONIC DYNAMIC STABILITY CHARACTERISTICS OF A SPACE SHUTTLE ORBITER

Richmond P. Boyden and Delma C. Freeman, Jr.

Langley Research Center
Hampton, Va. 23665

SUBSONIC AND TRANSONIC DYNAMIC STABILITY CHARACTERISTICS
OF A SPACE SHUTTLE ORBITER

Richmond P. Boyden and Delma C. Freeman, Jr.
Langley Research Center

SUMMARY

Subsonic and transonic forced oscillation tests of a 0.0165-scale model of a modified 089B shuttle orbiter have been made in the Langley 8-foot transonic pressure tunnel for several configurations over a Mach number range from 0.3 to 1.2.

The pitch, roll, and yaw damping were measured as well as normal force due to pitch rate and the cross derivatives yawing moment due to roll rate and rolling moment due to yaw rate. Static tests were also conducted for the same configurations and test conditions and these data are presented herein for comparison with the in-phase dynamic test results. The measured dynamic data and three-degrees-of-freedom longitudinal and lateral motion equations were utilized to compute the period and damping of the basic unaugmented vehicle along the entry trajectory.

The results of this investigation showed that the model exhibited positive damping in pitch except at an angle of attack of about 10° for Mach numbers of 0.98 and 1.2. The model had positive yaw damping throughout the test angle of attack and Mach range and had positive roll damping except for angles of attack in excess of 20° for Mach numbers of 0.98 and 1.2. There was generally good agreement between the appropriate parameters in the in-phase portion of the dynamic data and in the corresponding static data. The results from the longitudinal stability calculations showed the pitch damping had some large effects on the aperiodic divergent rate. The major result from the lateral stability analysis was that the unstable spiral mode divergence was very dependent on the value of the yaw damping and on the rolling moment due to yaw rate.

INTRODUCTION

As part of the space shuttle development effort, a program has been initiated at the NASA Langley Research Center to measure experimentally the dynamic deviatives of the shuttle orbiter under conditions which correspond to the entry to landing phases of flight and then use the measured derivatives to predict the vehicle dynamics for the orbiter with an unaugmented flight control system. Since adequate theoretical prediction techniques do not exist to estimate the damping at high angles of attack and since experimentally

measured data for these combinations of angle of attack and Mach number are not available, these results are unique. These tests are part of an overall program that will provide a consistent set of damping data for the shuttle orbiter from hypersonic to subsonic Mach numbers.

As part of this study, subsonic and transonic forced oscillation tests of a 0.0165-scale model of a modified 089B shuttle orbiter have been conducted in the Langley 8-foot transonic pressure tunnel. These tests were conducted for several configurations over a Mach number range from 0.3 to 1.2 measuring the pitch, roll, and yaw damping as well as the normal force due to pitch rate and the cross derivatives yawing moment due to roll rate and rolling moment due to yaw rate. Static tests were also run for the same configurations and test conditions and these data are presented herein for comparison with the in-phase portion of the dynamic test results. The measured dynamic data and three-degrees-of-freedom longitudinal and lateral motion equations were utilized to compute the period and damping of the basic unaugmented vehicle along the entry trajectory. The effects of variations of the damping and cross derivatives on the computed vehicle dynamics were also determined.

The results for the corresponding study of the shuttle orbiter for Mach numbers of 1.6 to 4.63 are contained in reference 1 and the hypersonic results are shown in reference 2.

SYMBOLS

All data presented are referred to the body axes system except for the static longitudinal data which are referred to the stability axes system. (See fig. 1.) The origin of the axes was located to correspond to the center-of-gravity positions shown in figure 2.

b reference span, meters

C_D drag coefficient, $\dfrac{\text{Drag force}}{q_\infty S}$

$C_{D_{\delta_e}}$ $= \dfrac{\partial C_D}{\partial \delta_e}$, per degree

C_L lift coefficient, $\dfrac{\text{Lift force}}{q_\infty S}$

$C_{L_{\delta_e}}$ $= \dfrac{\partial C_L}{\partial \delta_e}$, per degree

C_l rolling-moment coefficient, $\dfrac{\text{Rolling moment}}{q_\infty S b}$

2

$$C_{l_p} \quad = \frac{\partial C_l}{\partial\left(\frac{pb}{2V}\right)}, \text{ per radian}$$

$$C_{l_{\dot{p}}} \quad = \frac{\partial C_l}{\partial\left(\frac{\dot{p}b^2}{4V^2}\right)}, \text{ per radian}$$

$C_{l_p} + C_{l_{\dot{\beta}}} \sin \alpha$ damping-in-roll parameter, per radian

$$C_{l_r} \quad = \frac{\partial C_l}{\partial\left(\frac{rb}{2V}\right)}, \text{ per radian}$$

$$C_{l_{\dot{r}}} \quad = \frac{\partial C_l}{\partial\left(\frac{\dot{r}b^2}{4V^2}\right)}, \text{ per radian}$$

$C_{l_r} - C_{l_{\dot{\beta}}} \cos \alpha$ rolling moment due to yaw rate parameter, per radian

$$C_{l_\beta} \quad = \frac{\partial C_l}{\partial\beta}, \text{ per radian or per degree}$$

$$C_{l_{\dot{\beta}}} \quad = \frac{\partial C_l}{\partial\left(\frac{\dot{\beta}b}{2V}\right)}, \text{ per radian}$$

$C_{l_\beta} \sin \alpha - k^2 C_{l_{\dot{p}}}$ rolling moment due to roll displacement parameter, per radian

$C_{l_\beta} \cos \alpha + k^2 C_{l_{\dot{r}}}$ effective dihedral parameter, per radian

C_m pitching-moment coefficient, $\dfrac{\text{Pitching moment}}{q_\infty S \bar{c}}$

$$C_{m_q} \quad = \frac{\partial C_m}{\partial\left(\frac{q\bar{c}}{2V}\right)}, \text{ per radian}$$

$$C_{m_{\dot{q}}} \quad = \frac{\partial C_m}{\partial\left(\frac{\dot{q}\bar{c}^2}{4V^2}\right)}, \text{ per radian}$$

$C_{m_q} + C_{m_{\dot{\alpha}}}$ damping-in-pitch parameter, per radian

$$C_{m_\alpha} \quad = \frac{\partial C_m}{\partial\alpha}, \text{ per radian}$$

$$C_{m_{\dot{\alpha}}} \qquad = \frac{\partial C_m}{\partial\left(\frac{\dot{\alpha}\bar{c}}{2V}\right)}, \text{ per radian}$$

$$C_{m_{\alpha}} - k^2 C_{m_{\dot{q}}} \qquad \text{oscillatory longitudinal stability parameter, per radian}$$

$$C_{m_{\delta_e}} \qquad = \frac{\partial C_m}{\partial\delta_e}, \text{ per degree}$$

$$C_N \qquad \text{normal-force coefficient, } \frac{\text{Normal force}}{q_{\infty}S}$$

$$C_{N_q} \qquad = \frac{\partial C_N}{\partial\left(\frac{q\bar{c}}{2V}\right)}, \text{ per radian}$$

$$C_{N_{\dot{q}}} \qquad = \frac{\partial C_N}{\partial\left(\frac{\dot{q}\bar{c}^2}{4V^2}\right)}, \text{ per radian}$$

$$C_{N_q} + C_{N_{\dot{\alpha}}} \qquad \text{normal force due to pitch rate parameter, per radian}$$

$$C_{N_{\alpha}} \qquad = \frac{\partial C_N}{\partial\alpha}, \text{ per radian}$$

$$C_{N_{\dot{\alpha}}} \qquad = \frac{\partial C_N}{\partial\left(\frac{\dot{\alpha}\bar{c}}{2V}\right)}, \text{ per radian}$$

$$C_{N_{\alpha}} - k^2 C_{N_{\dot{q}}} \qquad \text{normal force due to pitch displacement parameter, per radian}$$

$$C_n \qquad \text{yawing-moment coefficient, } \frac{\text{Yawing moment}}{q_{\infty}Sb}$$

$$C_{n_p} \qquad = \frac{\partial C_n}{\partial\left(\frac{pb}{2V}\right)}, \text{ per radian}$$

$$C_{n_{\dot{p}}} \qquad = \frac{\partial C_n}{\partial\left(\frac{\dot{p}b^2}{4V^2}\right)}, \text{ per radian}$$

$$C_{n_p} + C_{n_{\dot{\beta}}} \sin\alpha \qquad \text{yawing moment due to roll rate parameter, per radian}$$

$$C_{n_r} \qquad = \frac{\partial C_n}{\partial\left(\frac{rb}{2V}\right)}, \text{ per radian}$$

$$C_{n_{\dot{r}}} = \frac{\partial C_n}{\partial\left(\frac{\dot{r}b^2}{4V^2}\right)}, \text{ per radian}$$

$C_{n_r} - C_{n_{\dot{\beta}}} \cos\alpha$ damping-in-yaw parameter, per radian

$$C_{n_\beta} = \frac{\partial C_n}{\partial\beta}, \text{ per radian or per degree}$$

$$C_{n_{\dot{\beta}}} = \frac{\partial C_n}{\partial\left(\frac{\dot{\beta}b}{2V}\right)}, \text{ per radian}$$

$C_{n_\beta}\cos\alpha + k^2 C_{n_{\dot{r}}}$ oscillatory directional-stability parameter, per radian

$C_{n_\beta}\sin\alpha - k^2 C_{n_{\dot{p}}}$ yawing moment due to roll displacement parameter, per radian

C_Y side-force coefficient, $\dfrac{\text{Side force}}{q_\infty S}$

$C_{Y_\beta} = \dfrac{\partial C_Y}{\partial\beta}$, per radian or per degree

$\bar{c}$ reference chord, meters

F_D drag force, N

F_L lift force, N

f frequency of oscillation, hertz

I_X, I_Y, I_Z moments of inertia about X, Y, and Z body axes, kg-m^2

I_{XZ} product of inertia, kg-m^2

k reduced frequency parameter, $\dfrac{\omega\bar{c}}{2V}$ in pitch; $\dfrac{\omega b}{2V}$ in roll and yaw, radians

l orbiter body length, meters

M free-stream Mach number

M_X rolling moment, N-m

M_Y pitching moment, N-m

M_Z yawing moment, N-m

P   period, seconds

p,q,r   angular velocities of model about X-, Y-, and Z-axis, respectively, radians/second

q_∞ free-stream dynamic pressure, N/m^2

R   Reynolds number based on body length

S   reference area, $meters^2$

$t_{1/2}$ time to damp to half-amplitude, seconds

V   free-stream velocity, meters/second

X,Y,Z   body system of axes

X_S,Y_S,Z_S stability system of axes

α angle of attack, degrees or radians

β angle of sideslip, degrees or radians

δ_{BF} body flap deflection, positive when trailing edge is down, degrees

δ_e elevon deflection, positive when trailing edge is down, degrees

ϕ roll angle, degrees or radians

ω angular velocity, $2\pi f$, radians/second

A dot over a quantity indicates a first derivative with respect to time.

6

MODEL AND APPARATUS

A drawing of the 0.0165-scale model used in the investigation is presented in figure 2. The model, a modified 089B shuttle orbiter, had a double-delta planform wing with 81° sweep on the fillet and 45° sweep on the main wing. The model had a vertical tail with a rudder that could be deflected for yaw control and flared from the basic 10° to 85° to provide a speed brake. (See fig. 3.) Wing trailing-edge control surfaces were utilized to provide both pitch and roll control and a body flap was utilized to produce longitudinal trim. Orbital maneuvering engines (OMS pods) were located as shown in figure 2 and were removed for part of the tests.

The subsonic and transonic static and dynamic tests were conducted in the Langley 8-foot transonic pressure tunnel. A photograph of the model mounted in the tunnel for forced oscillation tests is presented in figure 4. A description of the technique and apparatus for the forced oscillation tests is presented in reference 1.

TESTS

The forced oscillation tests were conducted to determine the damping in pitch $\left(C_{m_q} + C_{m_{\dot\alpha}}\right)$, yaw $\left(C_{n_r} - C_{n_{\dot\beta}} \cos \alpha\right)$, and roll $\left(C_{l_p} + C_{l_{\dot\beta}} \sin \alpha\right)$ and the change in normal force due to pitch rate $\left(C_{N_q} + C_{N_{\dot\alpha}}\right)$ and the cross derivatives yaw due to rolling velocity $\left(C_{n_p} + C_{n_{\dot\beta}} \sin \alpha\right)$ and the roll due to yawing velocity $\left(C_{l_r} - C_{l_{\dot\beta}} \cos \alpha\right)$. The dynamic longitudinal stability derivatives were measured for a pitch amplitude of 1^O for frequencies corresponding to values of the reduced frequency parameter k of 0.0050 to 0.0325. The dynamic lateral stability derivatives measured during the yaw oscillation tests were for a yaw amplitude of 1^O for frequencies corresponding to values of the reduced-frequency parameter k of 0.0096 to 0.0605. The dynamic derivatives measured during the roll oscillation tests were measured for an amplitude of $2\frac{1}{2}^O$ for frequencies corresponding to values of k of 0.0287 to 0.1112. Pitching oscillation tests were conducted with two representative center-of-gravity positions and results are presented for both positions.

The static tests were conducted to determine the static longitudinal and lateral stability characteristics of the model to aid in interpretation of the dynamic tests results. Both the static and dynamic force tests were conducted over an angle-of-attack range from -2^O to 22°. The static lateral stability characteristics were determined from the incremental differences in C_n, C_l, and C_Y measured over the angle-of-attack range at fixed angles of sideslip of 0° and 2^O. The test conditions were as follows:

Mach number	q_∞, N/m^2	R
0.30	5 980	3.2×10^6
.80	29 780	6.7
.90	33 950	7.1
.98	18 430	3.7
1.20	21 120	3.7

The static force data presented have been corrected for sting bending and all drag data presented are total drag in that the base drag has not been subtracted out.

For all Mach numbers the model was tested with transition fixed by application of No. 120 grit 2.54 centimeters aft on the nose and 1.27 centimeters streamwise on the wing and vertical tail. The grit size and location were chosen on the basis of the work in reference 3.

CALCULATIONS

Linearized three-degrees-of-freedom equations of motion as presented in reference 4 were used to calculate the period and damping of the phugoid, short-period and other oscillations, the damping of the longitudinal aperiodic modes, the period and damping of the Dutch roll oscillation, and the damping of the lateral aperiodic modes for the basic unaugmented vehicle. All the stability calculations and motion studies were made with the use of the measured stability derivatives combined with the static longitudinal and lateral data and mass properties presented in tables I, II, and III for flight conditions (Mach number, angle of attack, and altitude) that were representative of the nominal vehicle flight trajectory. (See fig. 5.) The static data and the mass properties were obtained from the shuttle data base for the current vehicle design at the time the analyses were made.

PRESENTATION OF RESULTS

An outline of the contents of the figures presented in this paper follows:

RESULTS AND DISCUSSION OF TESTS

Static Longitudinal Stability

The static longitudinal stability data for the model are presented in figures 6 to 8. These data, which were obtained by utilizing the forced oscillation model for the same test conditions as the dynamic tests, are presented to verify and to aid in the interpretation of the dynamic tests results. Presented in figure 6 are the results of static tests to determine the effect of removing the body flap on the longitudinal stability. As expected, removing the flap resulted in an increased pitching moment at zero lift because of the effective change in camber and a slight destabilizing effect at angles of attack above 10°. The effect of the vortex lift of this planform is evident in the increase in the slope of the lift curve at Mach numbers of 0.3, 0.8, and 0.9 in figure 6. The data of figures 7 and 8 show the effect of a large rudder flare tested in combination with a body flap deflection and the effect of orbital maneuvering system (OMS) installations, respectively.

Static Lateral Stability

The static lateral stability data for the model are presented in figures 9 to 12 and show the effect of the vertical tail, a combination of body flap deflection and rudder flare, OMS installation, and body flap, respectively. These data show the expected increments in directional stability and dihedral effect for the removal of the vertical tail. The other configuration changes show no significant effects on the static lateral characteristics.

Pitching Oscillation Tests

The oscillatory longitudinal stability parameters measured in the pitching oscillation tests at Mach numbers of 0.3, 0.8, 0.9, 0.98, and 1.2 are presented in figures 13 to 20. The in-phase with displacement parameter $C_{m_\alpha} - k^2 C_{m_{\dot{q}}}$ and the out-of-phase with displacement parameter $C_{m_q} + C_{m_{\dot{\alpha}}}$ are presented in figures 13 to 16. In order to determine the damping for varied flight conditions, tests were conducted with the most forward $(0.65l)$ and most aft $(0.67l)$ center-of-gravity locations. (See fig. 13.) A comparison of the in-phase derivative with the slopes determined from the results of the static tests is also presented in the figure. For all the Mach numbers except 0.98, there is very good agreement between the dynamic data and the static results. At a Mach number of 0.98 there are some differences between the static and dynamic results at angles of attack above 16°.

In general, the model exhibited positive pitch damping $\left(\text{negative values of } C_{m_q} + C_{m_{\dot{\alpha}}}\right)$ throughout the angle-of-attack range. For the near transonic Mach numbers (M = 0.8 to 0.98) as separation begins to occur on the wing at angles of attack in excess of 16°, there is a marked increase in the pitch damping. (See figs. 13(b) to 13(d).) This increase in damping is possibly the result of this region of separated flow lagging the body motion and therefore tending to damp out the body motion.

Shown in figures 13(d) (M = 0.98) and 13(e) (M = 1.2) are regions of very low damping and negative damping starting at an angle of attack of about 10°. These regions of negative damping also occur as nonlinearities in both the static C_{m_α}, in-phase parameter $\left(C_{m_\alpha} - k^2 C_{m_{\dot{q}}}\right)$ and changes in $C_{N_\alpha} - k^2 C_{N_{\dot{q}}}$ and $C_{N_q} + C_{N_{\dot{\alpha}}}$ (fig. 17(c)). These nonlinearities in $C_{m_\alpha} - k^2 C_{m_{\dot{q}}}$ and in $C_{m_q} + C_{m_{\dot{\alpha}}}$ are probably associated with separation caused by the mixed flow regions and standing shocks on the wing at the Mach numbers near 1.

The data of figure 14 present the effect on the pitch damping of removing the body flap. The data show that removal of the flap had essentially no effect on the pitch damping.

The effects of increased rudder flare (85°) combined with a body flap deflection are presented in figure 15. The increased rudder flare and body flap deflection resulted in a decrease in damping at the higher angles of attack; for the higher Mach numbers (0.98 and 1.2) there were regions of negative damping. This decreased damping is primarily due to alterations of the shock pattern on the aft portion of the wing and body caused by the bluntness of 85° flare.

The effects of the OMS pods installation are shown in figure 16. Removing the OMS pods had essentially no effect on the damping except at a Mach number of 0.98 (fig. 16(d)) where it resulted in a decrease in the pitch damping.

Presented in figures 17 to 20 are the changes in normal force due to pitching velocity $\left(C_{N_q} + C_{N_{\dot\alpha}}\right)$ and the in-phase with displacement parameter $\left(C_{N_\alpha} - k^2 C_{N_{\dot q}}\right)$. The normal force due to pitching velocity also had the regions of nonlinearities that were analogous to those noted in the discussion of the pitch damping. Presented also in figure 17 is the comparison of the in-phase parameter $C_{N_\alpha} - k^2 C_{N_{\dot q}}$ with that determined from the static test results. There is good agreement between the static and in-phase dynamic results.

Yawing Oscillation Tests

The oscillatory stability parameters measured in the yawing oscillation tests are presented in figures 21 to 26. The in-phase with displacement parameter $\left(C_{n_\beta} \cos\alpha + k^2 C_{n_{\dot r}}\right)$ and out-of-phase with displacement parameter $\left(C_{n_r} - C_{n_{\dot\beta}} \cos\alpha\right)$ are presented in figures 21 to 23. The model had positive damping in yaw (negative values of $C_{n_r} - C_{n_{\dot\beta}} \cos\alpha$) throughout the test angle of attack and Mach number range. Presented in figure 21 is the effect of removing the vertical tail on the yaw damping $\left(C_{n_r} - C_{n_{\dot\beta}} \cos\alpha\right)$ along with data showing a comparison of the in-phase parameter $\left(C_{n_\beta} \cos\alpha + k^2 C_{n_{\dot r}}\right)$ and $C_{n_\beta} \cos\alpha$ computed from the static tests. There appears to be reasonably good agreement between the static and dynamic results. Removing the vertical tail resulted in the expected destabilizing increment in the in-phase parameter and a reduction in yaw damping at a Mach number of 0.3. At the higher Mach numbers ($M \geqq 0.8$), there appears to be a tail contribution to yaw damping but it is not as well defined as at the lowest Mach number. The data presented in figure 22 show the effect of increasing the rudder flare to 85° as a speed brake and deflecting the body flap 13°. These results show that the increased speed brake deflections at all but the lowest test Mach number ($M = 0.3$) resulted in an increase in yaw damping and a decrease in directional stability. Data presented in figure 23 show that removing the OMS pods also resulted in an increase in damping at the higher Mach numbers.

The rolling moment due to yawing velocity $\left(C_{l_r} - C_{l_{\dot\beta}} \cos\alpha\right)$ is presented in figures 24 to 26. Also presented in figure 24 is a comparison of the in-phase parameter $\left(C_{l_\beta} \cos\alpha + k^2 C_{l_{\dot r}}\right)$ with $C_{l_\beta} \cos\alpha$ computed from the static data. The comparisons show the static data to have the same trends with α and the same level as the in-phase parameter. The measured value of $C_{l_r} - C_{l_{\dot\beta}} \cos\alpha$ is slightly positive at zero angle of attack with an increase with increased α. Configuration changes have little effect on this parameter.

Rolling Oscillation Tests

The oscillatory stability parameters measured in the rolling oscillation tests are presented in figures 27 to 31. The in-phase with displacement parameter $\left(C_{l_\beta} \sin \alpha - k^2 C_{l_{\dot{p}}}\right)$ and out-of-phase with displacement parameter $\left(C_{l_p} + C_{l_{\dot{\beta}}} \sin \alpha\right)$ are presented in figures 27 to 29. Data showing the effect of vertical tail on the roll damping are presented in figure 27 along with a comparison of $C_{l_\beta} \sin \alpha - k^2 C_{l_{\dot{p}}}$ with $C_{l_\beta} \sin \alpha$ computed from the static tests. There is good agreement between the static and dynamic test results up to angles of attack of about $8^{\rm O}$ to $10^{\rm O}$. The model exhibited positive roll damping $\left(\text{negative values of } C_{l_p} + C_{l_{\dot{\beta}}} \sin \alpha\right)$ at all but the highest angles of attack at Mach numbers of 0.98 and 1.2 (see figs. 27(d) and 27(e)) where the damping begins to decrease to the point where at angles of attack above $20^{\rm O}$, the model had negative damping. Results of tests to determine the effect of rudder flare and OMS pods (figs. 28 and 29) on the roll damping show only small effects on the damping level.

The yawing moment due to rolling velocity $\left(C_{n_p} + C_{n_{\dot{\beta}}} \sin \alpha\right)$ data measured in the roll tests are presented in figures 30 and 31. These results show that the parameter is nonlinear with angle of attack and has both positive and negative values. At the near transonic Mach numbers (M = 0.8 and 0.9) at high angles of attack, there was considerable scatter in the data that was apparently caused by a sting vibration and therefore the data for these conditions are not presented. The comparisons of the in-phase parameter $C_{n_\beta} \sin \alpha - k^2 C_{n_{\dot{p}}}$ with $C_{n_\beta} \sin \alpha$ computed from the static data show some discrepancies at the higher angles of attack. The configuration changes appeared to have some effect on the level of the cross derivative.

MOTION STUDY ANALYSIS

In order to assess better the impact of the results measured in the forced oscillation tests, three-degrees-of-freedom longitudinal and lateral motion equations have been used to calculate the vehicle longitudinal and lateral period and damping. These analyses were made by using the measured dynamic derivatives with the $\dot{\alpha}$ and $\dot{\beta}$ terms assumed to be zero, static data presented in table II, and vehicle mass properties as given in table III taken from the shuttle data base. The calculations were made by utilizing the basic airframe in that no stability augmentation was input. Variations in the stability derivatives were made to determine the effects of the individual derivatives on the calculated period and damping. Although the vehicle was designed to fly in the active control mode, analysis of the unaugmented vehicle characteristics would indicate the existence of significant anomalies that would have to be taken into consideration in the vehicle flight control system design.

Longitudinal Analysis

Because of the requirements for a large center-of-gravity travel for the shuttle orbiter ($0.65l$ to $0.67l$), the effect of center-of-gravity position on the vehicle longitudinal oscillatory and aperiodic modes was computed and these results are presented in figure 32. For these analyses the damping was assumed to vary linearly between the center-of-gravity positions tested. The calculations have been made for Mach numbers of 0.3, 0.6, 0.8, 0.9, 0.95, and 1.0 and for the conditions listed in table I. At the subsonic Mach number of 0.3 (fig. 32(a)) for the forward center of gravity ($0.65l$) where the vehicle is neutrally stable, the results show the characteristic short period and phugoid oscillations; however, as the center of gravity is moved aft and the vehicle becomes statically unstable, the short period and phugoid oscillations break down and the roots of the stability quartic combine to form a third oscillation and two aperiodic modes. The third oscillation has been discussed in reference 4. Experience from the supersonic transport work of reference 5 has shown that the third oscillation was of such long period that it creates no control problems. The unstable aperiodic mode is the main concern from these results. This mode is directly associated with the vehicle static stability and at the aft center of gravity ($0.675l$) the reciprocal of the time to damp to half amplitude is approximately -0.65 which corresponds to a time to double amplitude of 1.5 seconds. The feasibility of flying at this level of instability would depend directly upon the ability to determine the vehicle attitude accurately enough to prevent the motion from building to a level of pitch acceleration where recovery was not possible. At the higher Mach numbers (0.6, 0.8, 0.9, 0.95, and 1.0), there is no phugoid for the range of center-of-gravity positions shown in figure 32. However, there is a short period oscillation and an aperiodic divergence which goes to double amplitude at 0.6 Mach number for the center of gravity at $0.675l$ in 1.3 seconds and to double amplitude at Mach 1.0 in 8 seconds. The results show the higher Mach numbers to be less critical for the aft center of gravity as a result of the increased static margin due to the rearward shift of the aerodynamic center at transonic speeds.

In order to determine the importance of the pitch damping derivative C_{m_q} on the vehicle dynamics, calculations have been made to determine the effects of varying this parameter plus or minus an order of magnitude (10 times the measured value) and these results are presented in figure 33. For the lowest Mach number (M = 0.3), varying the value of C_{m_q}, as expected, did greatly affect the character of the short period which breaks down into two stable aperiodic modes for values of C_{m_q} near the measured value. However, the large effect was on the unstable aperiodic mode (see fig. 33(a)) which was very sensitive to small changes in C_{m_q} as C_{m_q} became positive. Examination of the longitudinal normal mode ratios as in reference 4 indicated that the aperiodic divergence would occur predominately in angle of attack. For the higher Mach numbers (M = 0.8, 0.9, 0.95, and 1.0) because of the level of static stability, changes in C_{m_q} had little effect

14

on the aperiodic modes but, as is evident, the short period oscillation remained intact and quite dependent upon the magnitude of C_{m_q}. The major results from these calculations are that as the vehicle becomes unstable, the pitch damping parameter C_{m_q} not only affects the short period oscillation but also has some large effects on the aperiodic mode divergent rate.

<center>Lateral Analysis</center>

The effect of center-of-gravity position on the lateral oscillatory and aperiodic modes is presented in figure 34 for Mach numbers of 0.3, 0.6, 0.8, 0.9, 0.95, and 1.0. These results show the characteristic Dutch roll oscillation and roll and spiral aperiodic modes. Varying the center of gravity did not appreciably change the characteristic motions or their values. The effect of the parameters C_{n_r}, C_{n_p}, C_{l_p}, and C_{l_r} on the calculated vehicle lateral oscillatory and aperiodic modes is presented in figures 35 to 38.

Yaw derivatives.- Presented in figure 35 is the effect of yaw damping C_{n_r} on the lateral period and damping. As pointed out in the previous discussion for the measured values of C_{n_r}, the analysis shows the characteristic Dutch roll oscillation and the aperiodic roll and spiral modes. For the Mach numbers of 0.3 and 0.6 the spiral mode was unstable for the measured values of the derivatives. Decreasing the yaw damping (less negative values of C_{n_r}) tended to decrease the stability of the Dutch roll oscillation, the spiral mode, and the roll aperiodic mode, as C_{n_r} became positive, the spiral mode became more unstable and increasingly sensitive to variations in C_{n_r}. The roll aperiodic mode and the Dutch roll oscillation tended to become less stable as Mach number increased, but remained stable for all values of C_{n_r} investigated.

The results of the analysis to determine the effect of the yawing moment due to roll rate on the calculated period and damping are presented in figure 36. Both the Dutch roll oscillation and the aperiodic roll mode are affected by C_{n_p}, increased positive values of C_{n_p} making the Dutch roll oscillation more stable and at the same time reducing the stability level of the aperiodic roll mode to zero at the highest C_{n_p} value studied.

Roll derivatives.- The effect of roll damping C_{l_p} on the calculated vehicle period and damping is presented in figure 37. As expected, the aperiodic roll mode was extremely sensitive to variations of C_{l_p} to the extent that $1/t_{1/2}$ as presented is multiplied by 10^{-1}. The sensitivity of the roll mode to C_{l_p} is greatly reduced by an increase in Mach number as can be seen by a comparison of the data at a Mach number of 0.3 (fig 37(a)) to

the data at a Mach number of 1.0 (fig. 37(c)). The Dutch roll oscillation is stable for negative values of C_{l_p}, but there are some unstable regions as C_{l_p} becomes positive.

The effect of the rolling moment due to yawing velocity on calculated vehicle damping is presented in figure 38. These results show that C_{l_r} affected the Dutch roll and both the roll and spiral aperiodic modes. The main point is that measured values of C_{l_r} resulted in an unstable spiral mode at the lower Mach numbers which became more unstable for small increases in C_{l_r}.

SUMMARY OF RESULTS

An investigation has been conducted to determine the subsonic and transonic dynamic stability characteristics of a 0.0165-scale model of a modified 089B shuttle orbiter. The results of this investigation may be summarized as follows:

1. The model exhibited positive damping in pitch except at an angle of attack of about 10^0 for Mach numbers of 0.98 and 1.20. The model had positive yaw damping throughout the test angle of attack and Mach number range and had positive roll damping except for angles of attack in excess of 20^0 for Mach numbers of 0.98 and 1.20.

2. There was generally good agreement between the appropriate parameters in the in-phase dynamic data and in the corresponding static data.

3. The results from the longitudinal stability calculations showed that small changes in the pitch damping caused a breakdown of the short period oscillation at a Mach number of 0.3; the significant result was that the aperiodic divergence was very sensitive to small changes in the pitch damping for positive values of the pitch damping.

4. The lateral stability calculations showed that the yaw damping affected the Dutch roll oscillation, decreased yaw damping tending to decrease the stability of the Dutch roll oscillation; the major effect was on the unstable spiral mode where the divergent rate was very dependent upon the value of the yaw damping and on the rolling moment due to yaw rate.

Langley Research Center
National Aeronautics and Space Administration
Hampton, Va. 23665
July 15, 1975

REFERENCES

1. Freeman, Delma C., Jr.; Boyden, Richmond P.; and Davenport, Edwin E.: Supersonic Dynamic Stability Characteristics of a Space Shuttle Orbiter. NASA TN D-8043, 1975.

2. Uselton, Bob L.; and Jenke, Leroy M.: Pitch-, Yaw-, and Roll-Damping Characteristics of a Shuttle Orbiter at $M_\infty = 8$. AEDC-TR-74-129, U.S. Air Force, May 1975.

3. Braslow, Albert L.; Hicks, Raymond M.; and Harris, Roy V., Jr.: Use of Grit-Type Boundary-Layer-Transition Trips on Wind-Tunnel Models. NASA TN D-3579, 1966.

4. Etkin, Bernard: Dynamics of Flight. John Wiley & Sons, Inc., 1962.

5. Freeman, Delma C., Jr.: Low-Subsonic Flight and Force Investigation of a Supersonic Transport Model With a Double-Delta Wing. NASA TN D-4719, 1968.

TABLE I.- FLIGHT CONDITIONS FOR ANALYSIS

[Nominal trajectory shown in fig. 5]

Mach number	α, deg	Altitude, m	Velocity, m/sec	q_∞, N/m^2
0.3	12.0	914	129.0	10 170
.6	12.0	7 240	186.8	10 017
.8	13.0	11 030	236.1	10 117
.9	13.5	12 500	258.2	10 175
.95	13.5	13 260	273.1	10 055
1.0	11.5	17 230	289.1	5 975

TABLE II.- ORBITER STATIC AERODYNAMICS USED IN ANALYSIS

[Derived from shuttle data base]

α, deg	M = 0.2	M = 0.6	M = 0.9	M = 1.2
Untrimmed lift coefficient				
0	0.065	-0.104	-0.120	0.056
5	.155	.142	.152	.234
7.5	.270	.265	.280	.372
10	.392	.399	.412	.500
12.5	.510	.530	.545	.630
15	.644	.669	.674	.759
20	.878	.934	.900	.986
25	1.104	1.129	.918	1.123
Untrimmed drag coefficient				
0	0.065	0.067	0.087	0.169
5	.065	.068	.100	.184
7.5	.074	.078	.128	.210
10	.090	.095	.161	.242
12.5	.112	.125	.213	.295
15	.151	.178	.276	.357
20	.288	.349	.428	.510
25	.479	.537	.536	.668
Untrimmed pitching moment coefficient (forward center of gravity)				
0	0.051	0.056	0.089	0.062
5	.051	.055	.060	.003
7.5	.051	.054	.043	-.019
10	.051	.054	.024	-.033
12.5	.050	.054	.003	-.041
15	.049	.050	-.007	-.052
20	.026	.026	0	-.077
25	.015	.034	0	-.058

TABLE II.- Continued

α, deg	M = 0.2	M = 0.6	M = 0.9	M = 1.2
$C_{m_{\delta_e}}$ (forward center of gravity)				
0	-0.008	-0.009	-0.009	-0.006
5	-.008	-.009	-.009	-.006
7.5	-.008	-.009	-.009	-.006
10	-.008	-.009	-.009	-.006
12.5	-.008	-.009	-.009	-.006
15	-.008	-.009	-.009	-.006
20	-.007	-.009	-.009	-.006
25	-.007	-.007	-.009	-.006
$C_{L_{\delta_e}}$				
0	0.0185	0.020	0.017	0.0075
5	.0180	.021	.017	.0075
7.5	.0175	.021	.017	.0075
10	.0175	.021	.017	.0075
12.5	.0175	.018	.017	.0075
15	.0175	.018	.017	.0075
20	.0160	.016	.015	.0075
25	.0135	.014	.010	.0075
$C_{D_{\delta_e}}$				
0	0.0016	0.0012	0.0006	-0.0004
5	.0022	.0028	.0020	.0004
7.5	.0031	.0041	.0028	.0012
10	.0040	.0054	.0036	.0020
12.5	.0046	.0059	.0048	.0022
15	.0052	.0064	.0060	.0024
20	.0070	.0078	.0066	.0040
25	.0080	.0091	.0071	.0050

TABLE II.- Concluded

α, deg	M = 0.2	M = 0.6	M = 0.9	M = 1.2
C_{n_β} per degree				
0	0.00155	0.00190	0.00310	0.00285
5	.00180	.00180	.00275	.00250
7.5	.00190	.00180	.00235	.00180
10	.00195	.00180	.00190	.00125
12.5	.00195	.00180	.00120	.00040
15	.00190	.00175	.00040	-.00225
20	.00175	.00140	-.00100	-.00280
25	.00160	.00080	-.00100	-.00325
C_{l_β} per degree				
0	0.00041	0.00073	0.00002	-0.00069
5	-.00049	-.00067	-.00068	-.00083
7.5	-.00099	-.00097	-.00089	-.00096
10	-.00119	-.00147	-.00101	-.00109
12.5	-.00150	-.00167	-.00163	-.00111
15	-.00160	-.00166	-.00187	-.00118
20	-.00171	-.00151	-.00204	-.00128
25	-.00166	-.00143	-.00222	-.00180
C_{Y_β} per degree				
0	-0.0190	-0.0195	-0.0230	-0.0225
5	-.0190	-.0195	-.0230	-.0210
7.5	-.0190	-.0195	-.0225	-.0200
10	-.0190	-.0195	-.0220	-.0190
12.5	-.0185	-.0195	-.0210	-.0180
15	-.0185	-.0200	-.0195	-.0175
20	-.0180	-.0220	-.0170	-.0155
25	-.0200	-.0210	-.0140	-.0310

TABLE III.- ORBITER MASS PROPERTIES

[Derived from shuttle data base]

Mass, kg 84 096

I_Y, kg-m^2 . . . . 7 710 400

I_X, kg-m^2 . . . . 1 014 100

I_Z, kg-m^2 . . . . 7 870 400

I_{XZ}, kg-m^2 . . . . 199 300
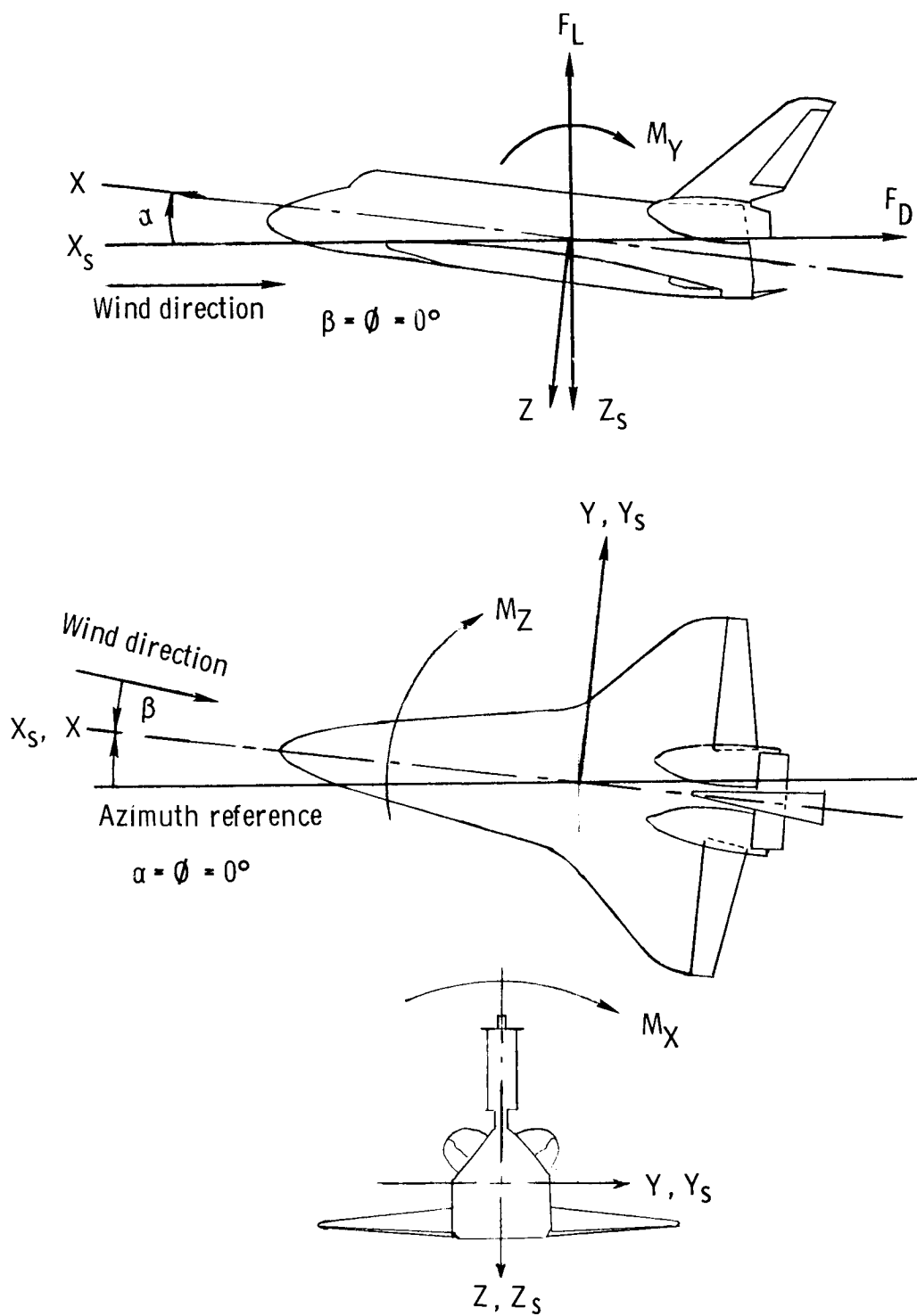
Figure 1.- System of axes used in investigation.   Arrows indicate positive
direction of moments, forces, and angles.

Reference dimensions

Area	S = 680 cm²
MAC	c̄ = 19.899 cm
Center of gravity	x = 35.149 cm (forward)
	x = 36.230 cm (aft)
Length	l = 54.076 cm
Span	b = 39.259 cm

39.259

17.412

45°

81°

OMS pods

Rudder flare

Body flap

Z_{cg} = 15.682

54.076

Z = 16.764

Water-line zero, Z_{ref} = 0

Forward center of gravity = 0.65 l

Aft center of gravity = 0.67 l
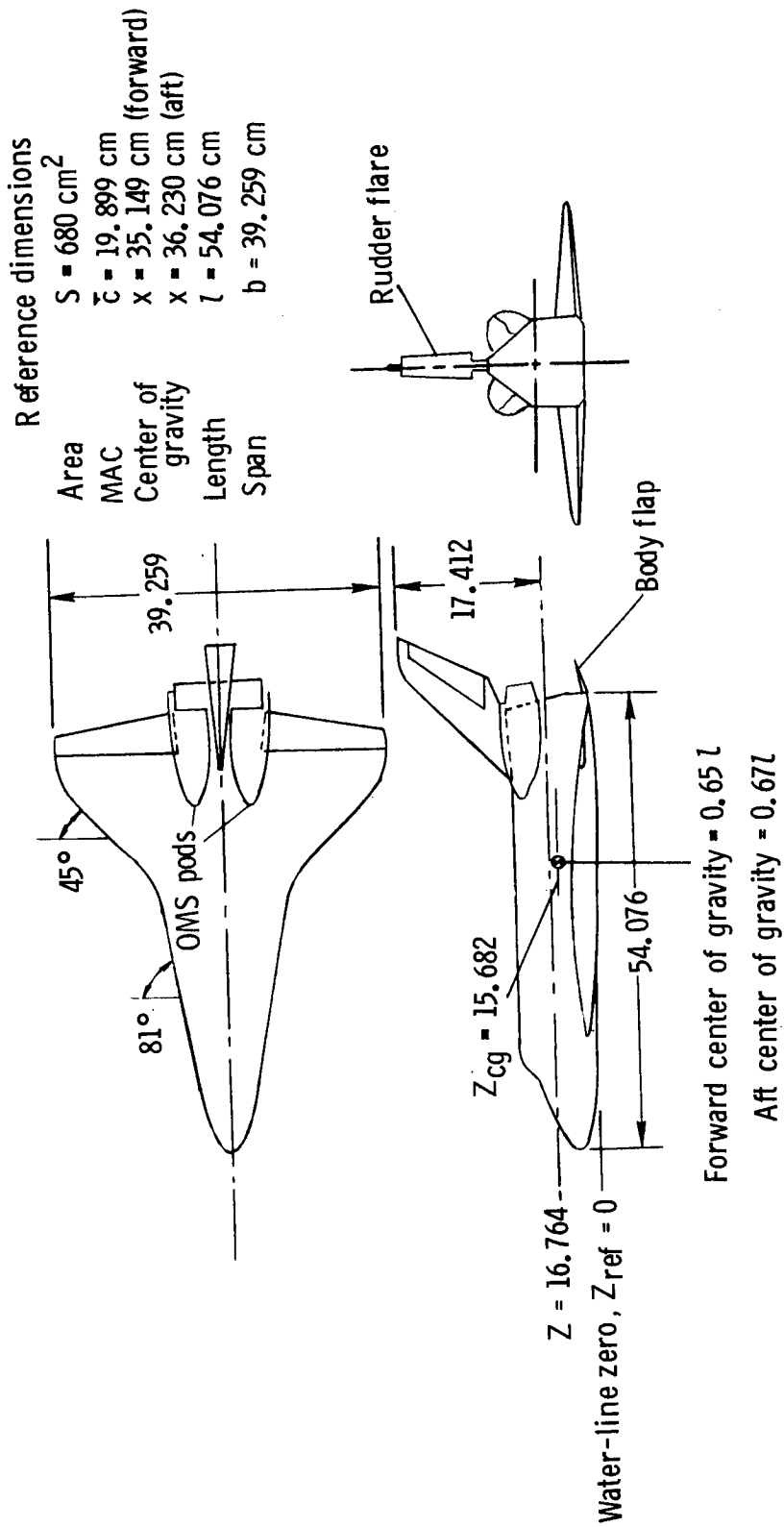
Figure 2.- Sketch of configuration tested. All dimensions are given in centimeters.
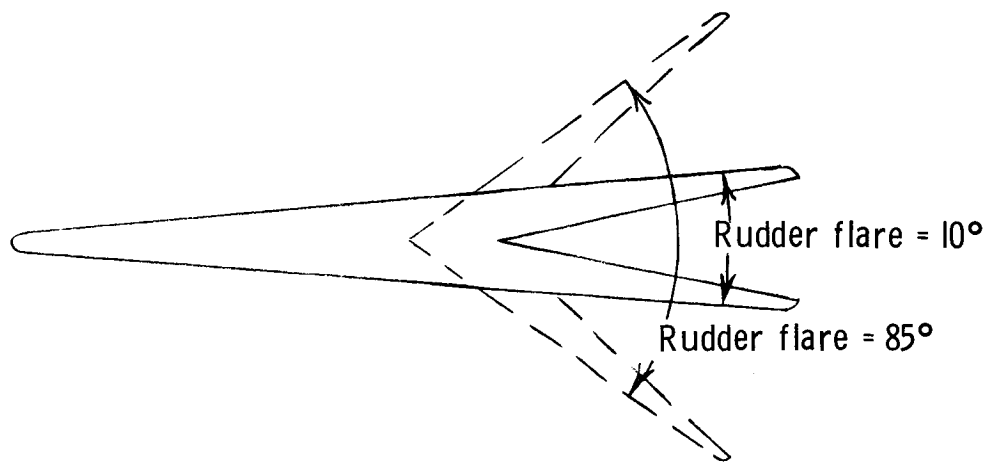
Figure 3.- Rudder flare angle definition.
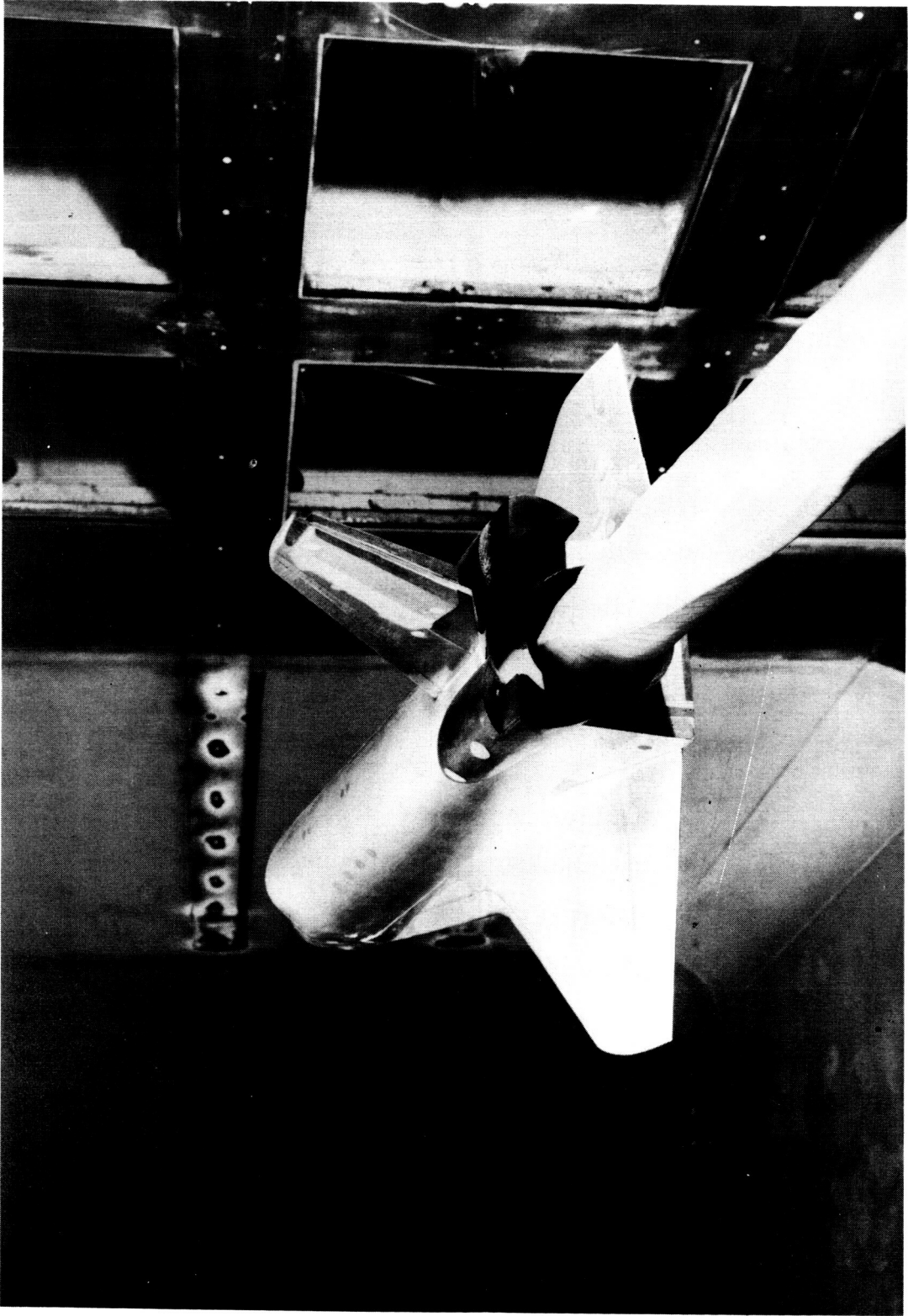
L-73-4860

Figure 4.- Photograph of model mounted for forced oscillation tests in the Langley 8-foot transonic pressure tunnel.
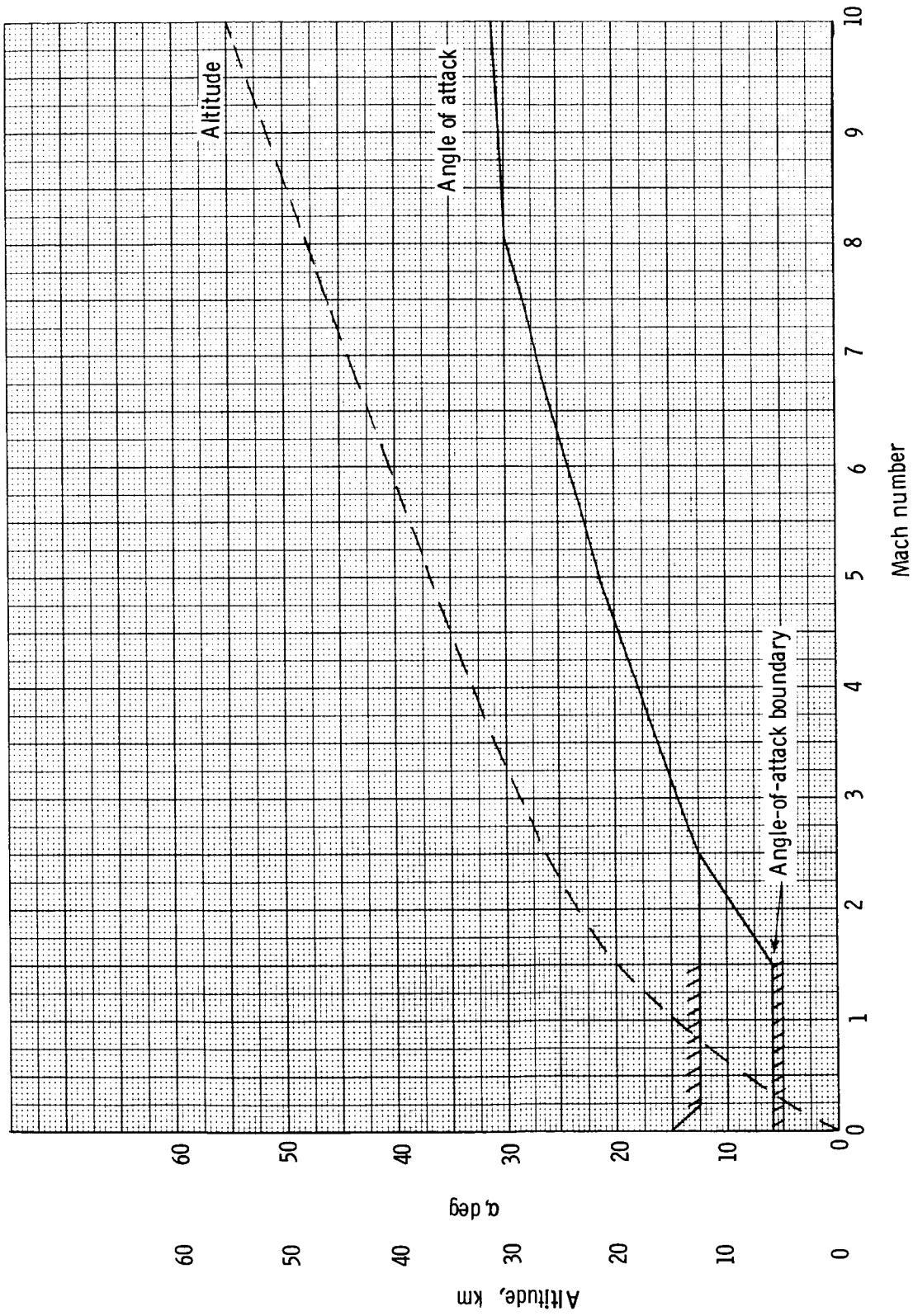
Figure 5.- Nominal shuttle entry flight profile. Forward center of gravity.
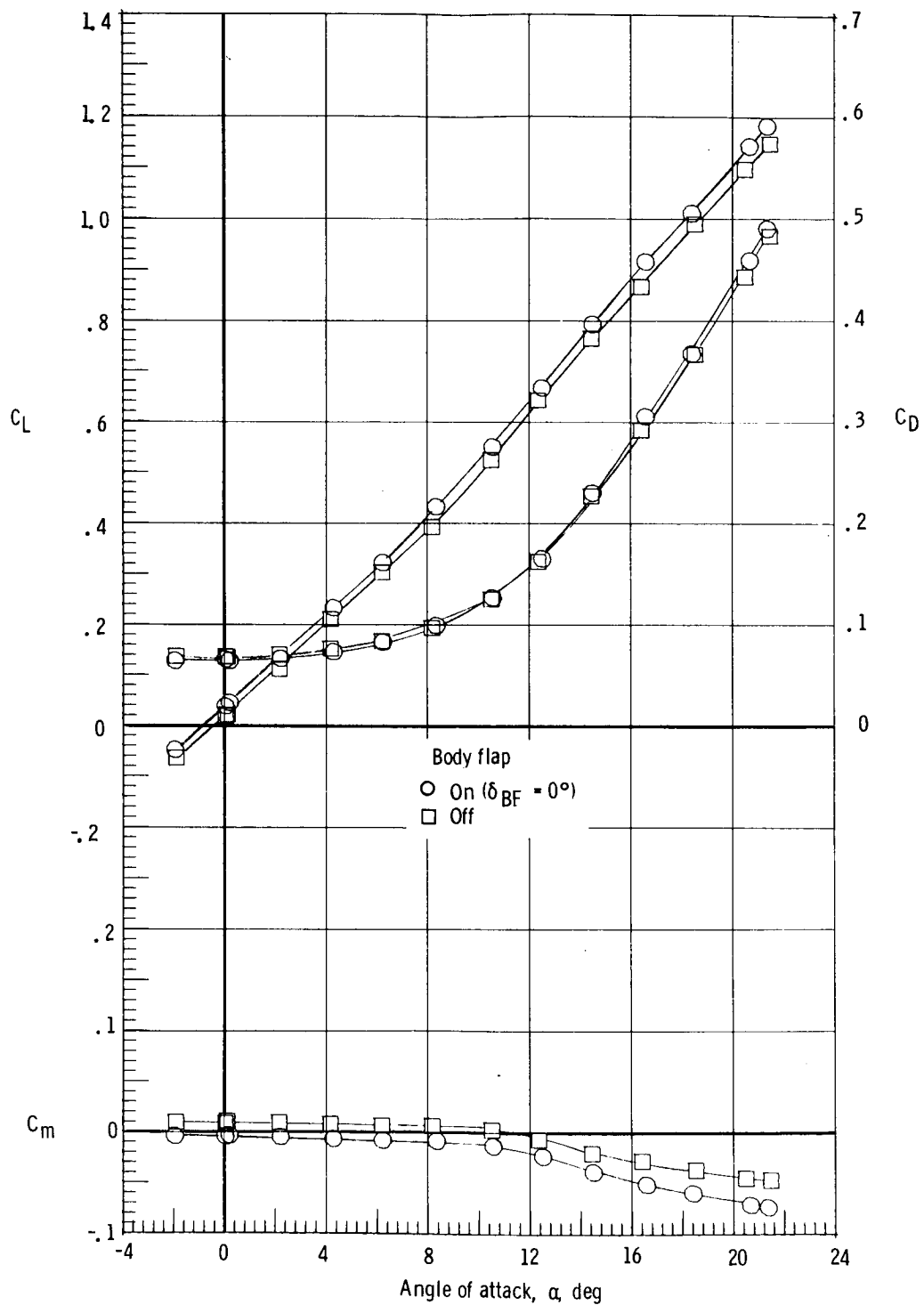
(a)   M = 0.3.

Figure 6.- Effect of body flap on static longitudinal characteristics.   Forward center of gravity; $\delta_e = 0°$; rudder flare, $10°$.
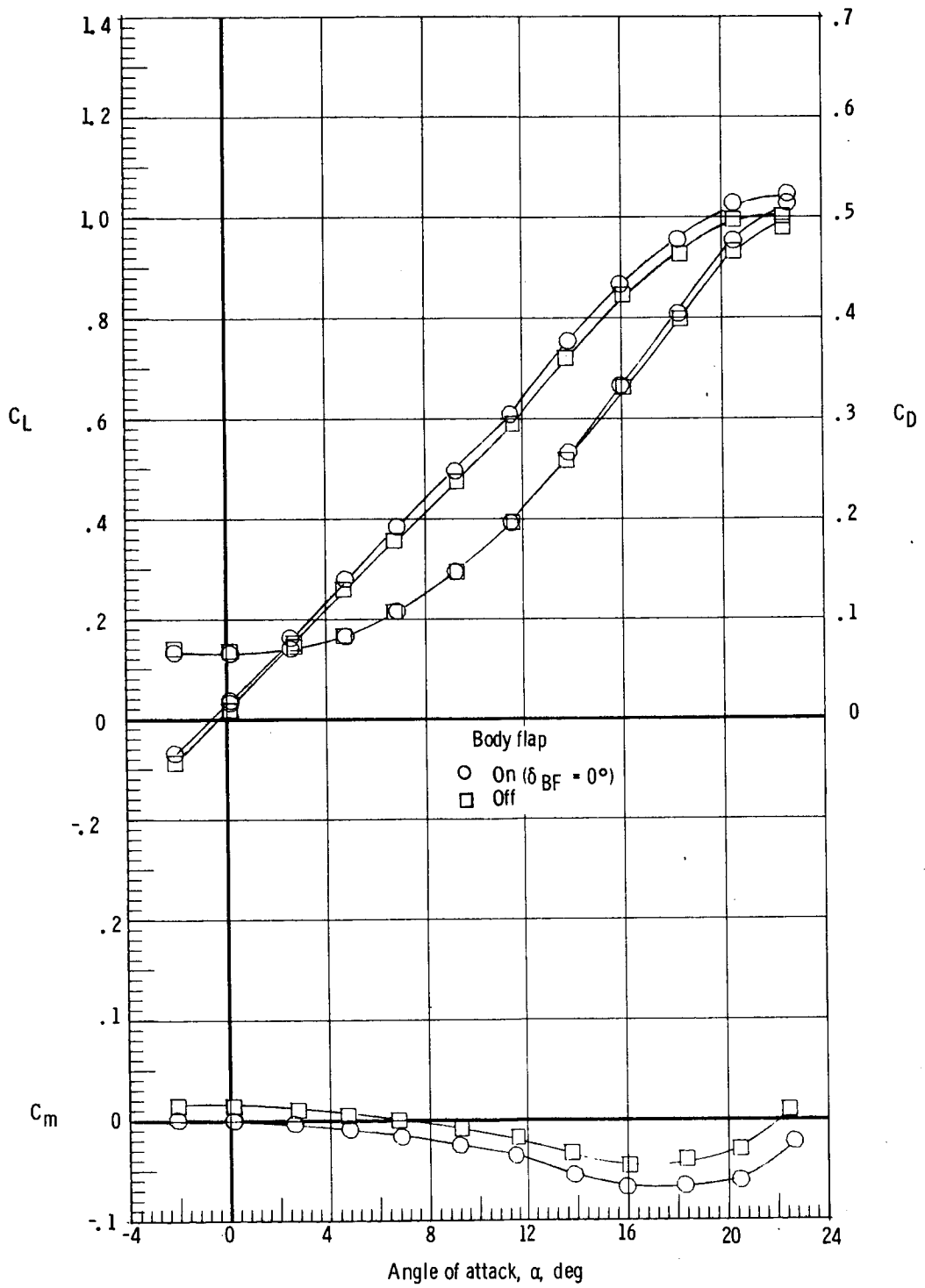
(b) M = 0.8.

Figure 6.- Continued.
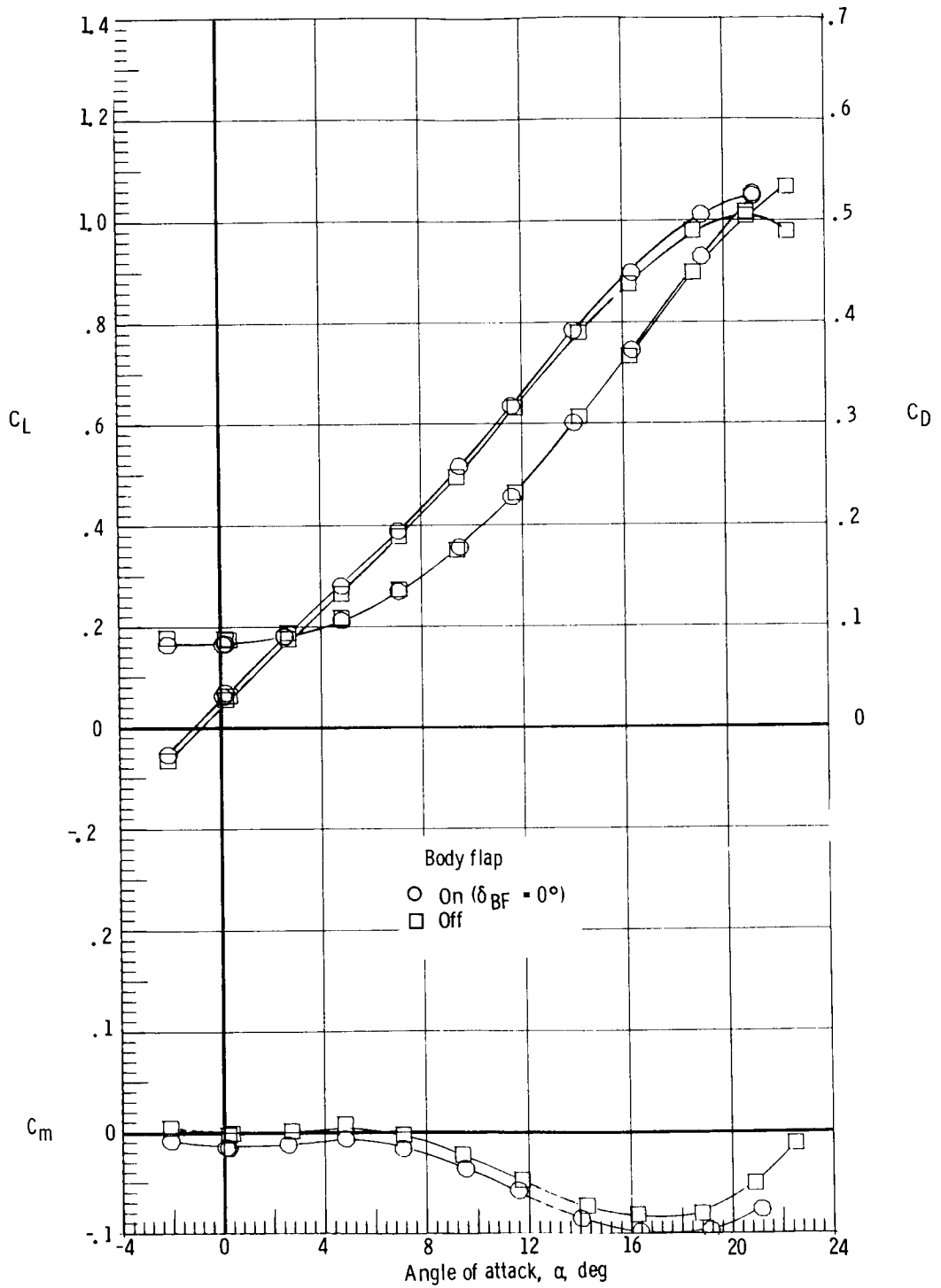
(c) M = 0.9.

Figure 6.- Continued.
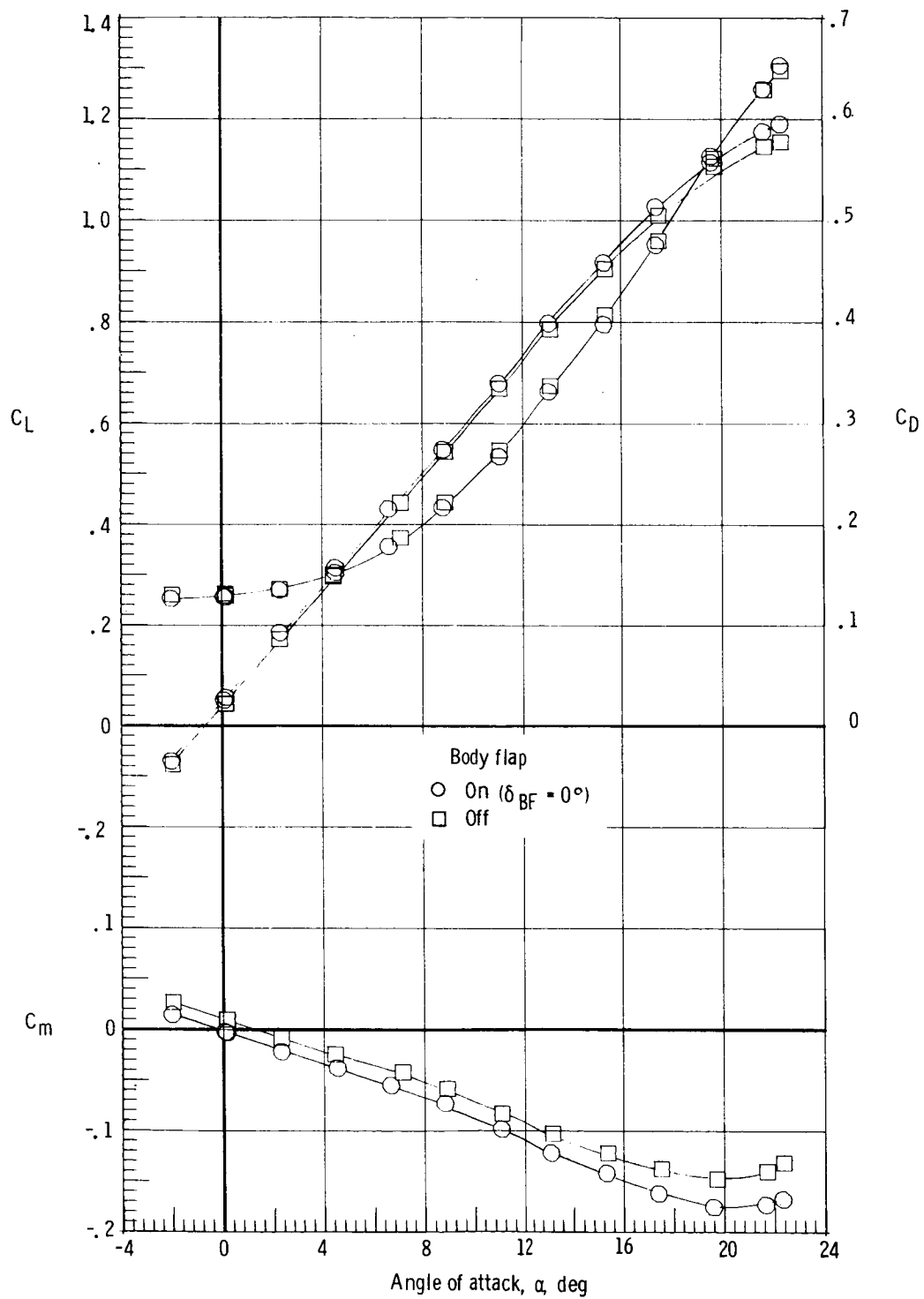
(d) M = 0.98.

Figure 6.- Continued.
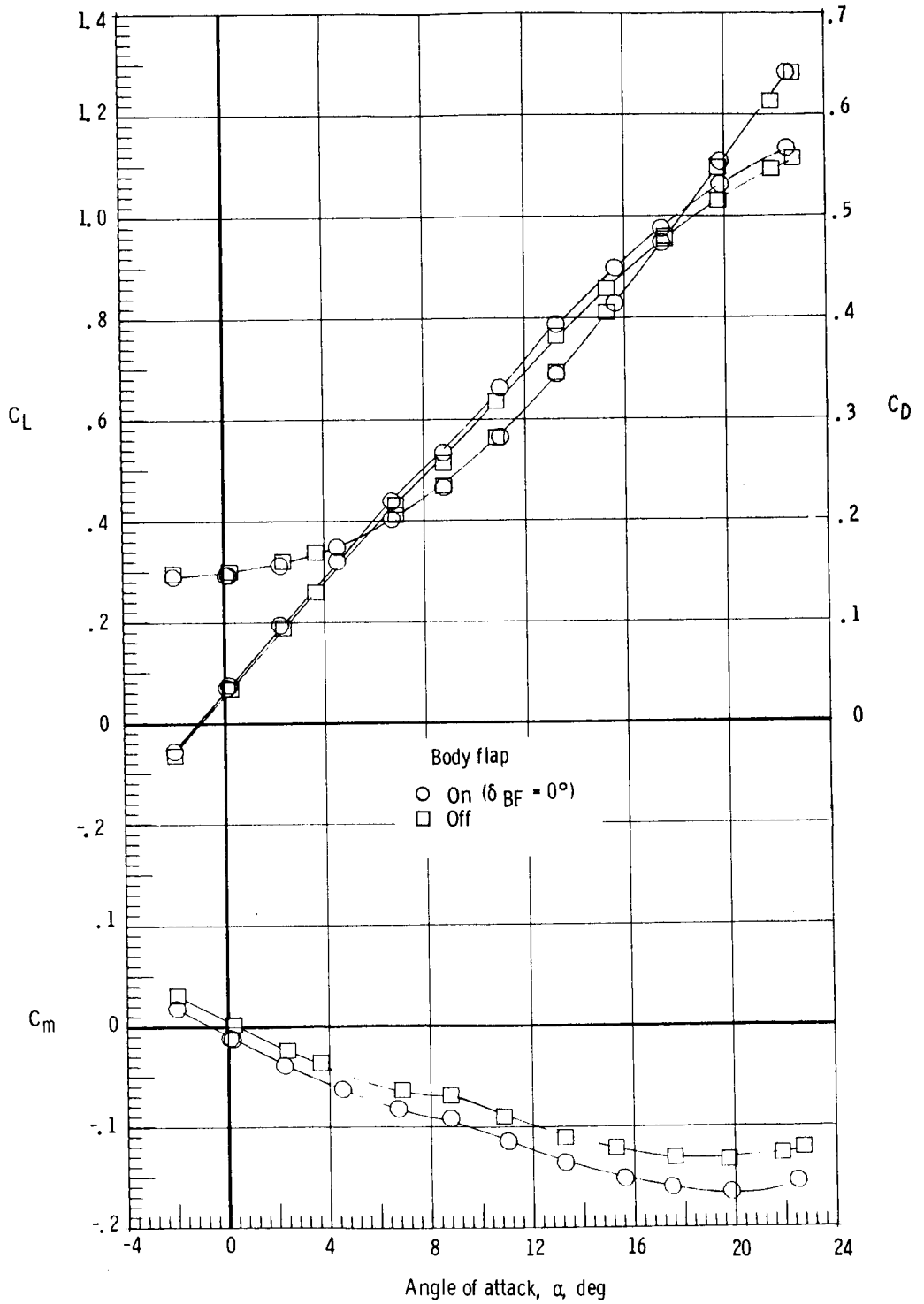
(e) M = 1.2.

Figure 6.- Concluded.
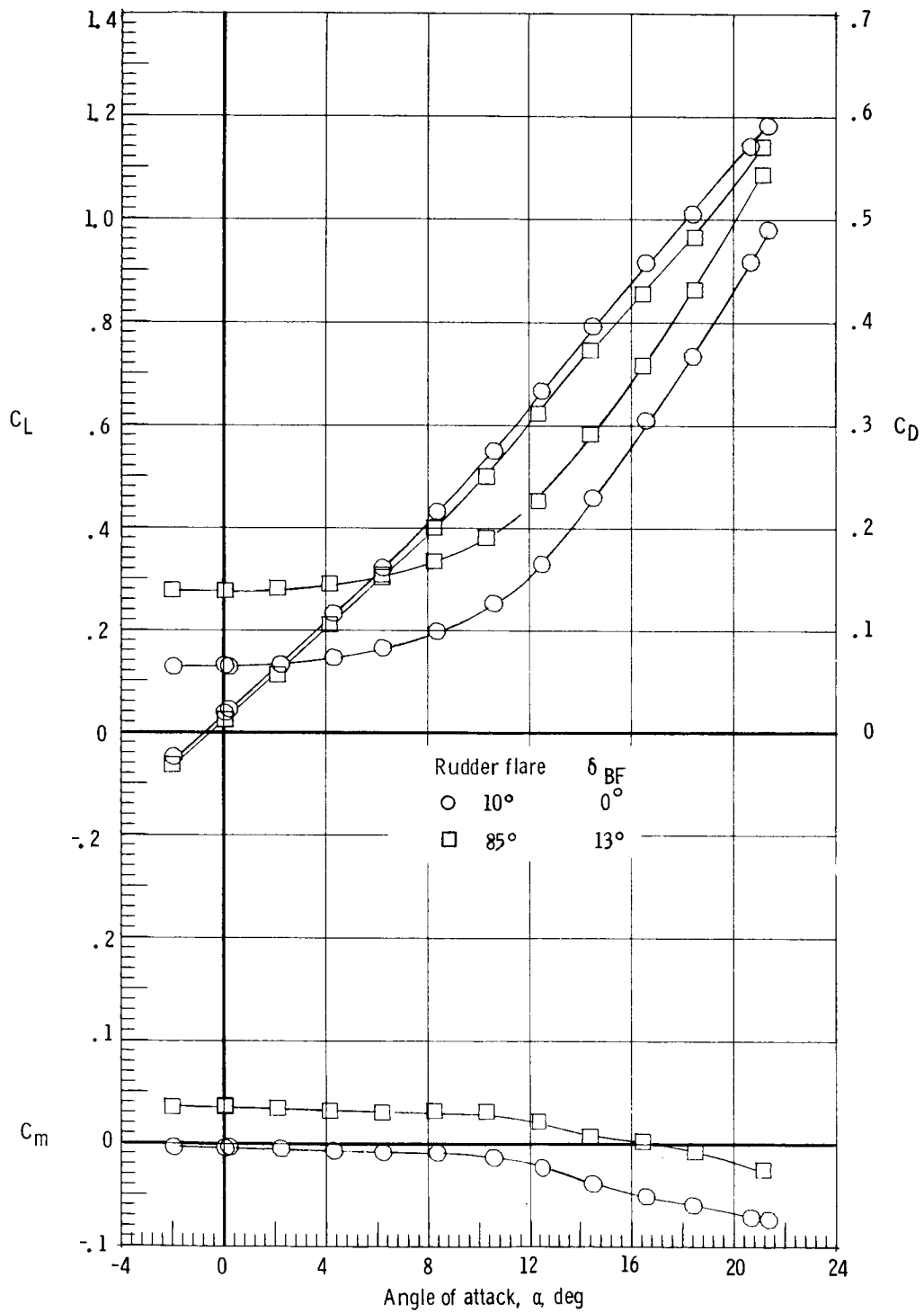
(a) M = 0.3.

Figure 7.- Effect of body flap deflection and rudder flare on static longitudinal characteristics.   Forward center of gravity; $\delta_e = 0^o$.
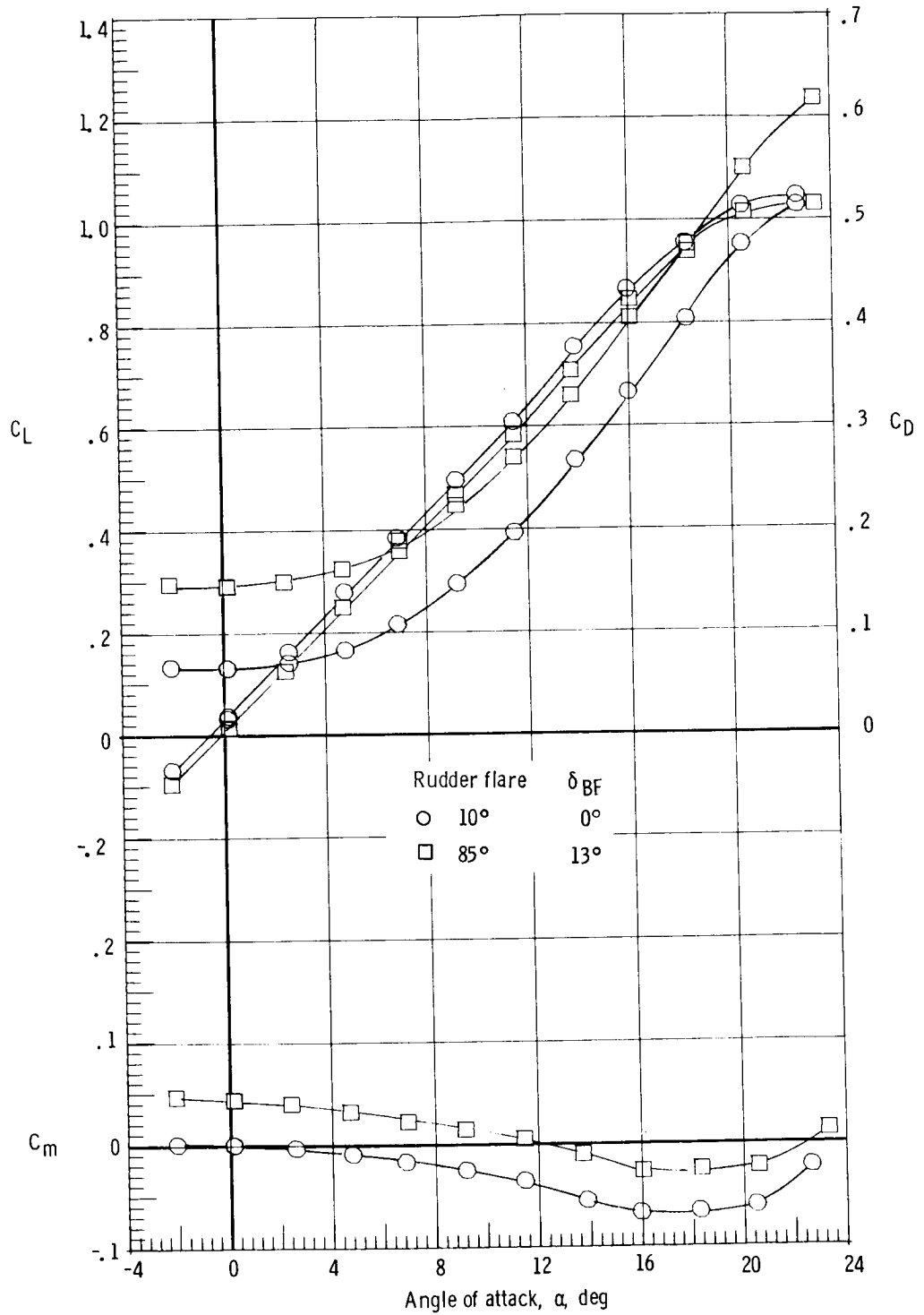
(b) M = 0.8.

Figure 7.- Continued.
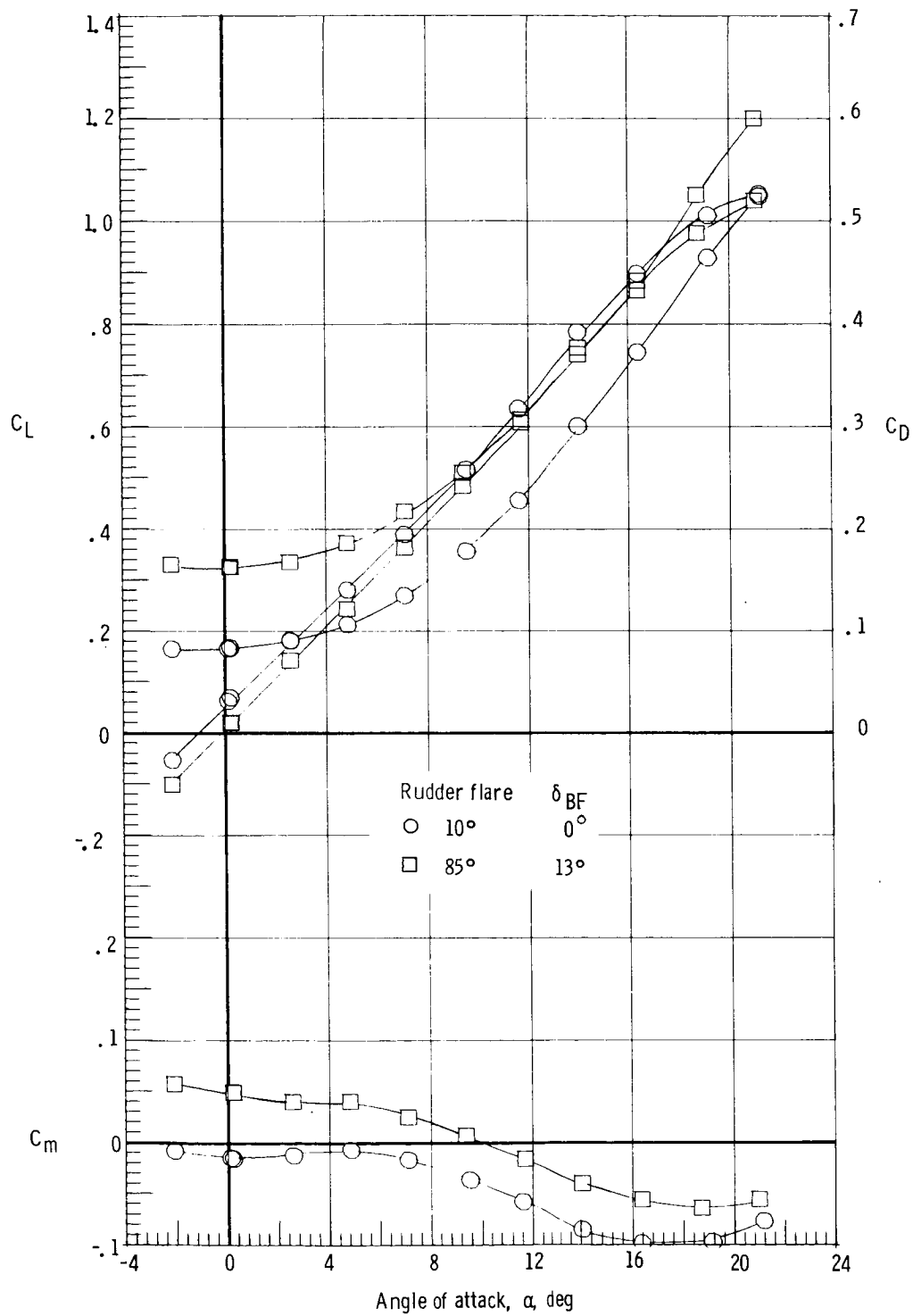
(c) M $\approx$ 0.9.

Figure 7.- Continued.
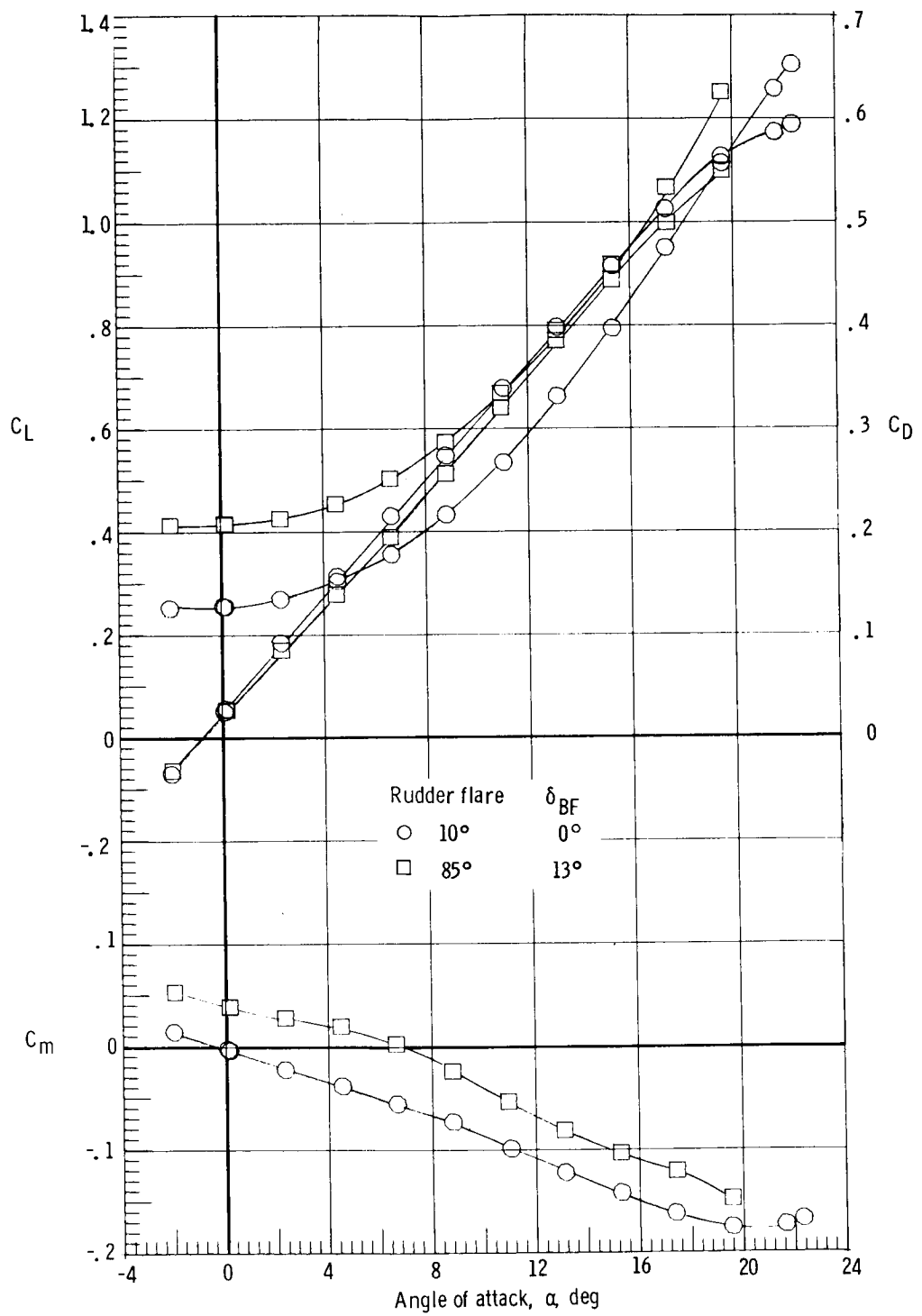
(d)   M = 0.98.

Figure 7.- Continued.
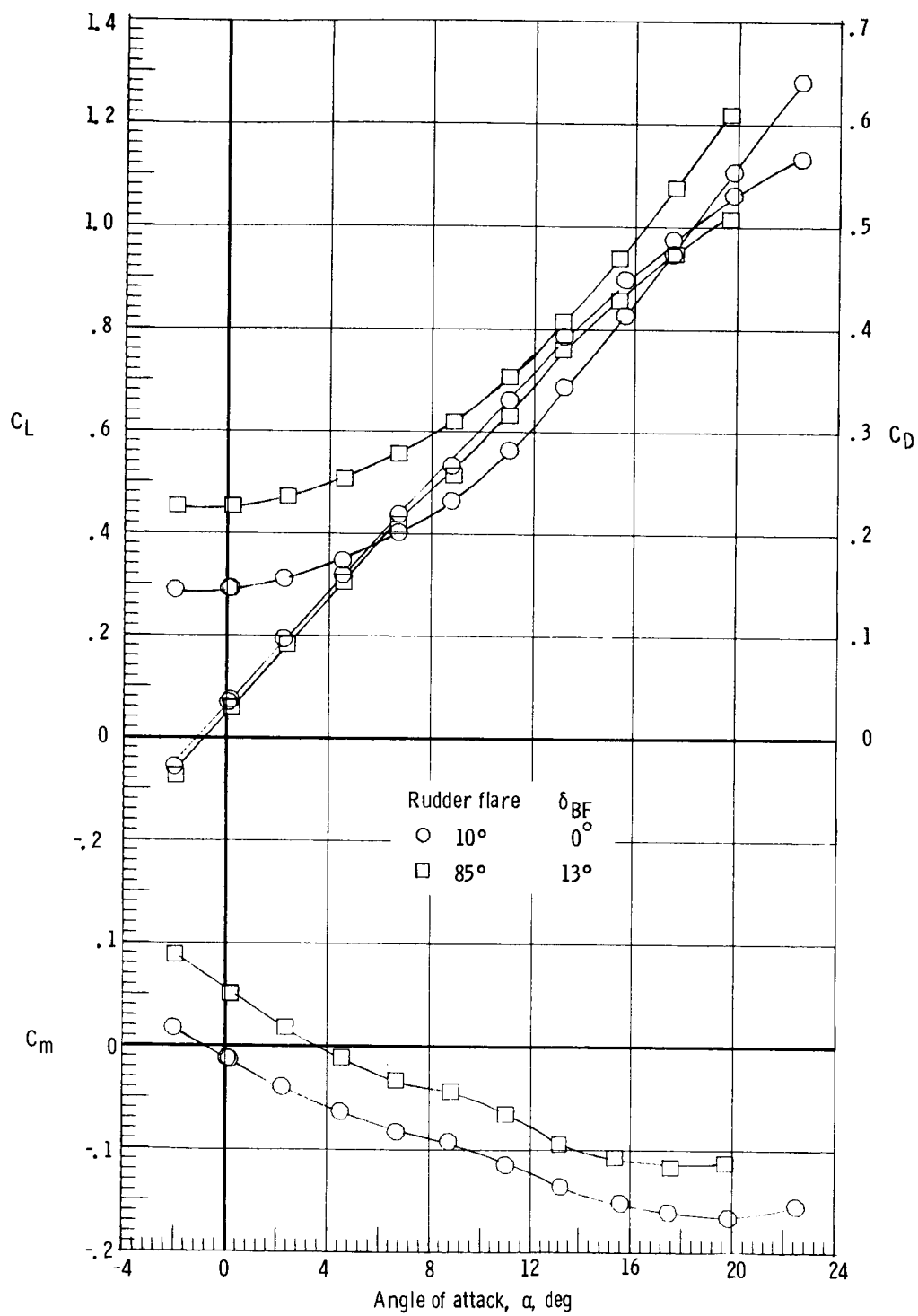
(e) M = 1.2.

Figure 7.- Concluded.
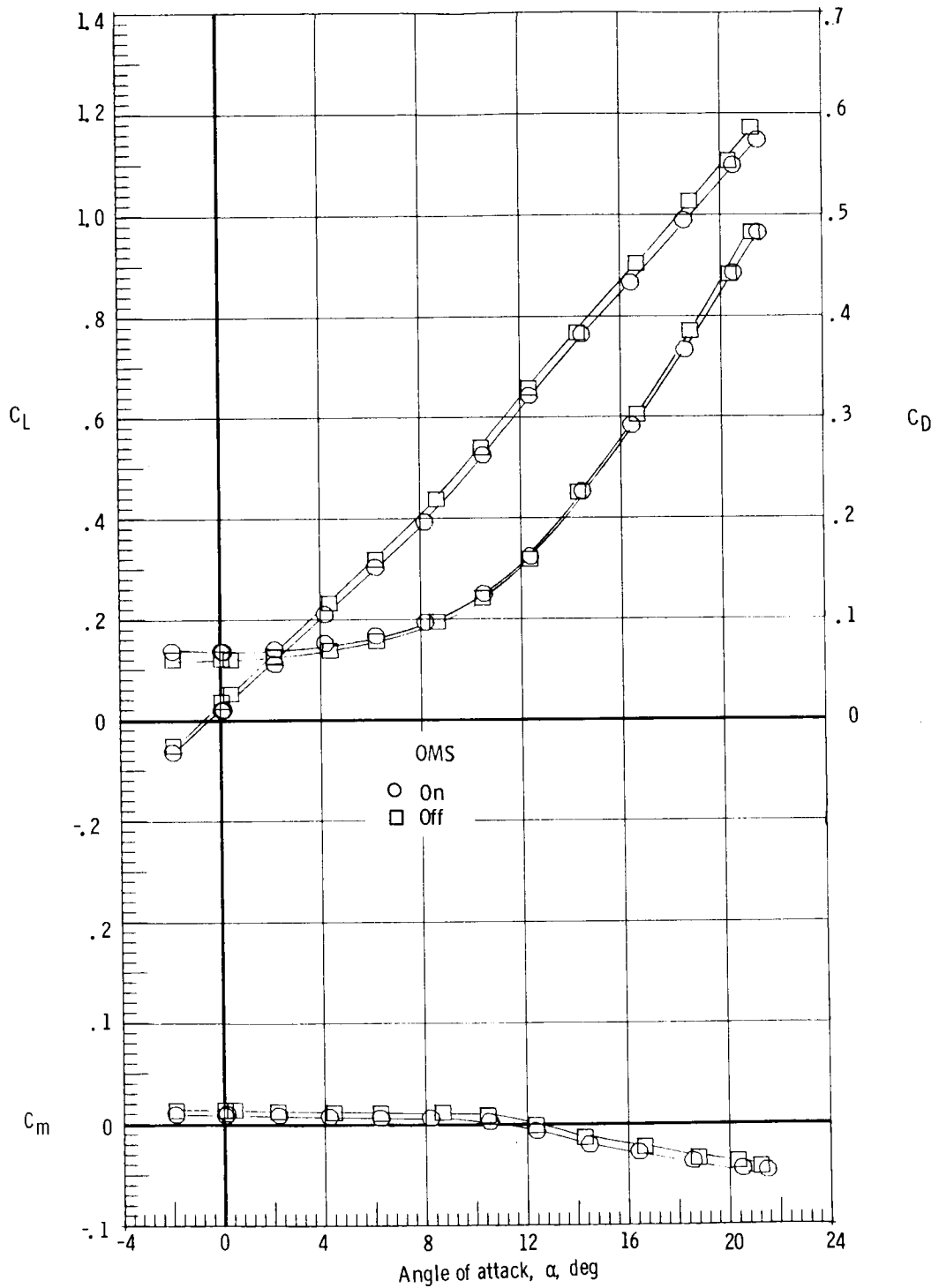
(a) M = 0.3.

Figure 8.- Effect of OMS installation on static longitudinal characteristics. Forward center of gravity; $\delta_e = 0^o$; rudder flare, 10°; body flap off.
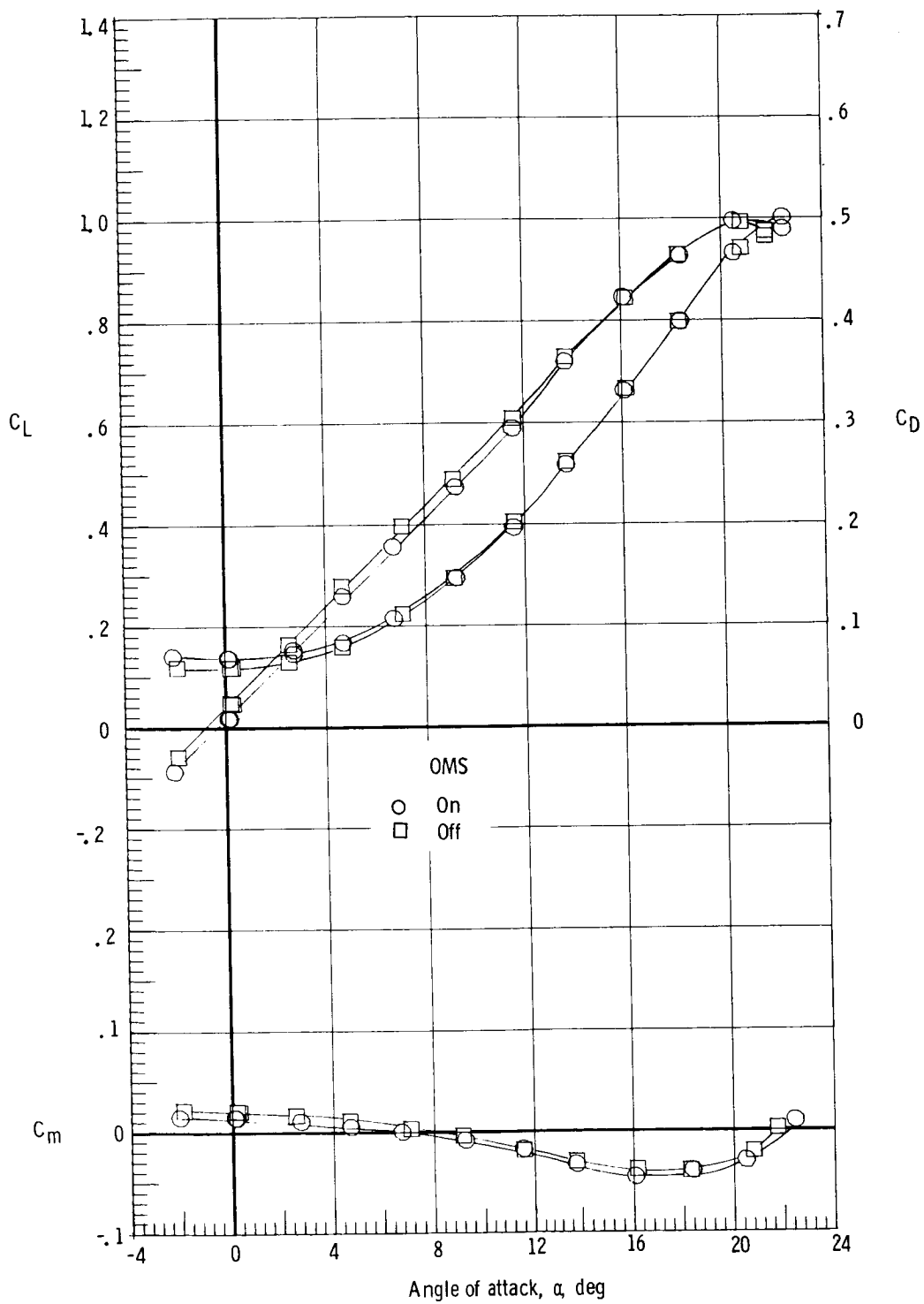
(b) M ≈ 0.8.

Figure 8.- Continued.
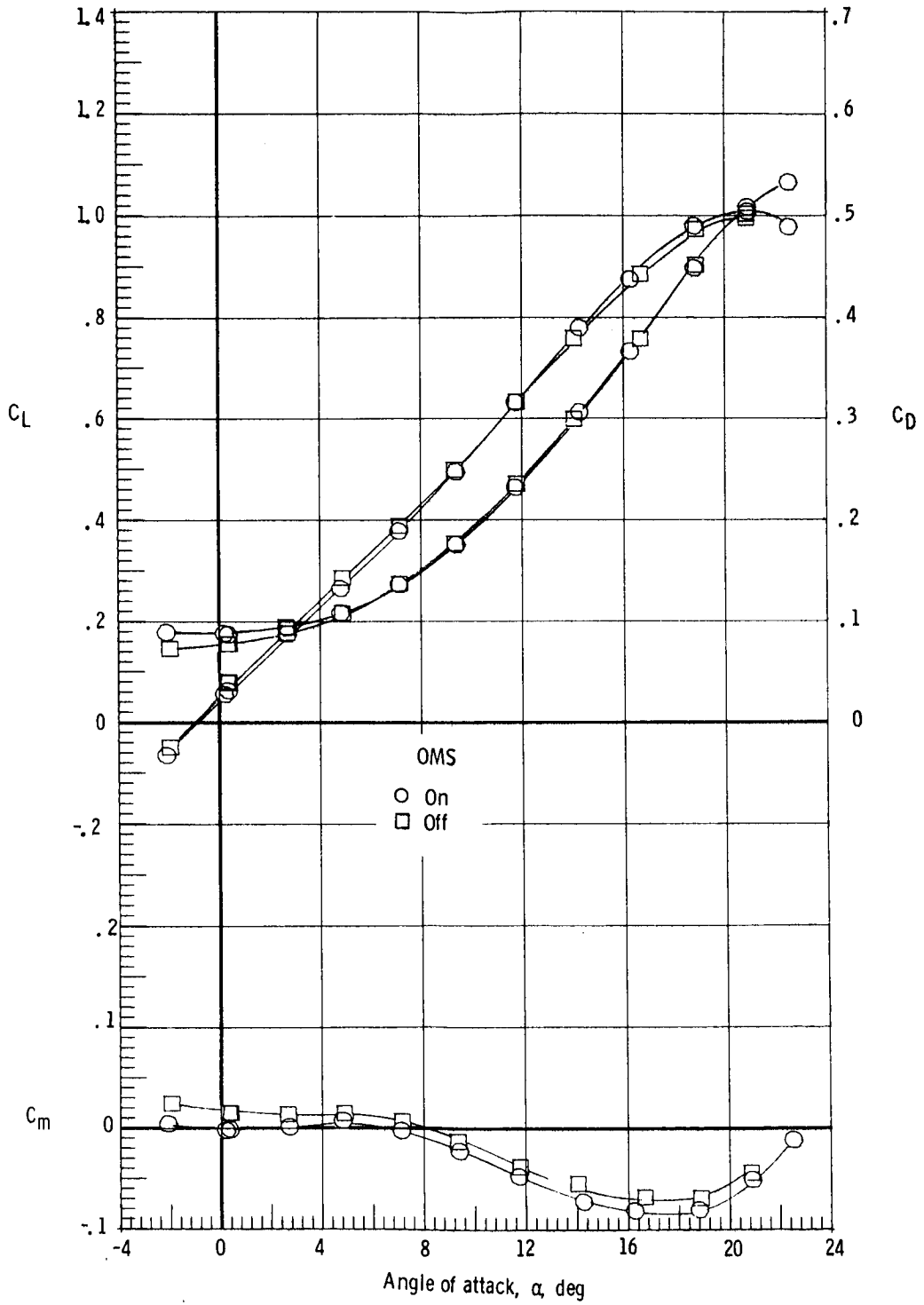
(c) M = 0.9.

Figure 8.- Continued.
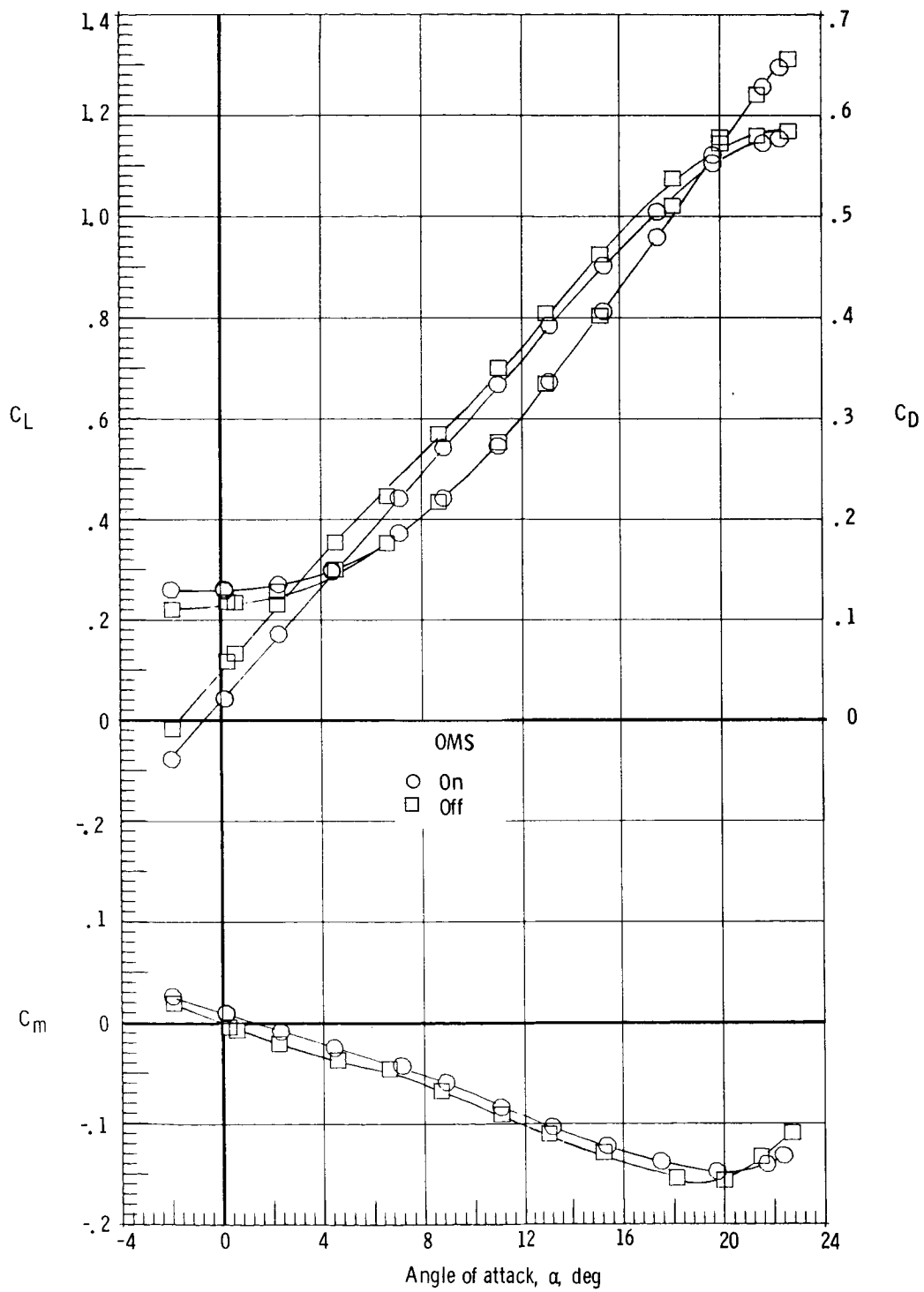
(d)   M = 0.98.

Figure 8.- Continued.
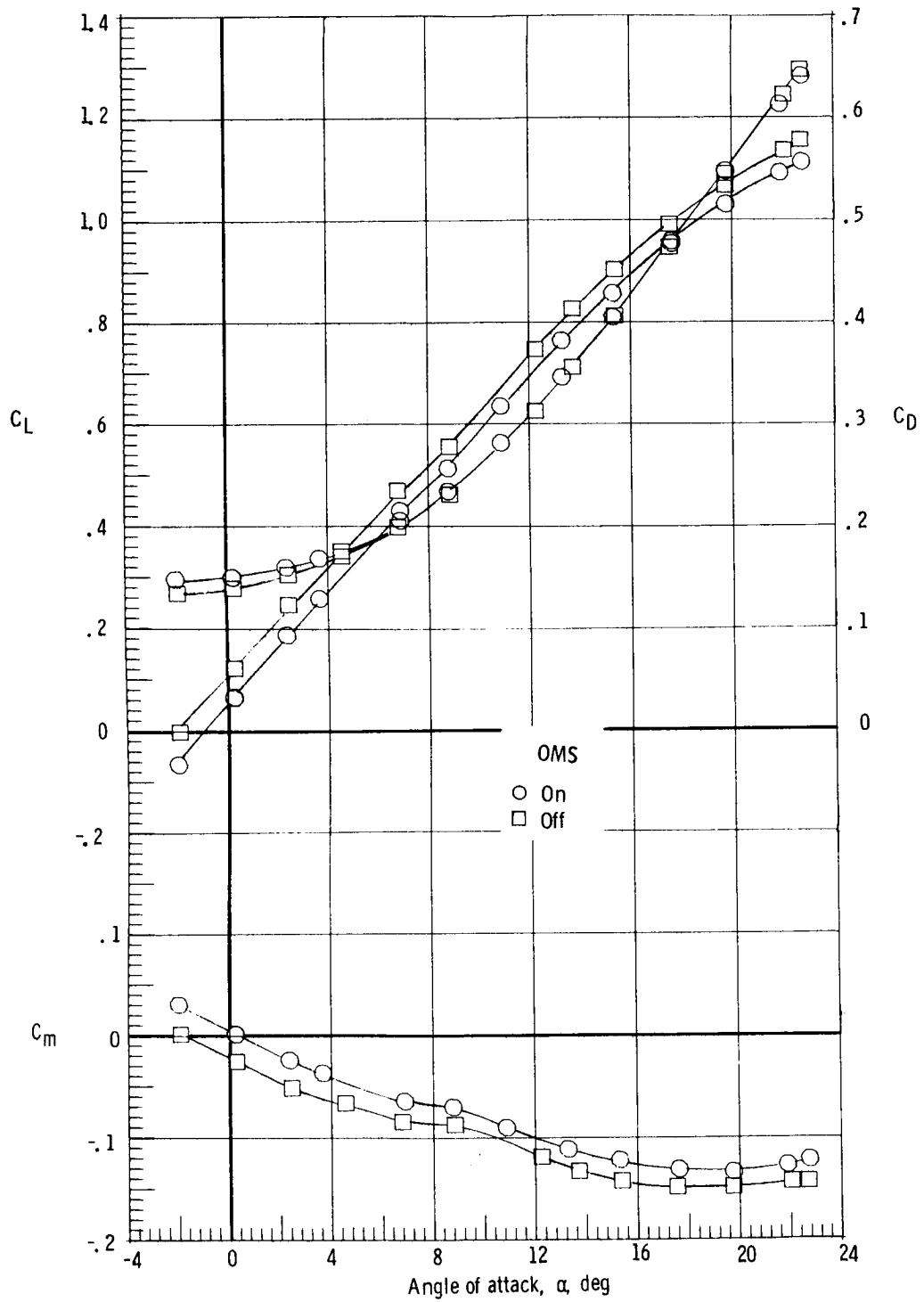
(e)   M = 1.2.

Figure 8.- Concluded.
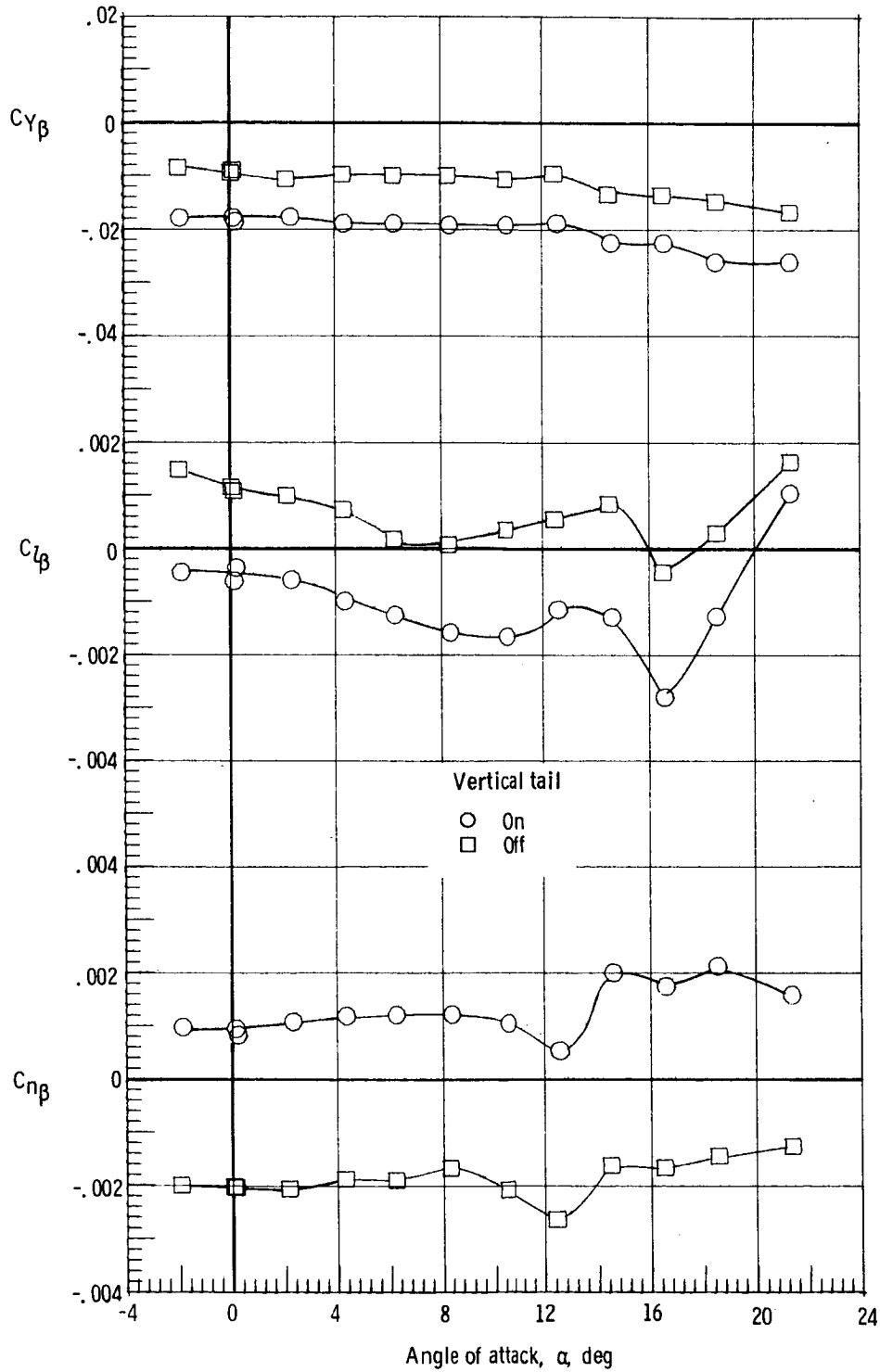
(a) M = 0.3.

Figure 9.- Effect of vertical tail on the static lateral characteristics. Forward
center of gravity; $\delta_e = 0^o$; rudder flare, 10°.
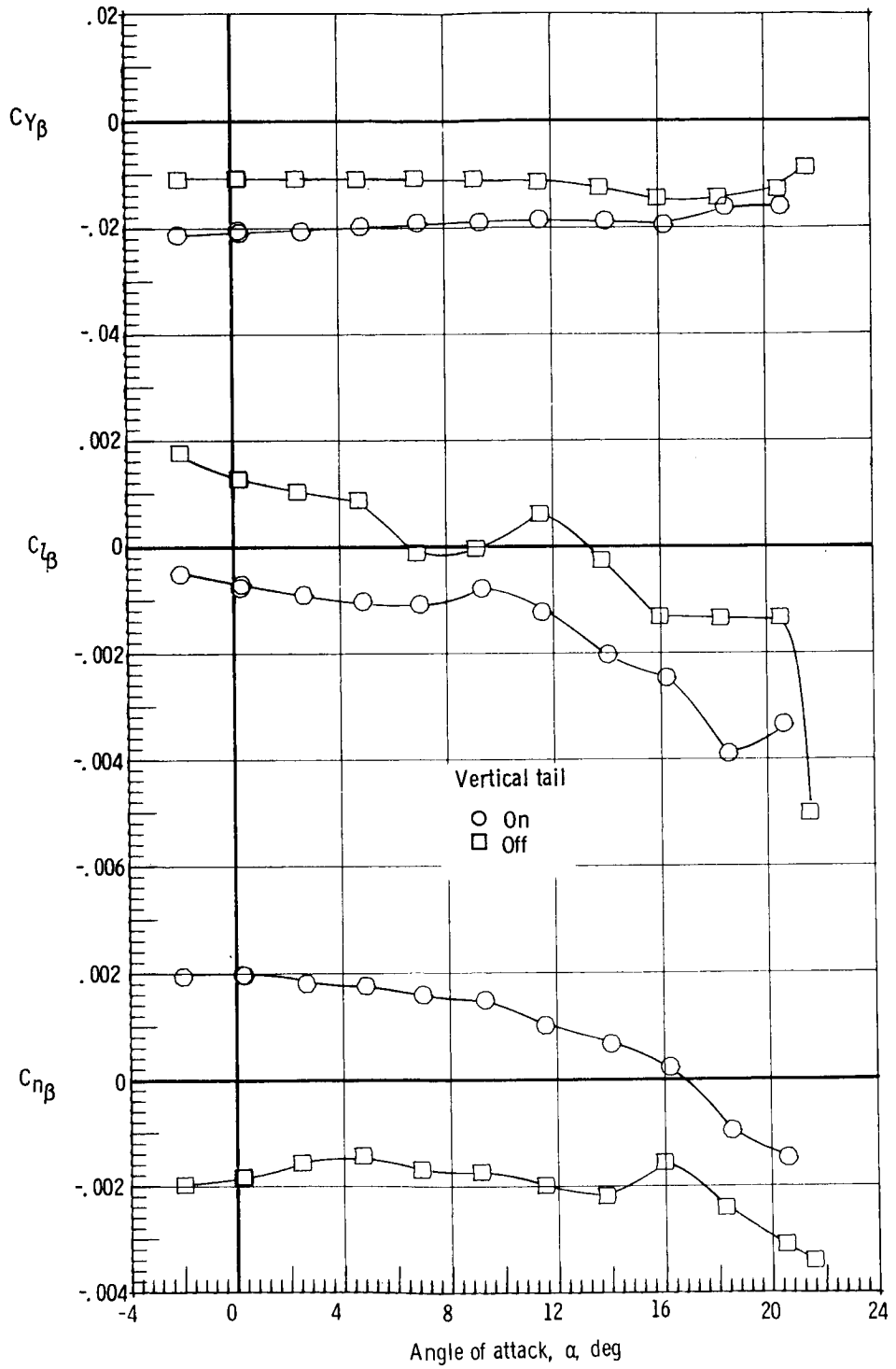
(b)   M = 0.8.

Figure 9.- Continued.
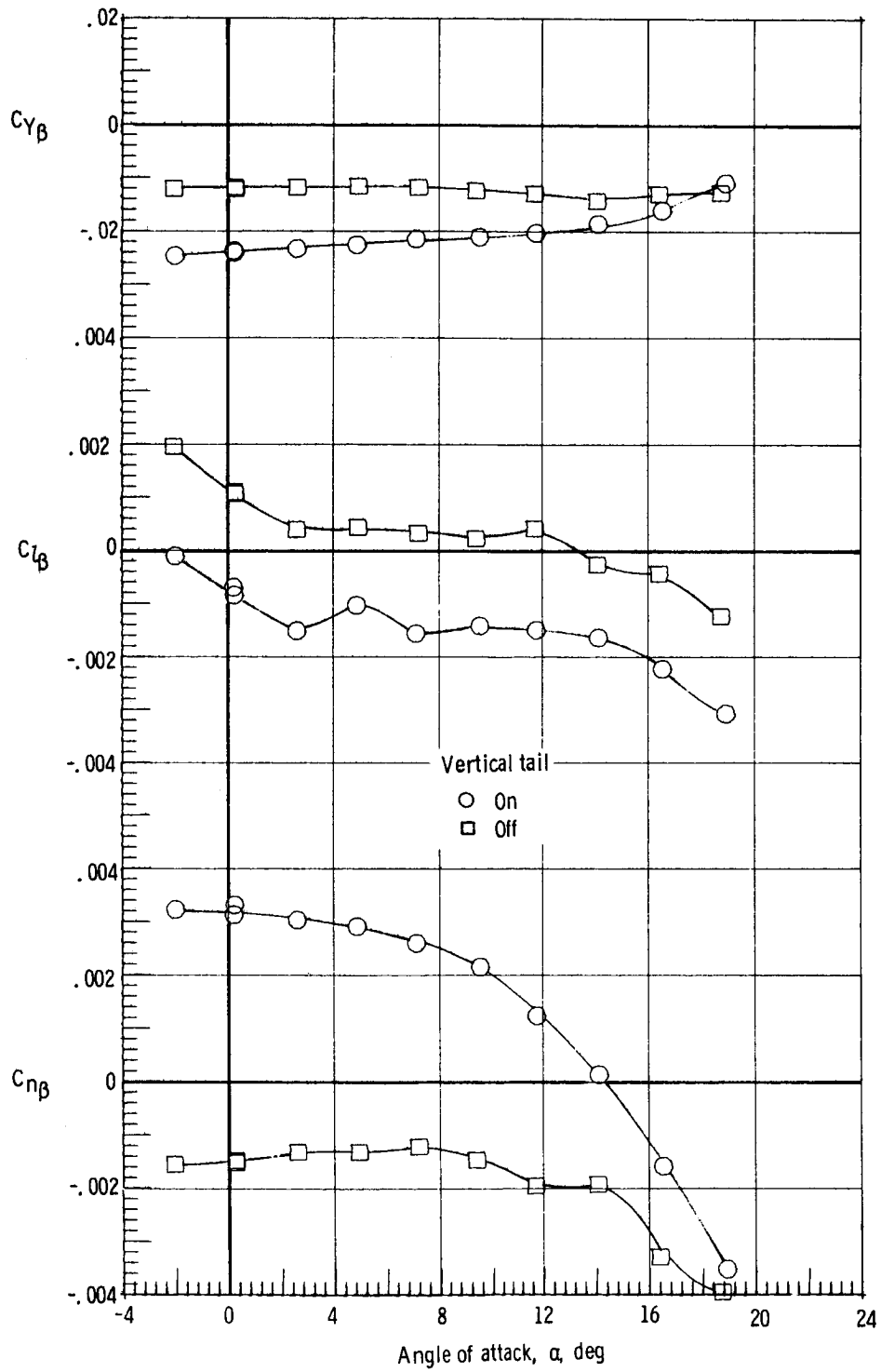
(c) M = 0.9.

Figure 9.- Continued.
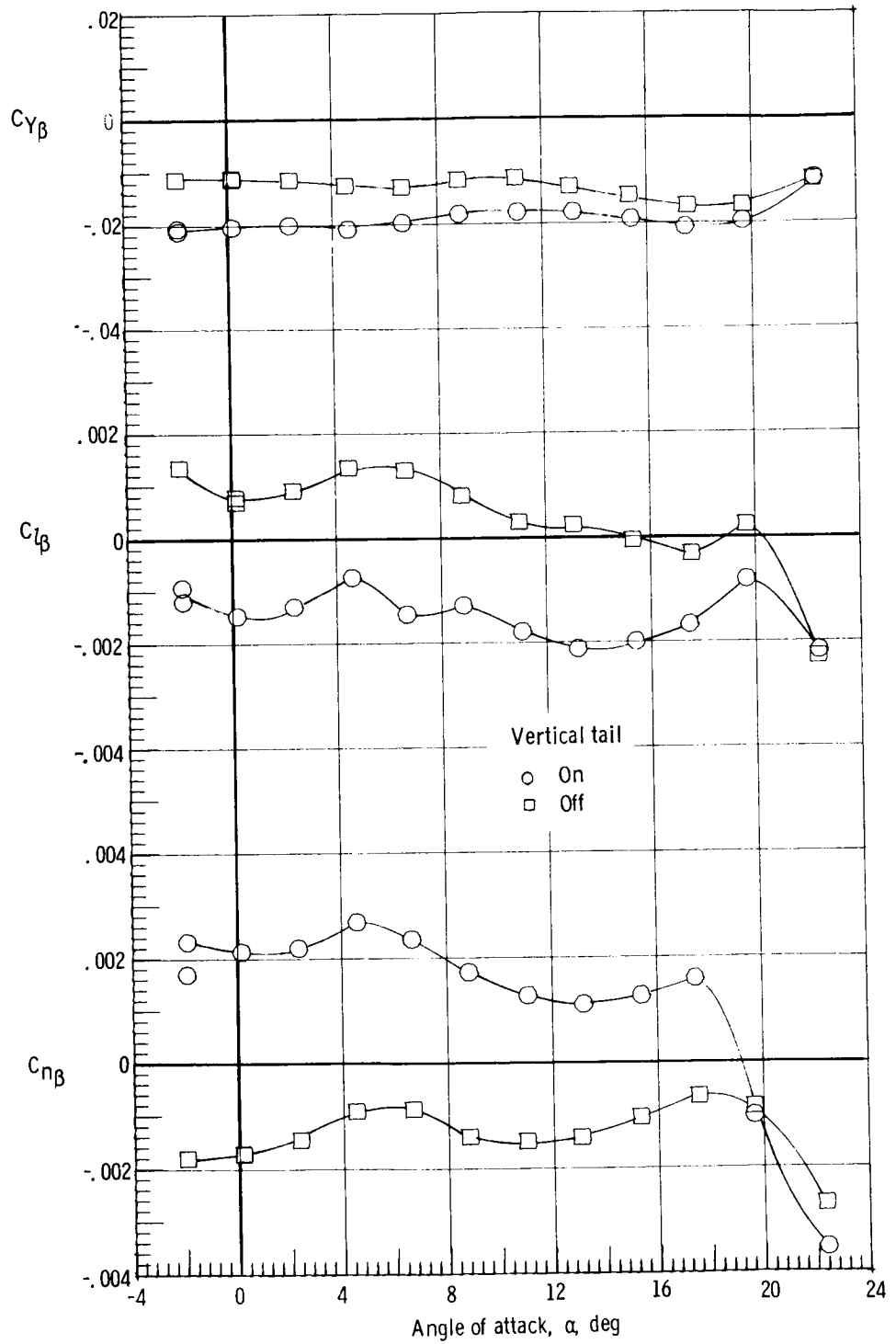
(d) M = 0.98.

Figure 9.- Continued.
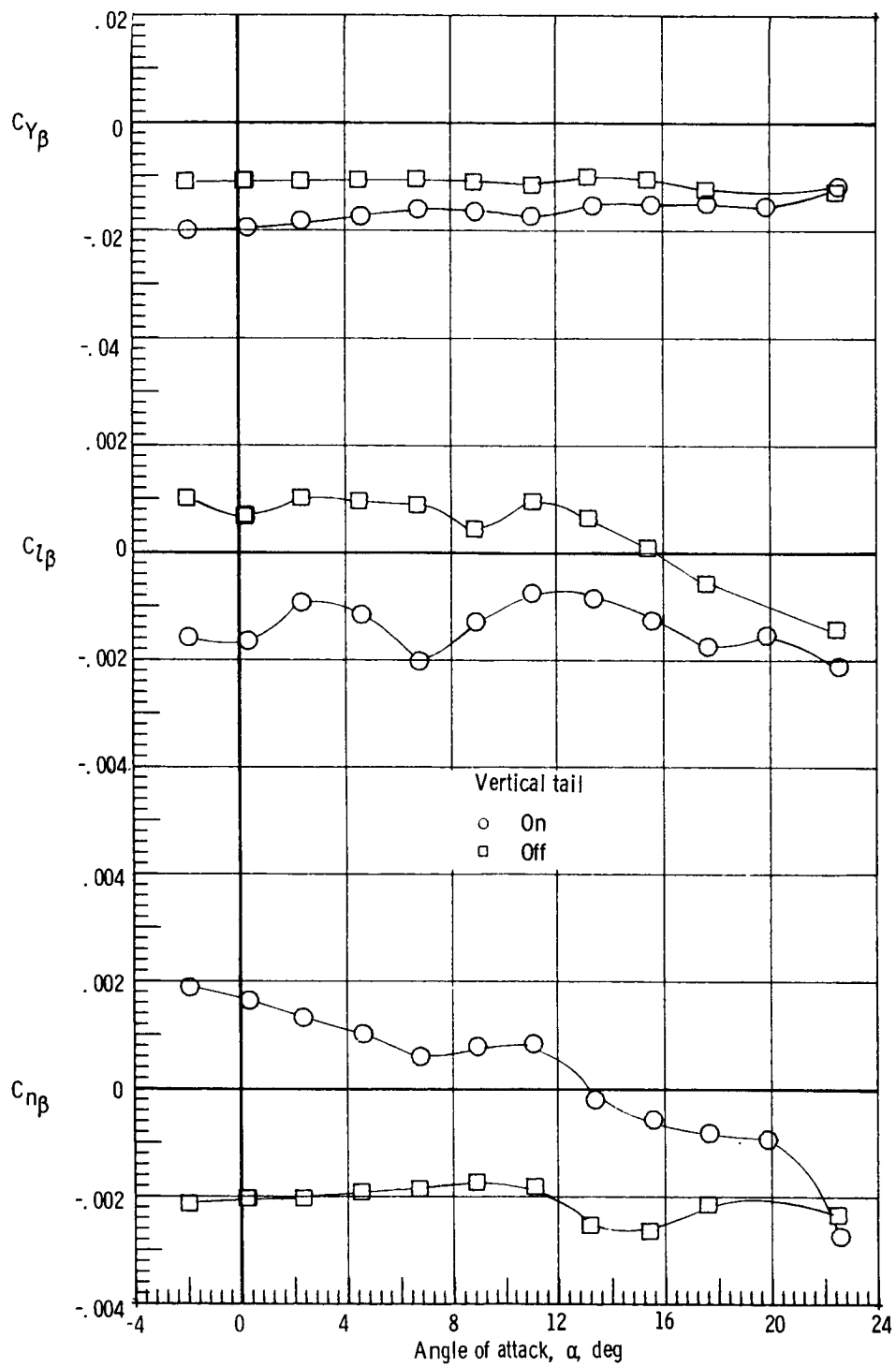
(e) M = 1.2.

Figure 9.- Concluded.
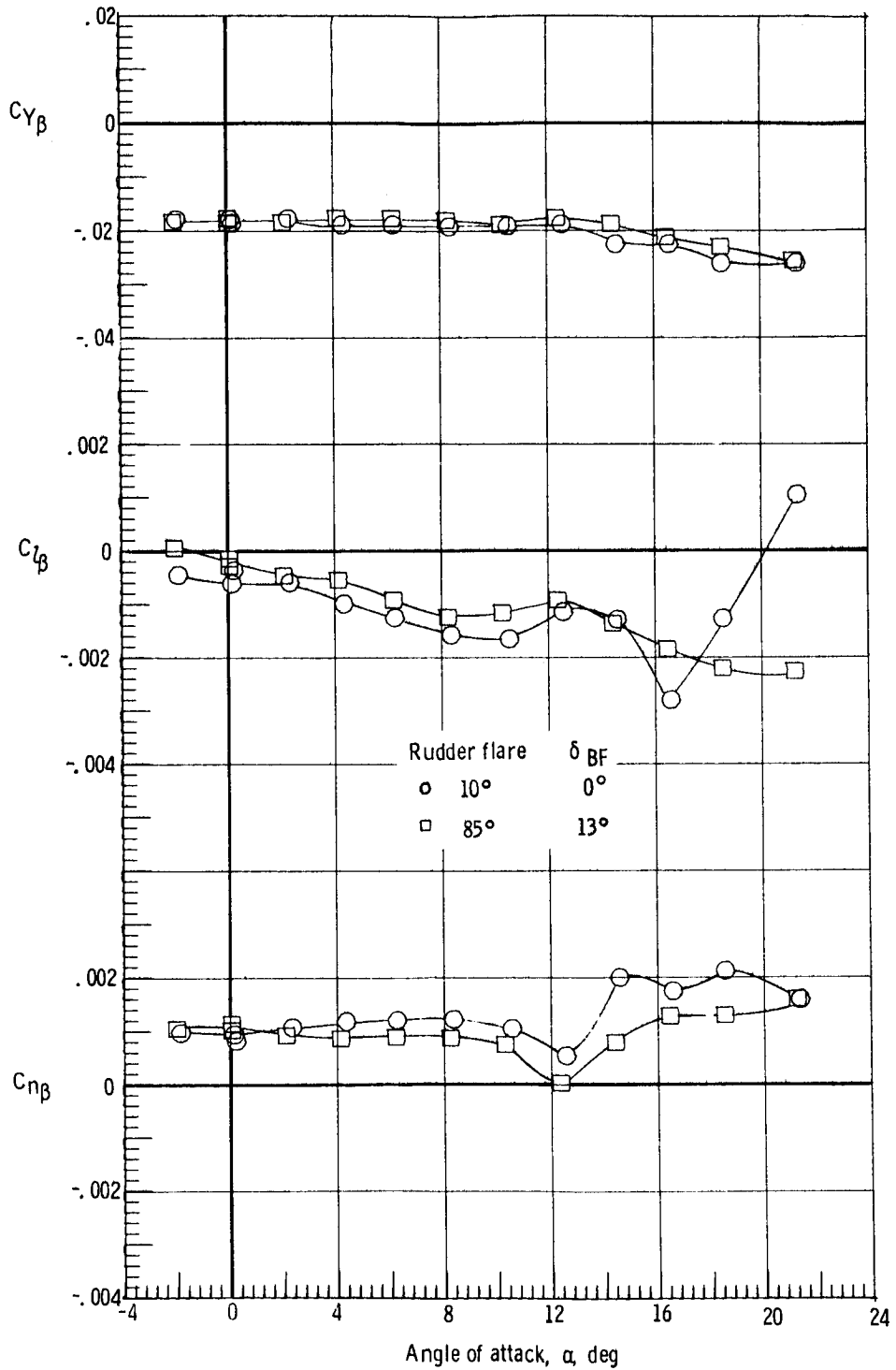
(a)   M = 0.3.

Figure 10.- Effect of rudder flare and body flap deflection on the static lateral characteristics.   Forward center of gravity; $\delta_e = 0^O$.
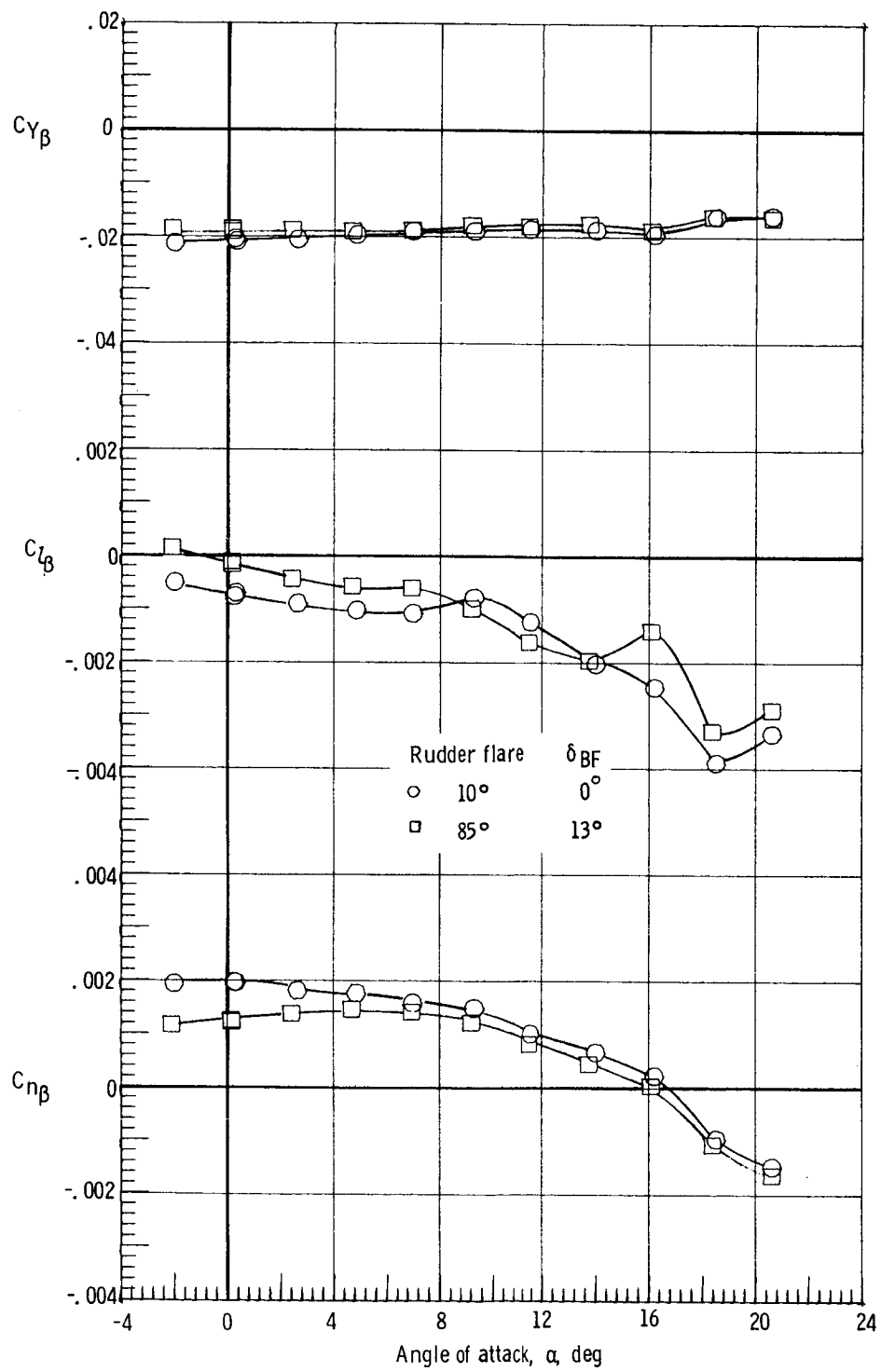
(b) M = 0.8.

Figure 10.- Continued.
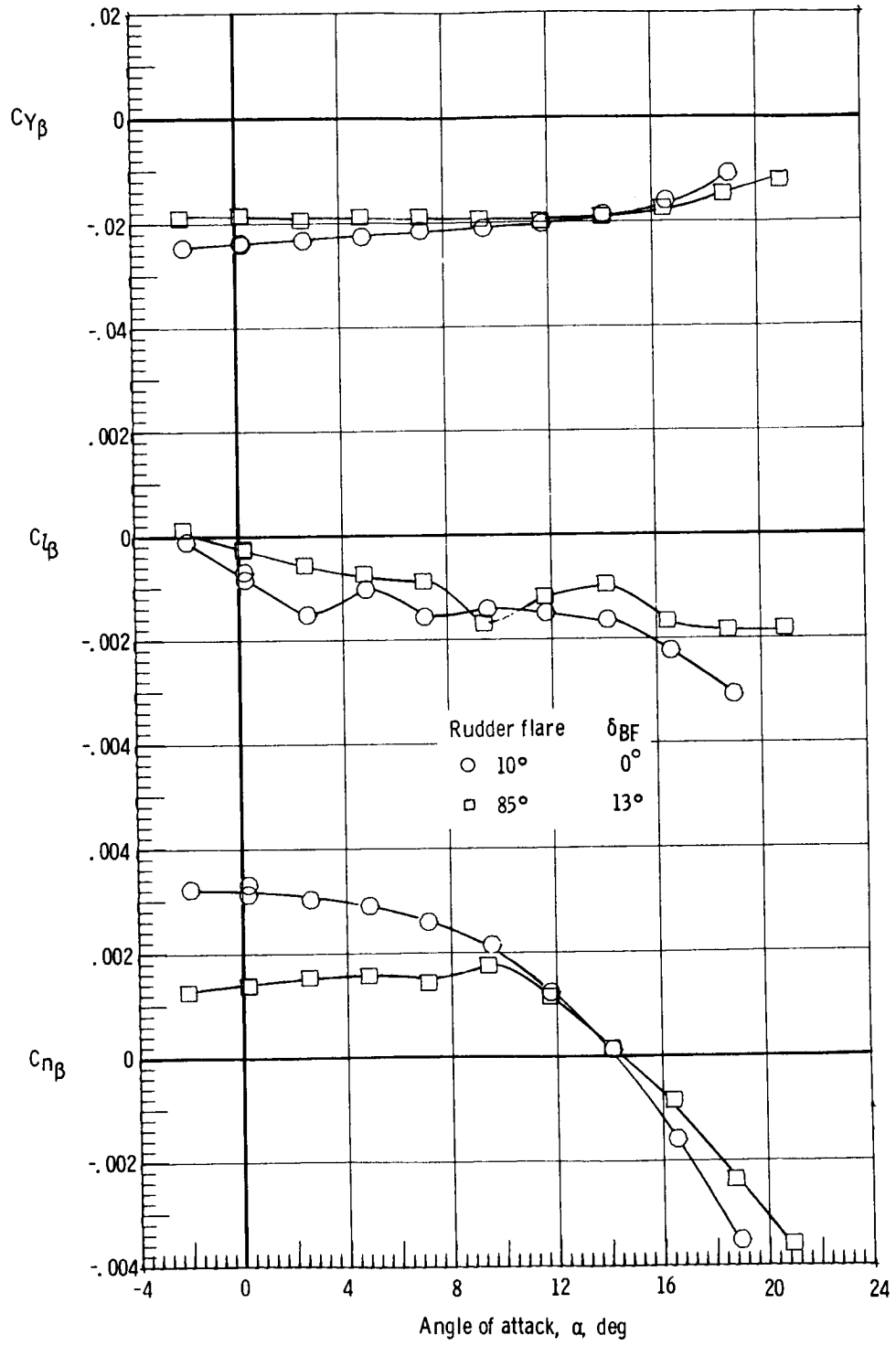
(c)   M = 0.9.

Figure 10.- Continued.
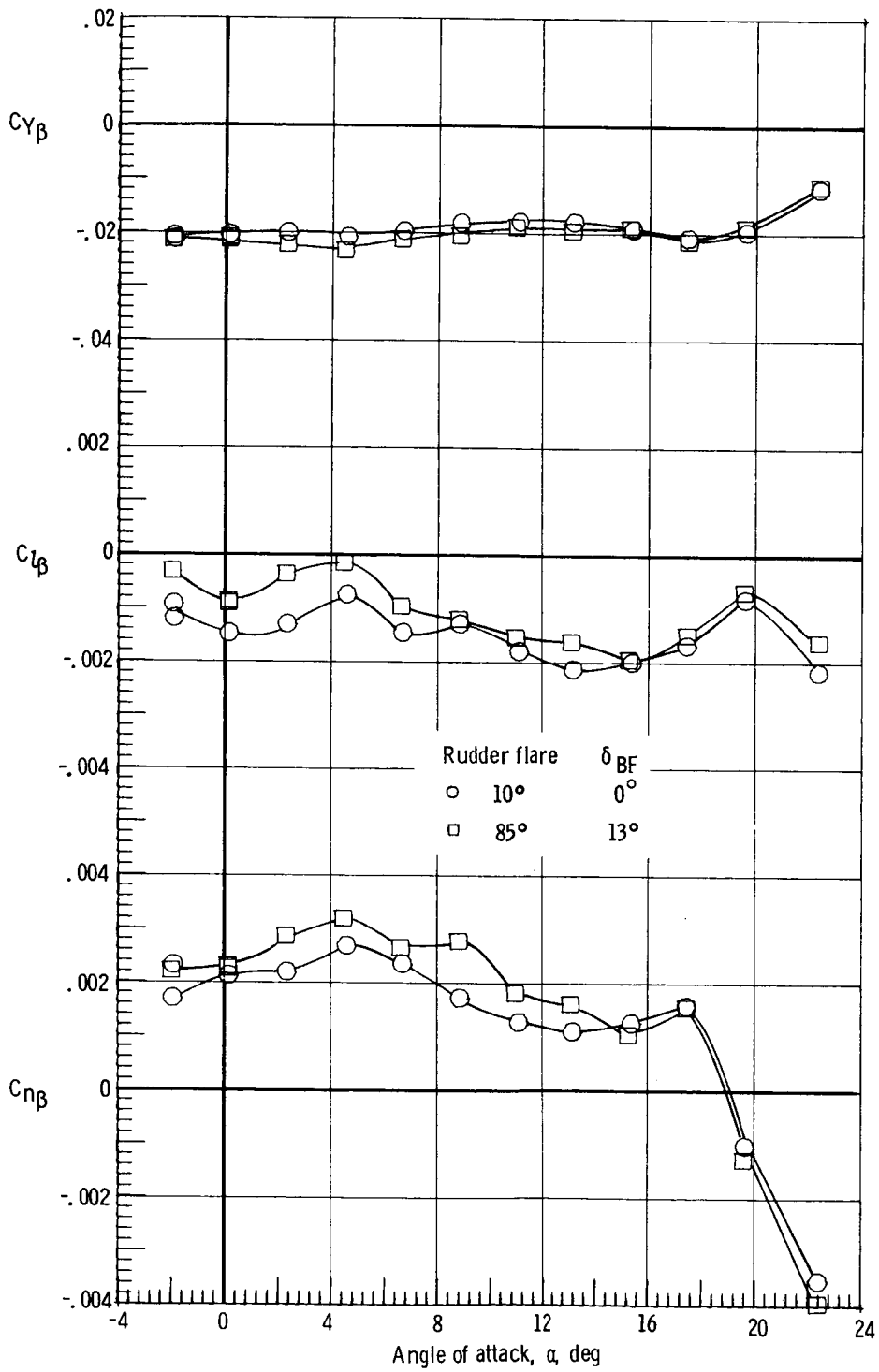
(d) M = 0.98.

Figure 10.- Continued.
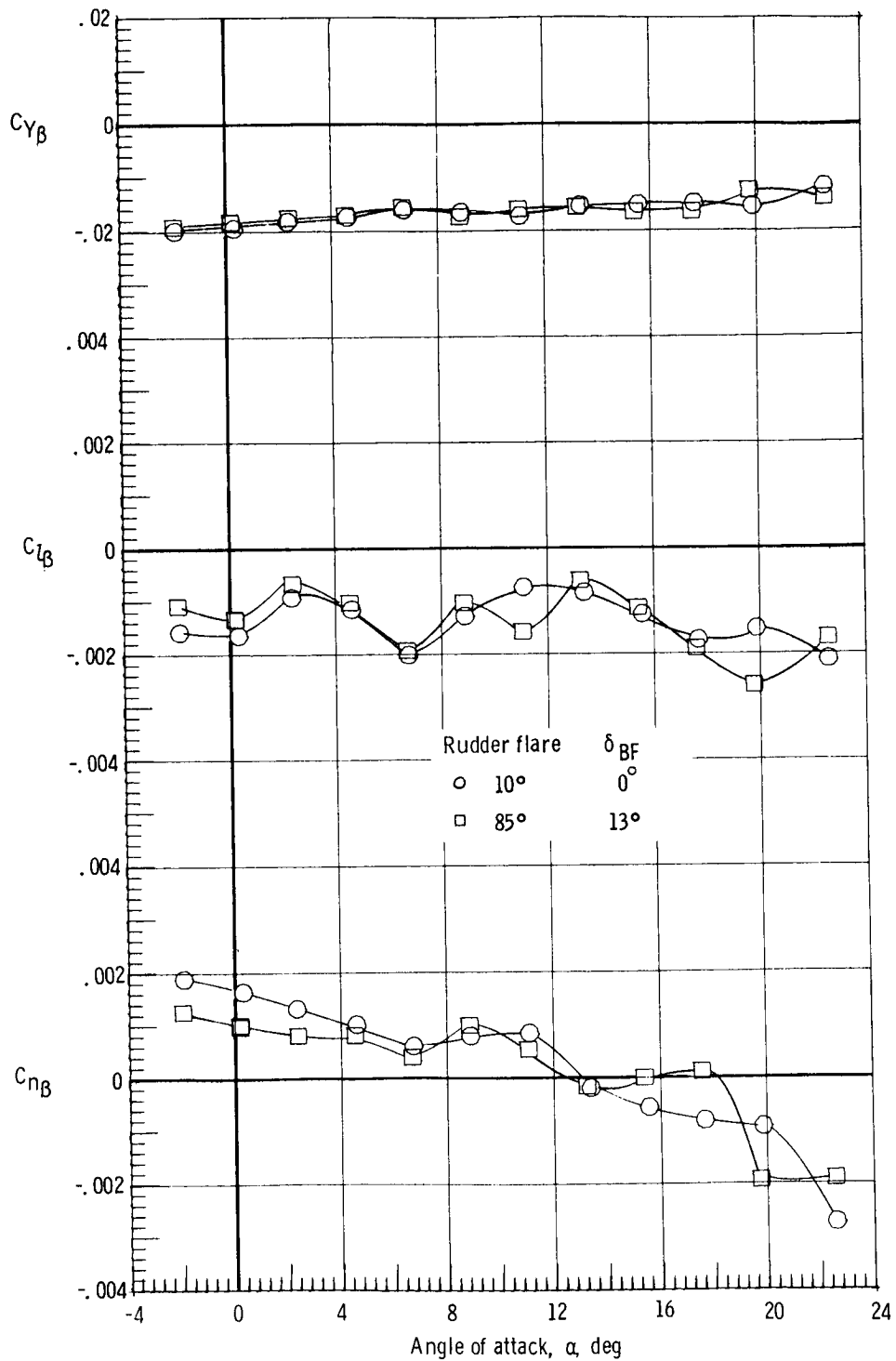
(e) M = 1.2.

Figure 10.- Concluded.
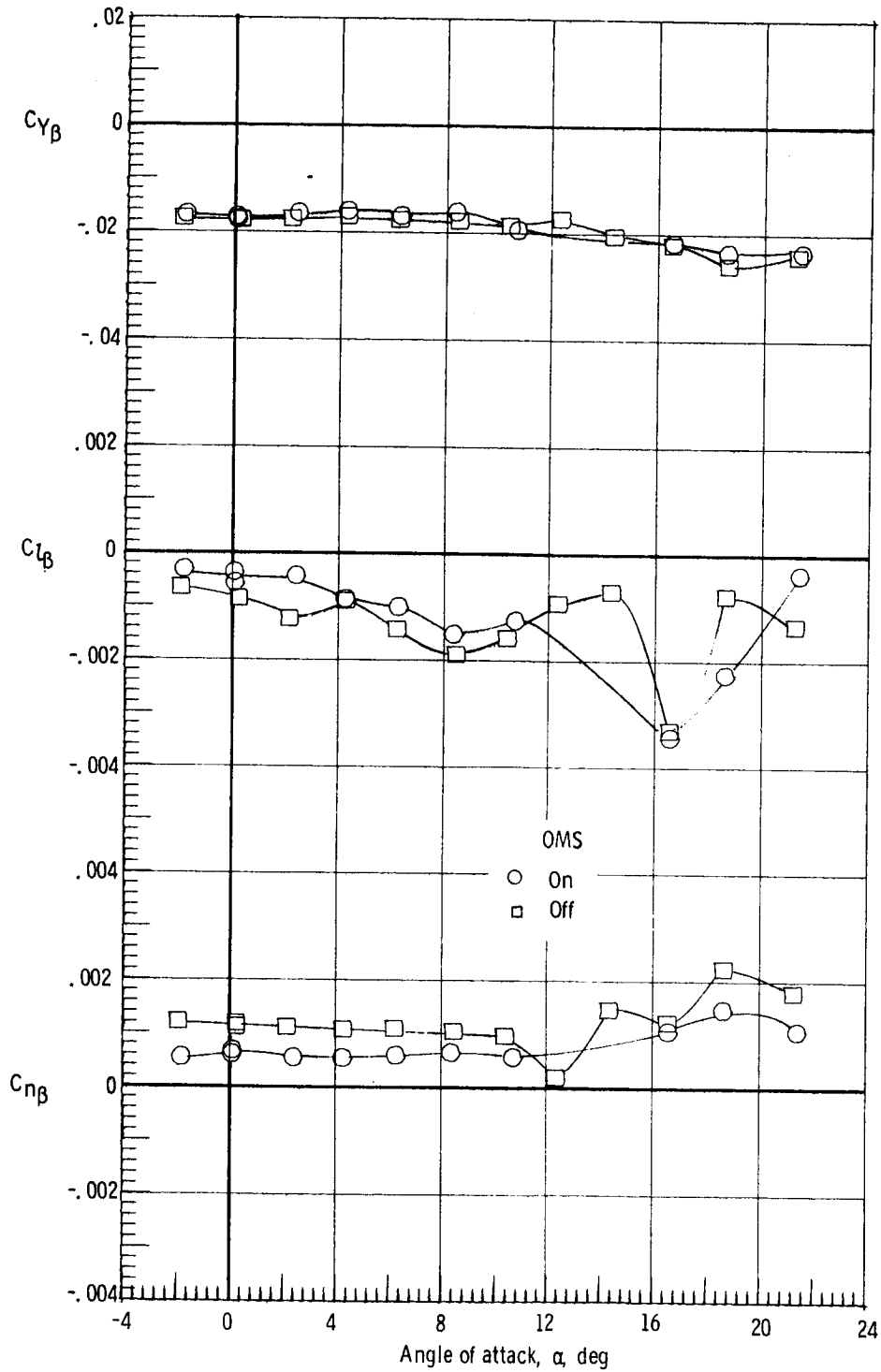
(a)   M = 0.3.

Figure 11.- Effect of OMS installation on the static lateral characteristics of the model. Forward center of gravity; $\delta_e = 0^O$; rudder flare, 10°; body flap off.

(b)   M = 0.8.

Figure 11.- Continued.
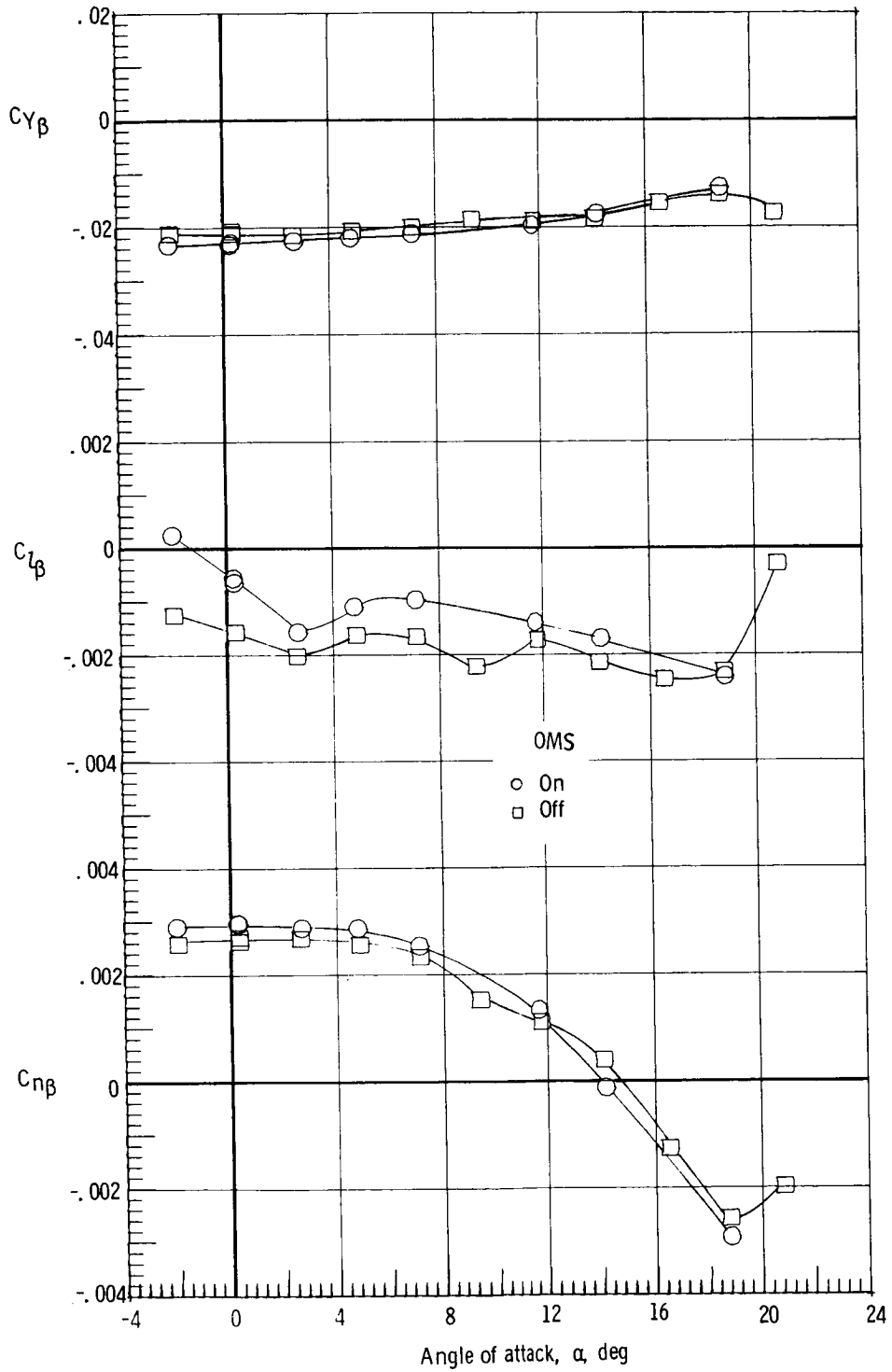
(c) M = 0.9.

Figure 11.- Continued.
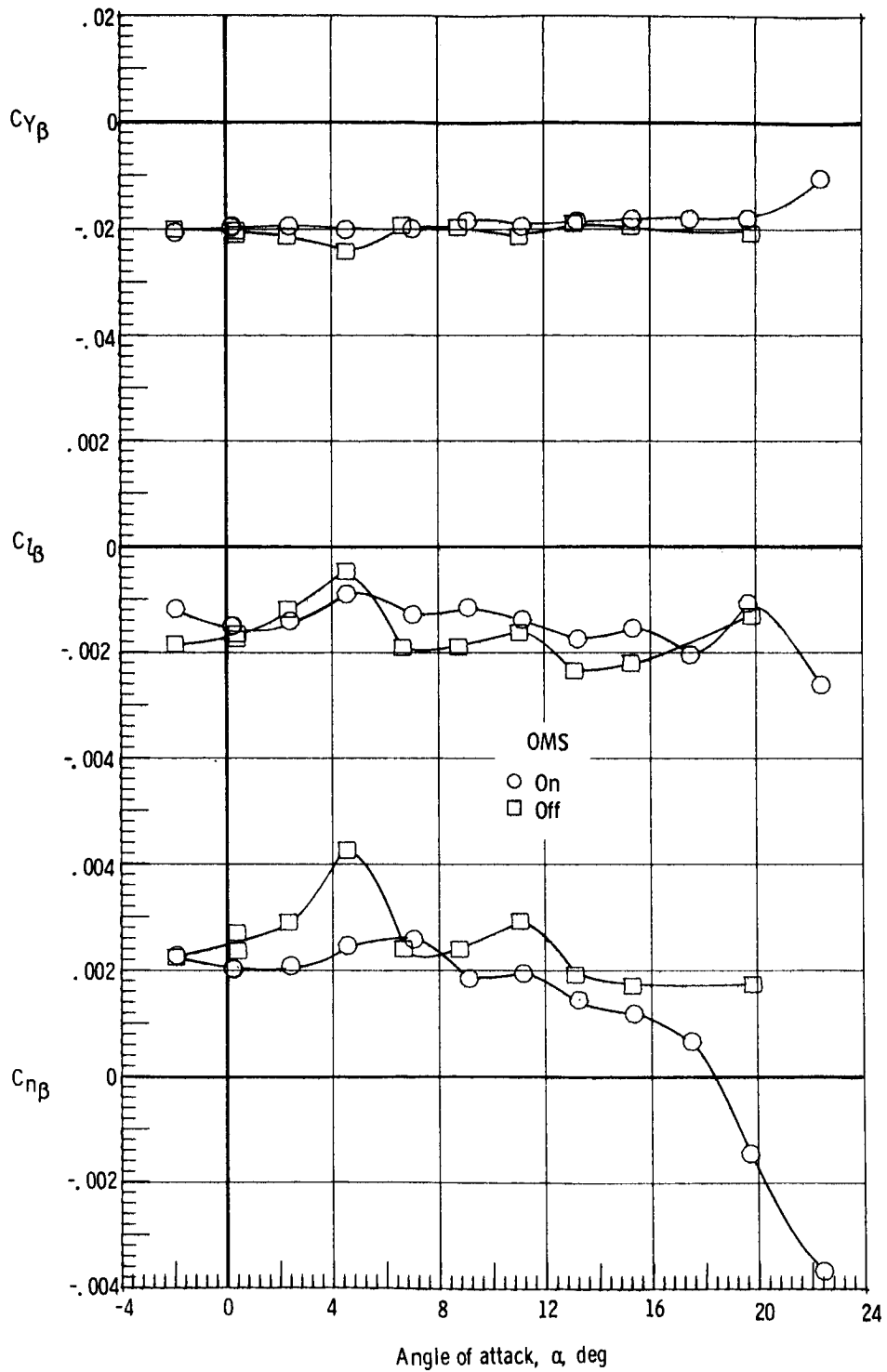
(d) M = 0.98.

Figure 11.- Continued.
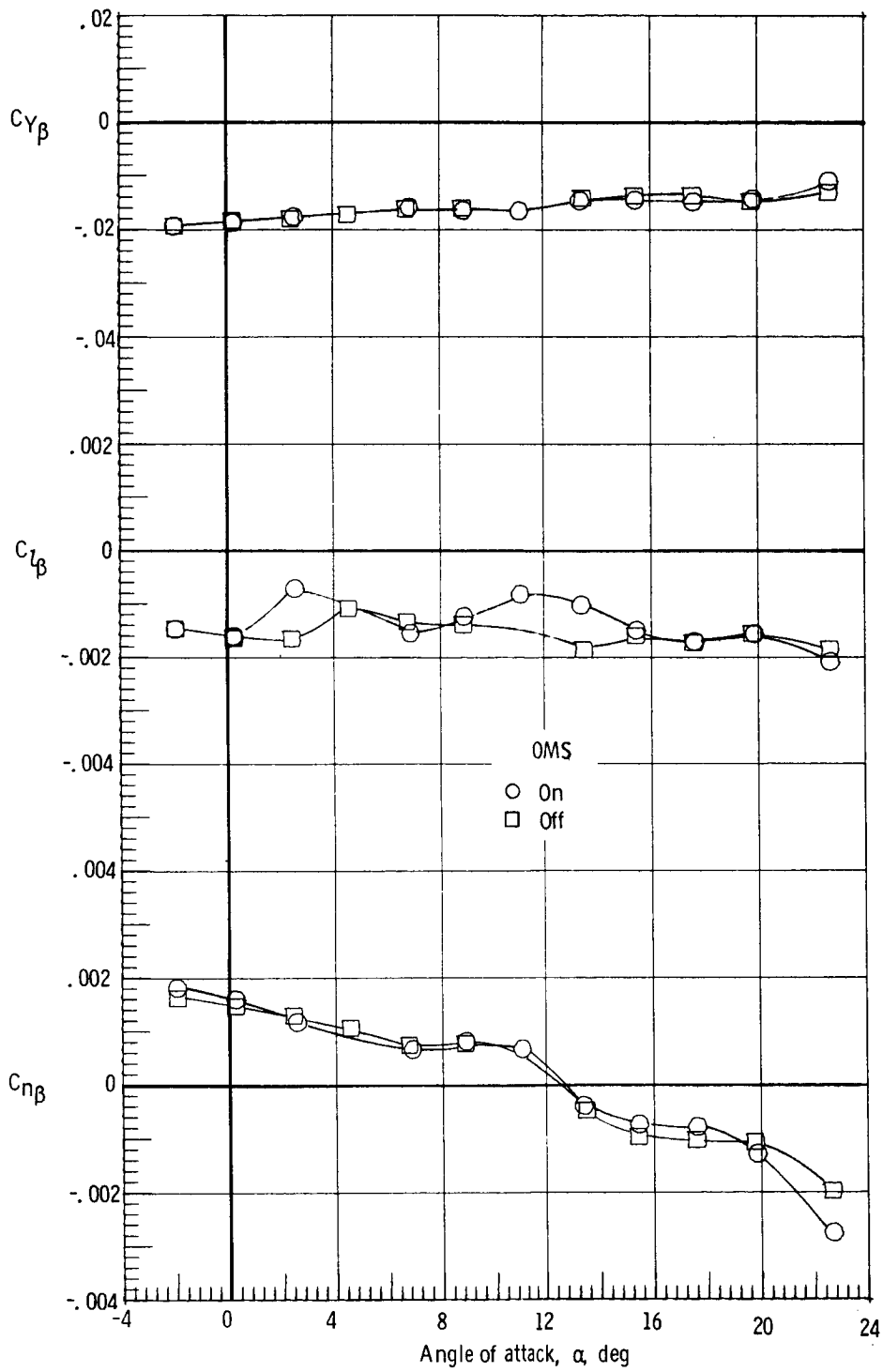
(e) M = 1.2.

Figure 11.- Concluded.
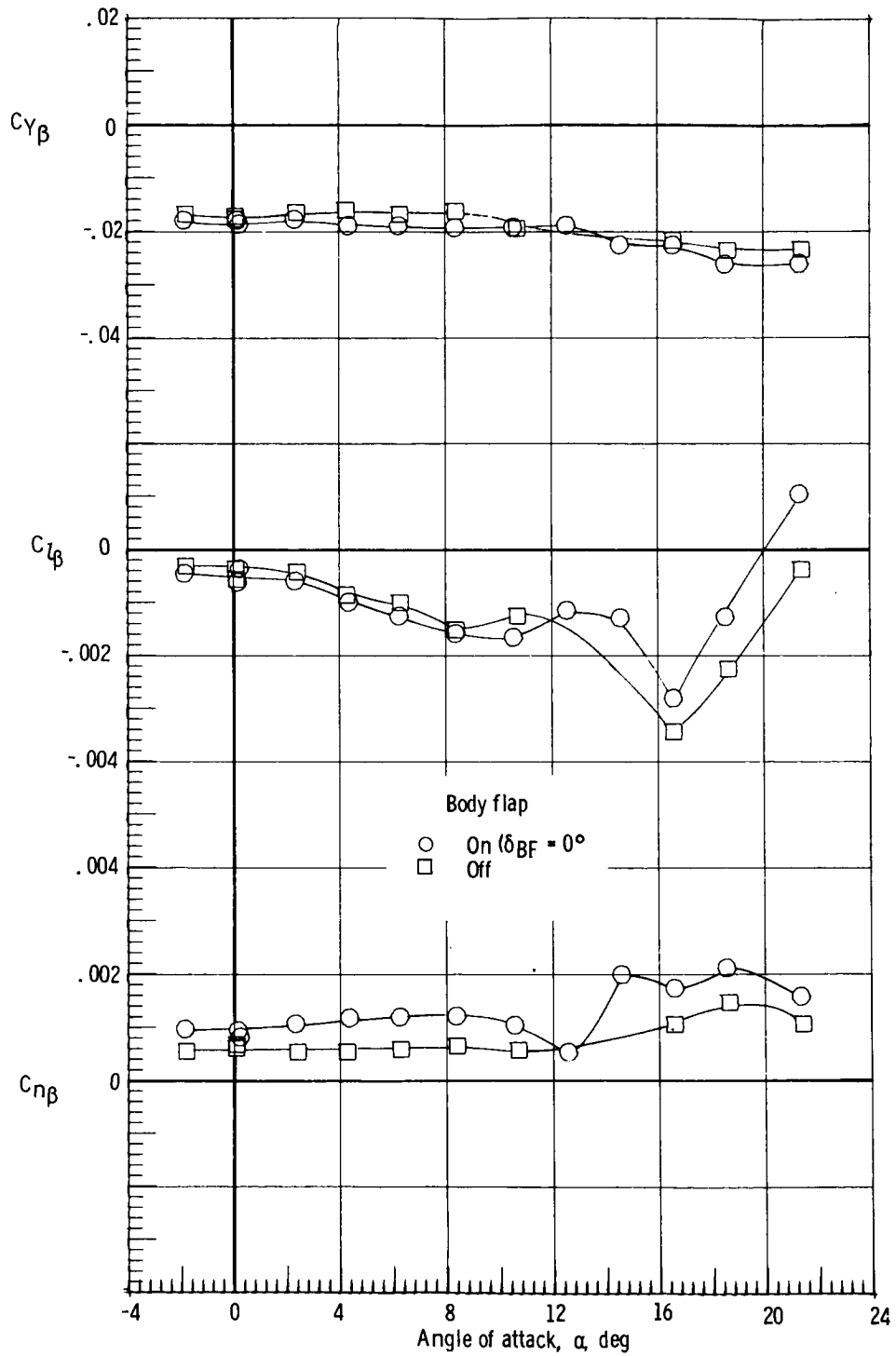
(a)   M = 0.3.

Figure 12.- Effect of body flap on the static lateral characteristics of the model.
Forward center of gravity; $\delta_e = 0^O$; rudder flare, 10°.
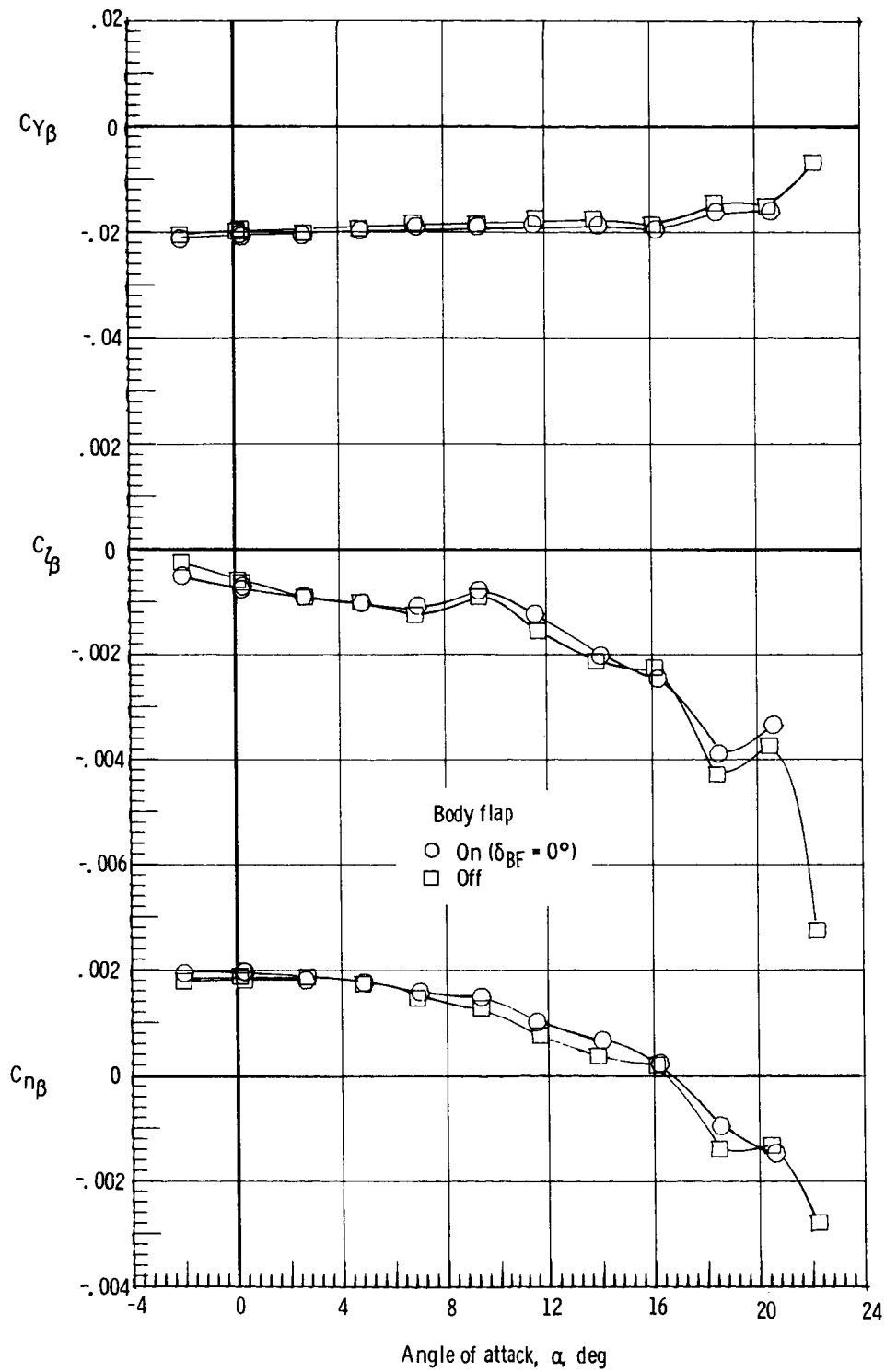
(b) M = 0.8.

Figure 12.- Continued.
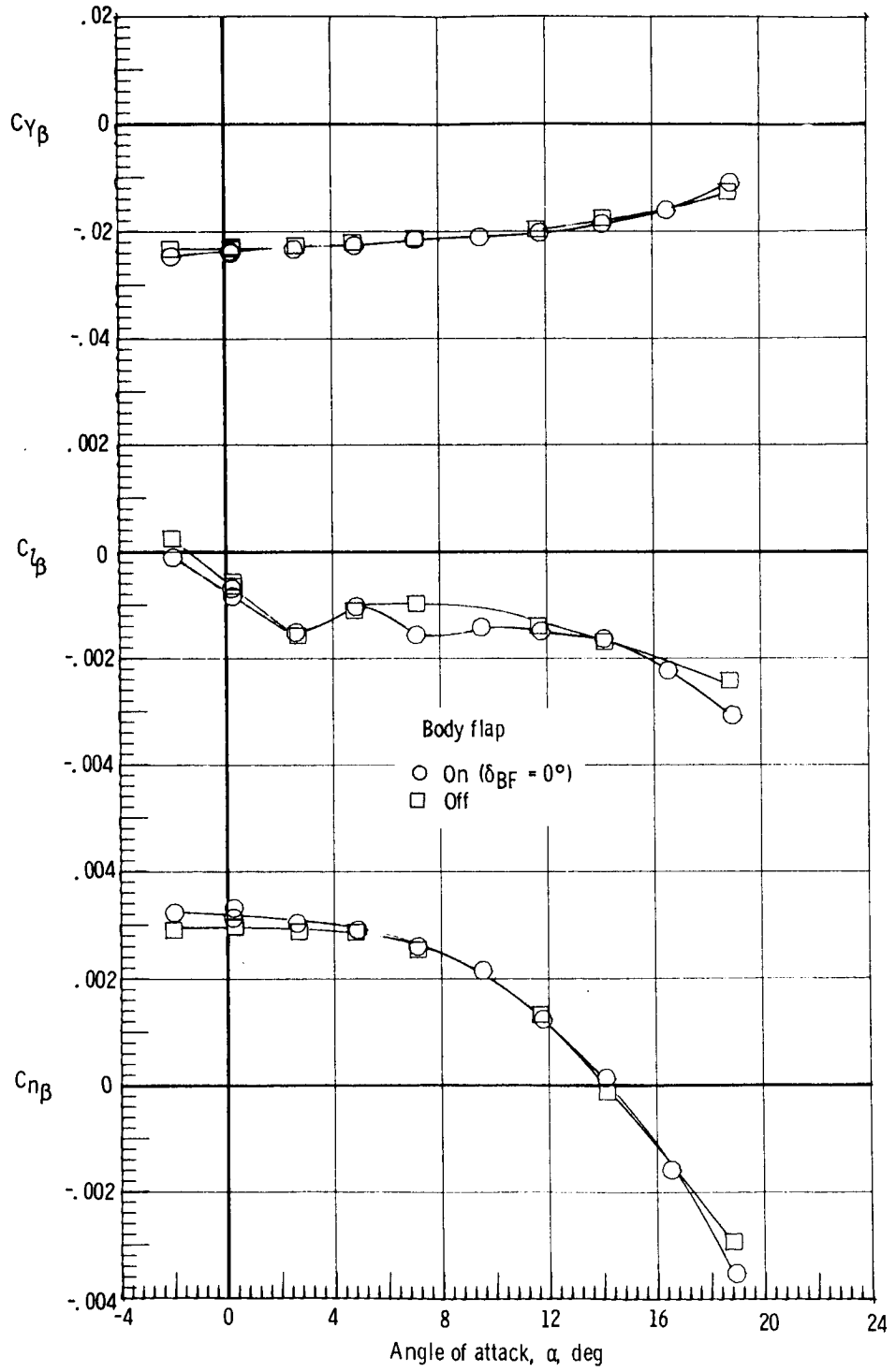
(c) M = 0.9.

Figure 12.- Continued.
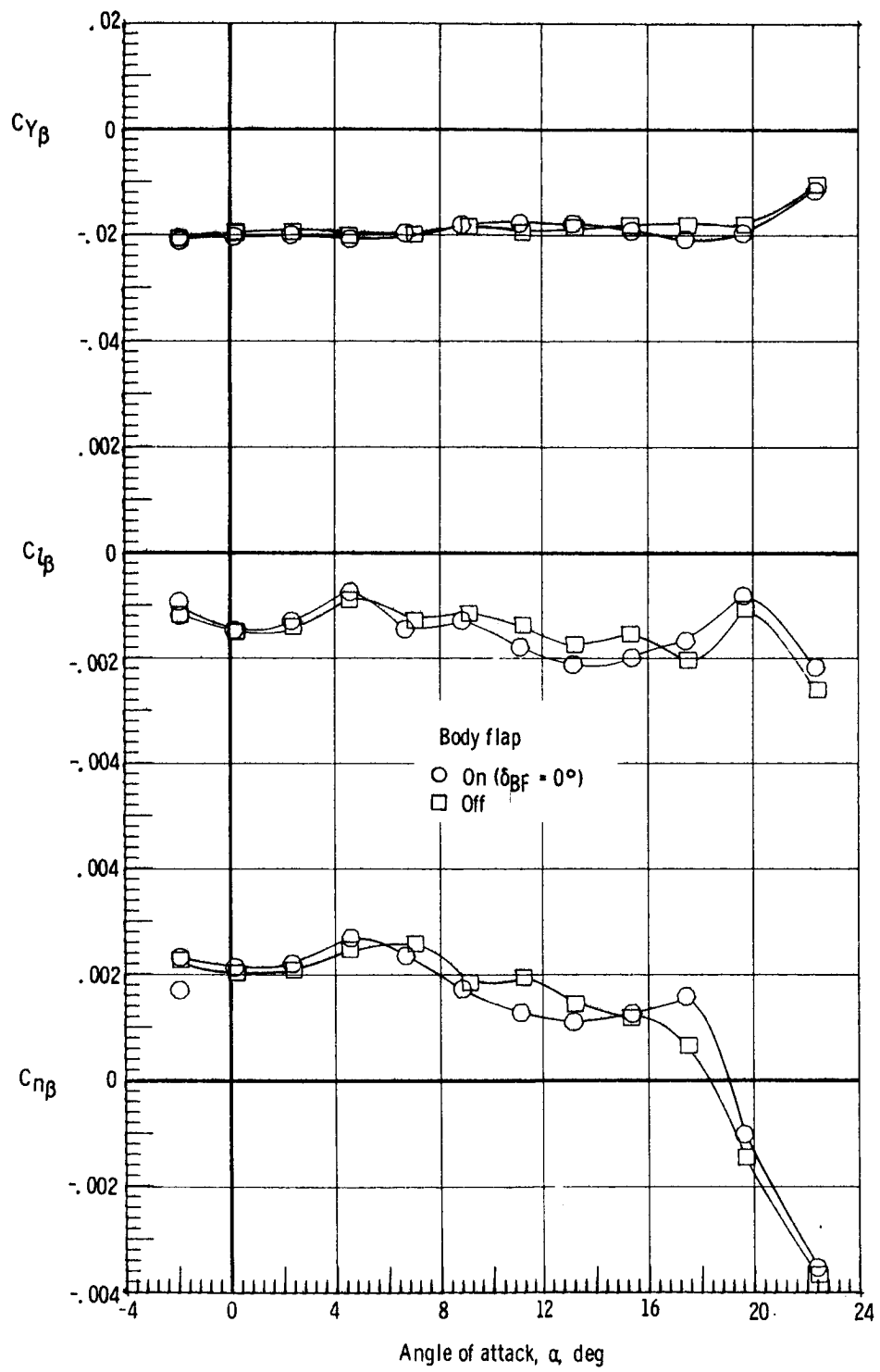
(d)   M = 0.98.

Figure 12.- Continued.
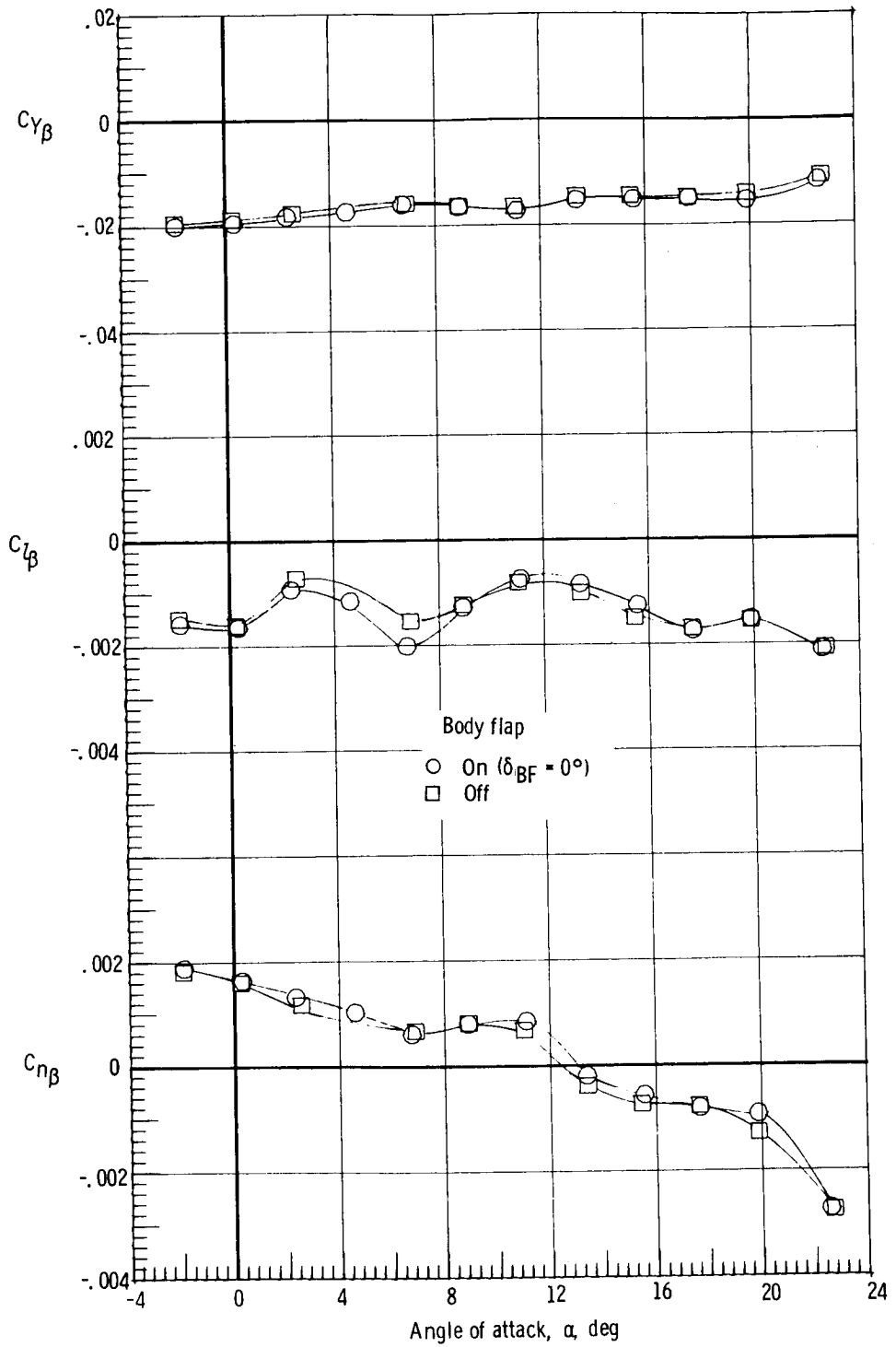
(e)   M = 1.2.

Figure 12.- Concluded.
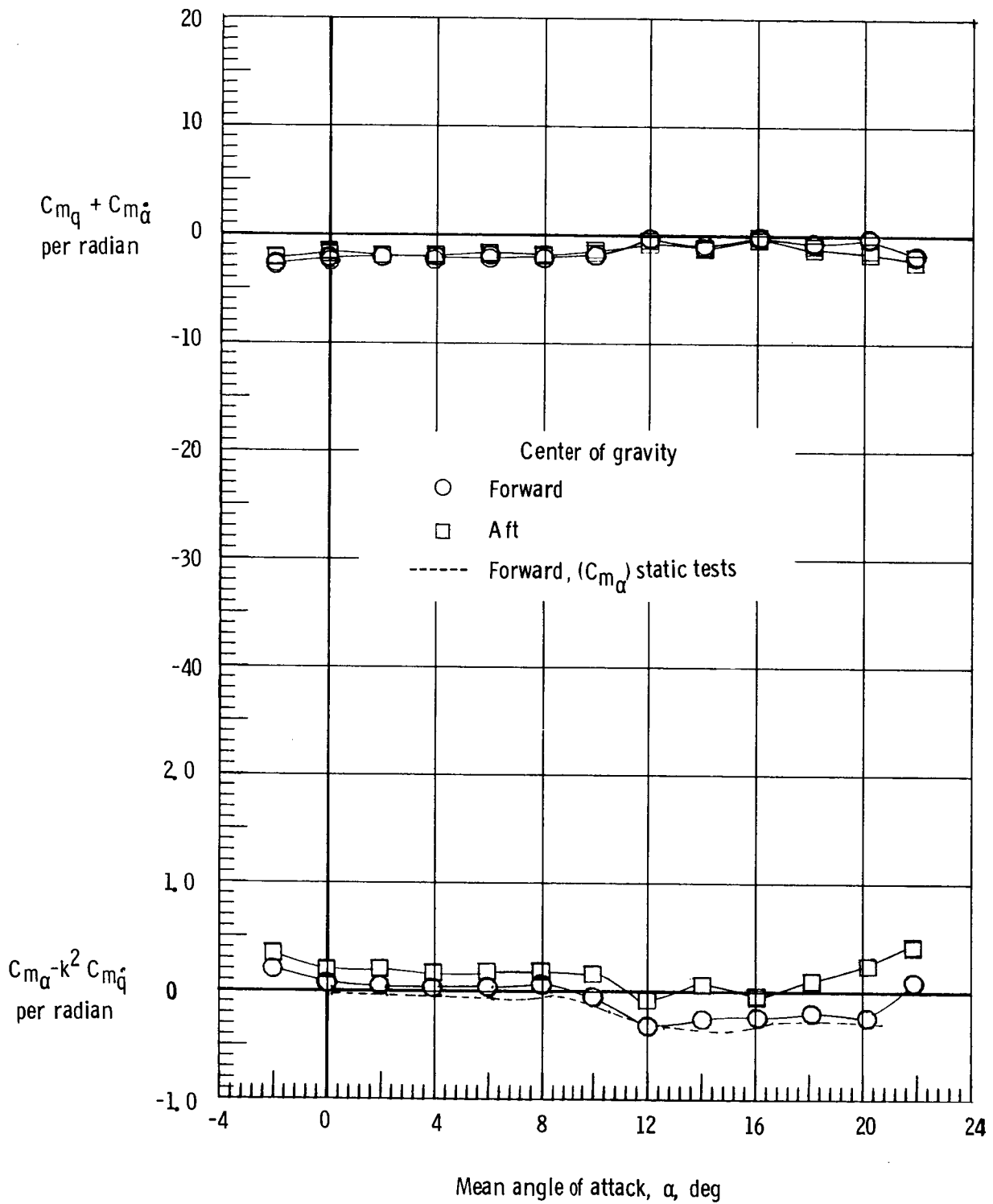
(a) M = 0.3.

Figure 13.- Effect of center-of-gravity position on the damping in pitch parameter and on the oscillatory stability in pitch parameter. $\delta_e = 0^o$; rudder flare, 10°; $\delta_{BF} = 0^o$.
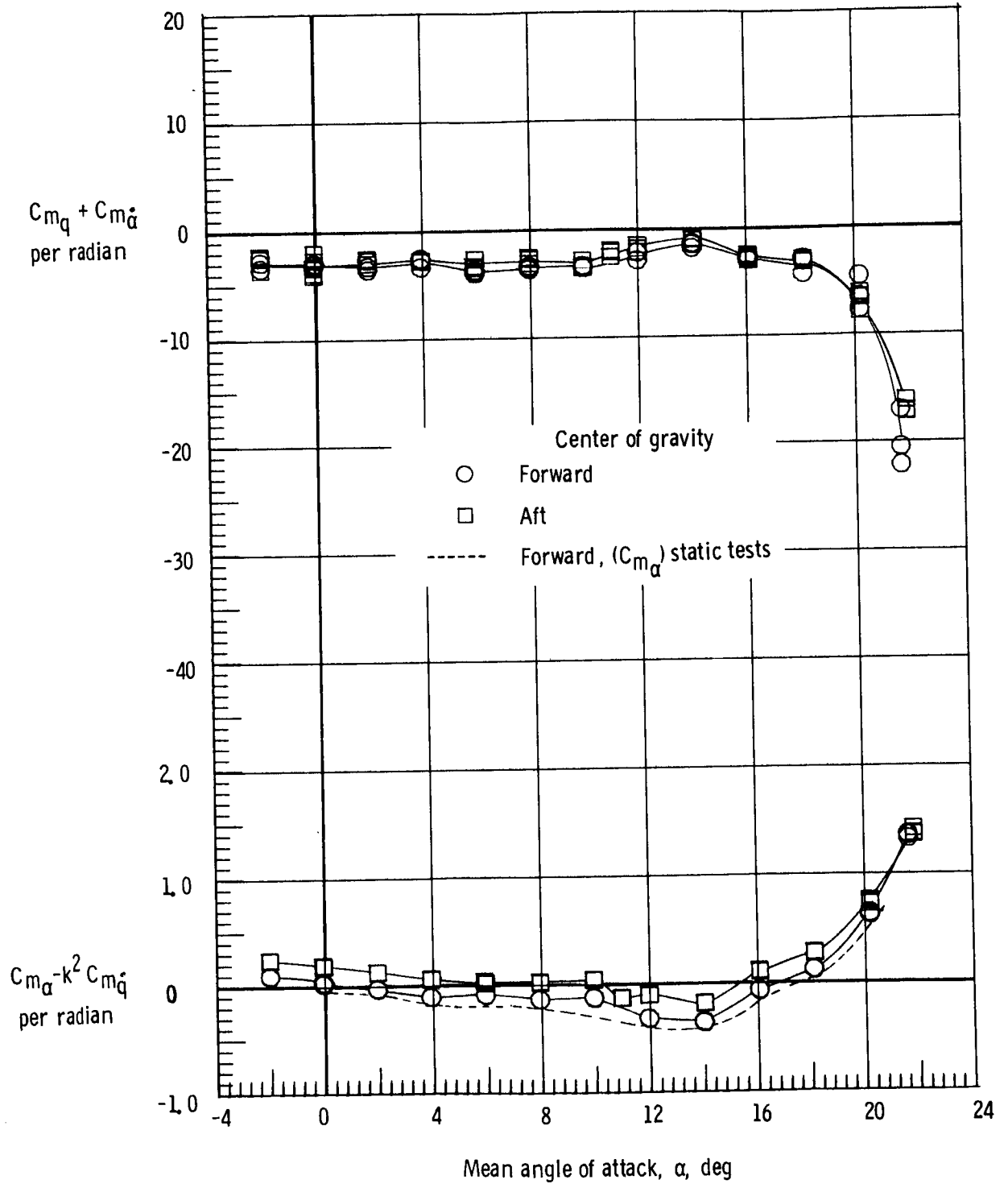
(b)   M = 0.8.

Figure 13.- Continued.
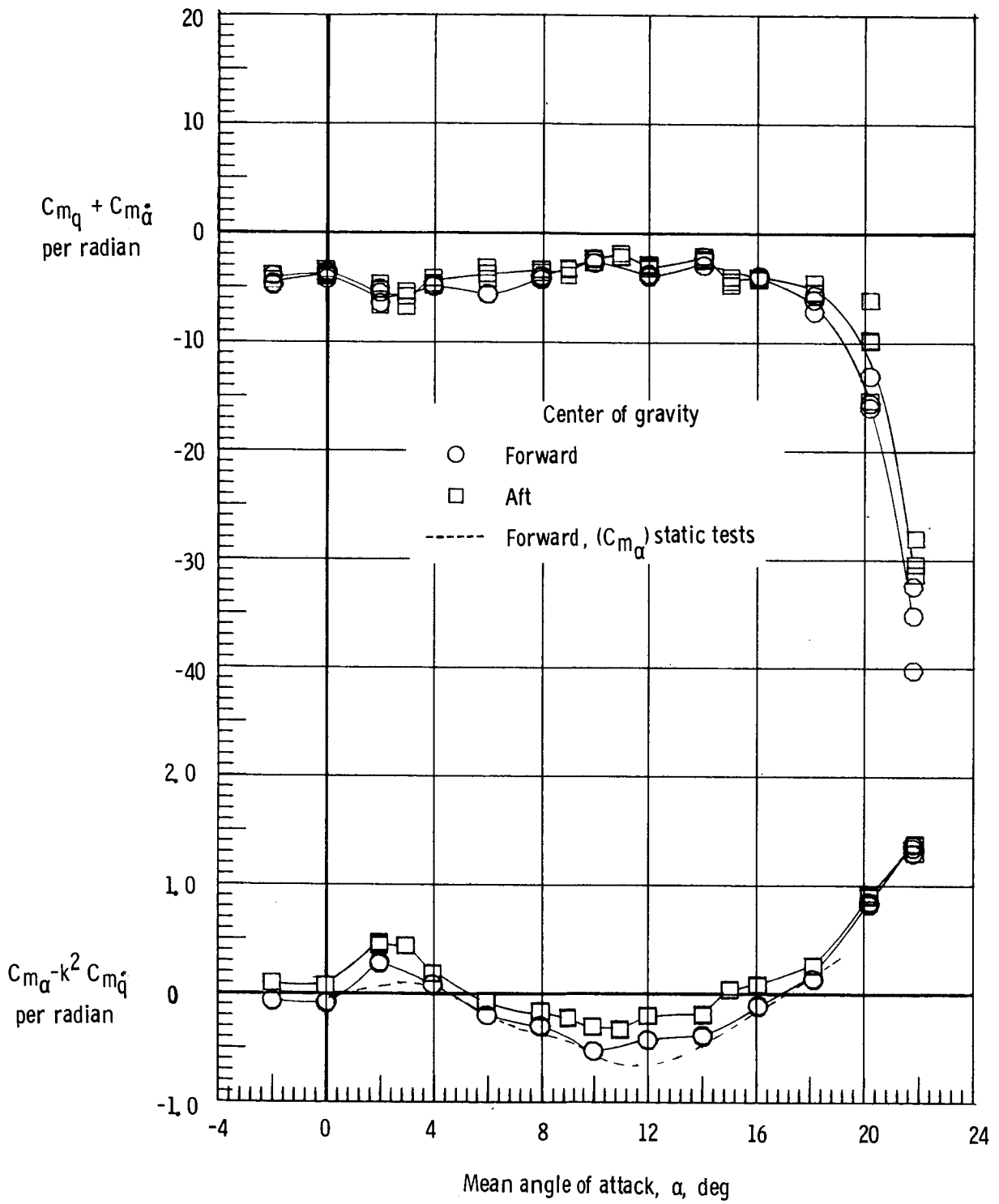
(c)   M = 0.9.

Figure 13.- Continued.
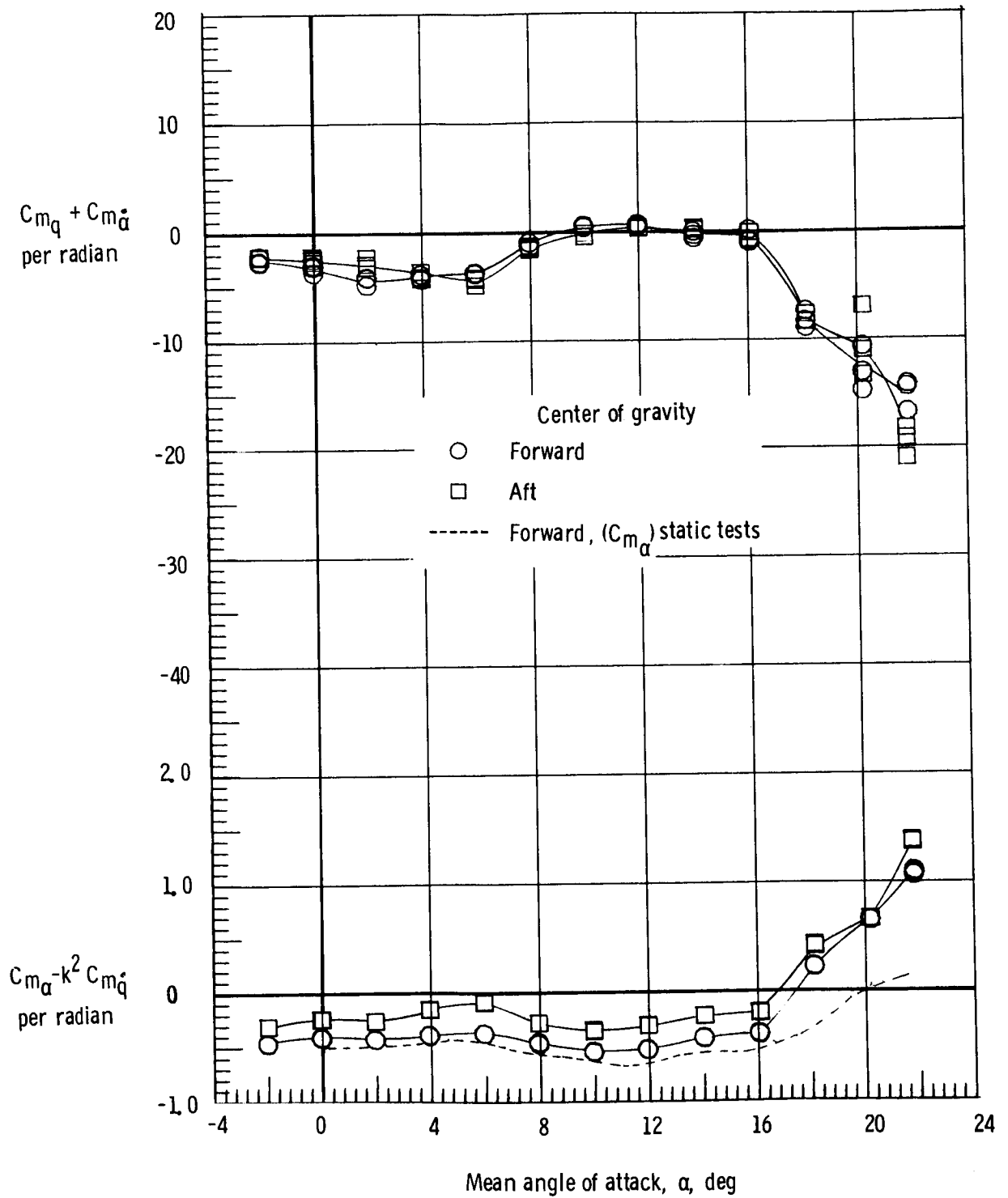
(d)   M = 0.98.

Figure 13.– Continued.
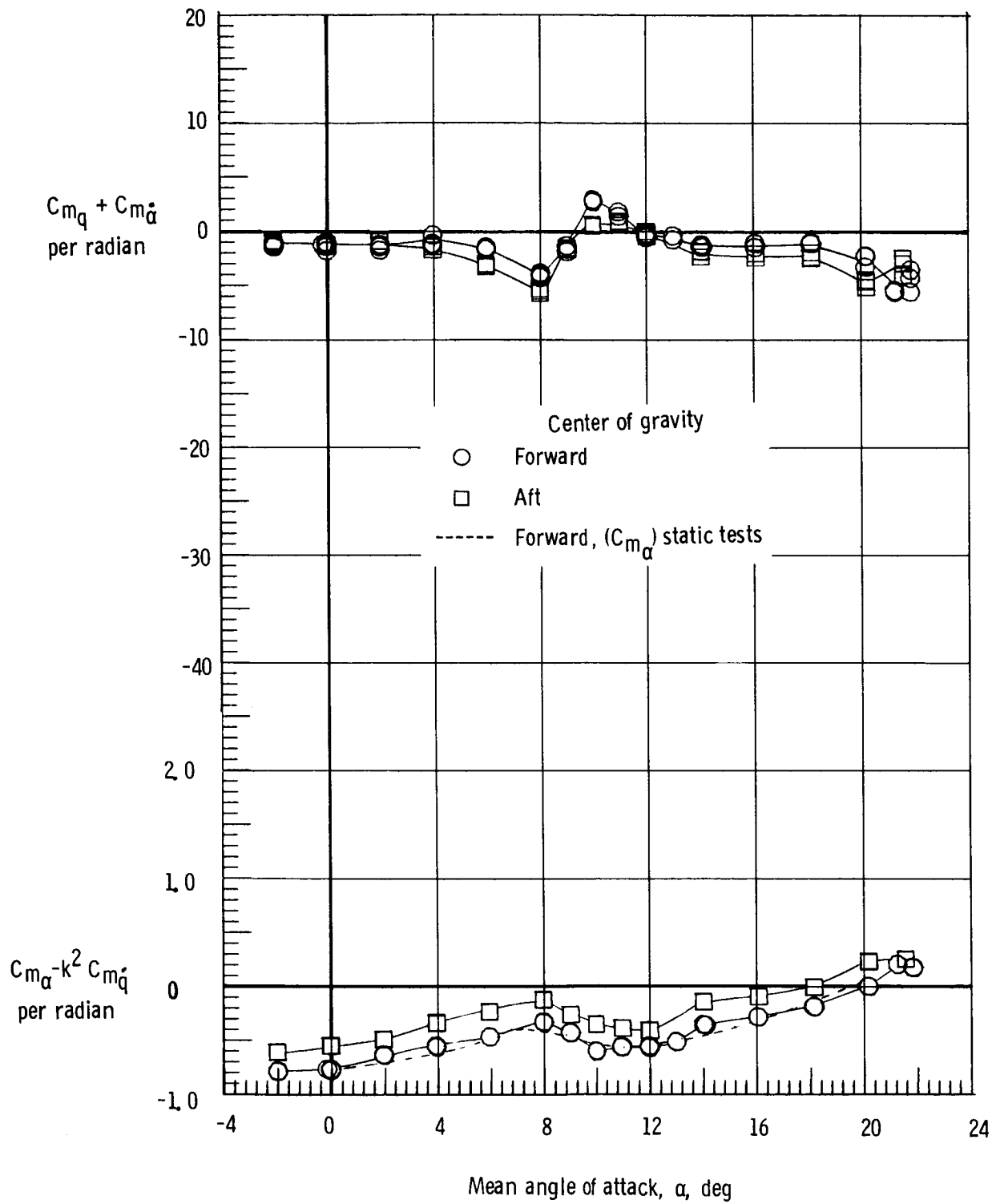
(e) M = 1.2.

Figure 13.- Concluded.
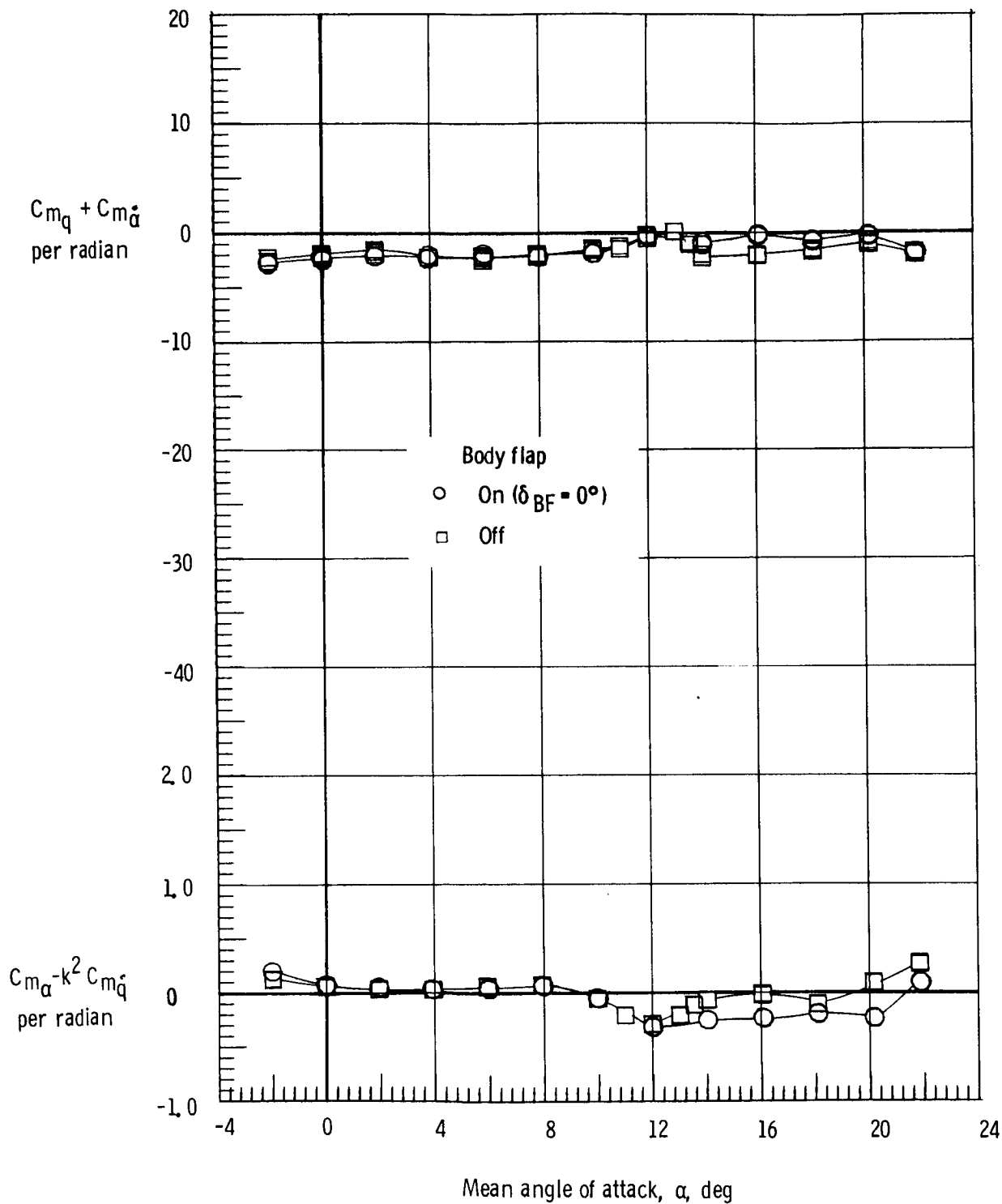
(a) M = 0.3.

Figure 14.- Effect of body flap on the damping in pitch parameter and on the oscillatory stability in pitch parameter. Forward center of gravity; $\delta_e = 0^O$; rudder flare, 10°.

(b) M = 0.8.

Figure 14.- Continued.

Mean angle of attack, α, deg
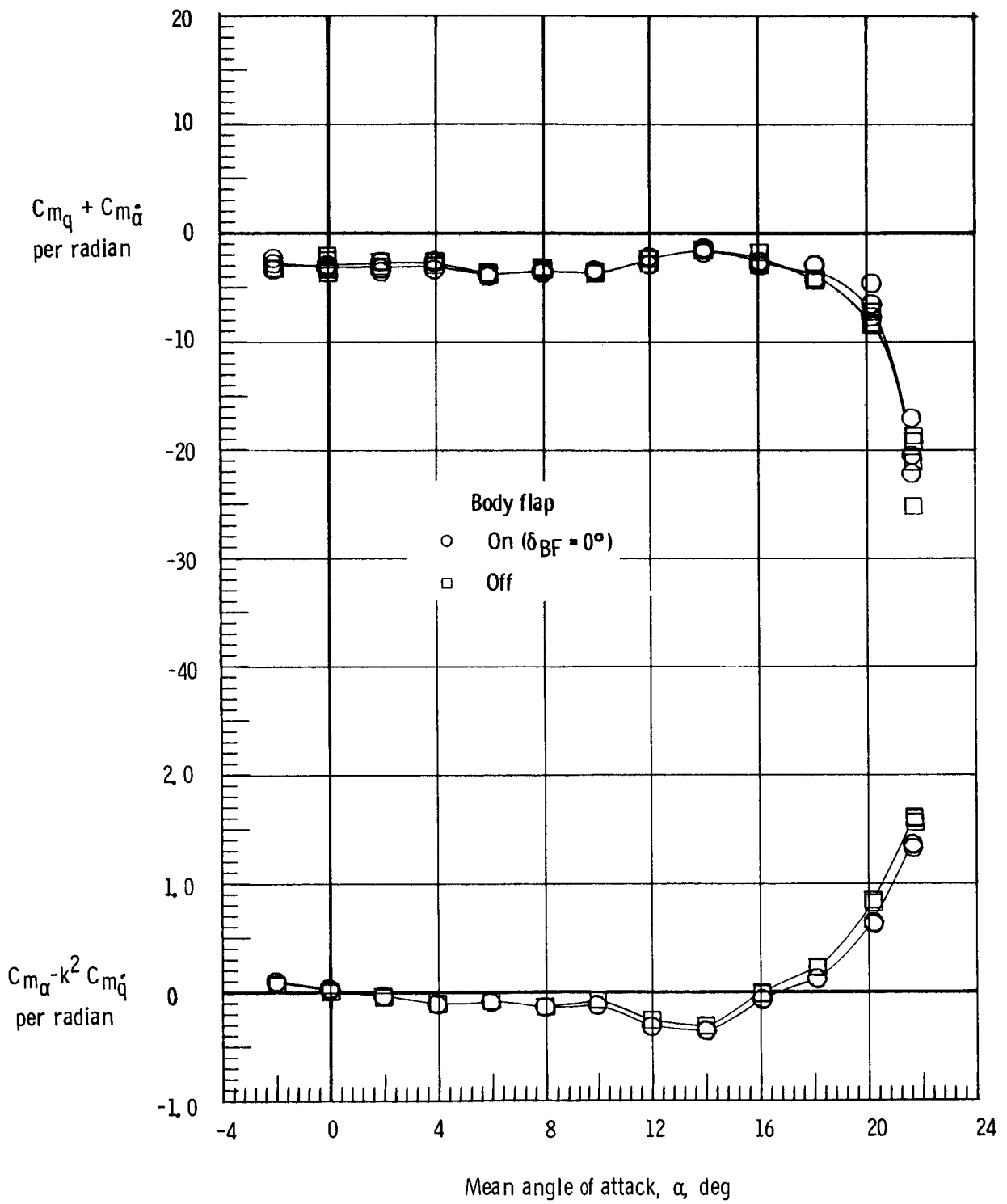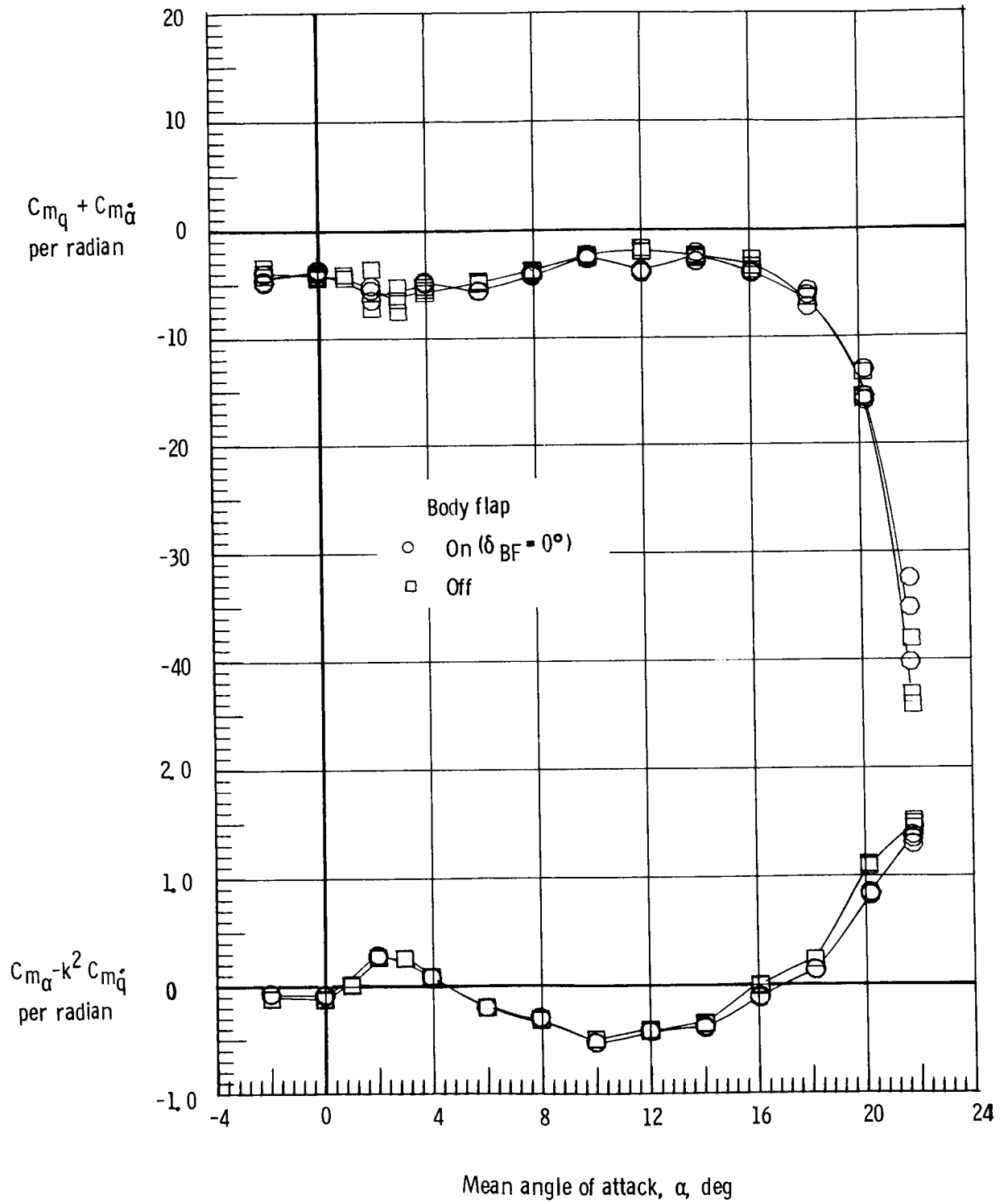
(c)   M = 0.9.

Figure 14.- Continued.
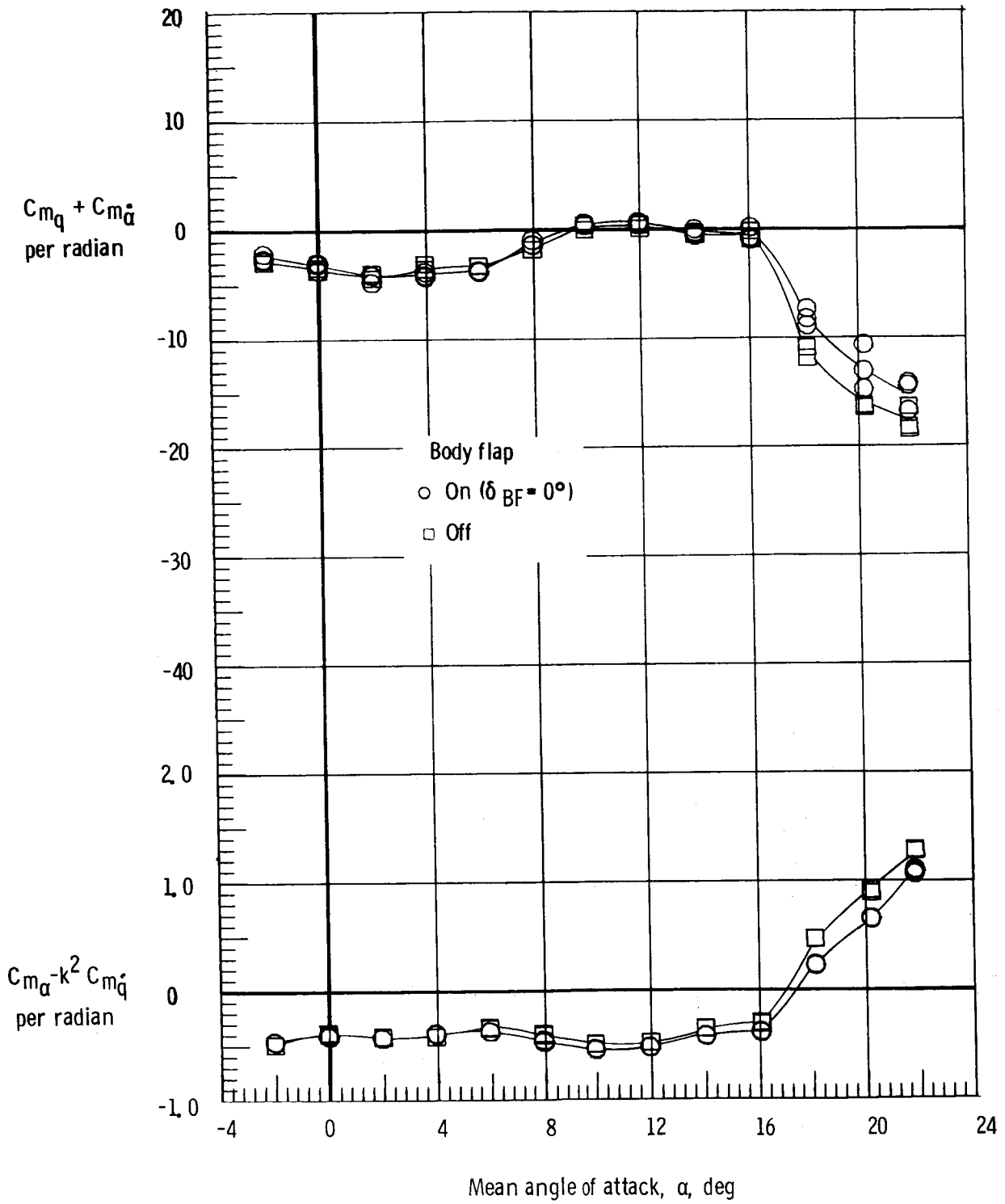
(d) M = 0.98.

Figure 14.- Continued.
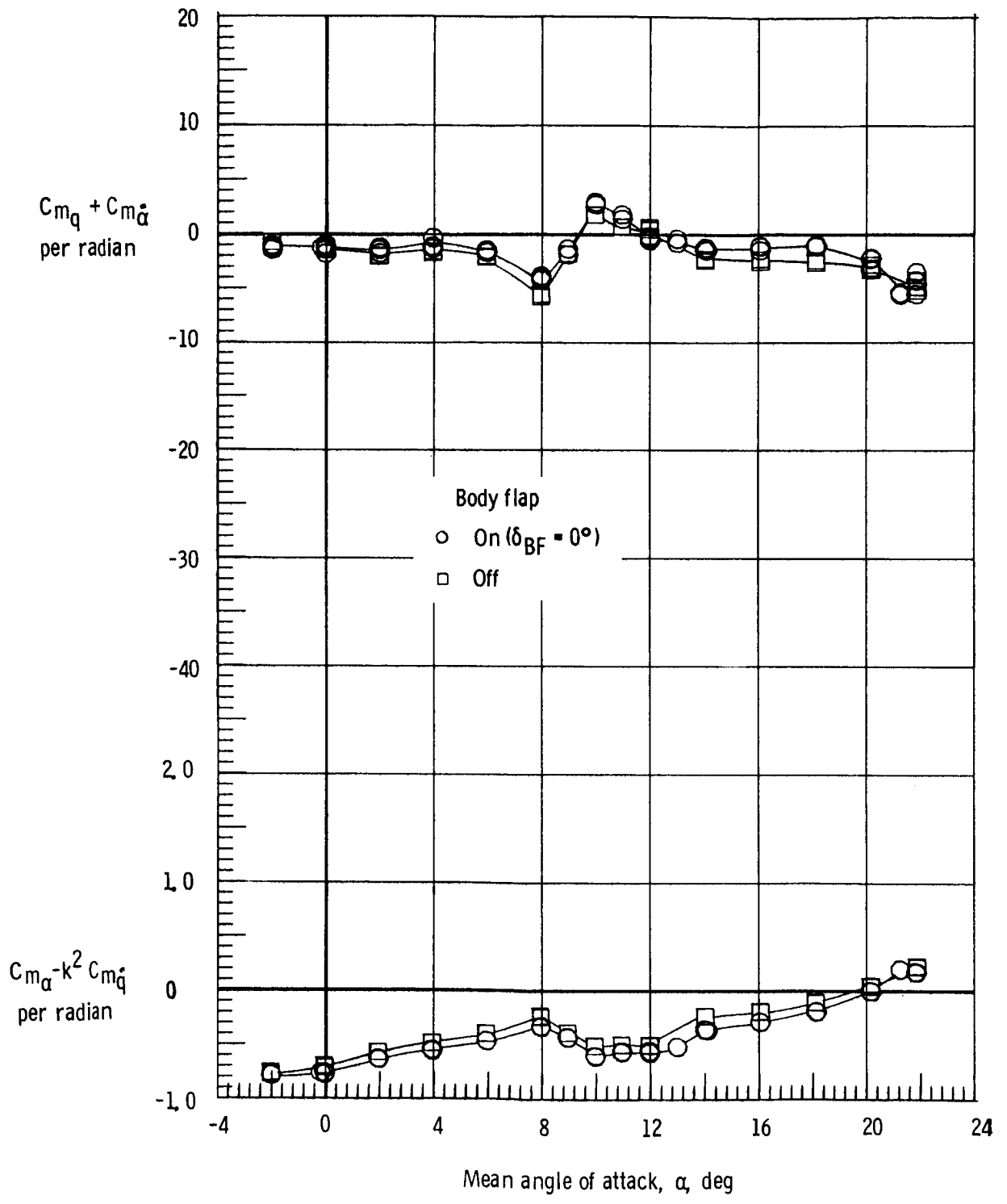
(e) M = 1.2.

Figure 14.- Concluded.
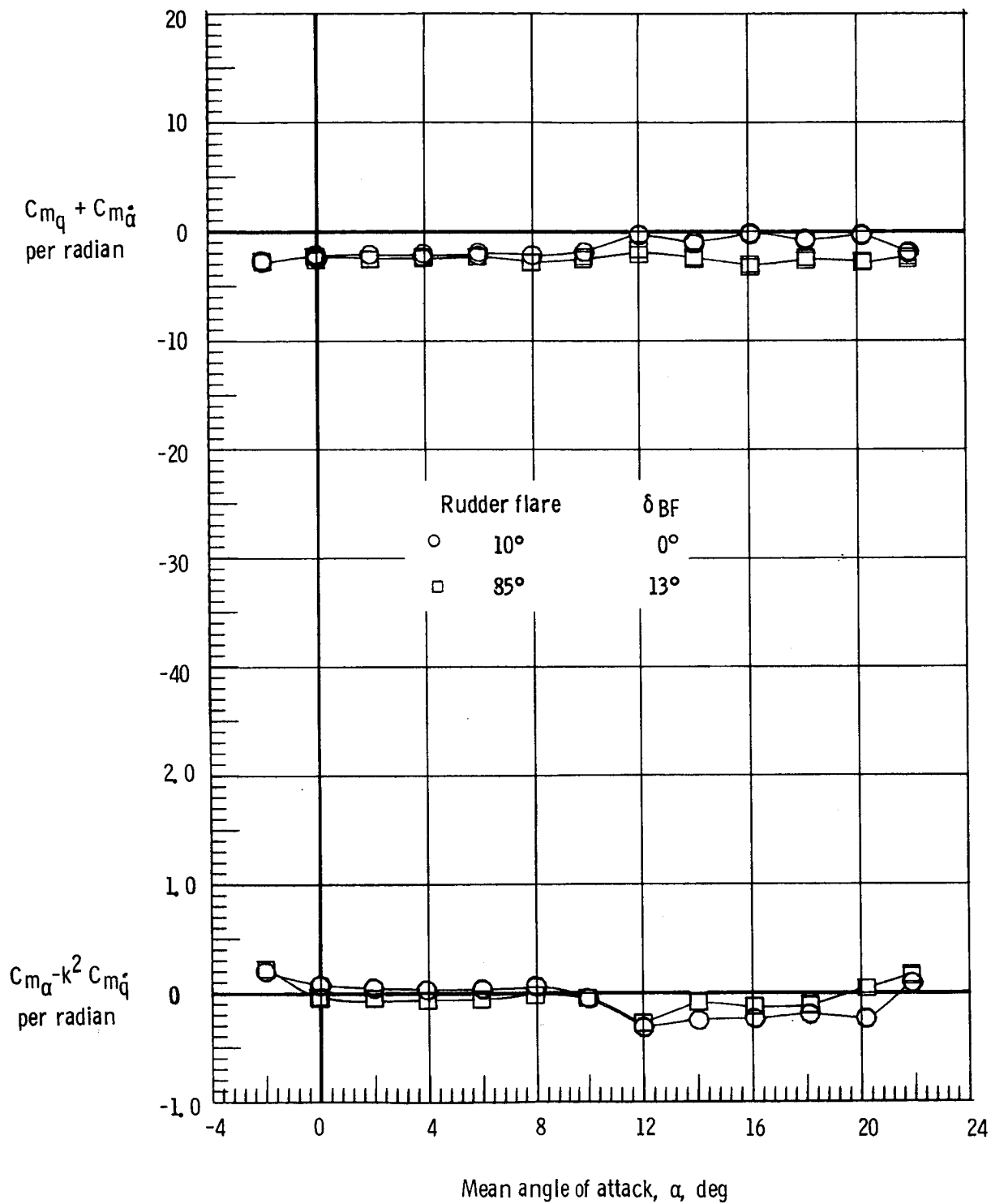
(a) M = 0.3.

Figure 15.- Effect of rudder flare and body flap deflection on the damping in pitch
parameter and on the oscillatory stability in pitch parameter.   Forward center
of gravity; $\delta_e = 0^o$.
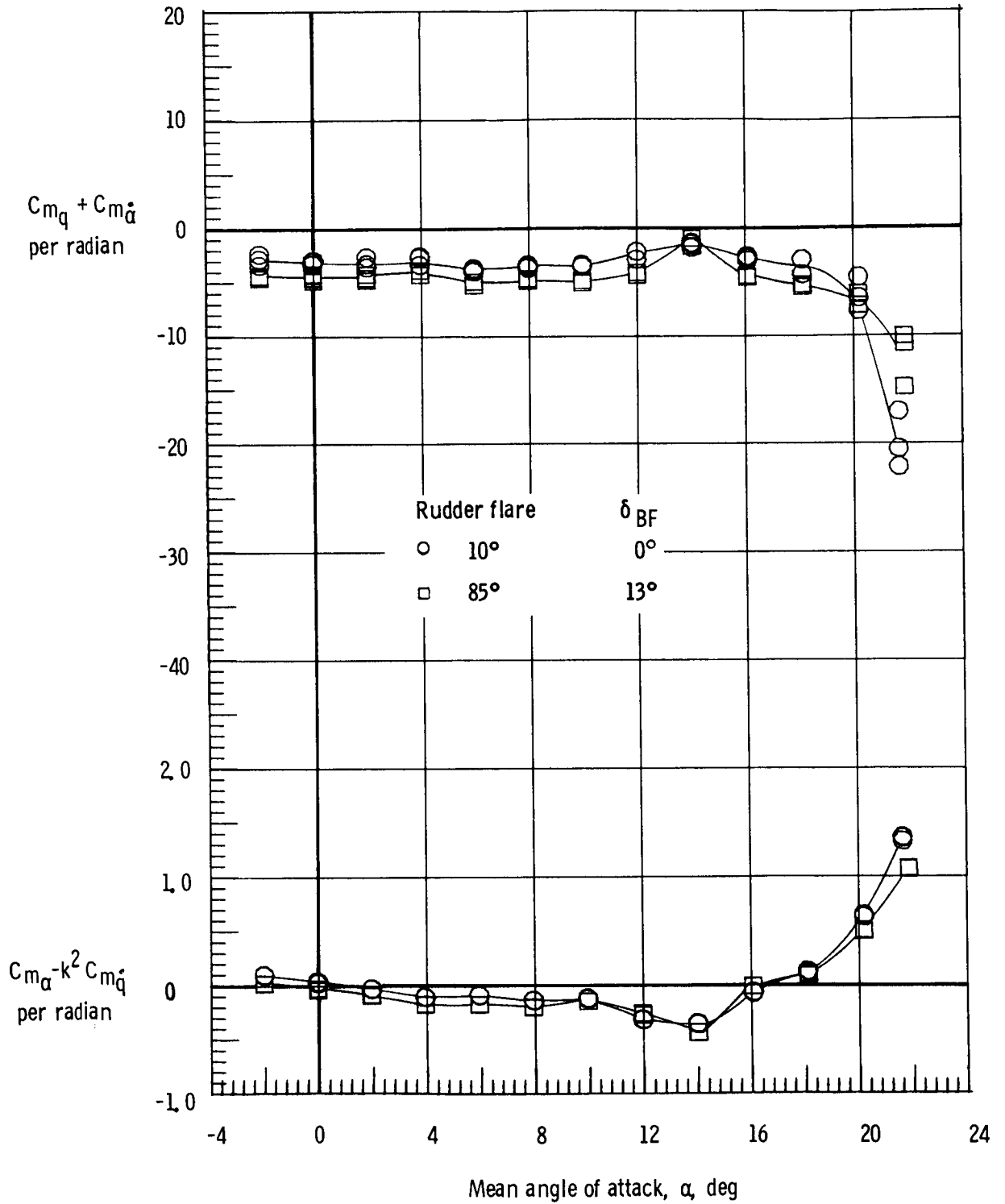
(b) M = 0.8.

Figure 15.- Continued.
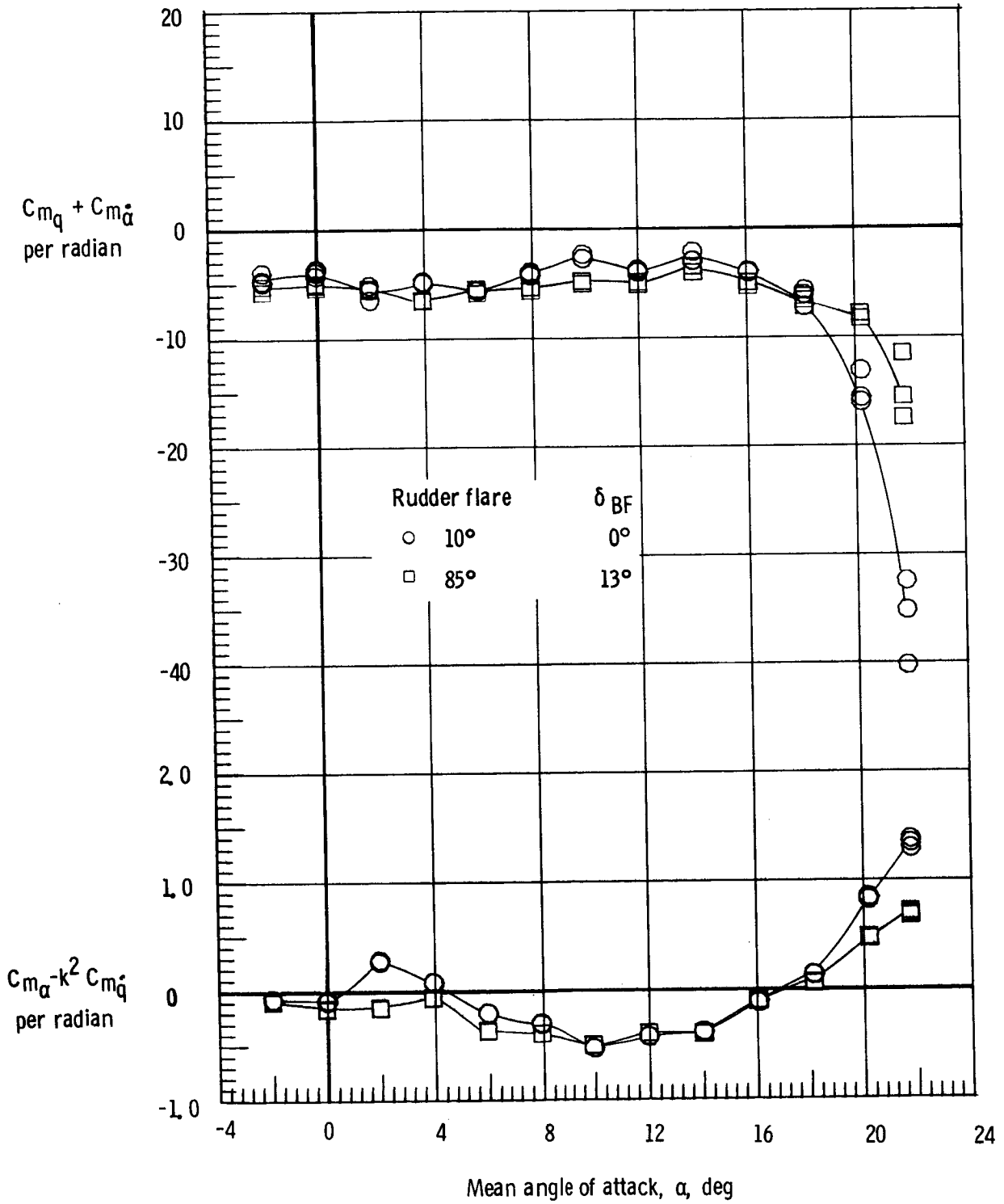
(c) M = 0.9.

Figure 15.- Continued.
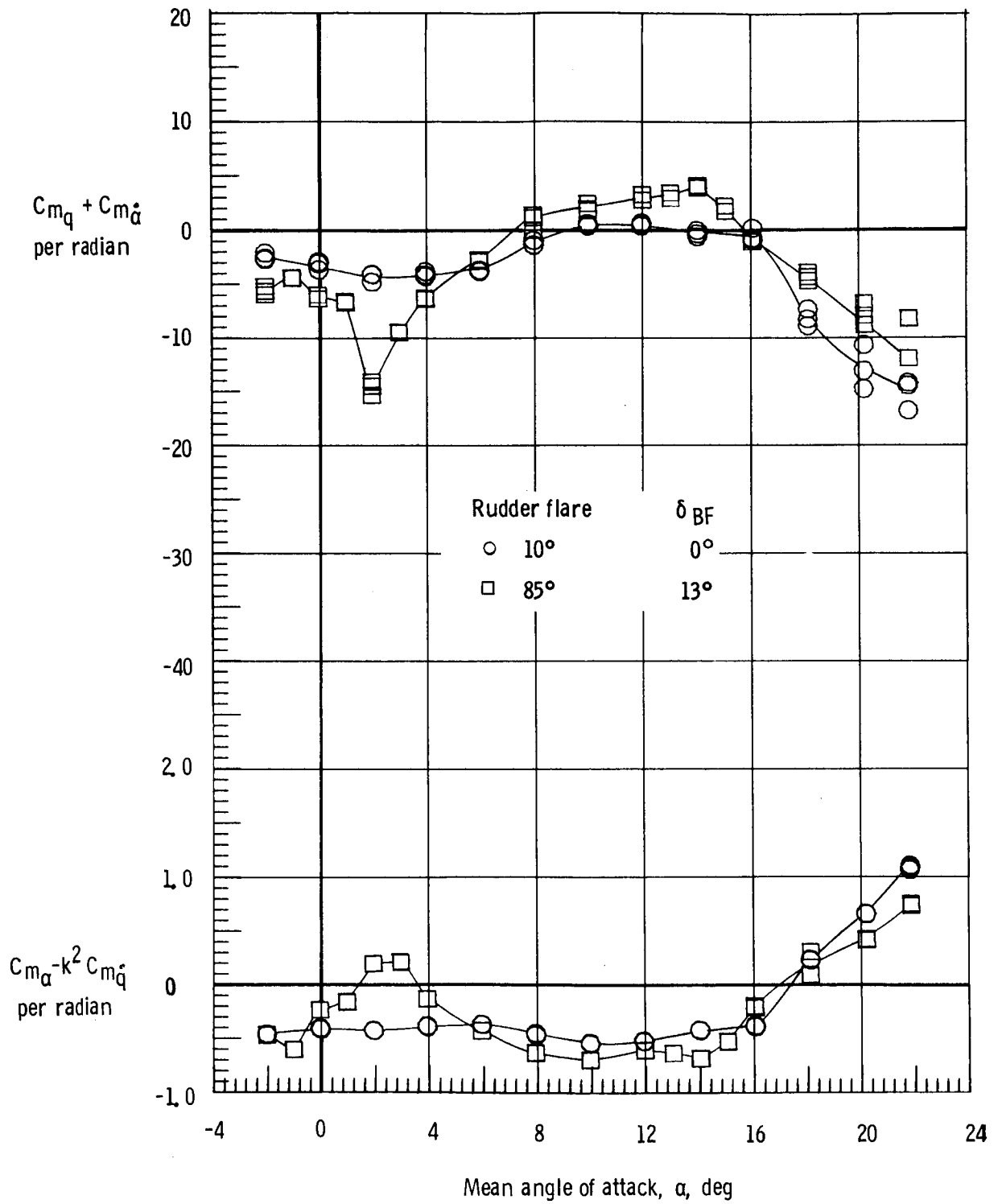
(d) M ≈ 0.98.

Figure 15.- Continued.
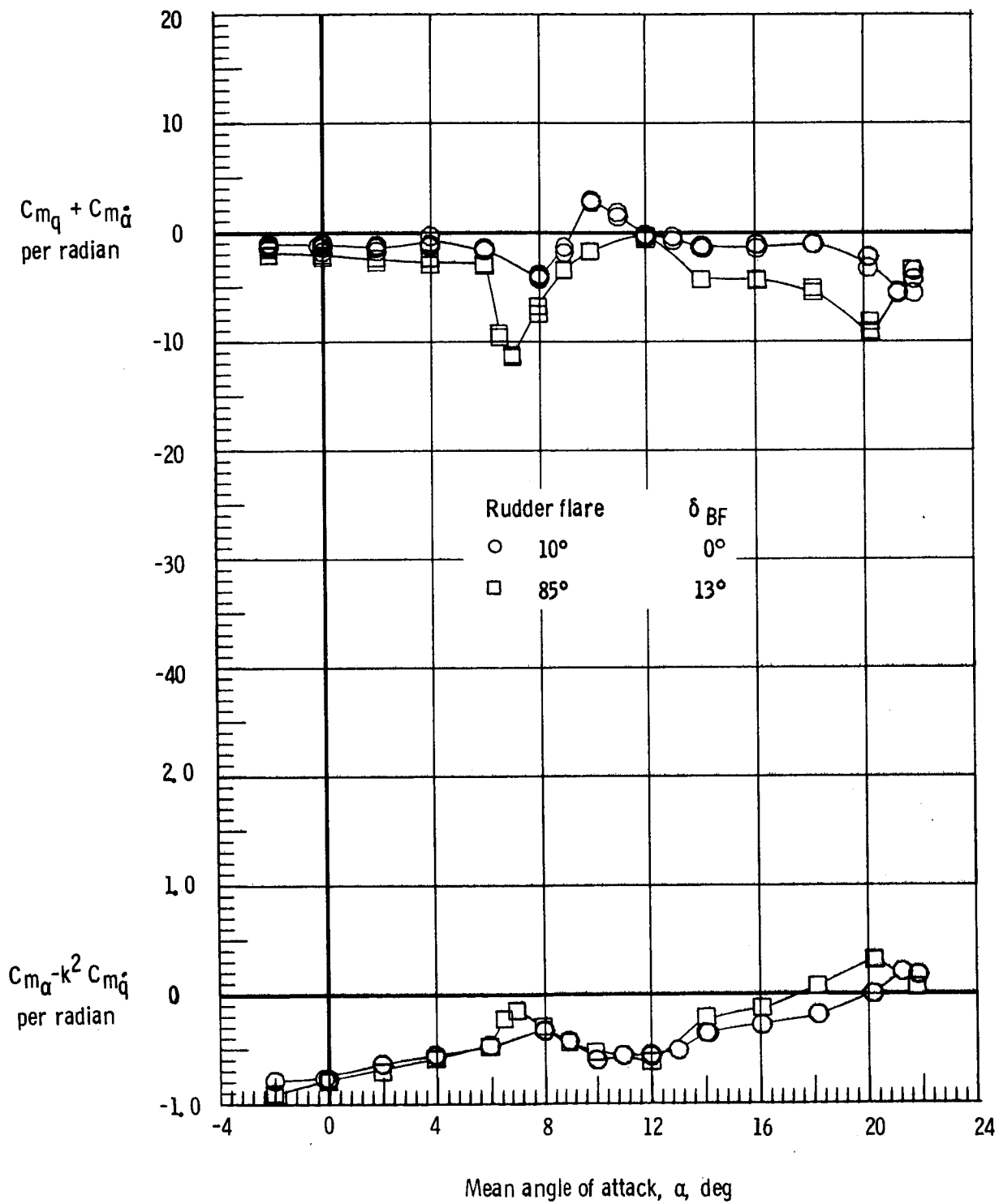
(e) M = 1.2.

Figure 15.- Concluded.
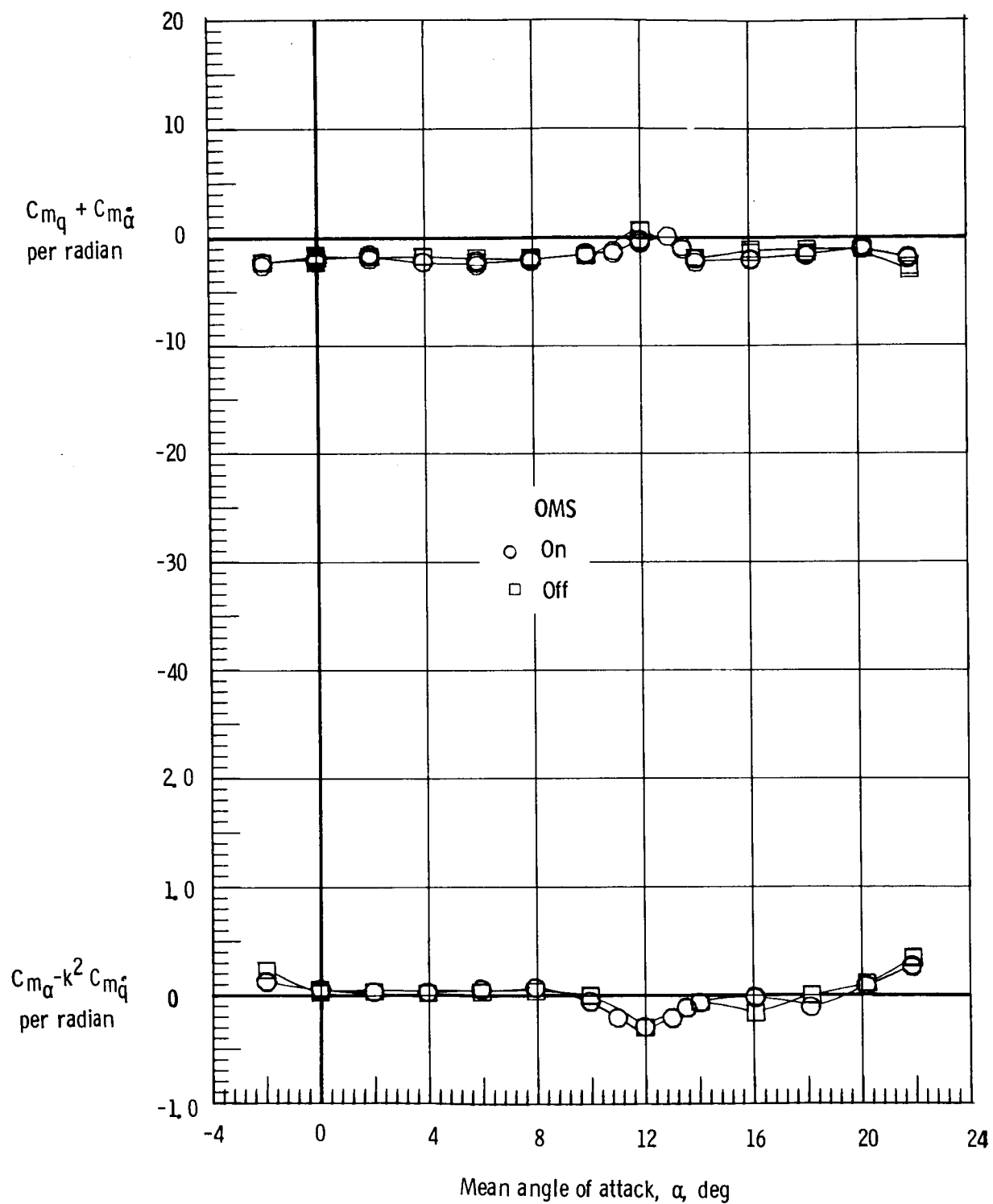
(a)   M = 0.3.

Figure 16.- Effect of OMS installation on the damping in pitch parameter and on the oscillatory stability in pitch parameter.   Forward center of gravity; rudder flare, 10°; body flap off.

(b) M = 0.8.

Figure 16.- Continued.

Mean angle of attack, α, deg
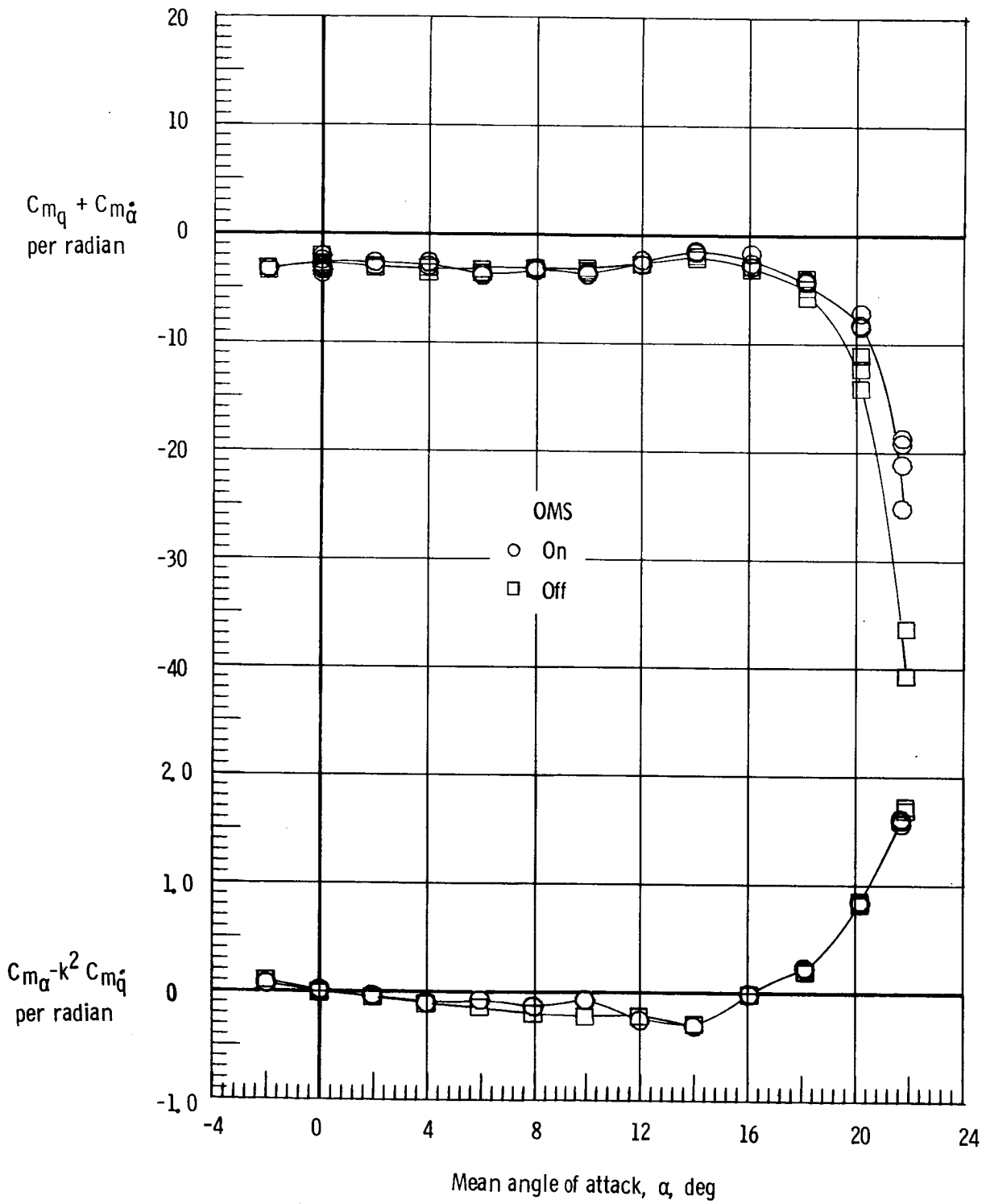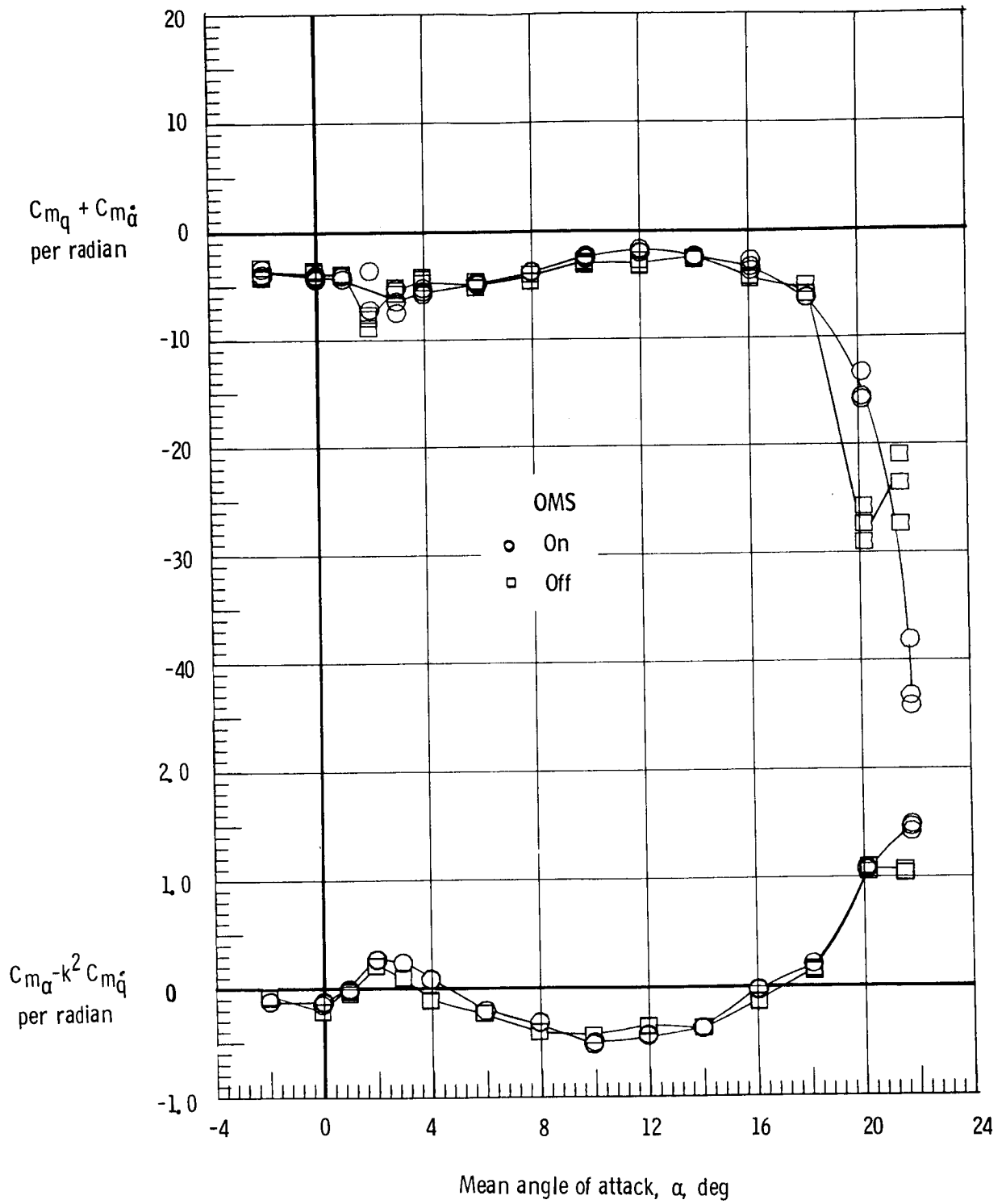
(c)   M = 0.9.

Figure 16.- Continued.
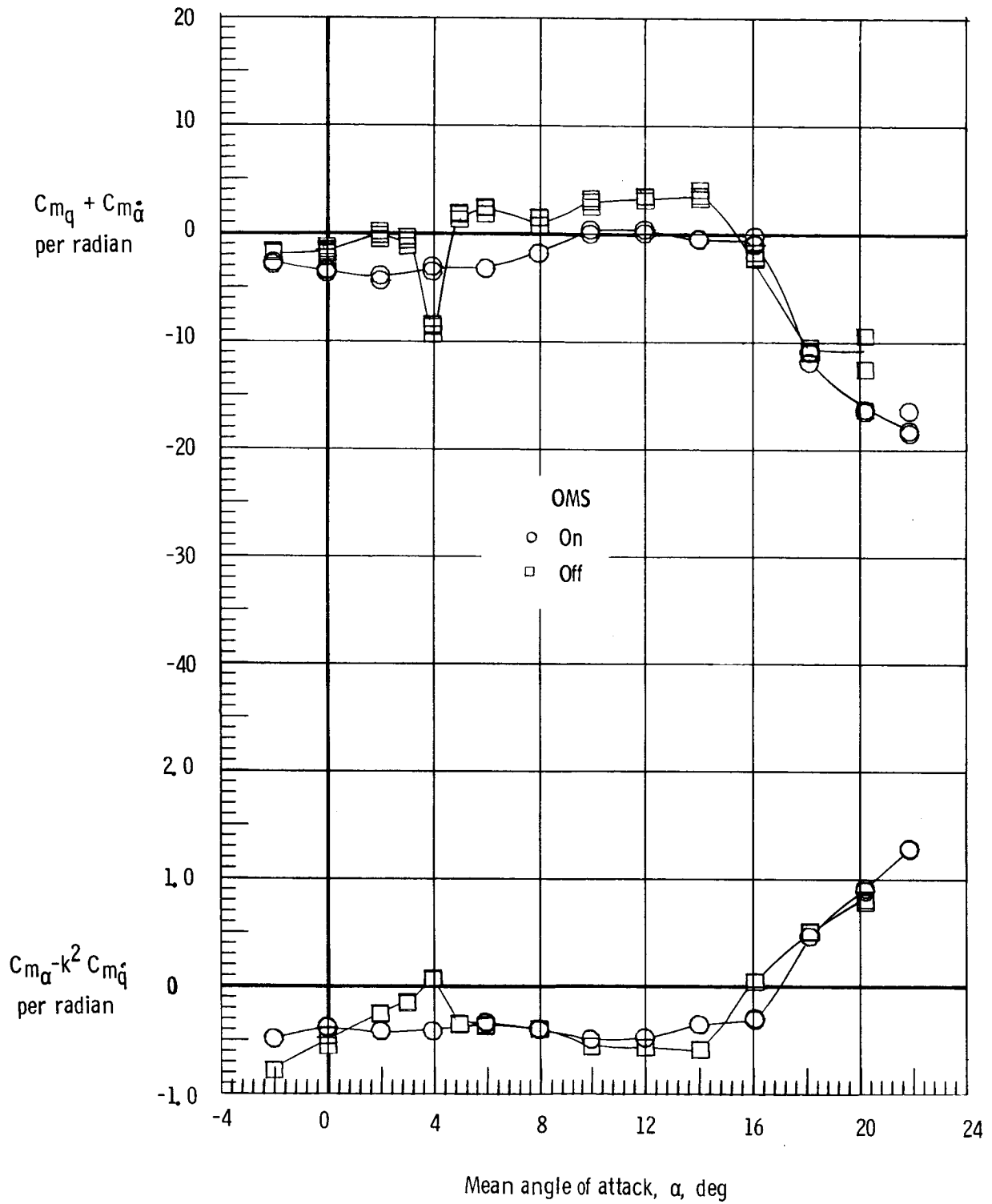
(d) M = 0.98.

Figure 16.- Continued.
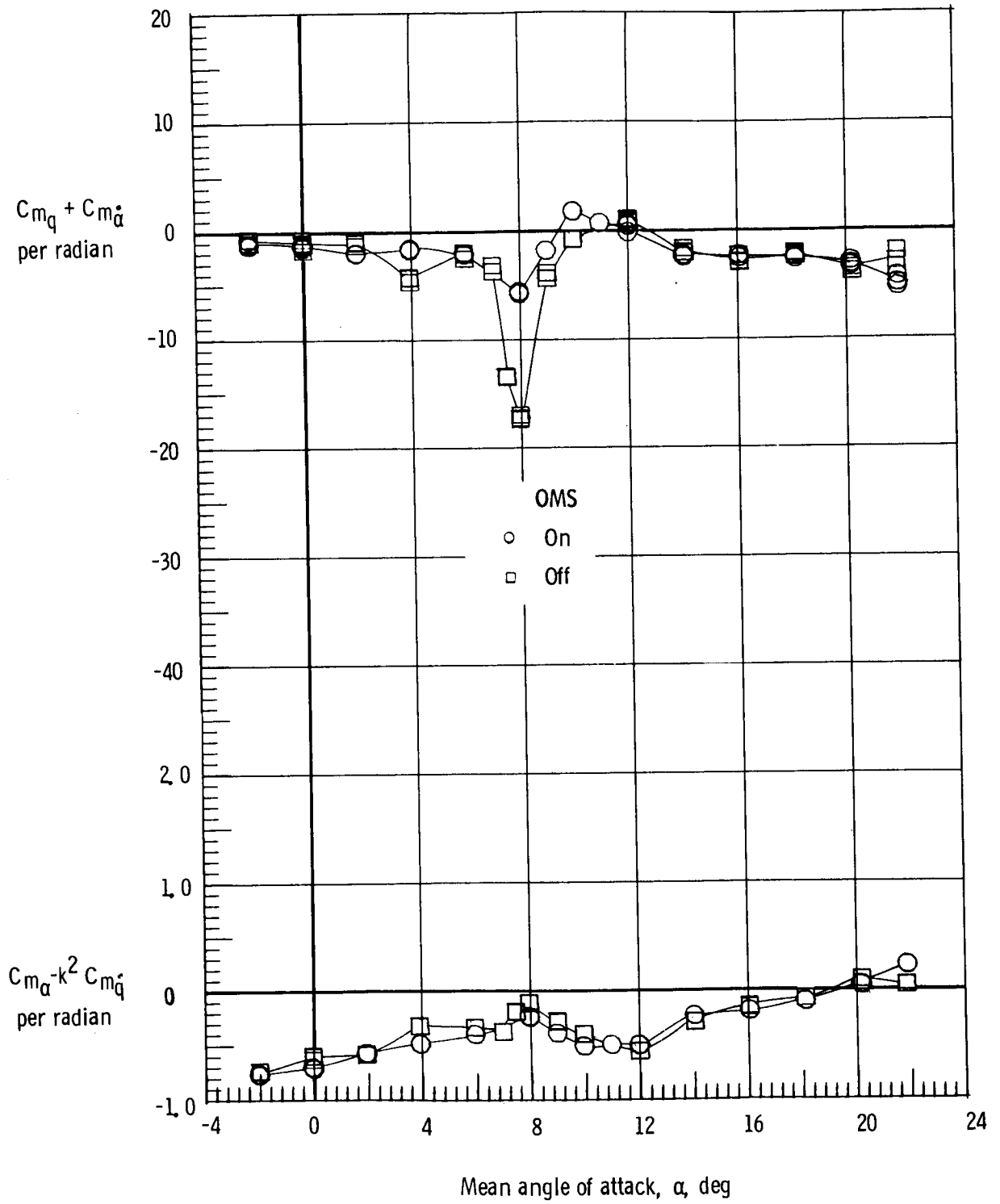
(e) M = 1.2.

Figure 16.- Concluded.
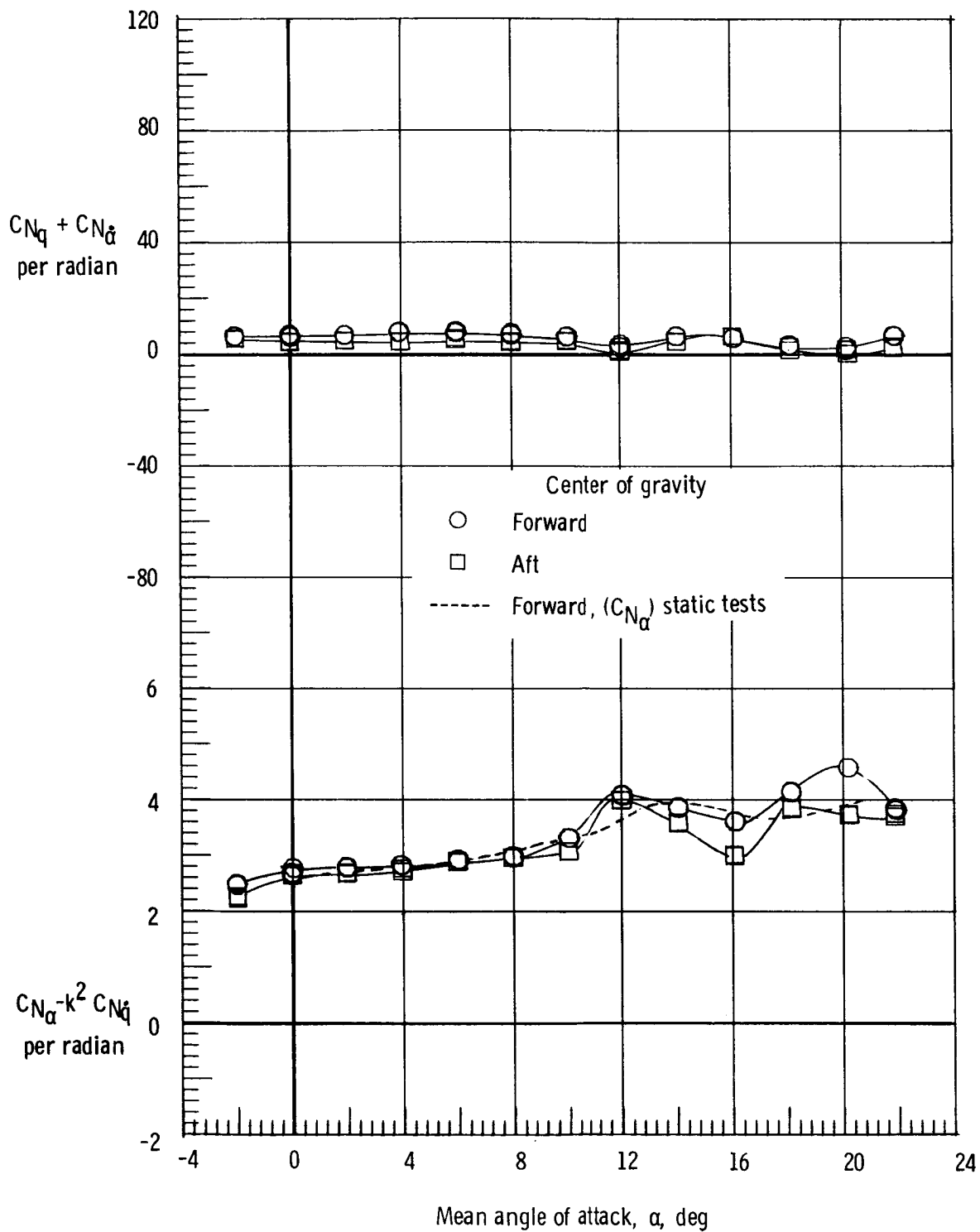
(a) M = 0.3.

Figure 17.- Effect of center-of-gravity position on normal force due to pitch rate
parameter and normal force due to pitch displacement parameter. δ_e = 0°;
rudder flare, 10°; δ_{BF} = 0°.
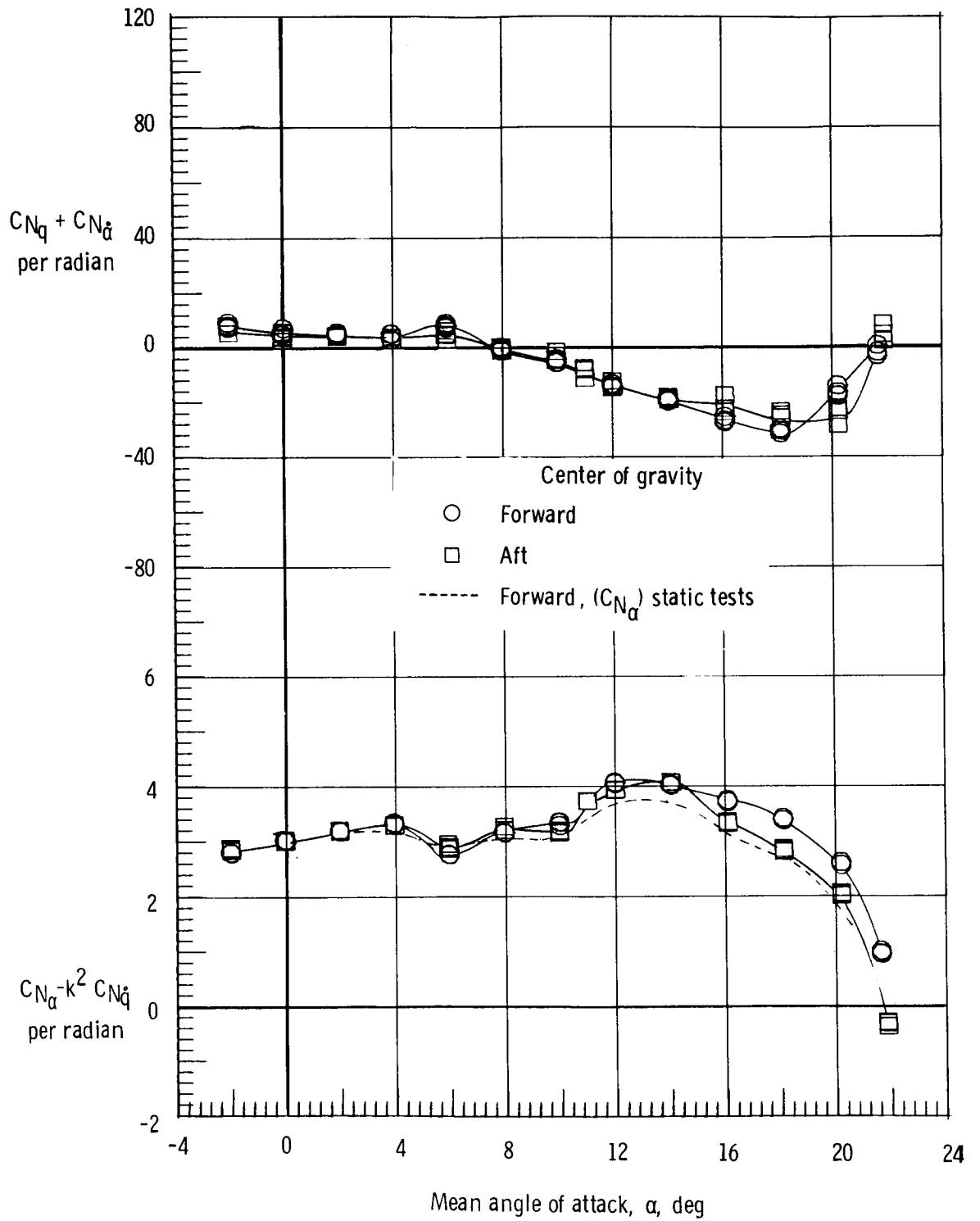
(b)   M = 0.8.

Figure 17.- Continued.
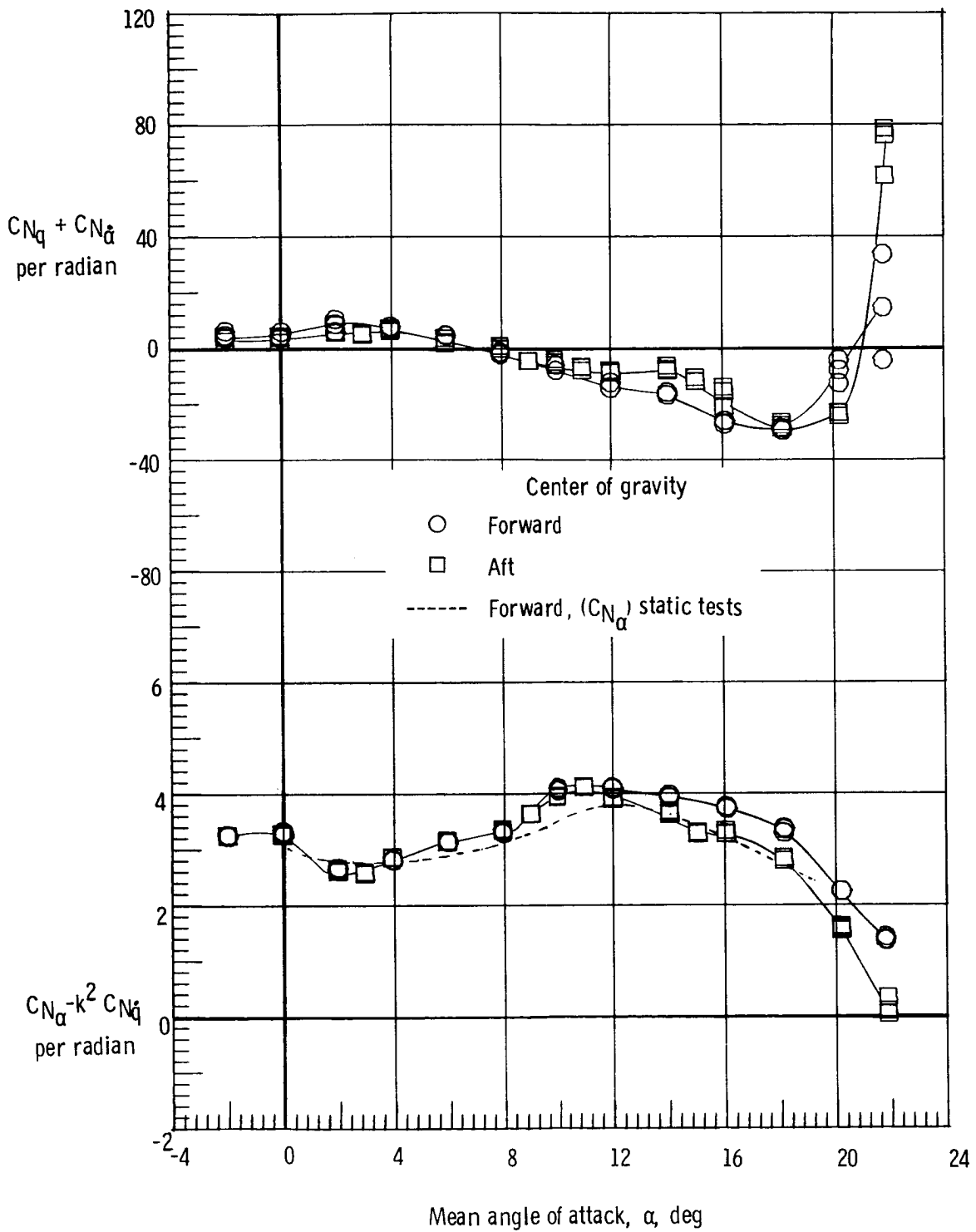
(c) M = 0.9.

Figure 17.- Continued.
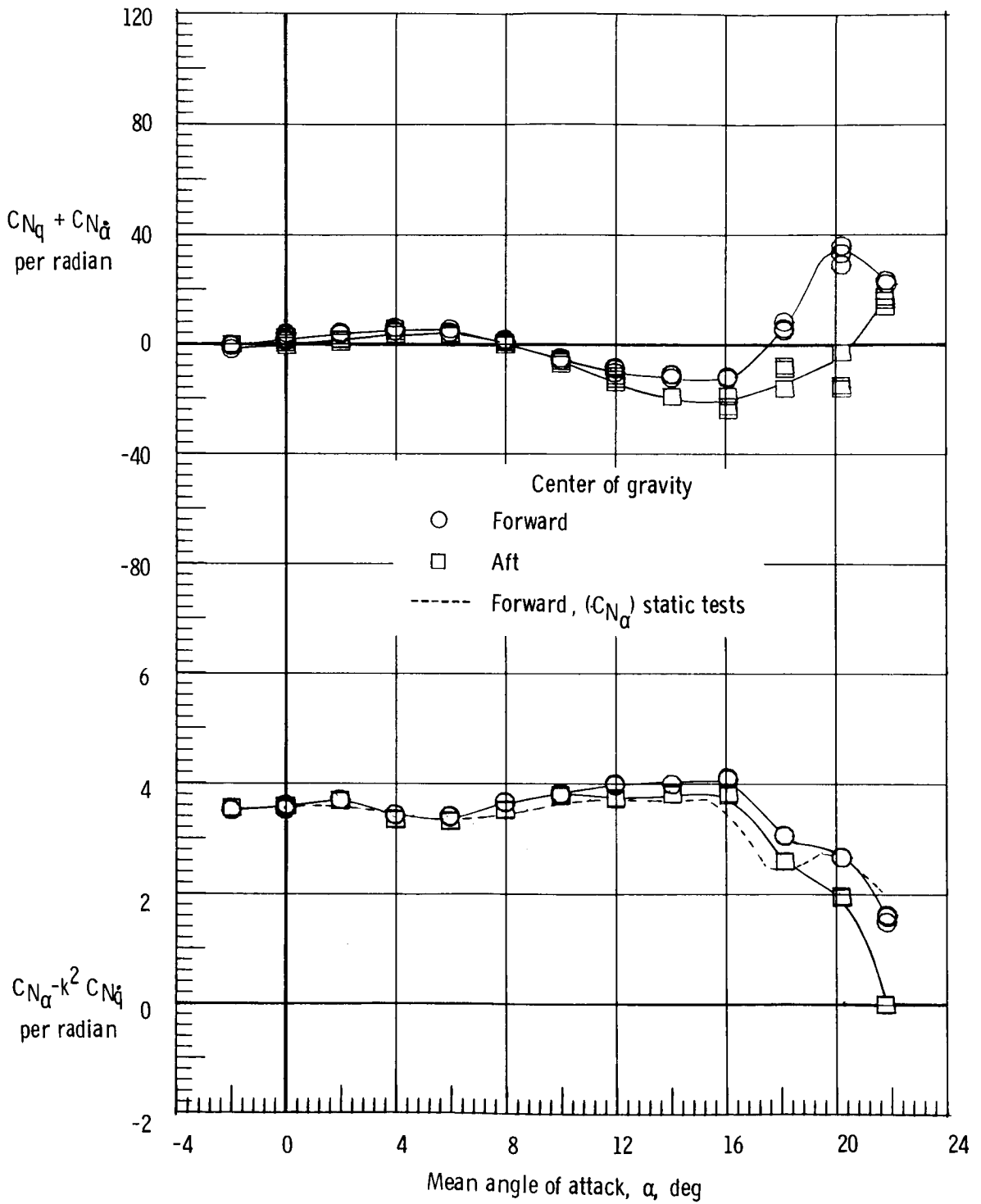
(d) M = 0.98.

Figure 17.- Continued.
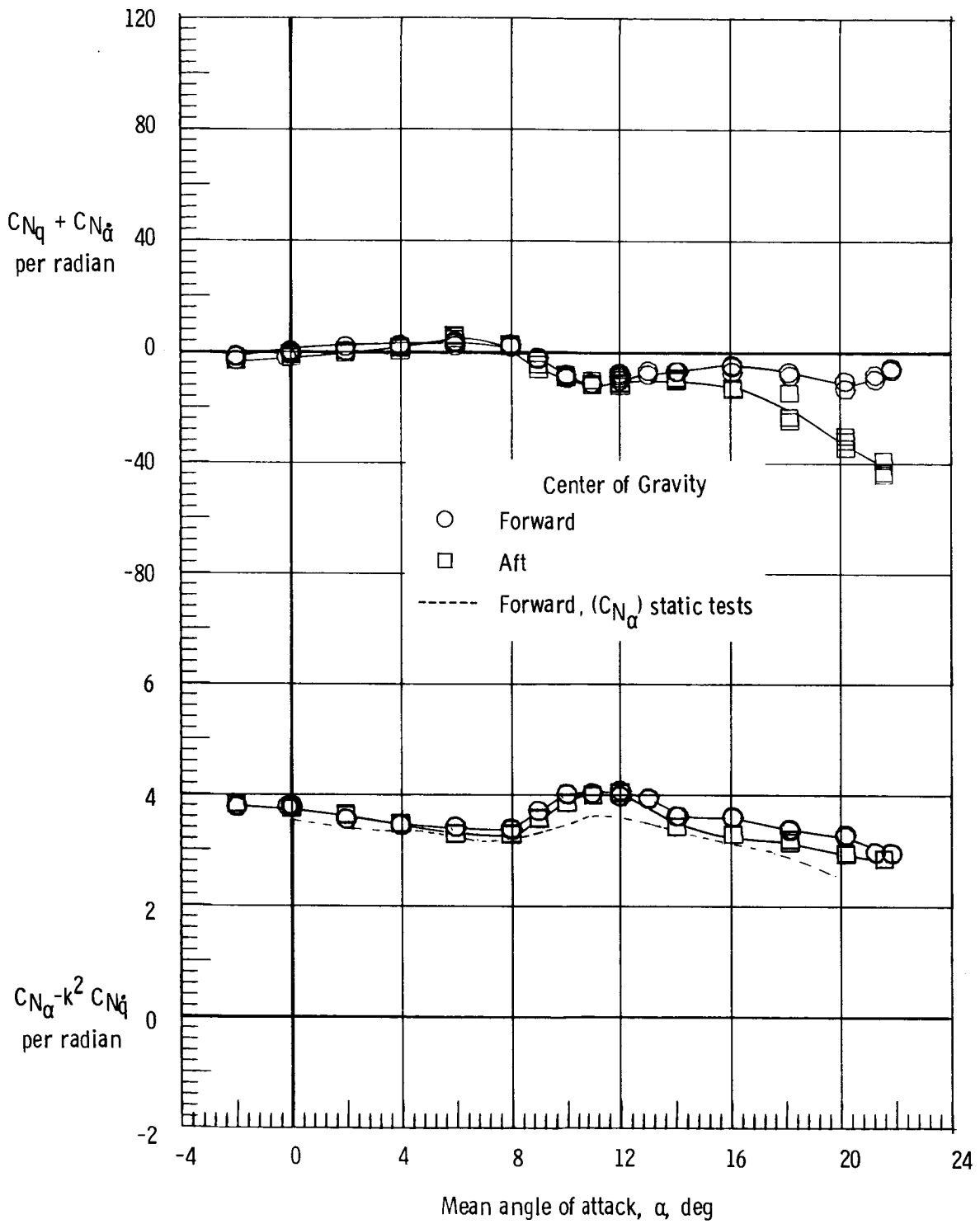
(e) M = 1.2.

Figure 17.- Concluded.
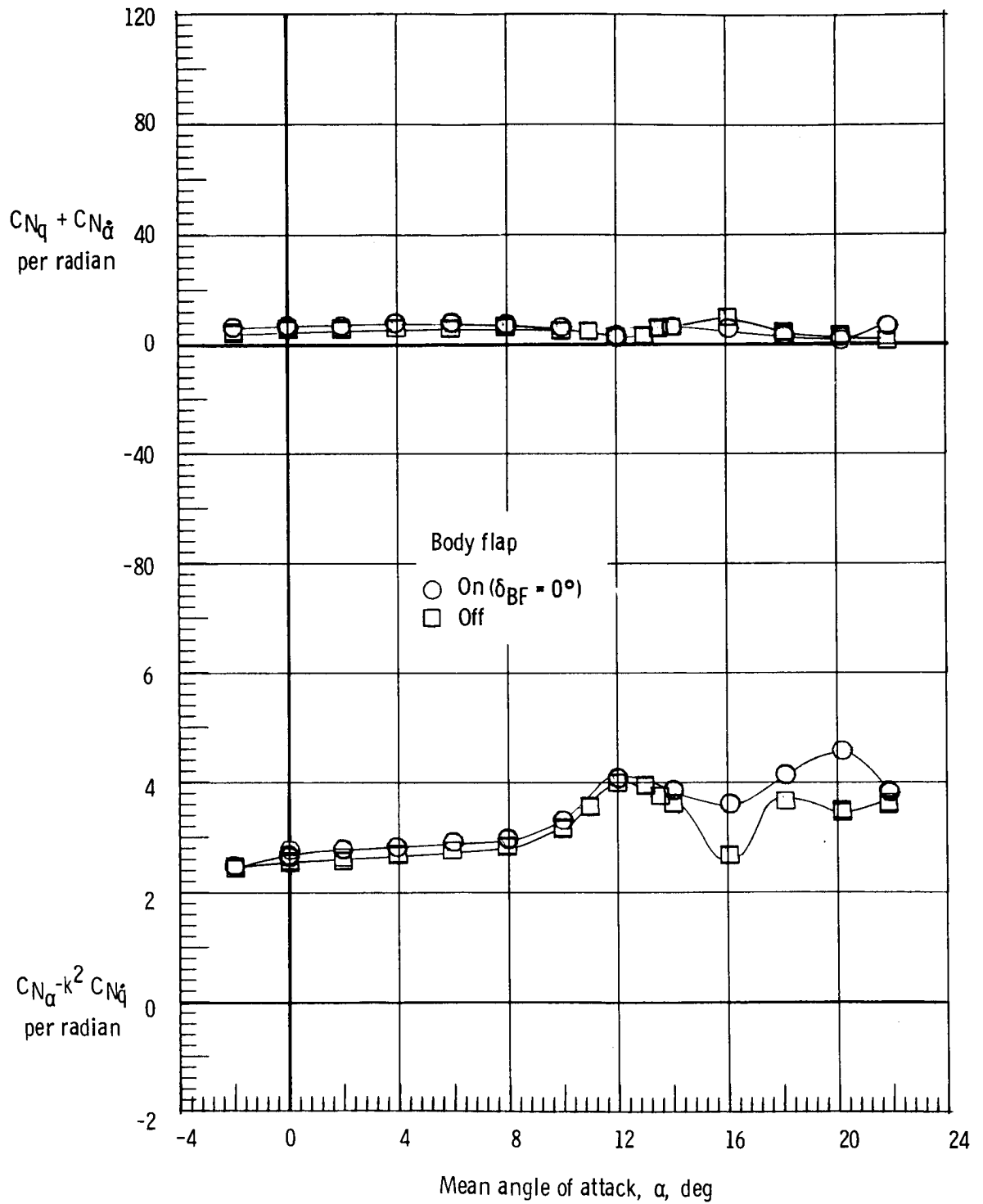
(a) M = 0.3.

Figure 18.- Effect of body flap on normal force due to pitch rate parameter and
   normal force due to pitch displacement parameter. Forward center of gravity;
   $\delta_e = 0^{\circ}$; rudder flare, 10°.
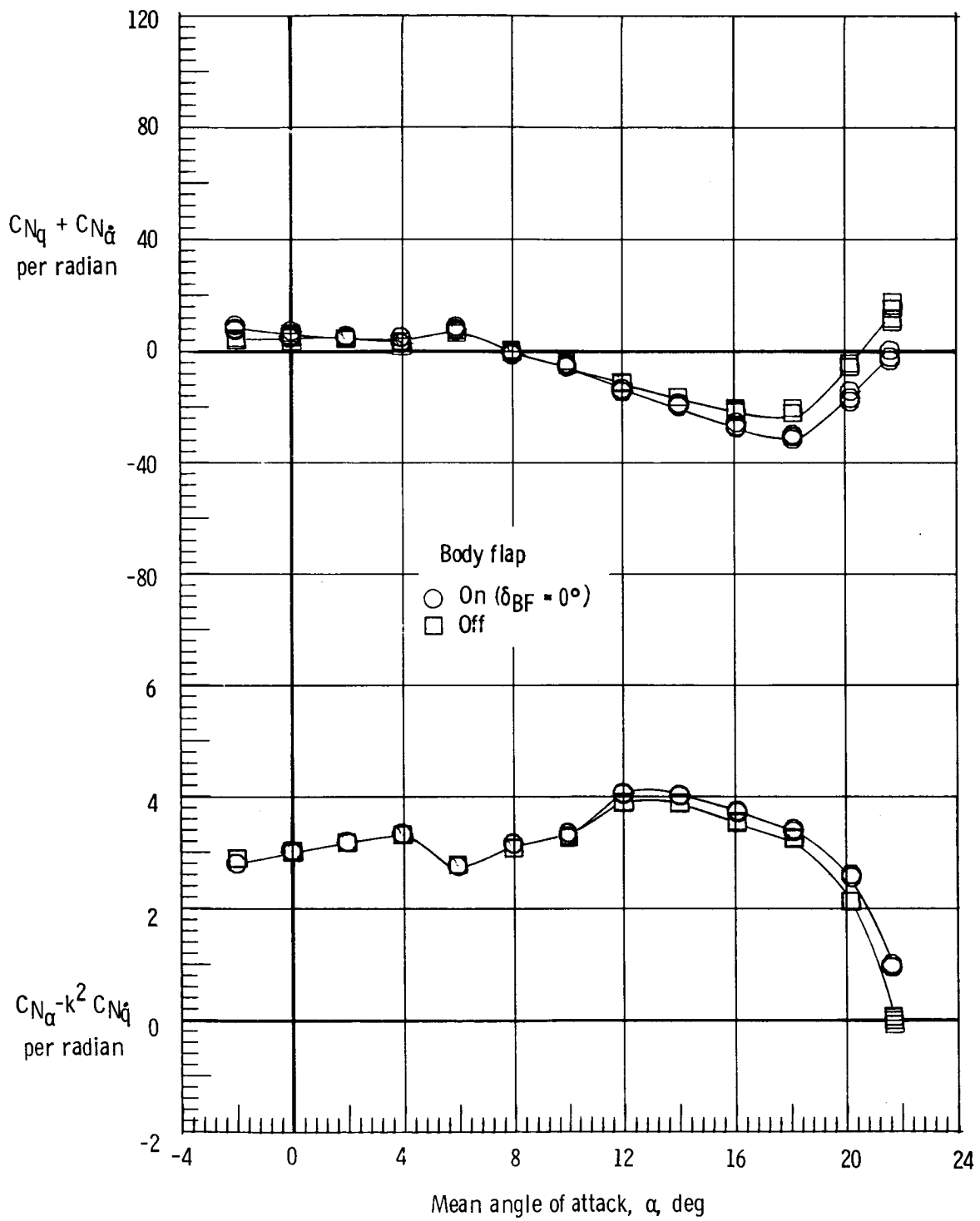
(b) M = 0.8.

Figure 18.– Continued.
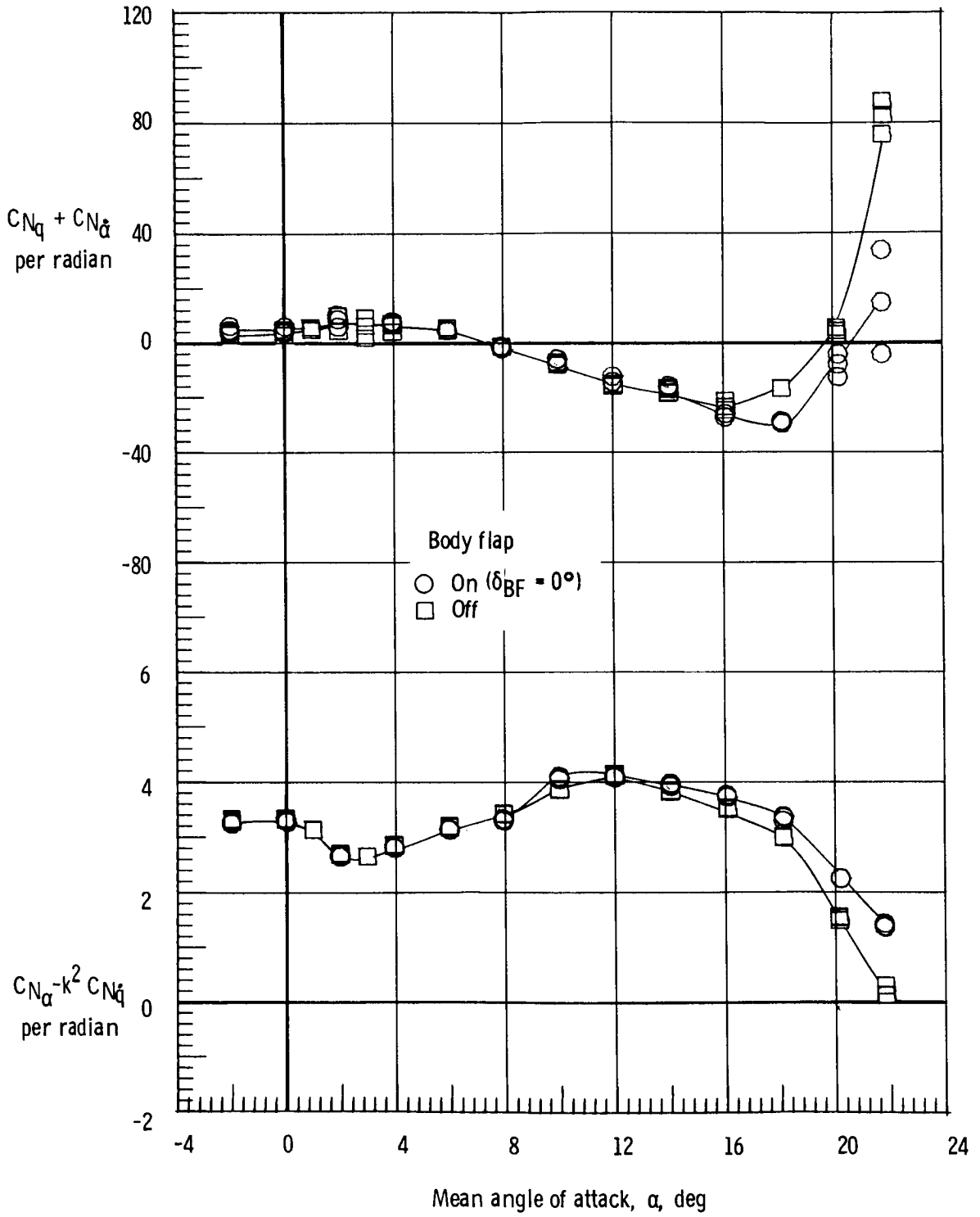
(c)   M = 0.9.

Figure 18.- Continued.
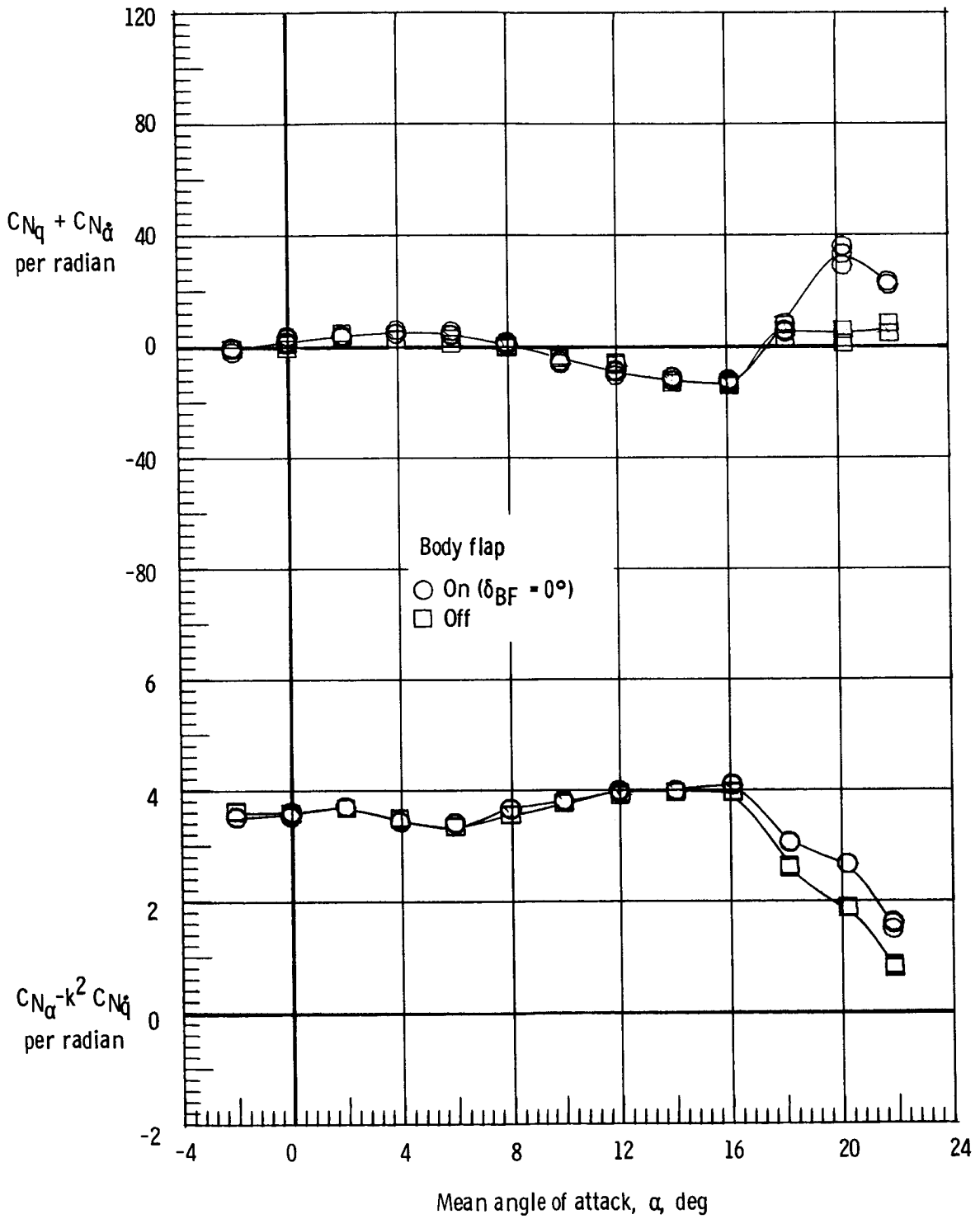
(d)   M = 0.98.

Figure 18.- Continued.
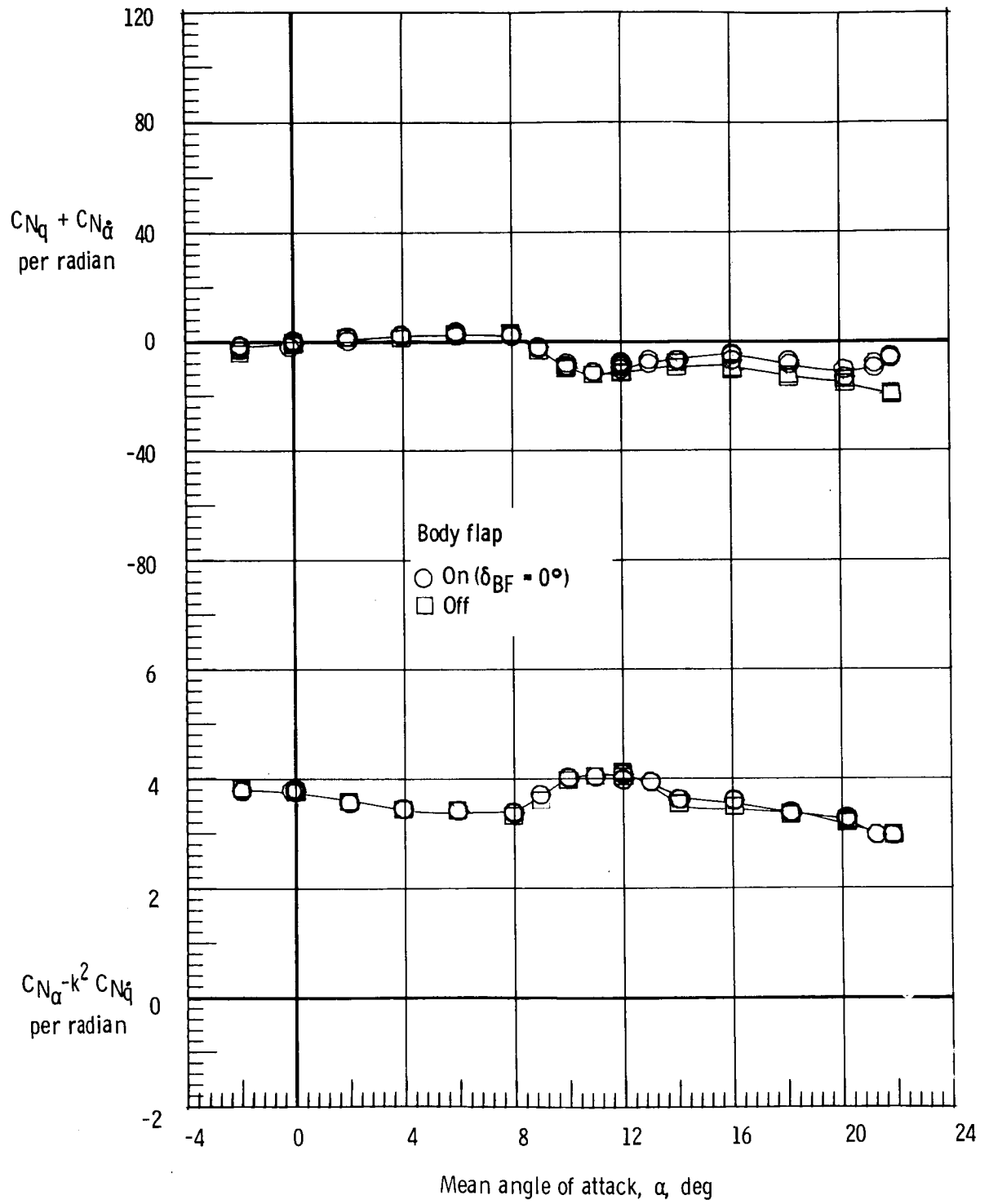
(e) M = 1.2.

Figure 18.- Concluded.
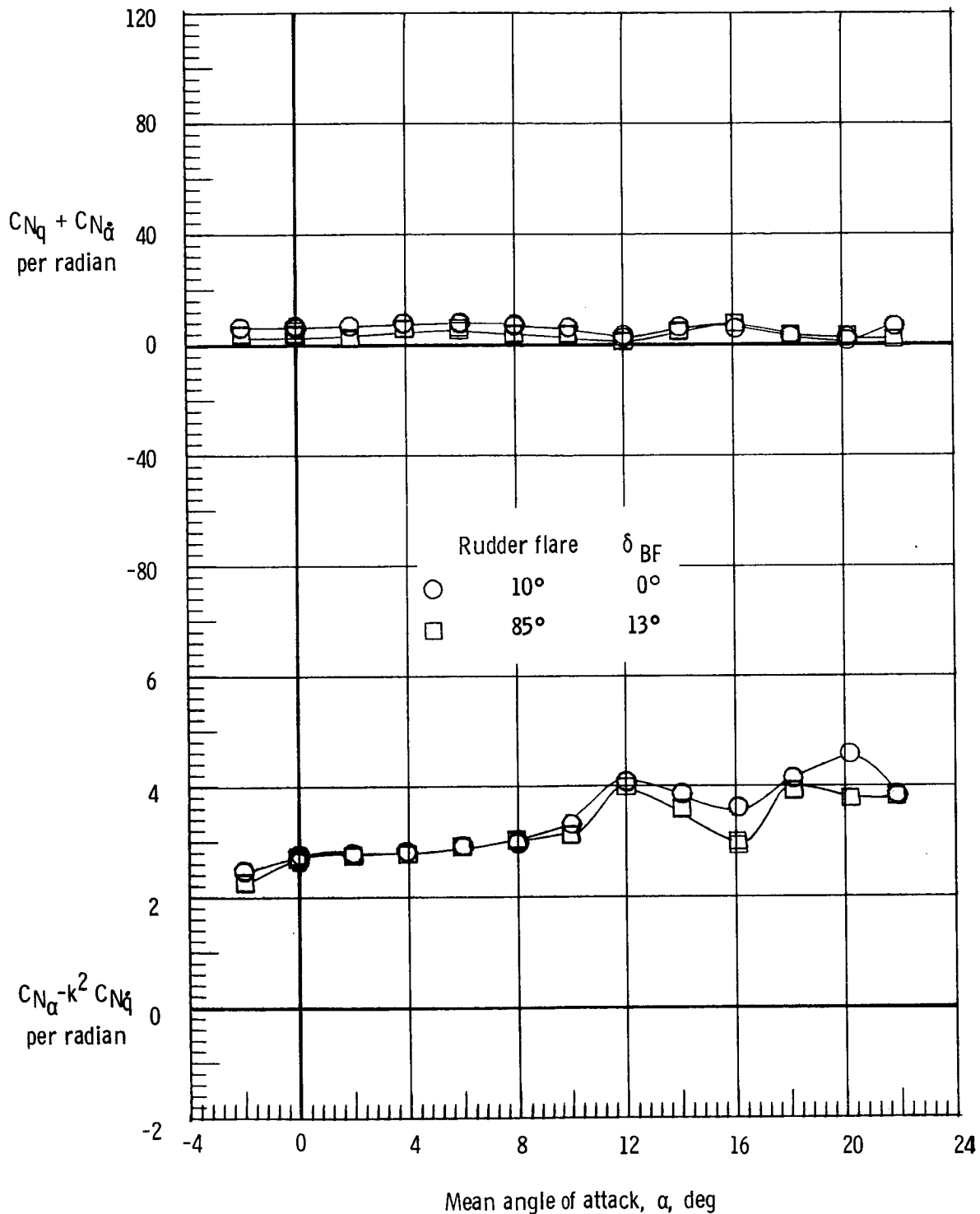
(a) M = 0.3.

Figure 19.- Effect of rudder flare and body flap deflection on normal force due to pitch rate parameter and normal force due to pitch displacement parameter. Forward center of gravity; $\delta_e = 0^O$.
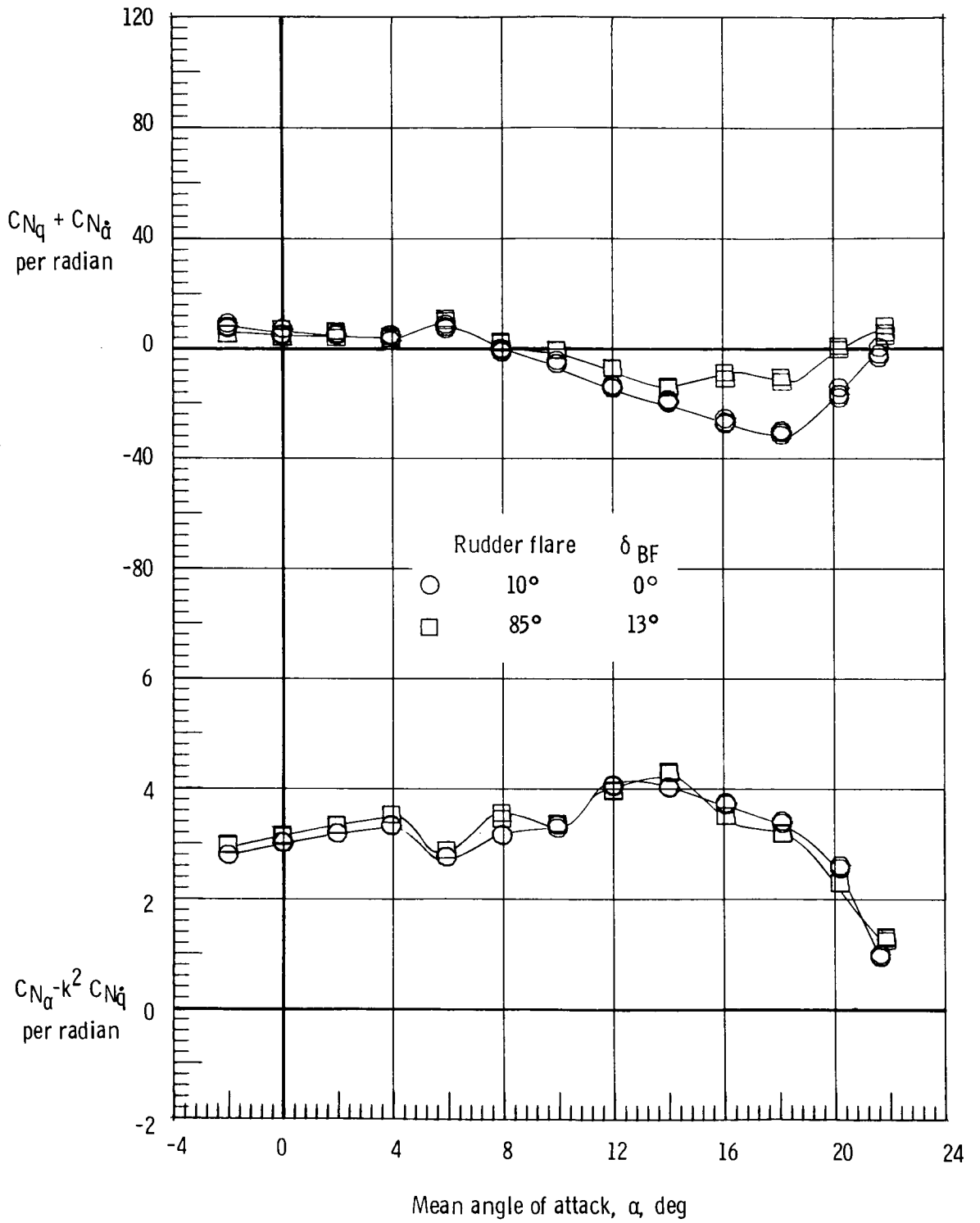
(b) M $\approx$ 0.8.

Figure 19.- Continued.
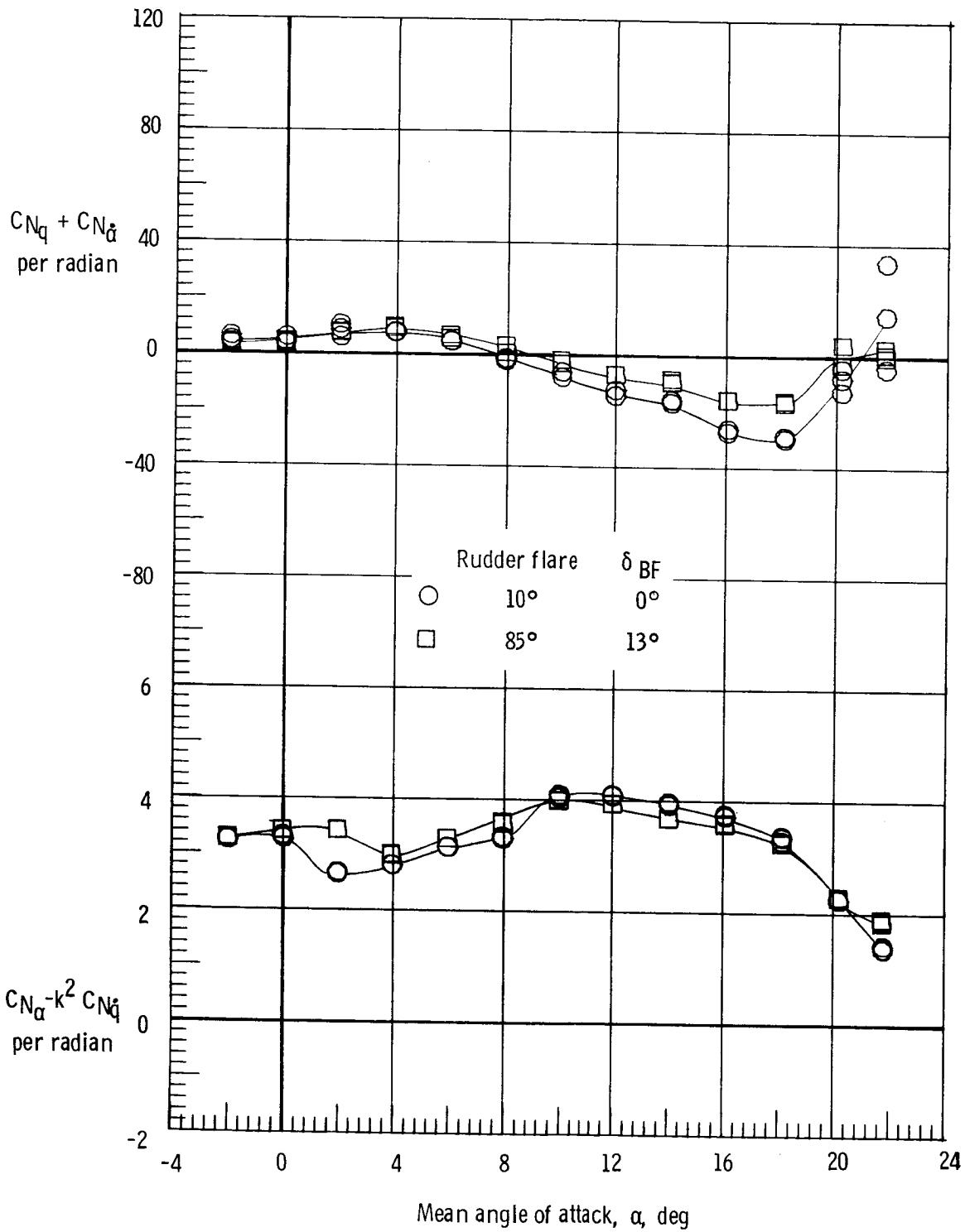
(c)   M ≈ 0.9.

Figure 19.- Continued.

(d) M = 0.98.

Figure 19.- Continued.

Mean angle of attack, α, deg
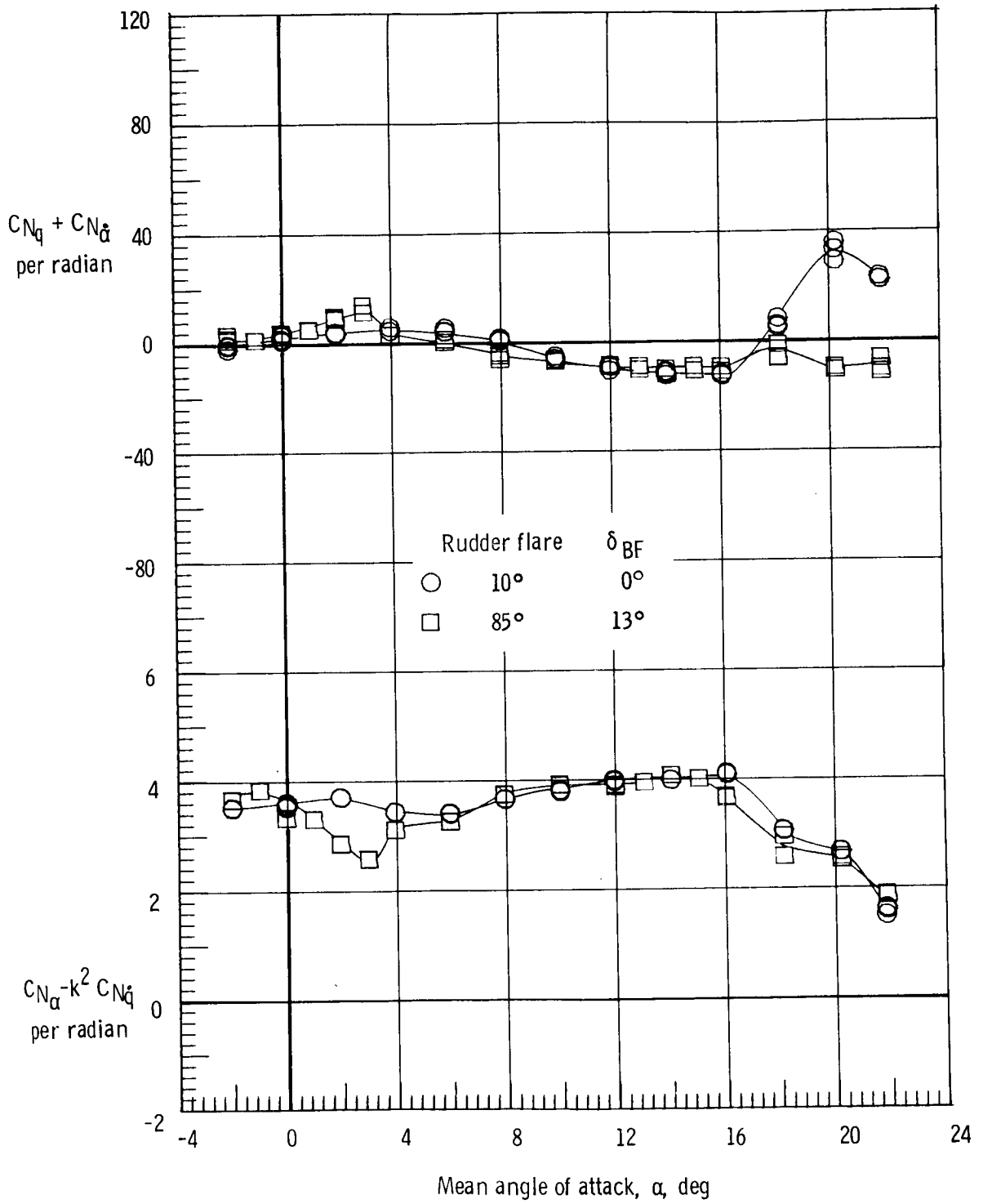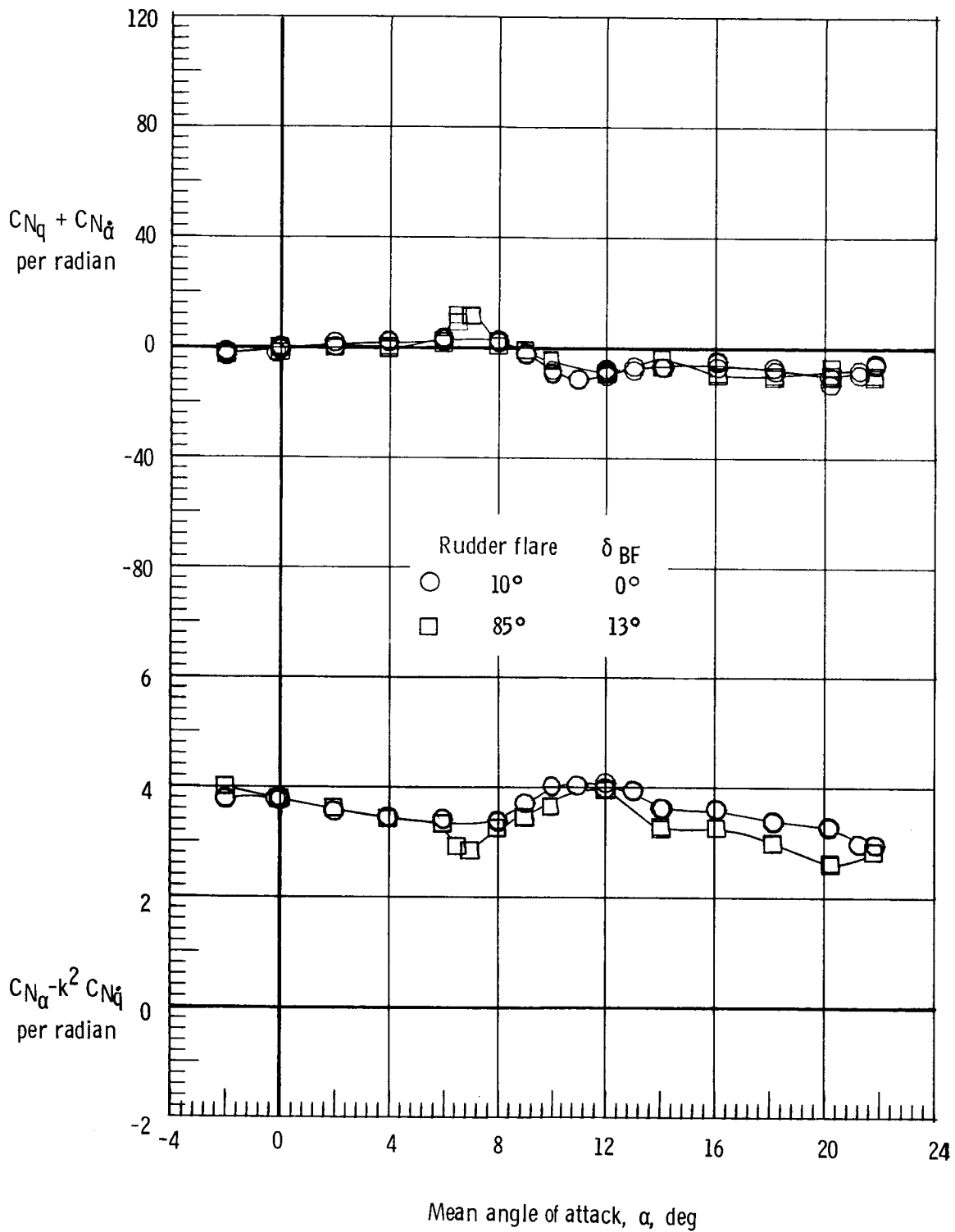
(e) M = 1.2.

Figure 19.- Concluded.
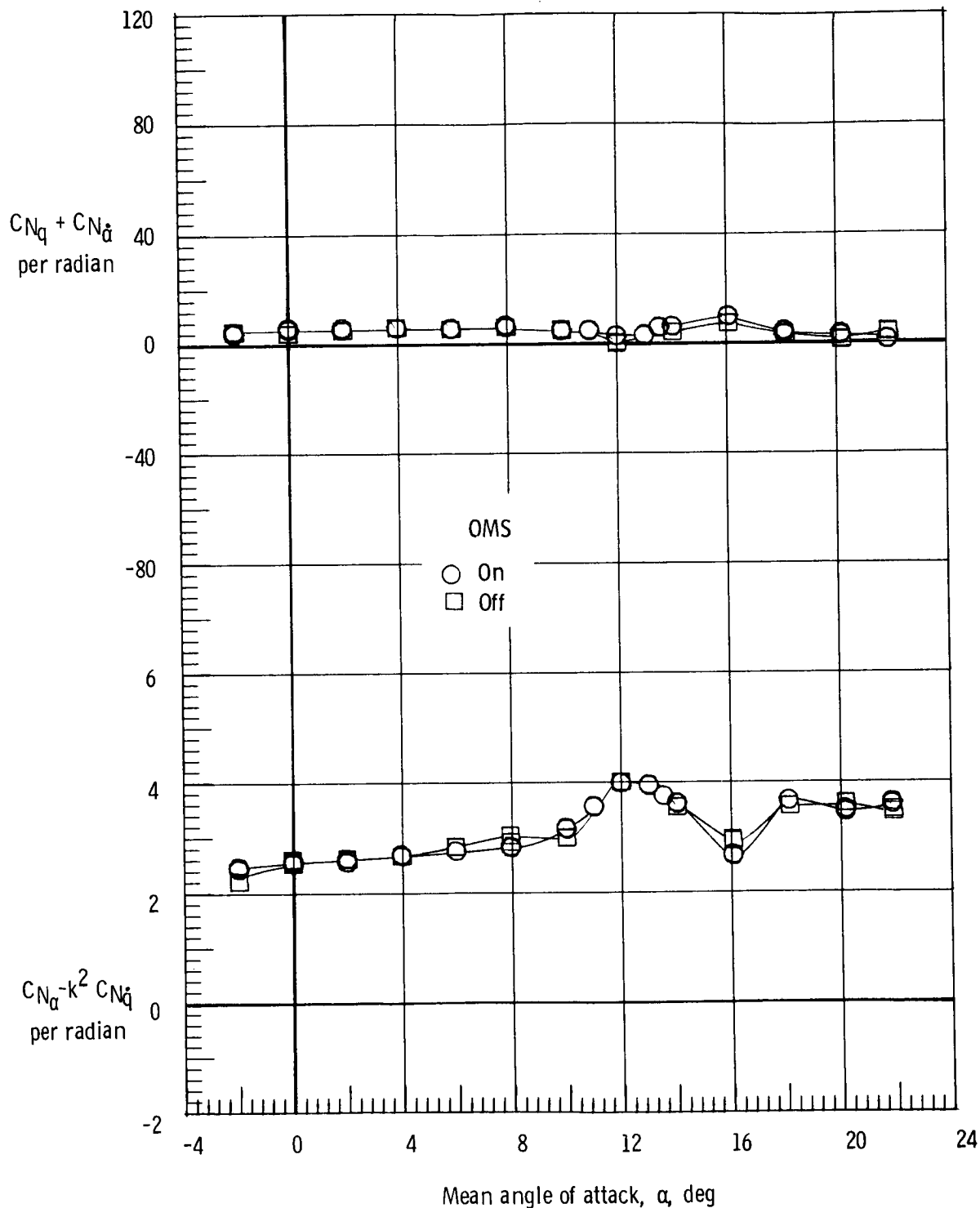
(a)   M = 0.3.

Figure 20.- Effect of OMS installation on normal force due to pitch rate parameter and
normal force due to pitch displacement parameter.   Forward center of gravity;
rudder flare, 10°; body flap off.

98

(b) M = 0.8.

Figure 20.– Continued.

(c) M = 0.9.

Figure 20.– Continued.

Mean angle of attack, α, deg
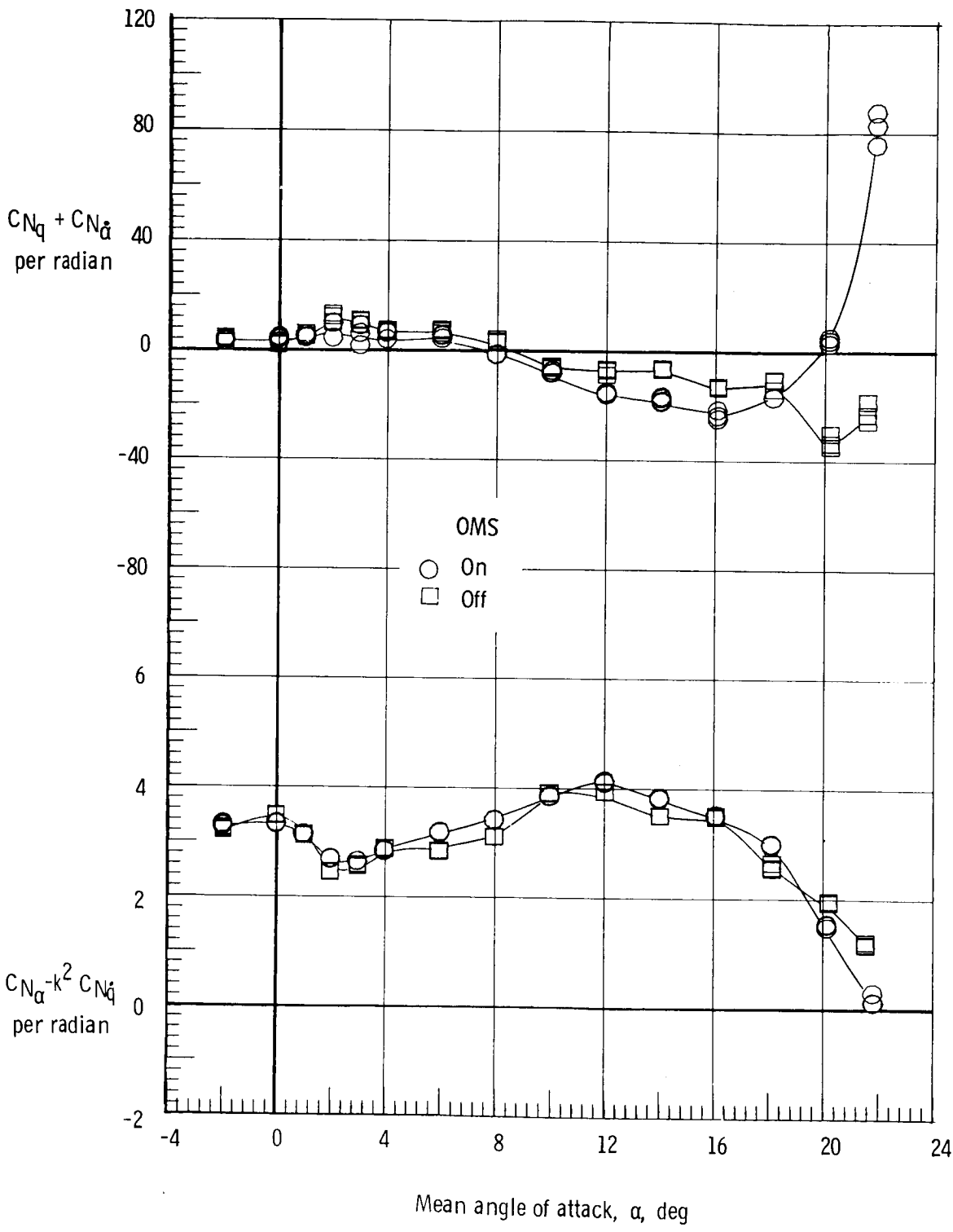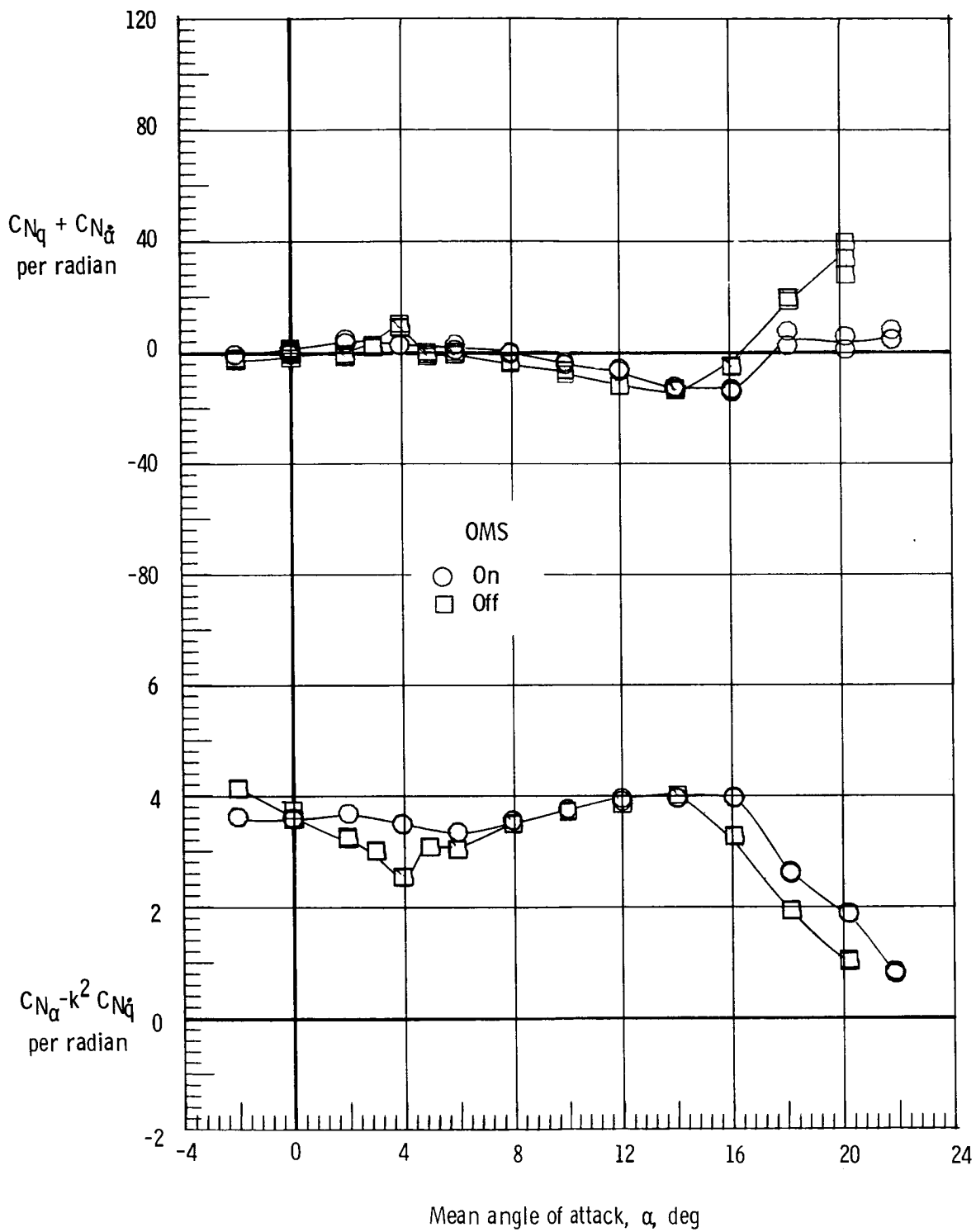
(d)   M = 0.98.

Figure 20.- Continued.
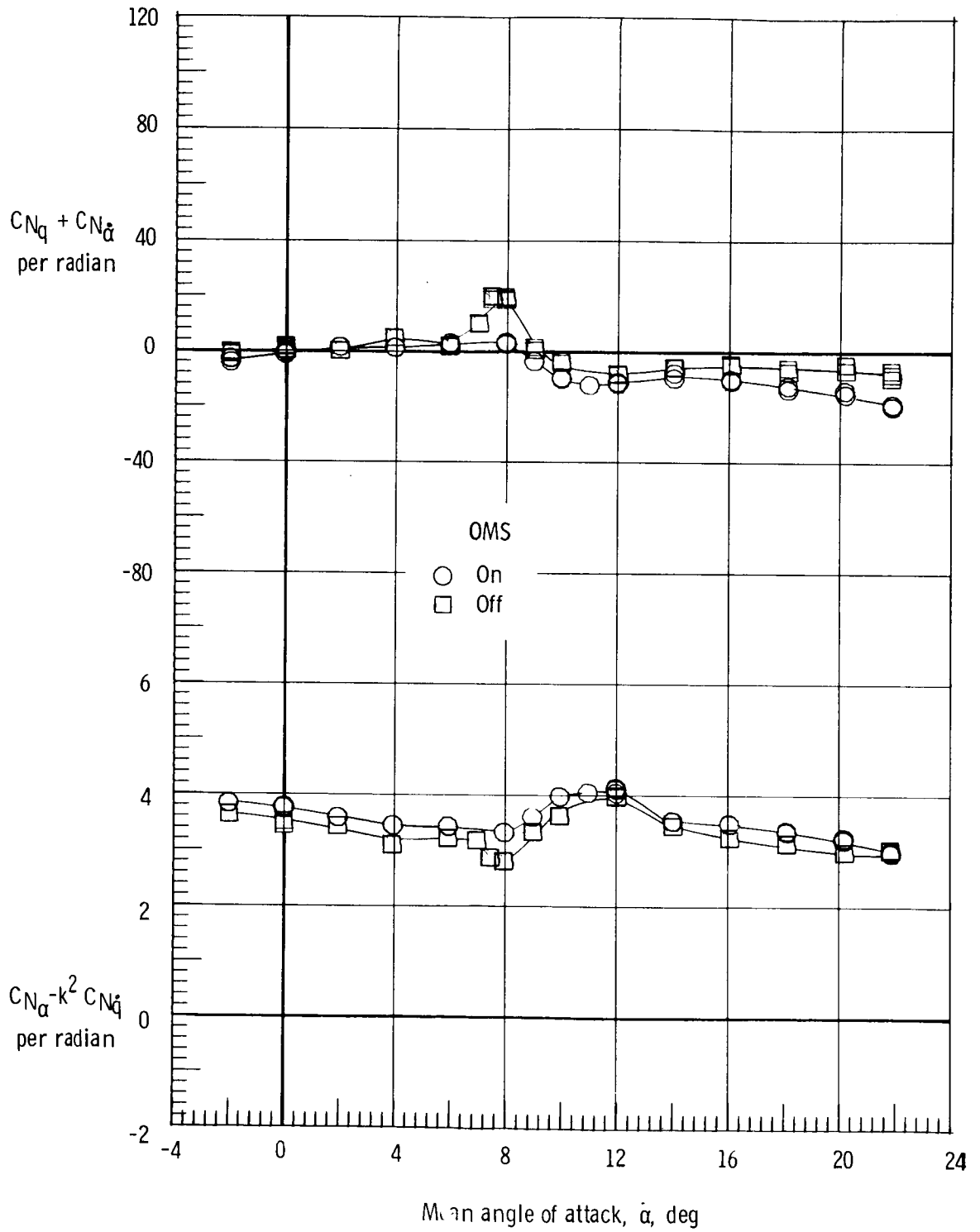
(e)   M = 1.2.

Figure 20.- Concluded.
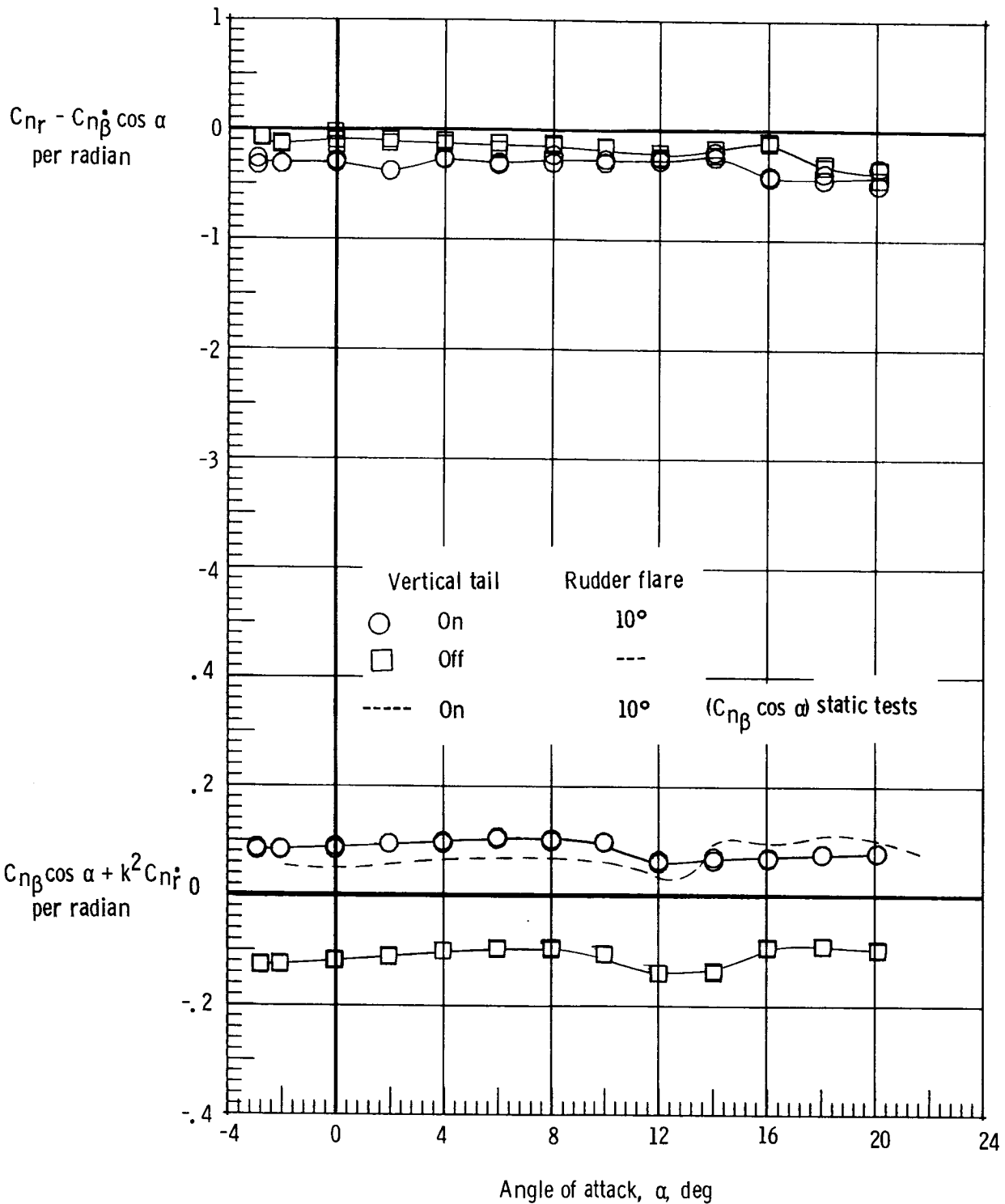
(a)   M = 0.3.

Figure 21.- Effect of vertical tail on the damping in yaw parameter and on the oscillatory directional stability parameter. Forward center of gravity; $\delta_{BF} = 0^{\circ}$.

$C_{n_r} - C_{n_{\dot{\beta}}} \cos \alpha$
per radian

$C_{n_\beta} \cos \alpha + k^2 C_{n_{\dot{r}}}$
per radian

Vertical tail	Rudder flare
○ On	10°
☐ Off	---
----- On	10° $(C_{n_\beta} \cos \alpha)$ static tests

Angle of attack, α, deg
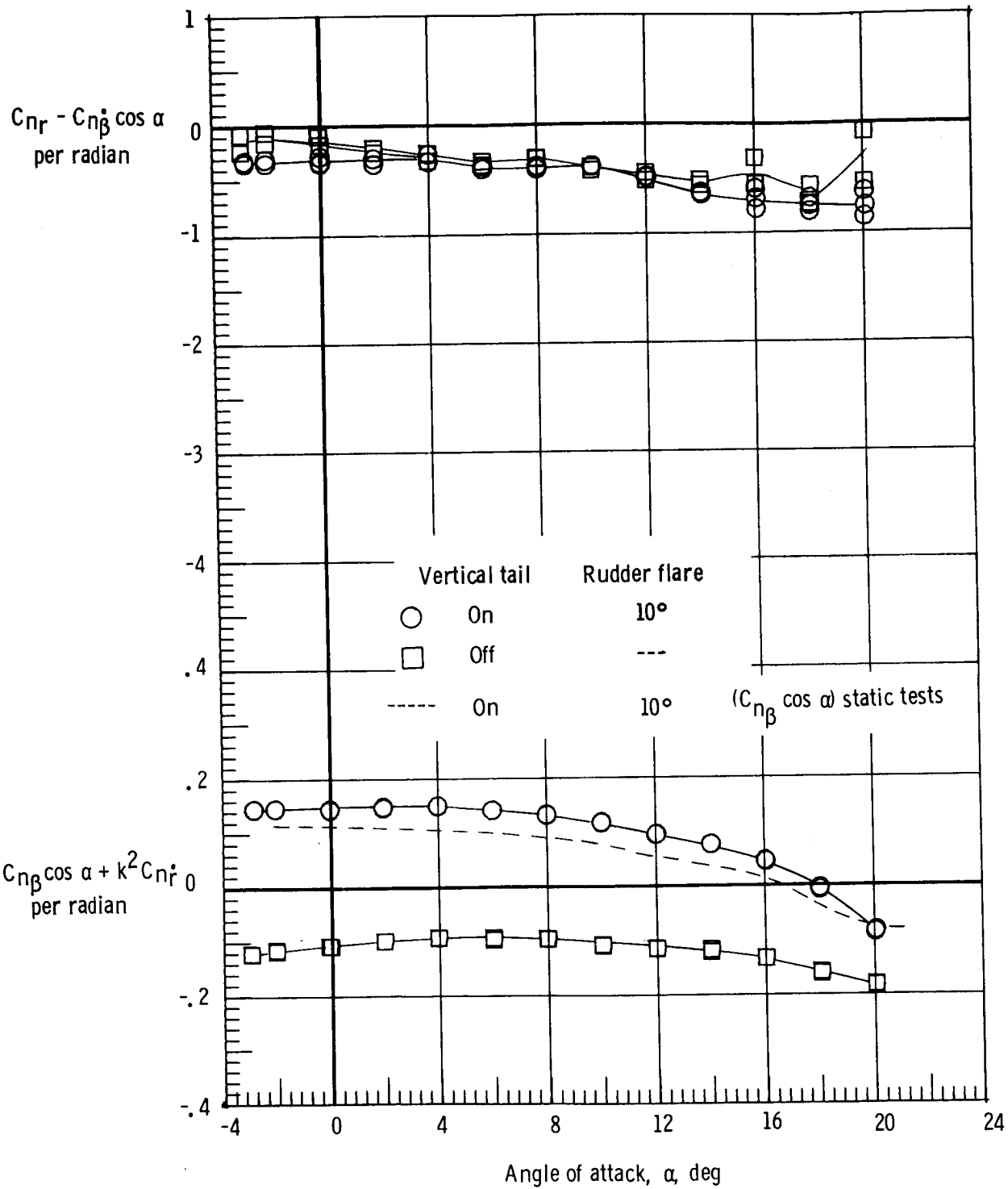
(b)   M = 0.8.

Figure 21.- Continued.
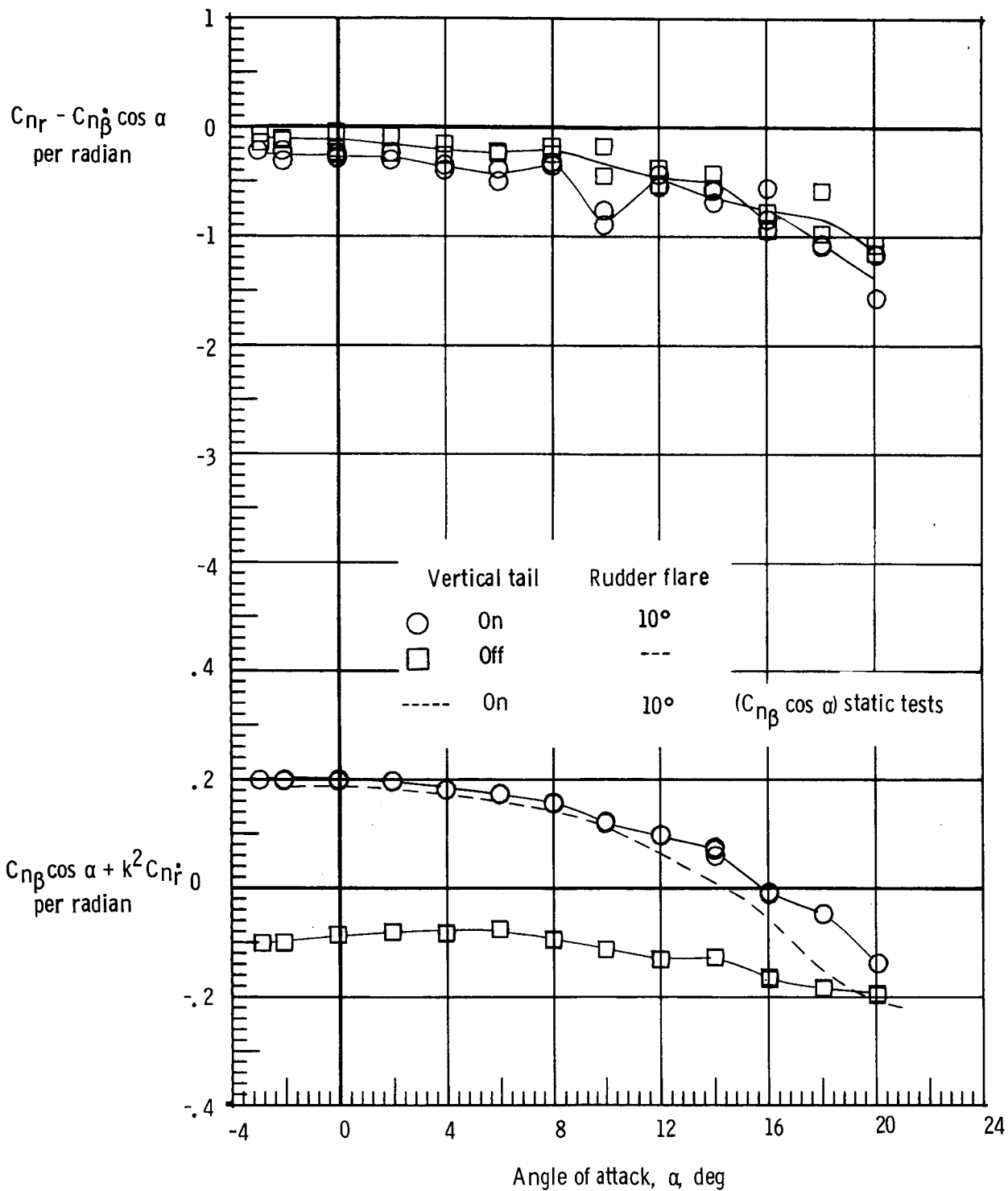
(c) M = 0.9.

Figure 21.- Continued.
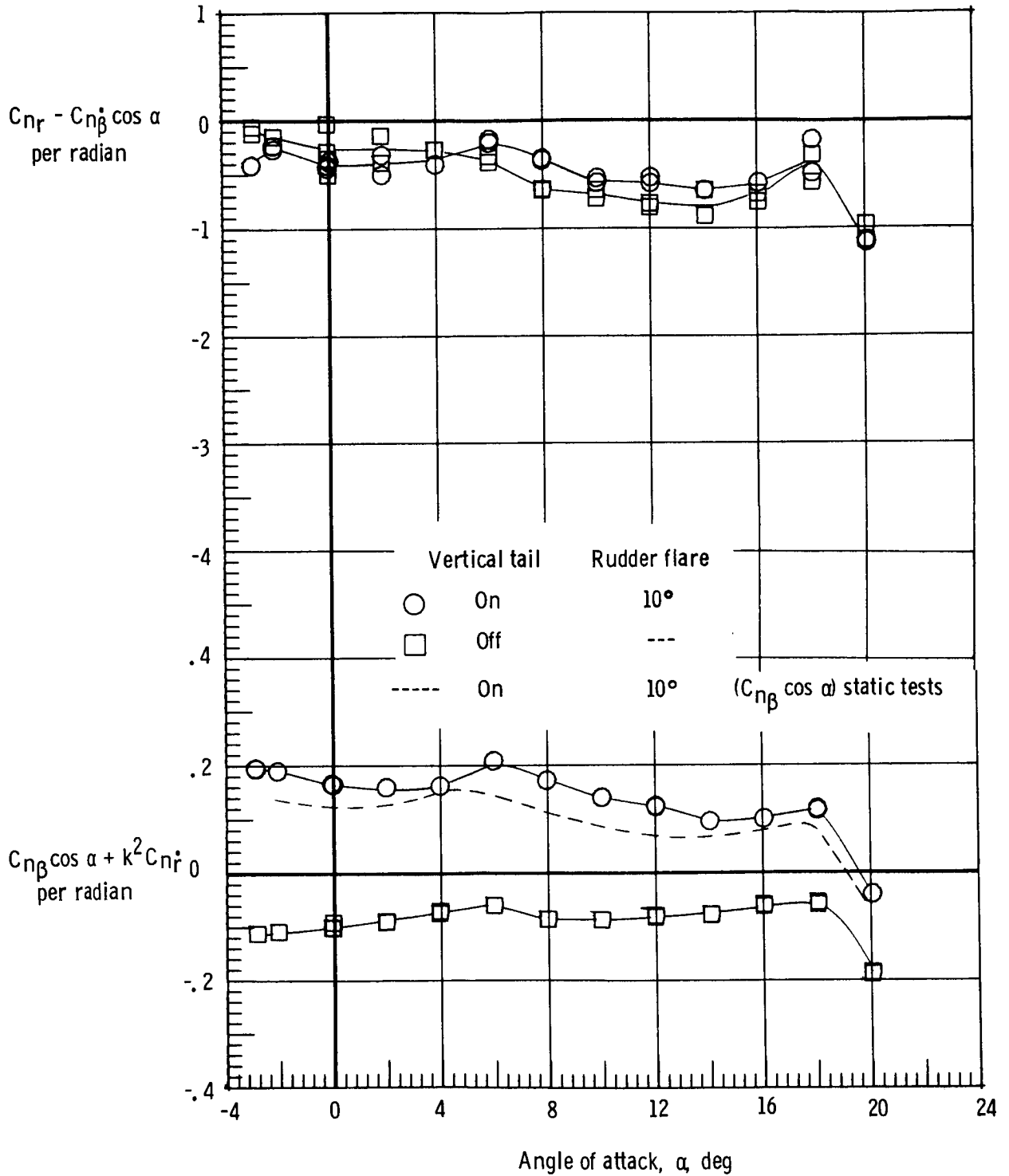
(d)   M = 0.98.

Figure 21.- Continued.
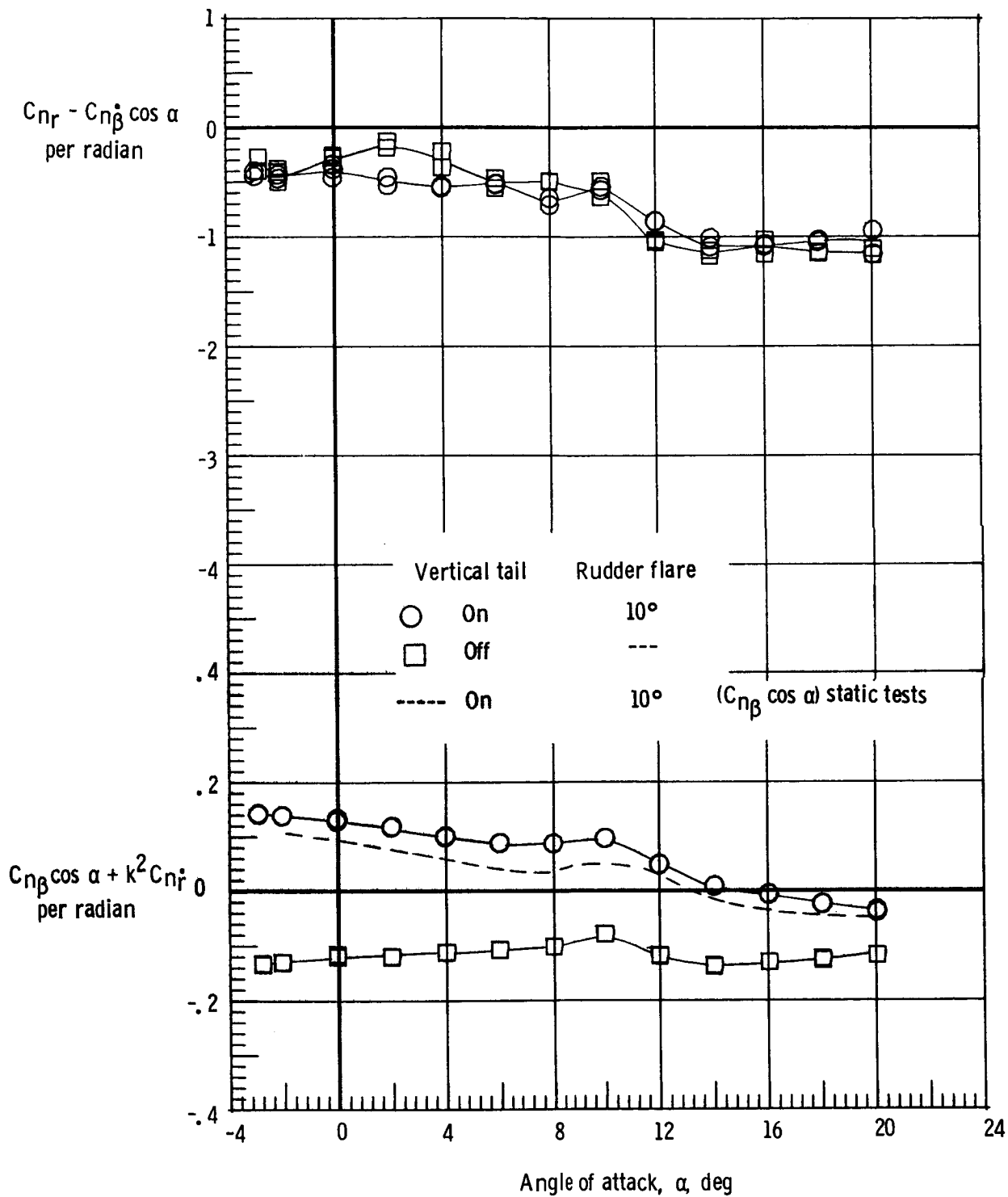
(e) M = 1.2.

Figure 21.- Concluded.
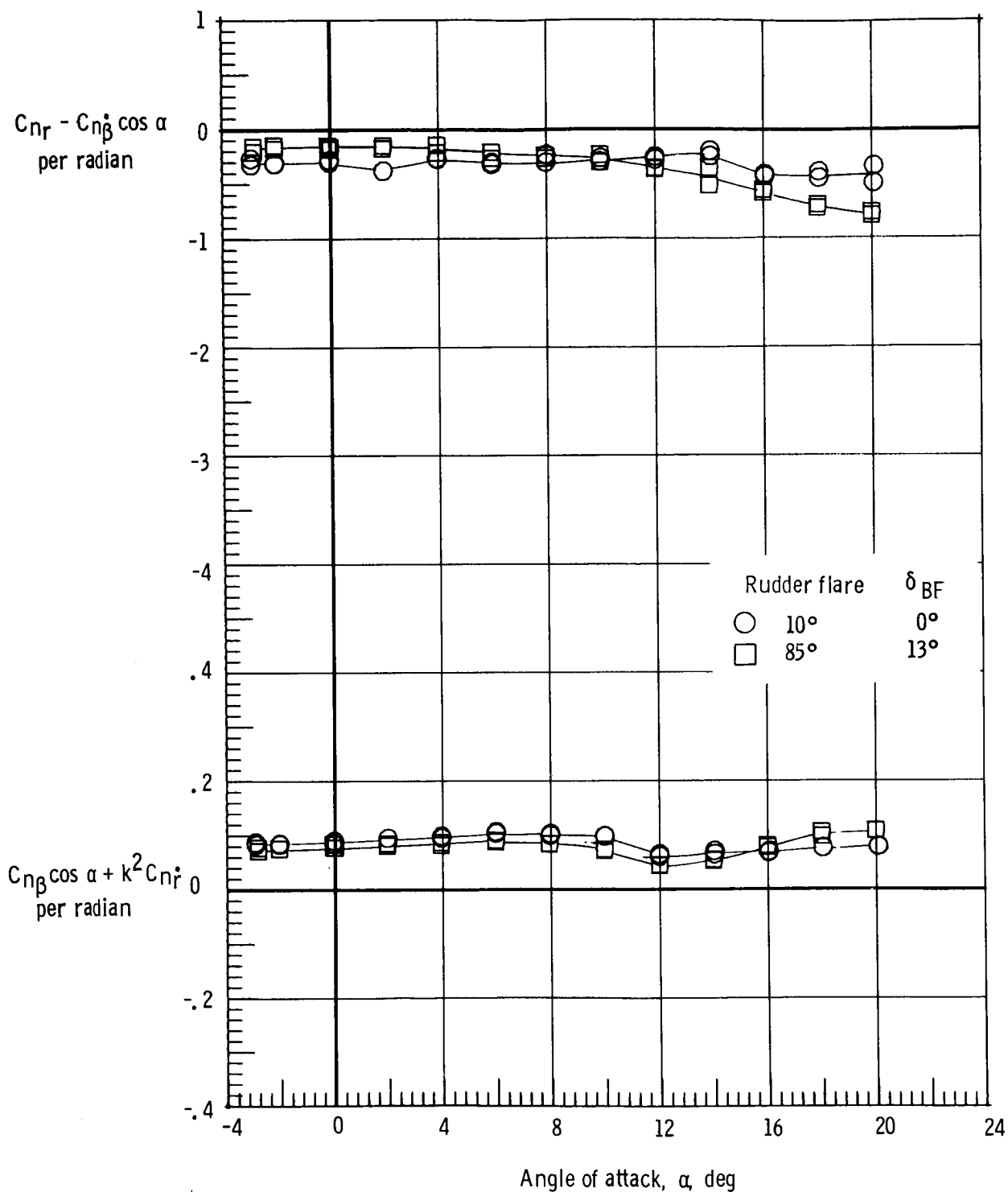
(a) M = 0.3.

Figure 22.- Effect of rudder flare and body flap deflection on the damping in yaw
parameter and on the oscillatory directional stability parameter. Forward
center of gravity.
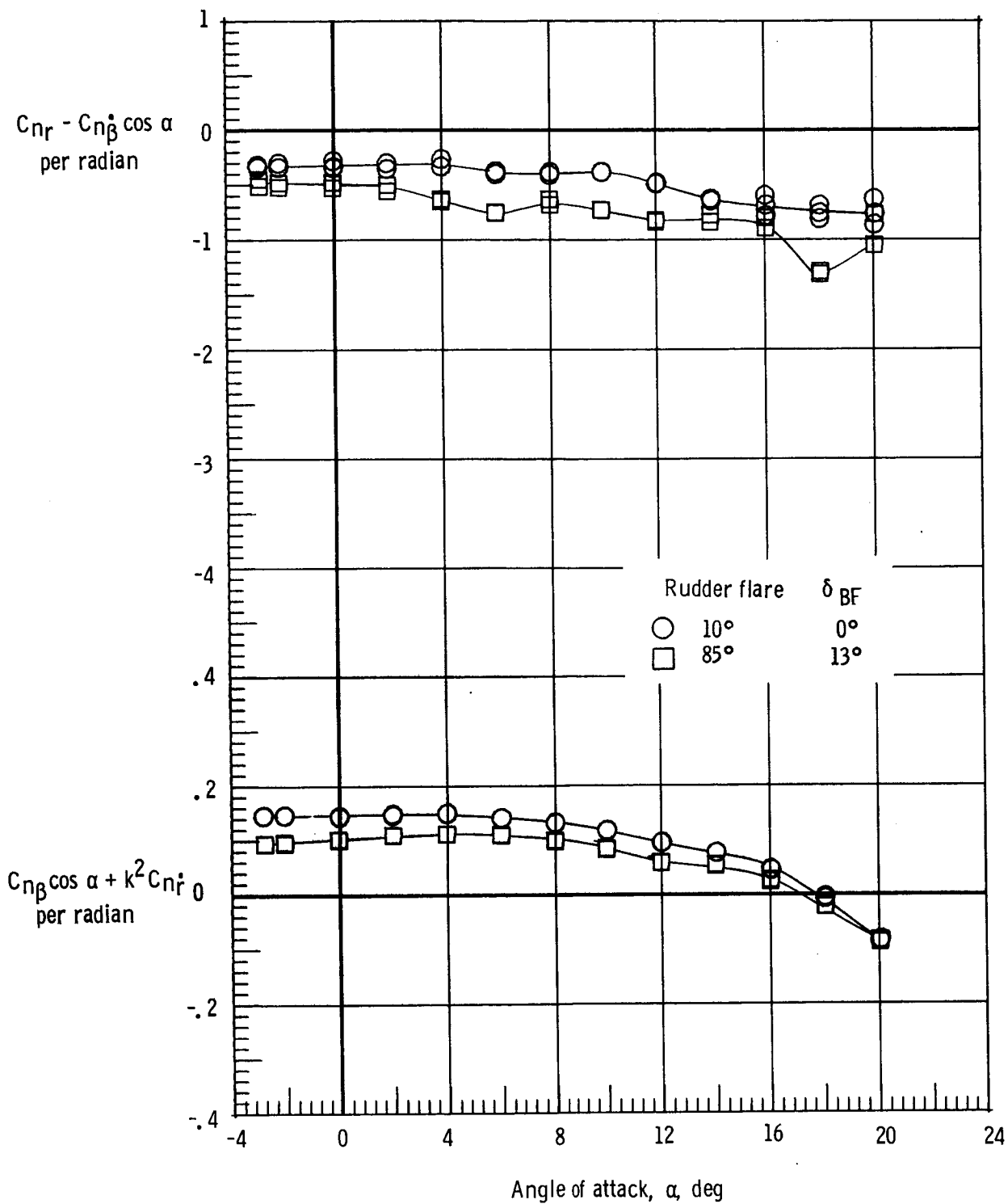
(b) M = 0.8.

Figure 22.- Continued.
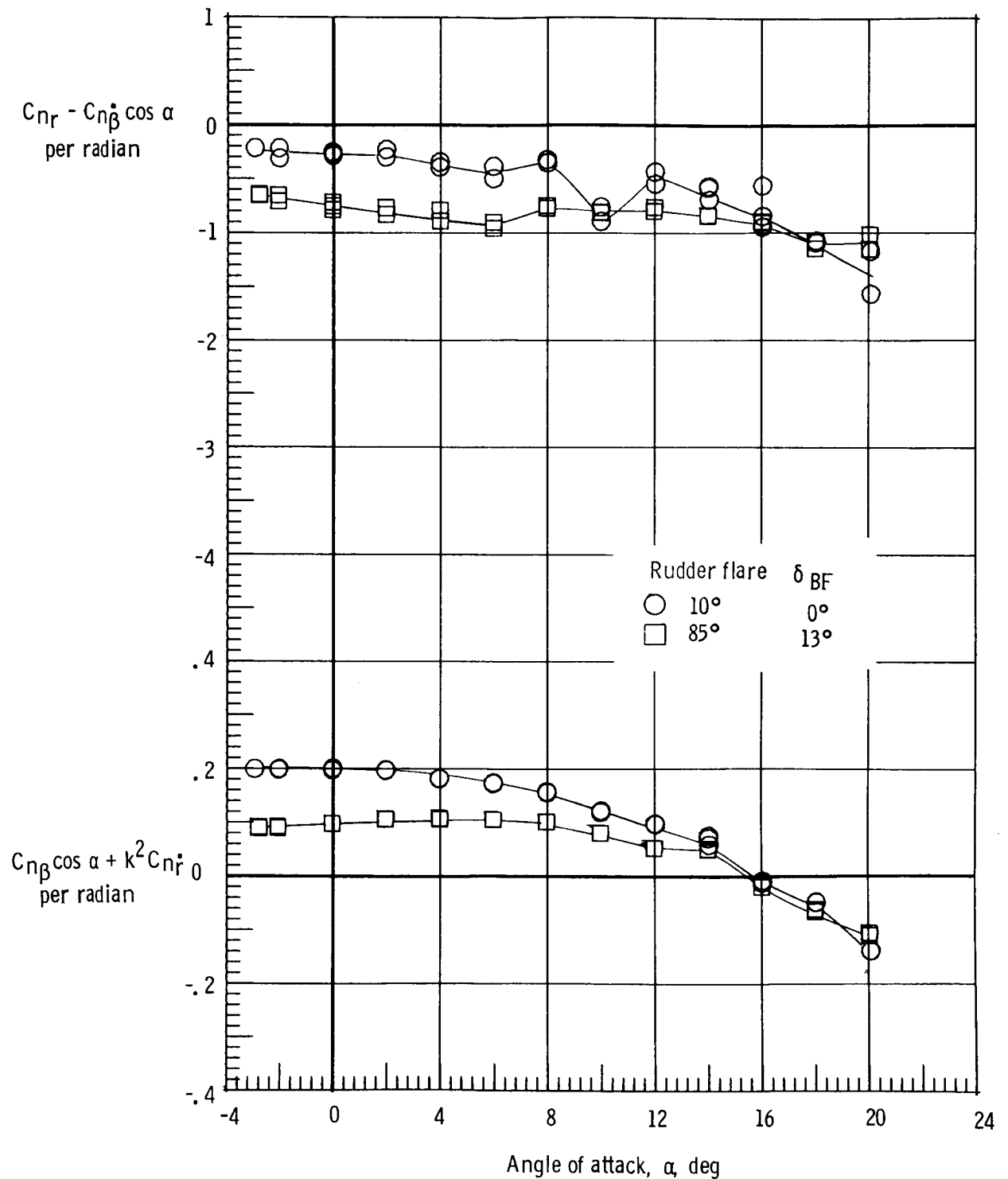
(c) M = 0.9.

Figure 22.- Continued.
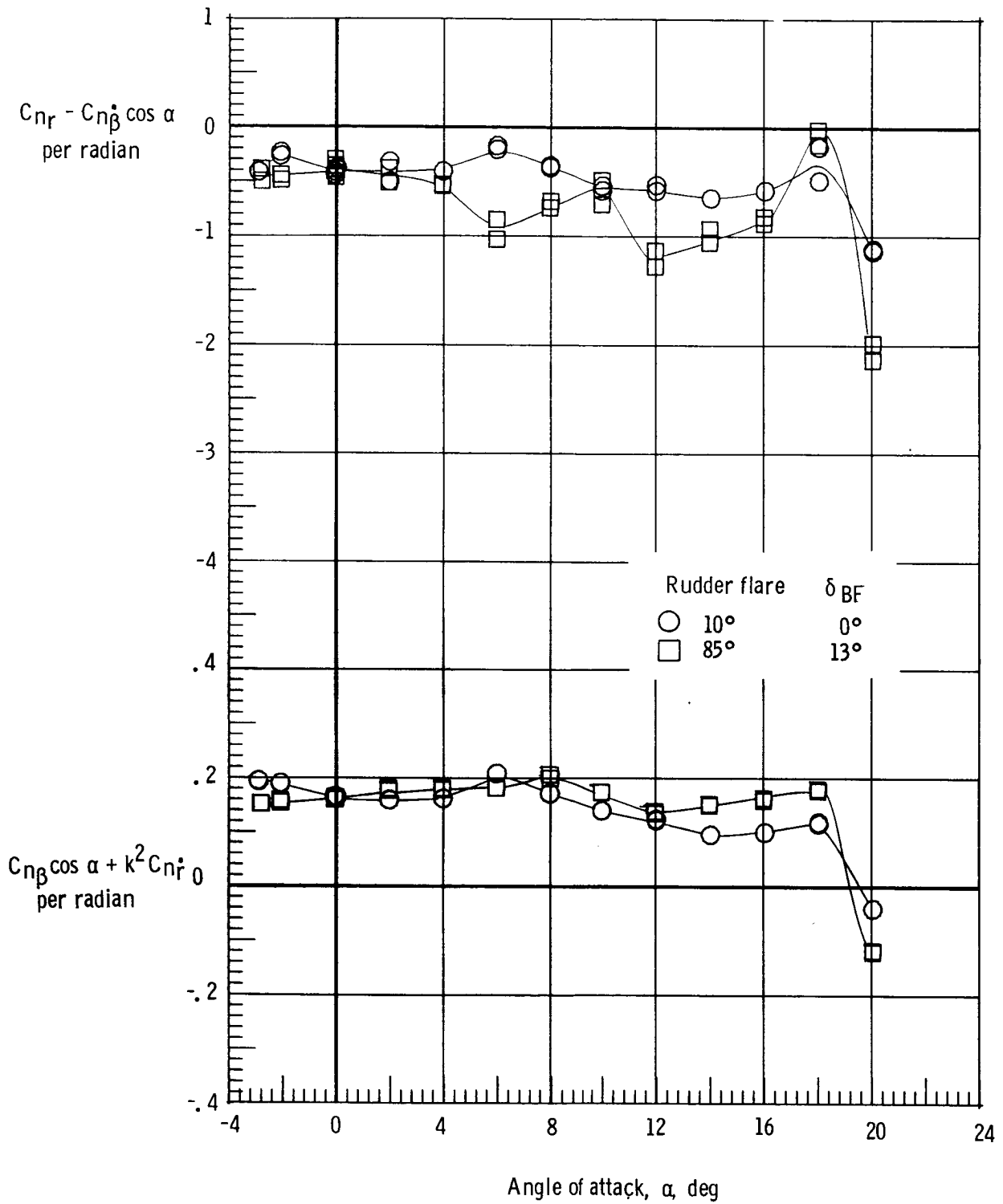
(d)   M = 0.98.

Figure 22.- Continued.

111
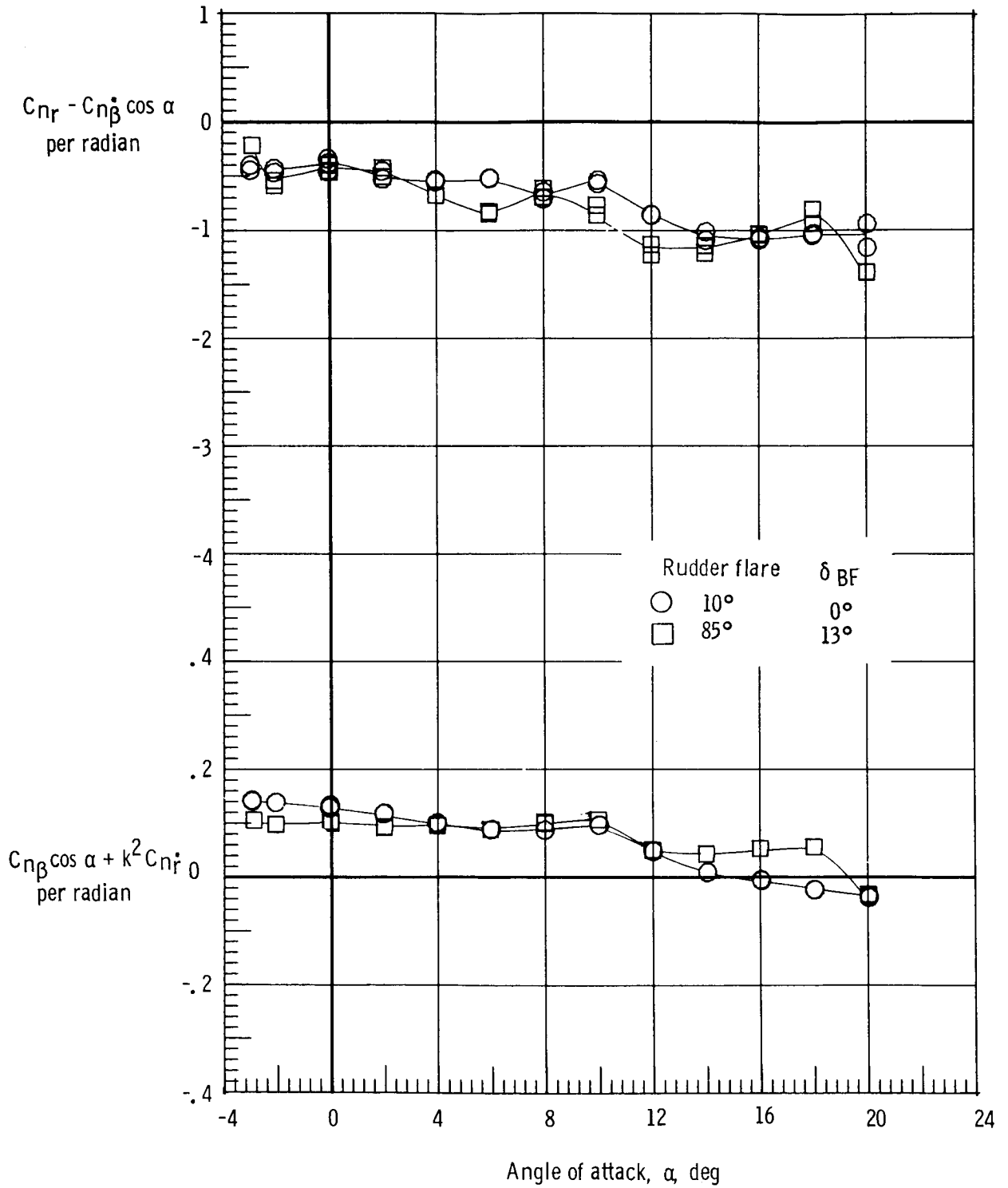
(e) M = 1.2.

Figure 22.- Concluded.
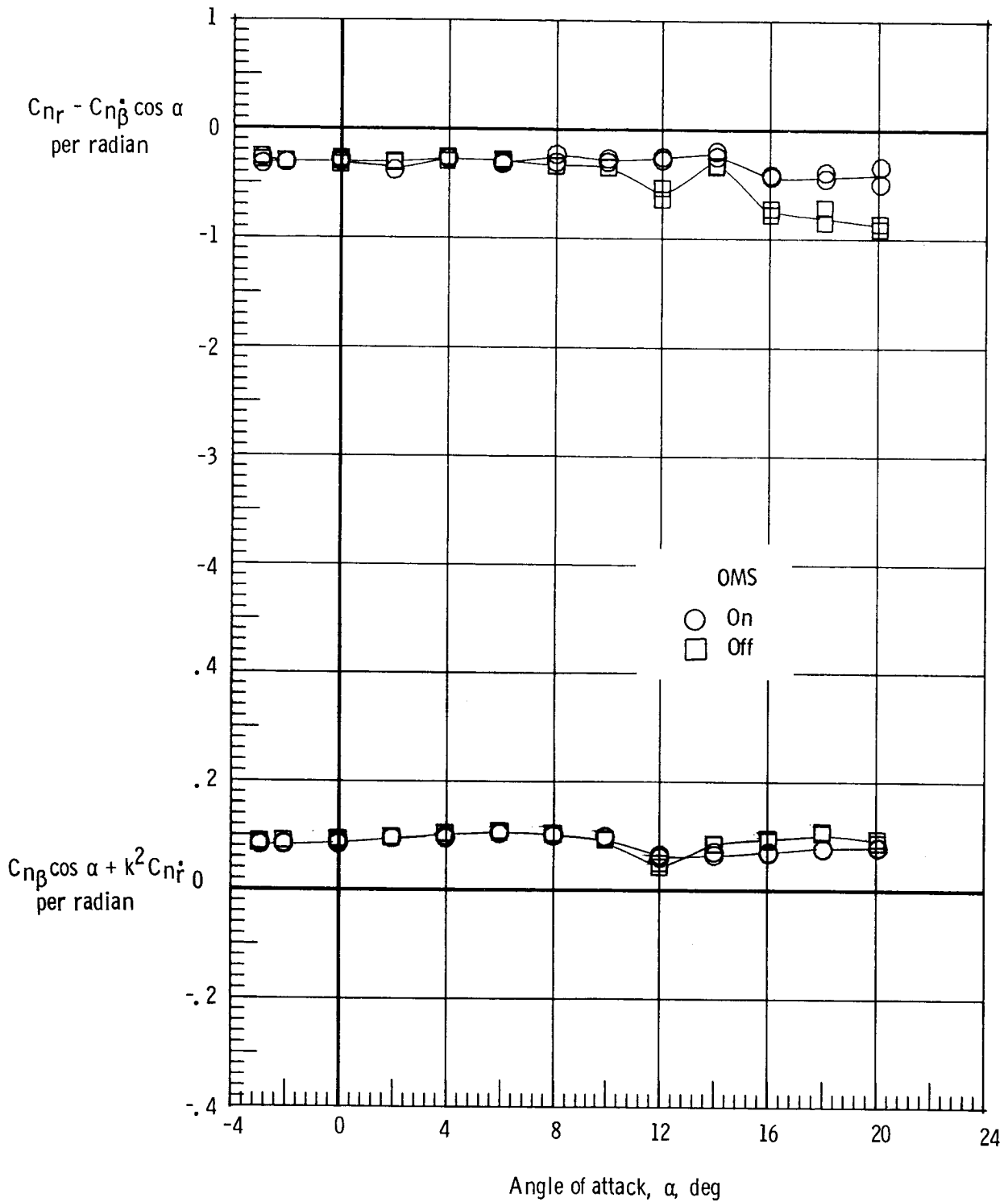
(a) M = 0.3.

Figure 23.- Effect of OMS installation on the damping in yaw parameter and on the oscillatory directional stability parameter. Forward center of gravity; rudder flare, 10°; $\delta_{BF} = 0^O$.
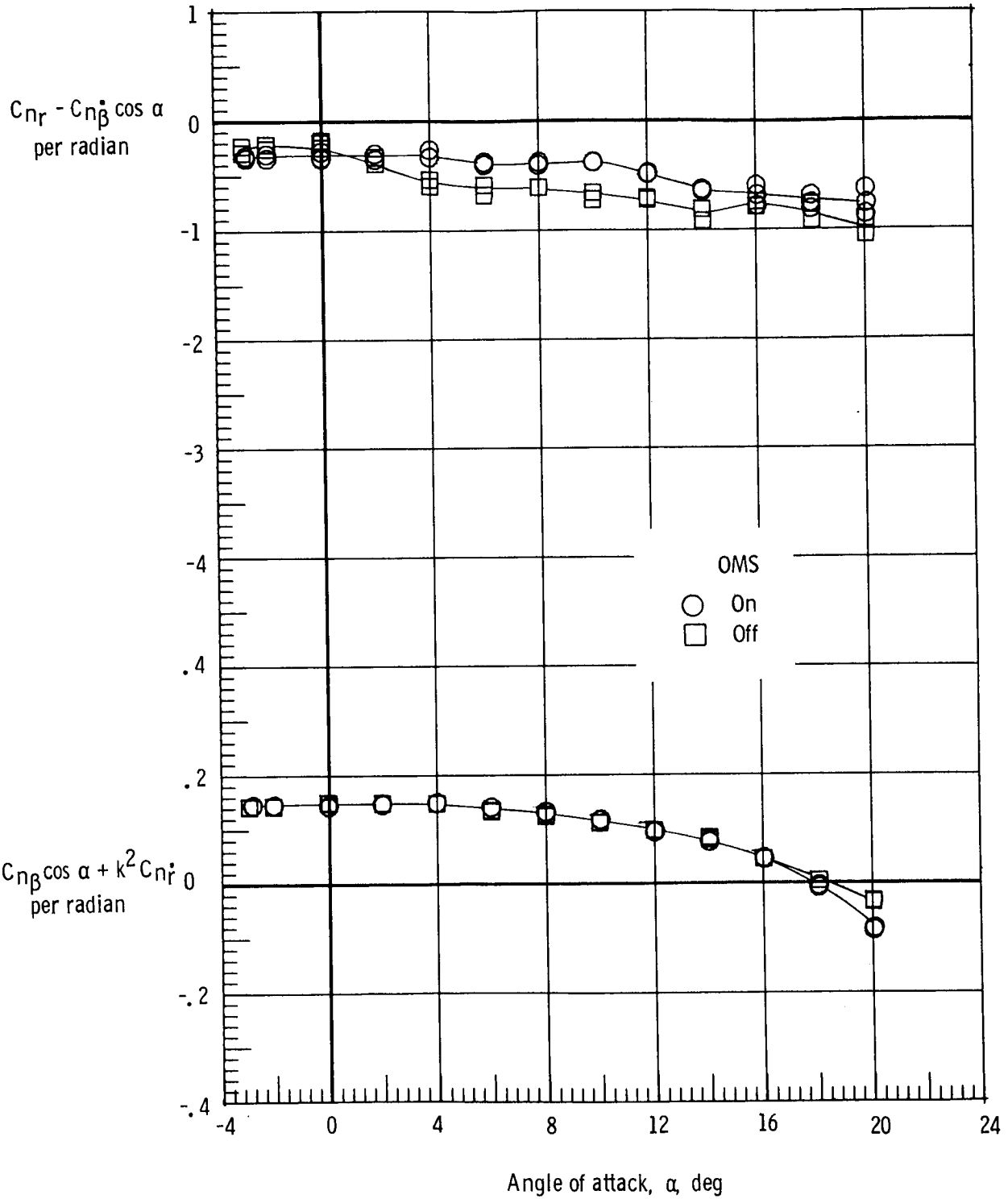
(b) M = 0.8.

Figure 23.- Continued.
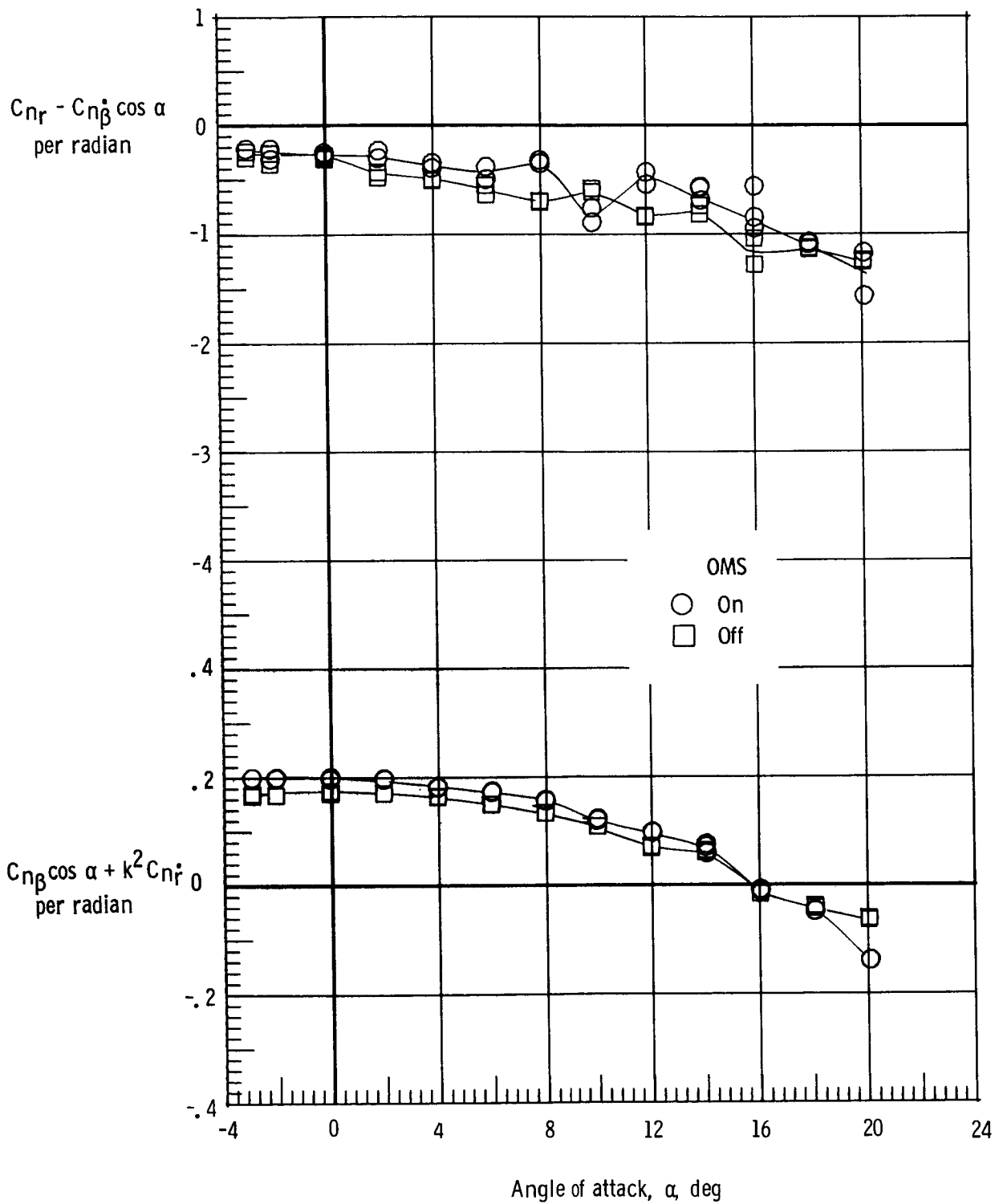
(c) M = 0.9.

Figure 23.- Continued.
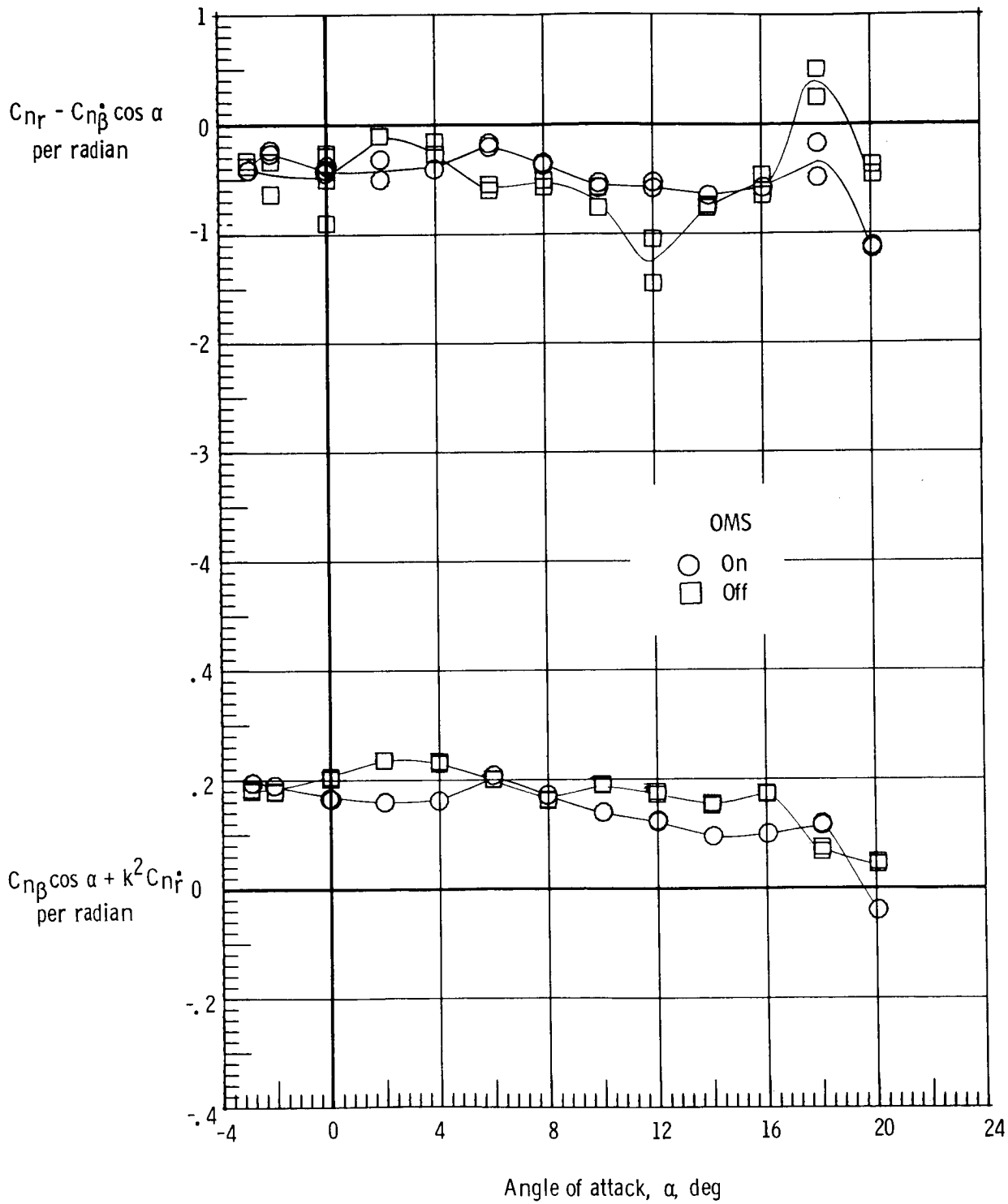
(d) M = 0.98.

Figure 23.- Continued.
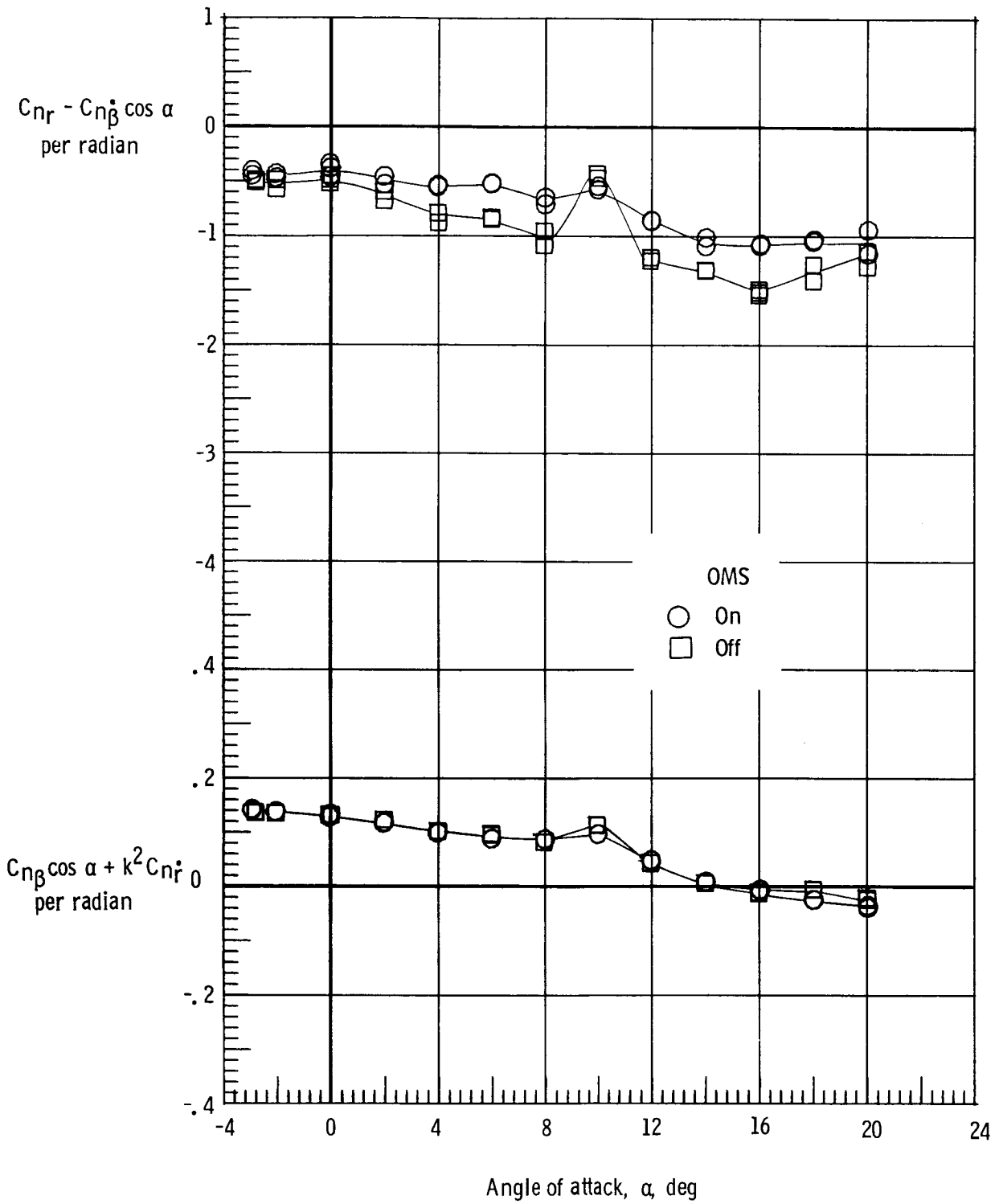
(e)   M = 1.2.

Figure 23.- Concluded.
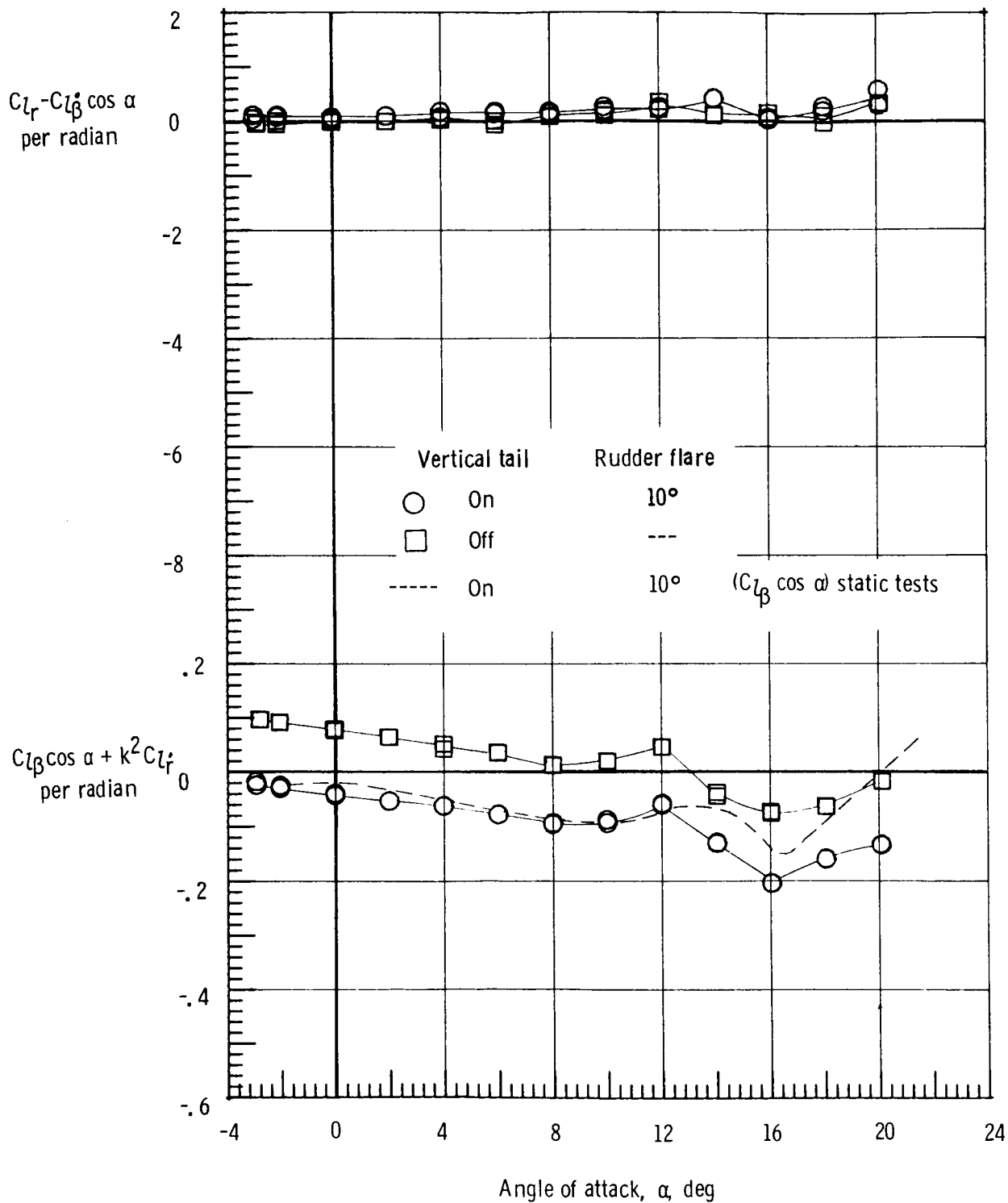
(a) M = 0.3.

Figure 24.- Effect of vertical tail on rolling moment due to yaw rate parameter
and effective dihedral parameter. Forward center of gravity; $\delta_{BF} = 0^O$.
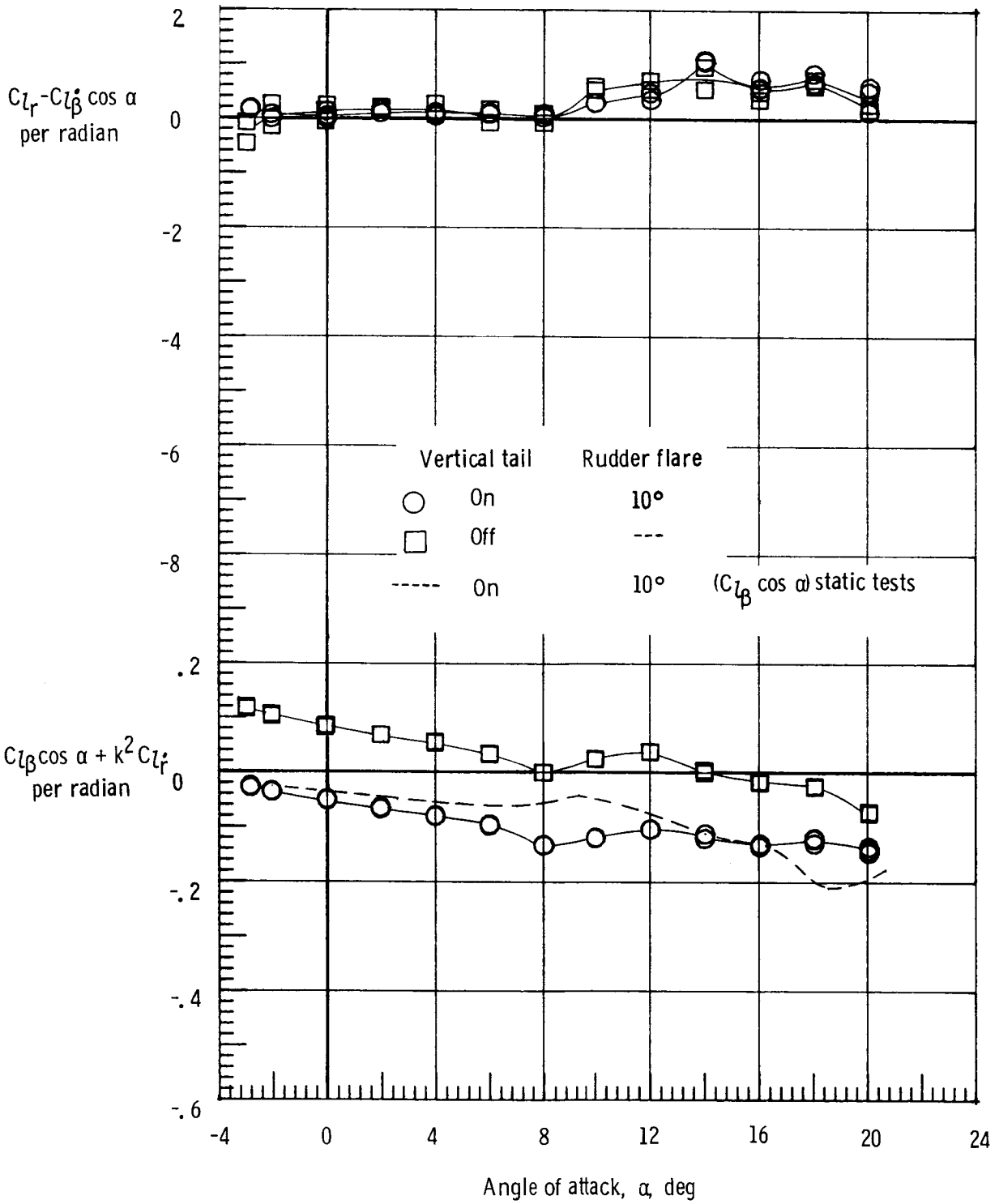
(b) M = 0.8.

Figure 24.- Continued.
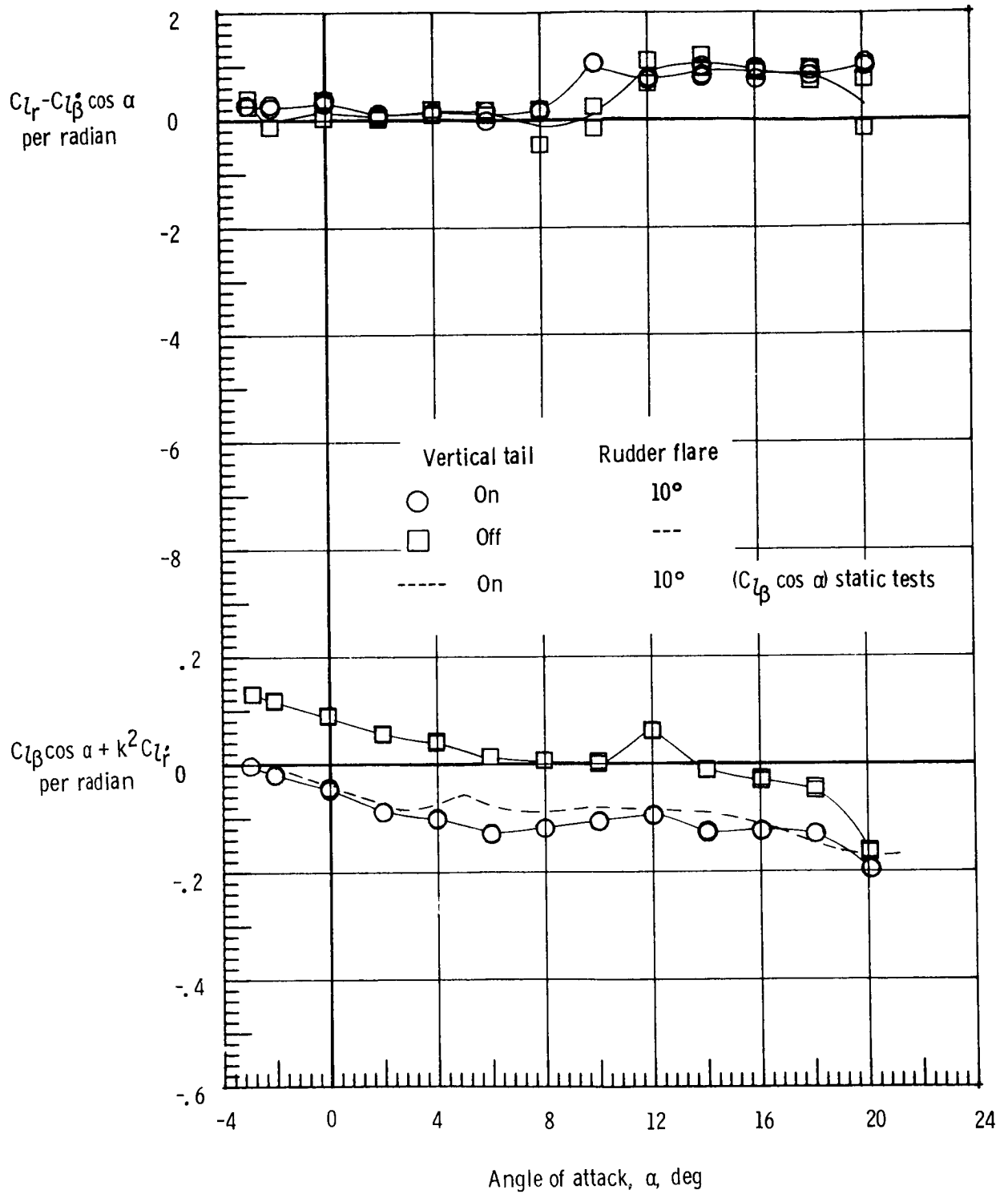
Figure 24.- Continued.
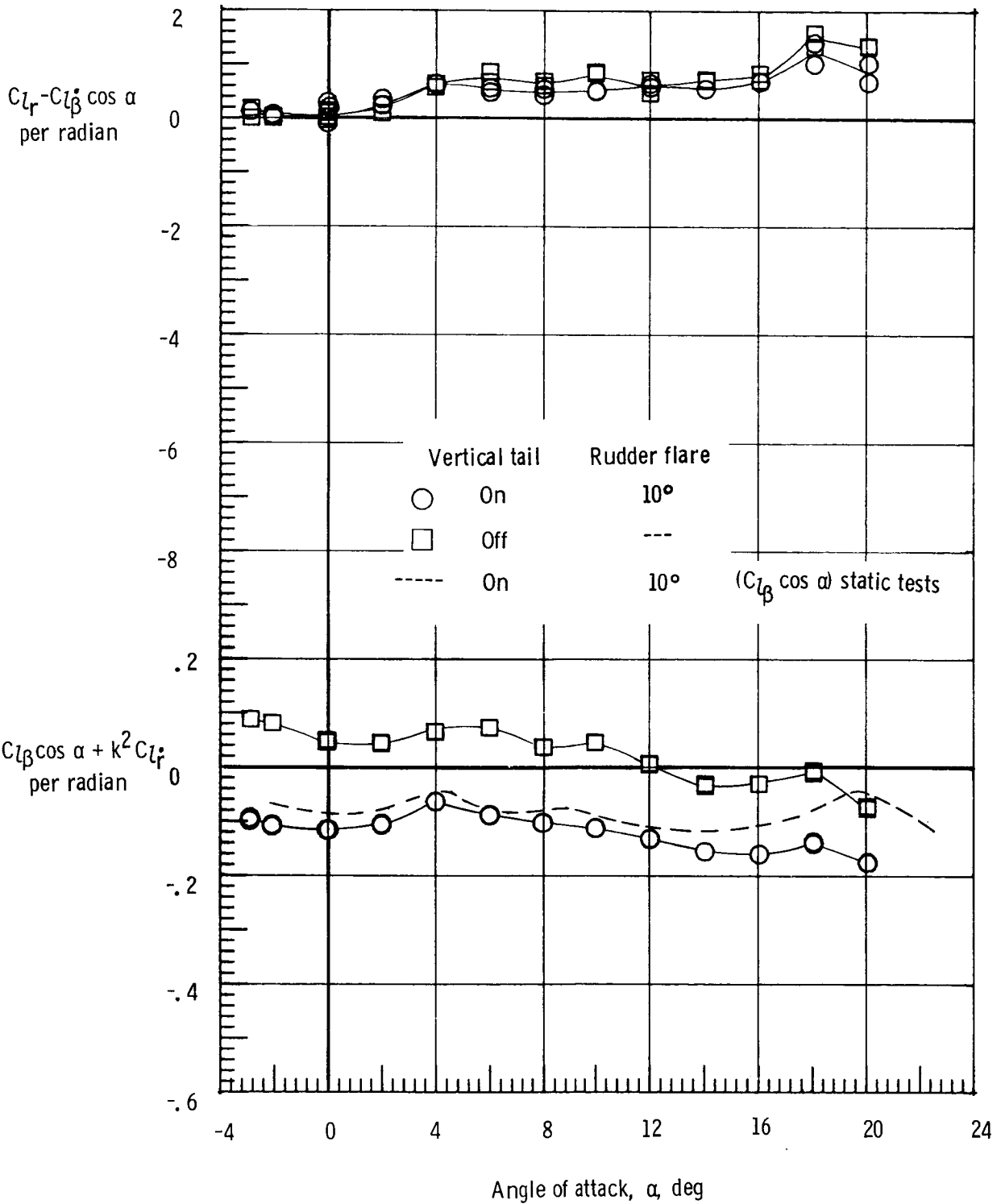
(d) M = 0.98.

Figure 24.- Continued.
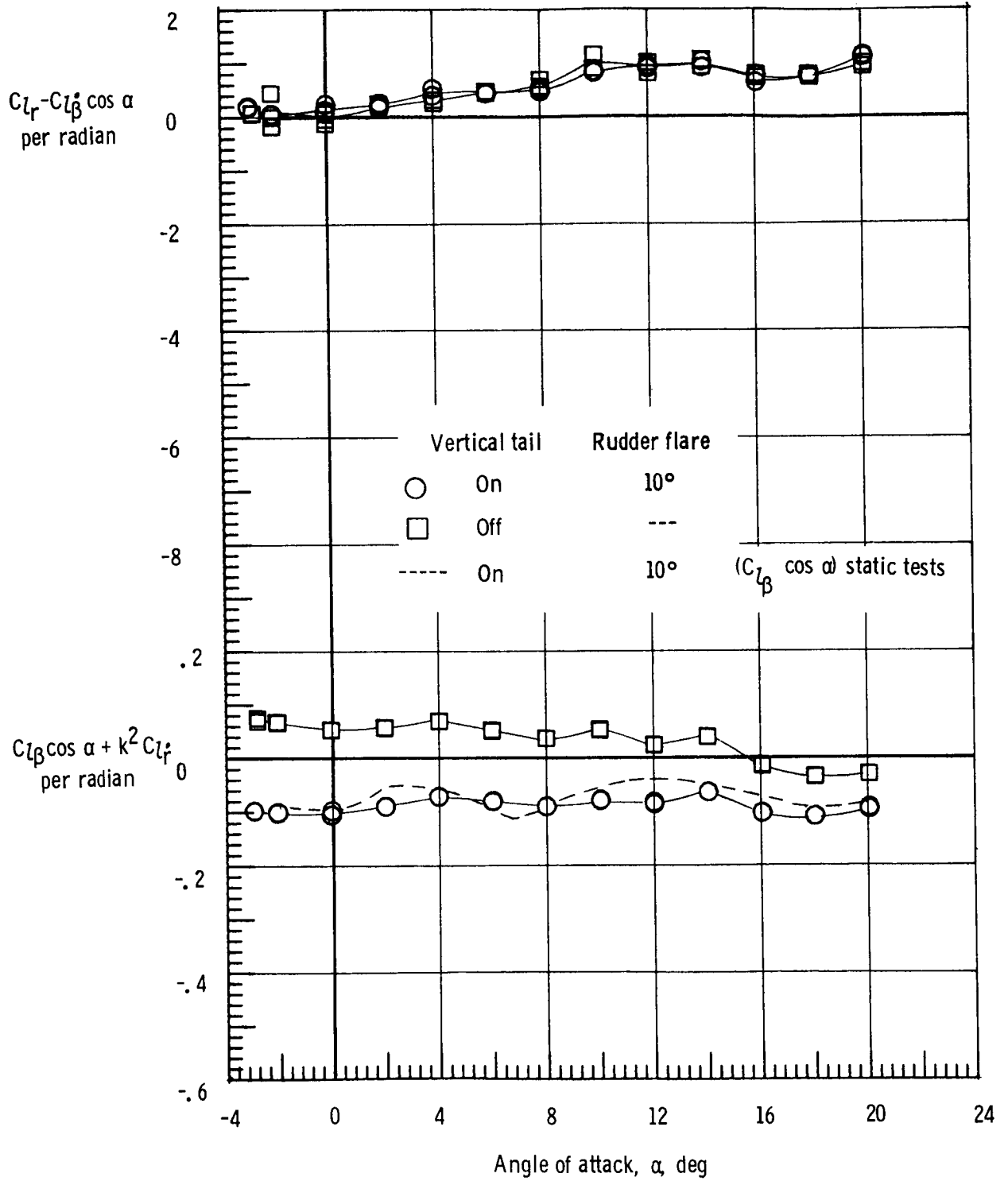
(e) M = 1.2.

Figure 24.- Concluded.
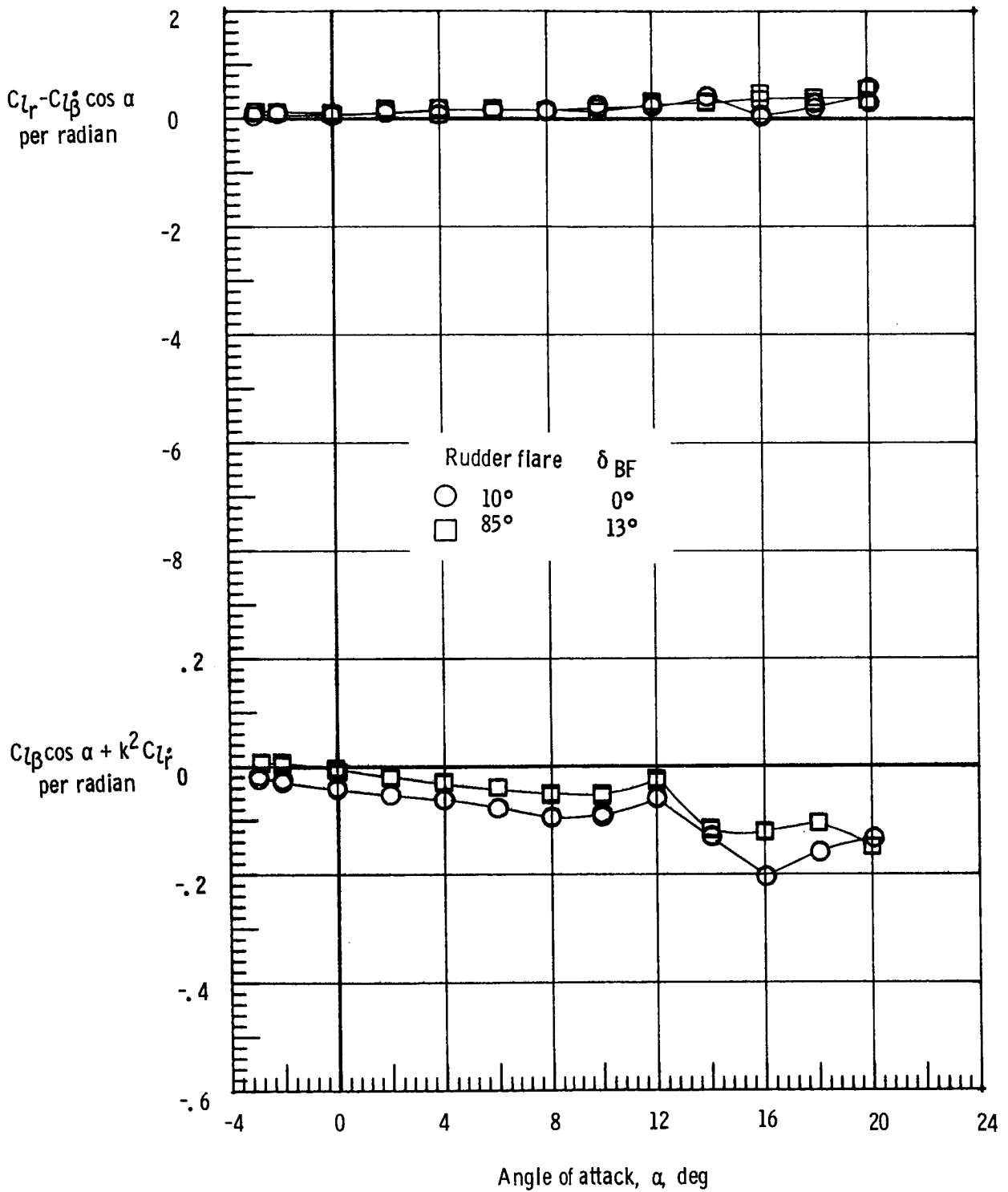
(a) M = 0.3.

Figure 25.- Effect of rudder flare and body flap deflection on rolling moment due to yaw rate parameter and effective dihedral parameter. Forward center of gravity.
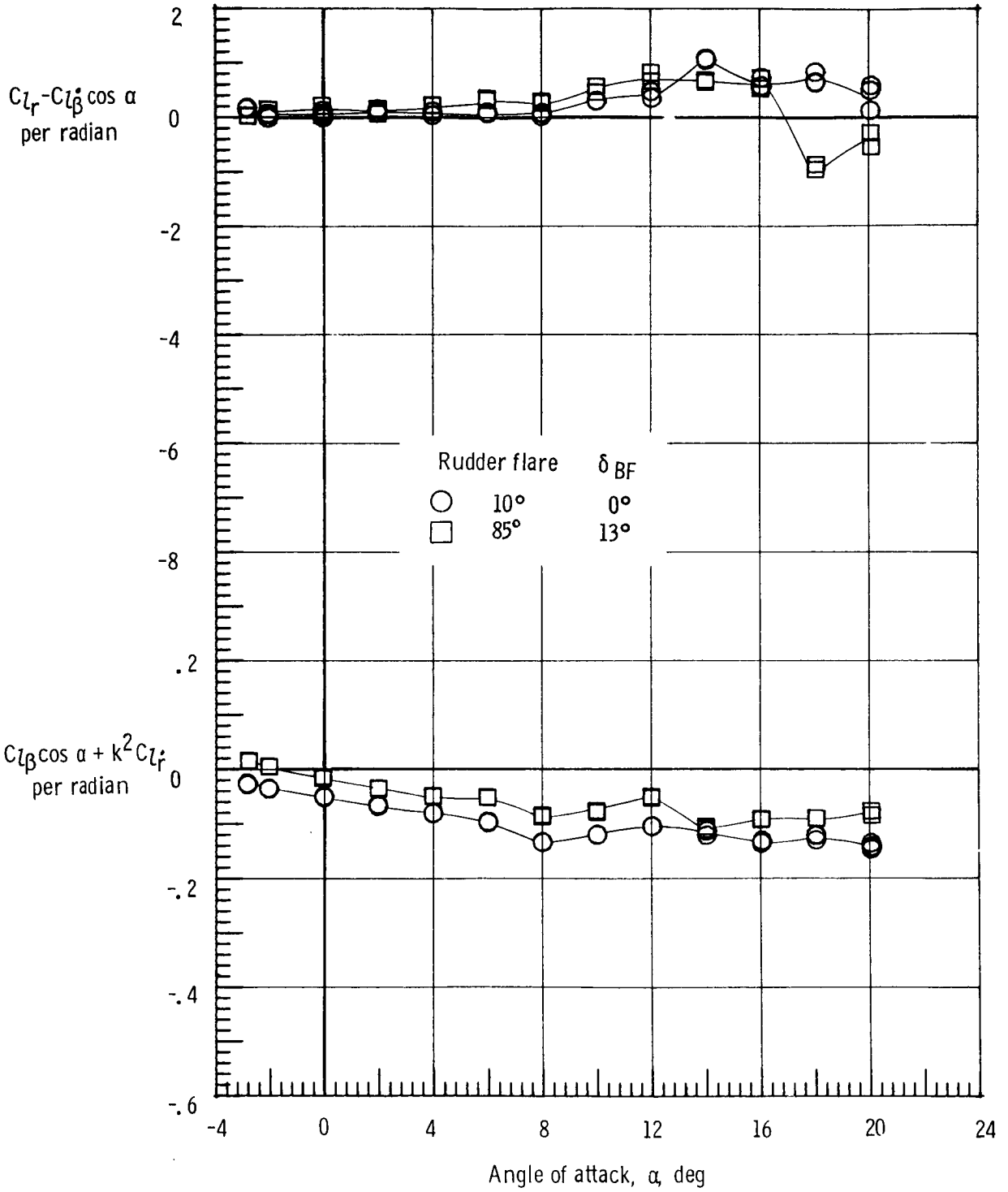
(b) M = 0.8.

Figure 25.- Continued.
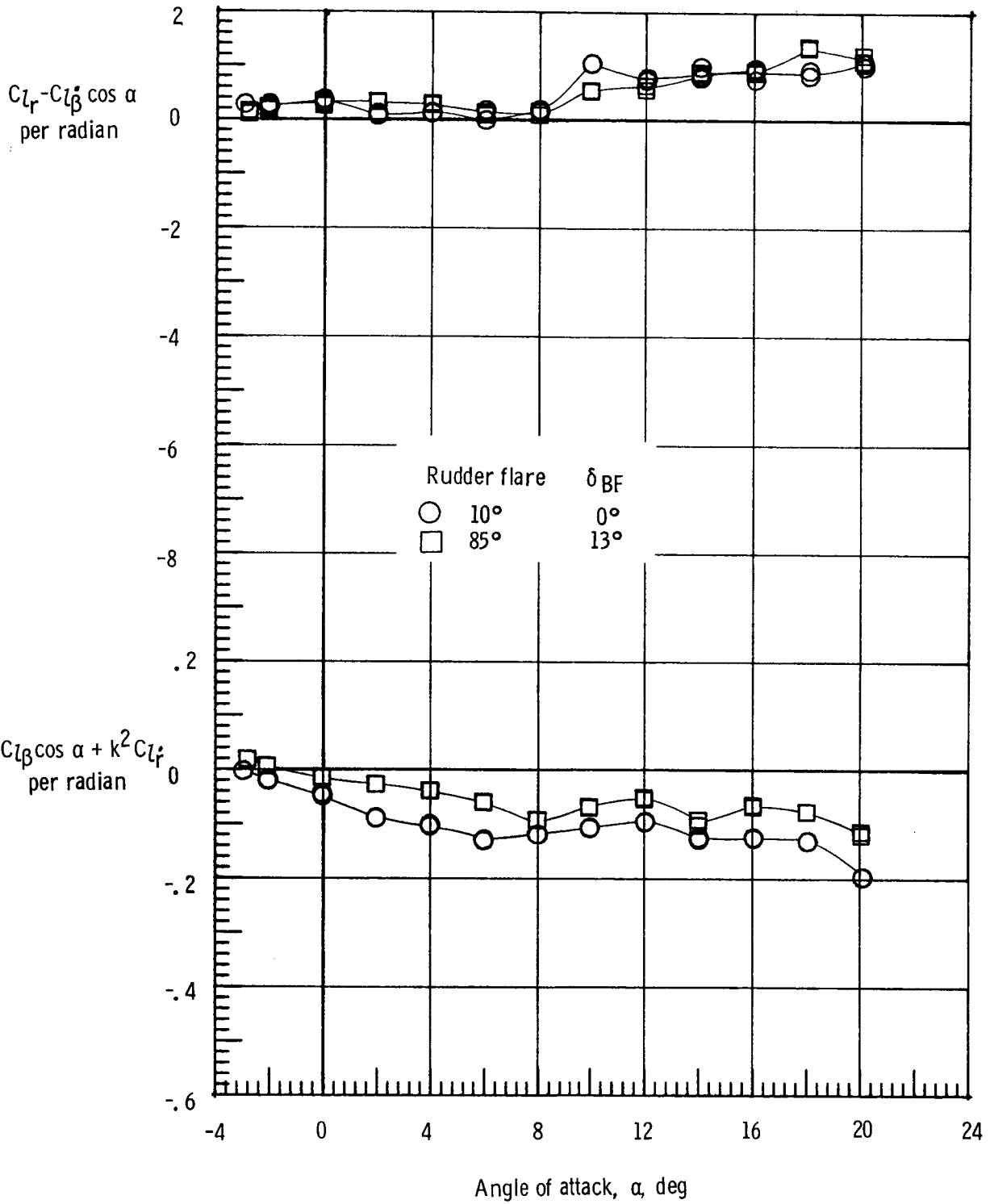
(c) M = 0.9.

Figure 25.- Continued.
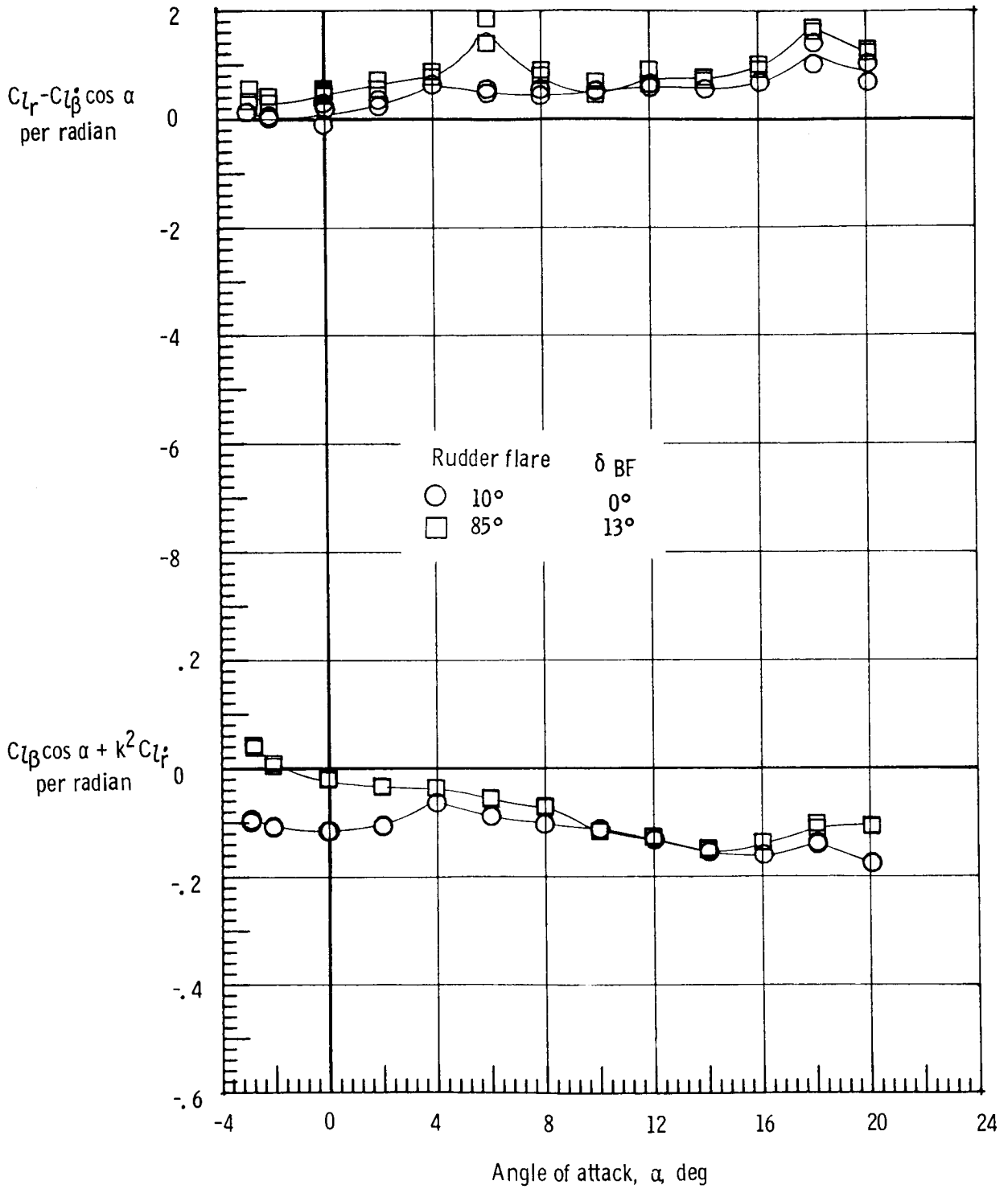
(d)   M = 0.98.

Figure 25.- Continued.
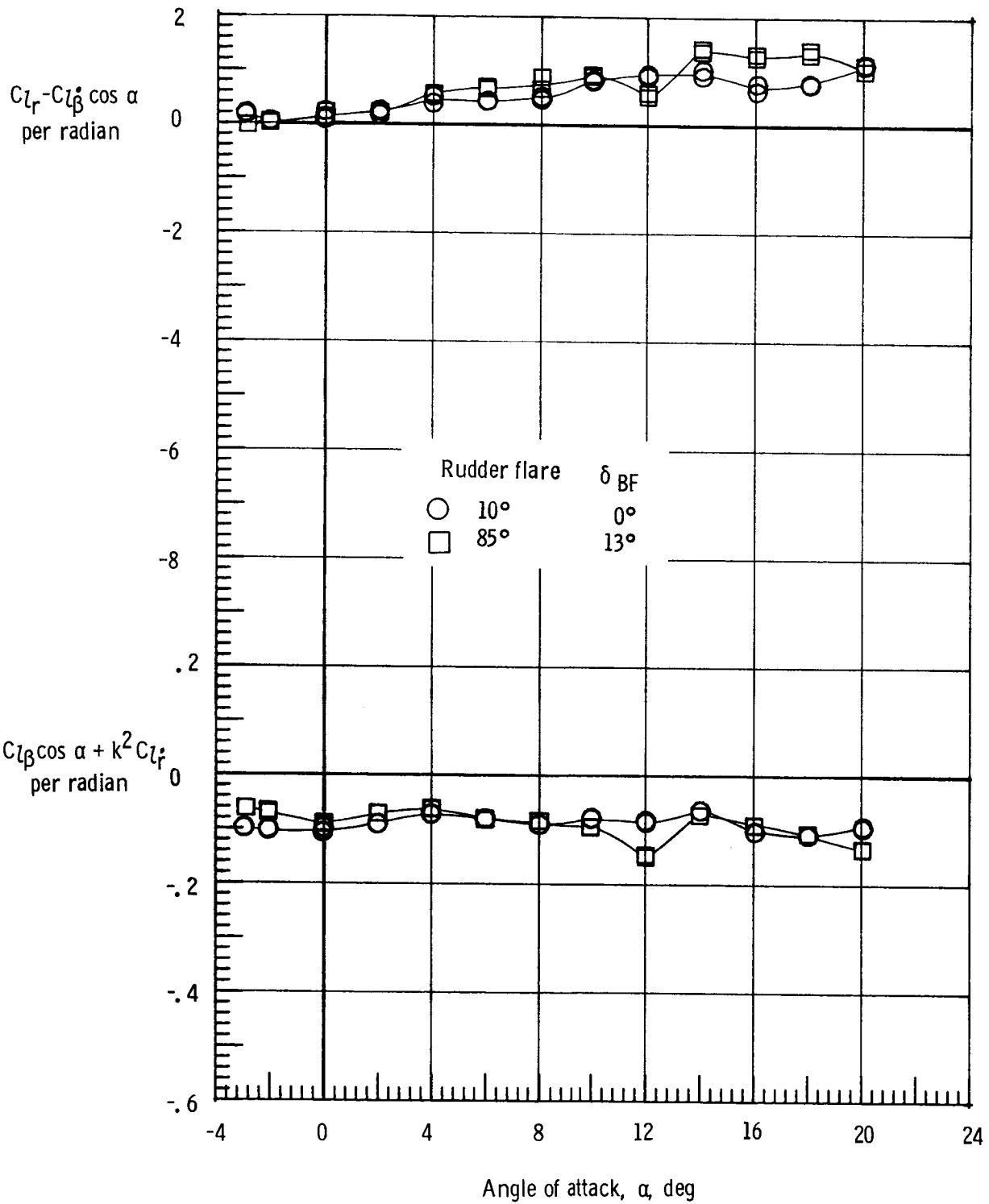
(e) M = 1.2.

Figure 25.- Concluded.
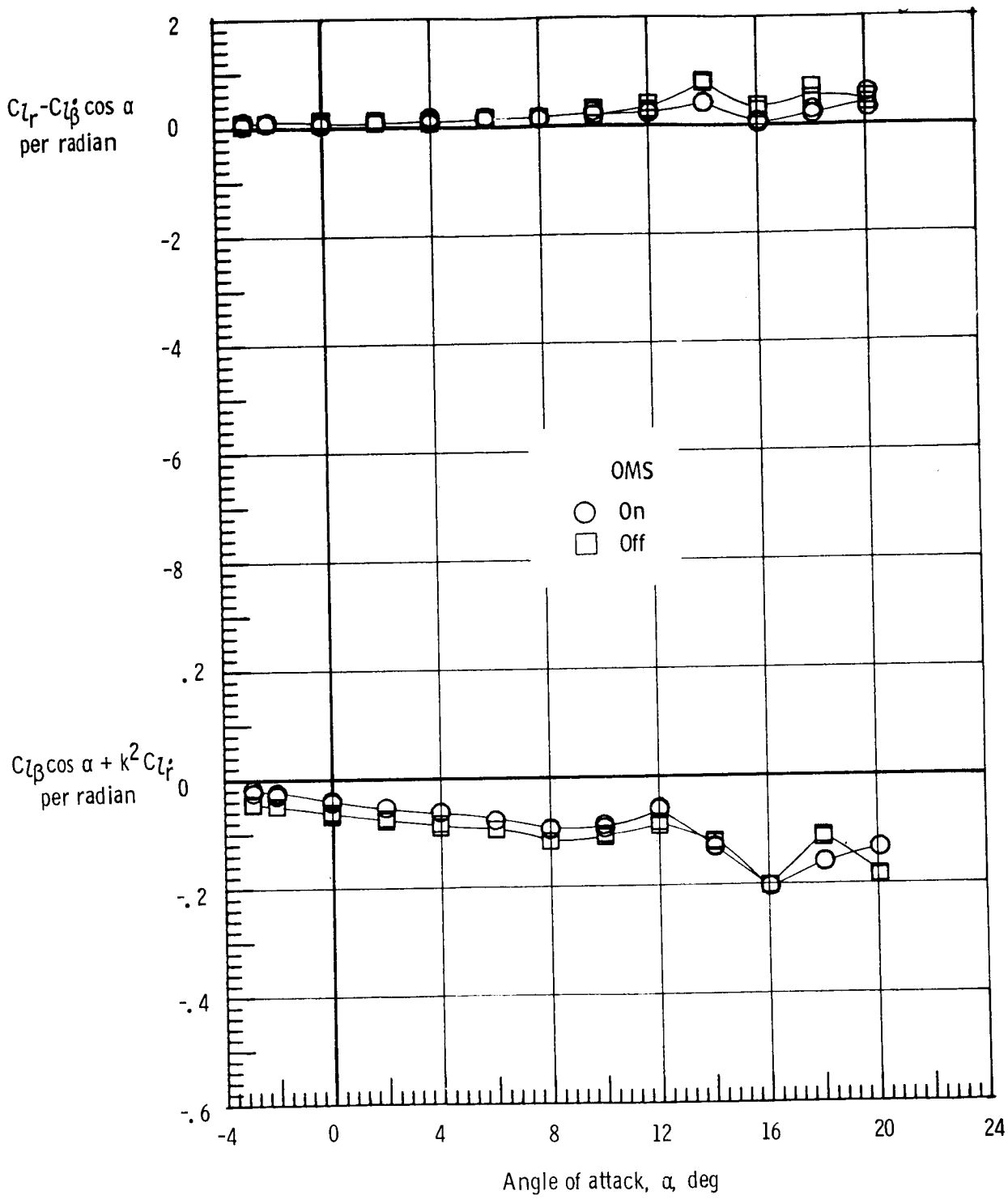
(a) M = 0.3.

Figure 26.- Effect of OMS installation on rolling moment due to yaw rate parameter and effective dihedral parameter. Forward center of gravity; rudder flare, 10°; $\delta_{BF} = 0°$.

128
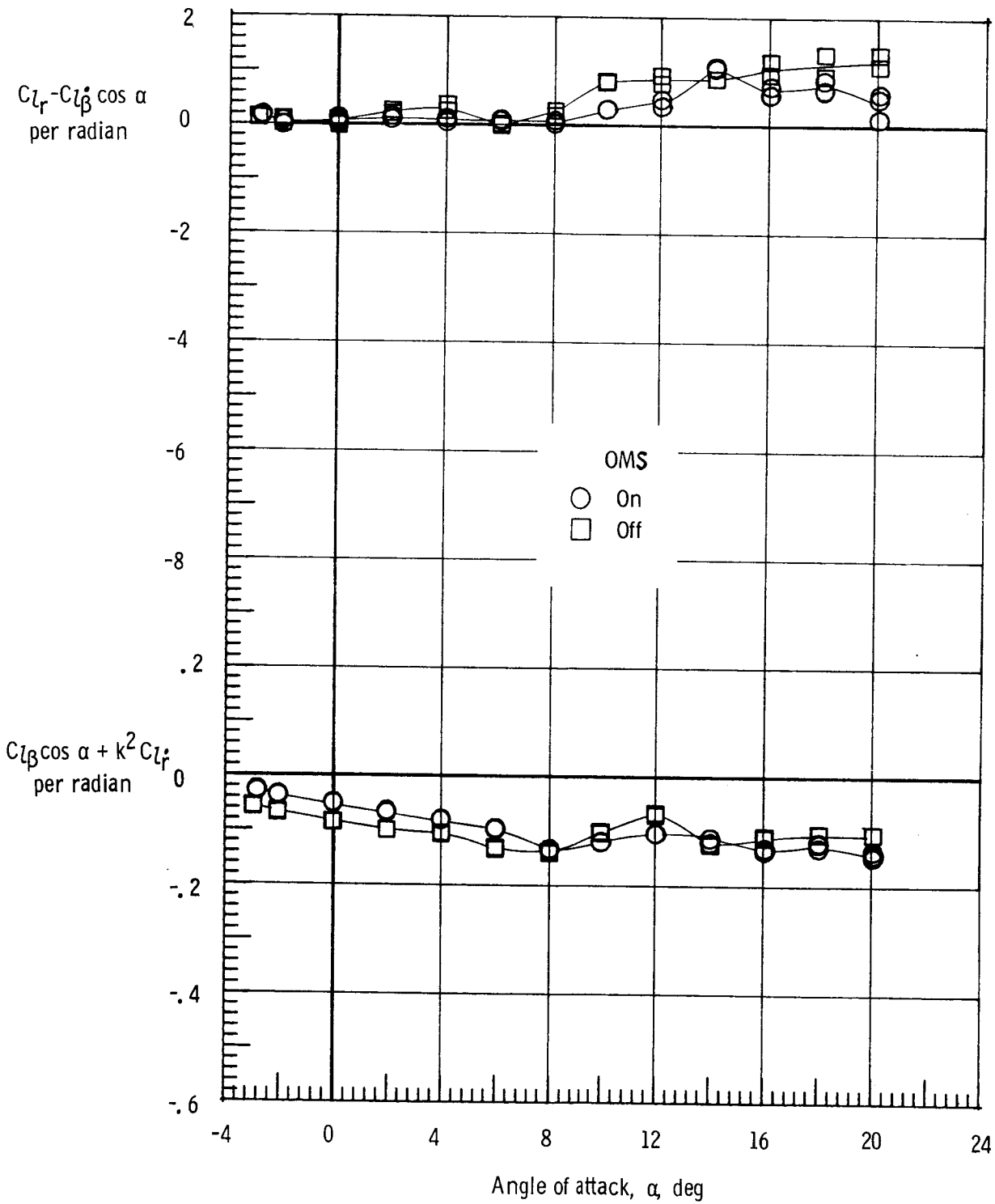
(b) M = 0.8.

Figure 26.- Continued.
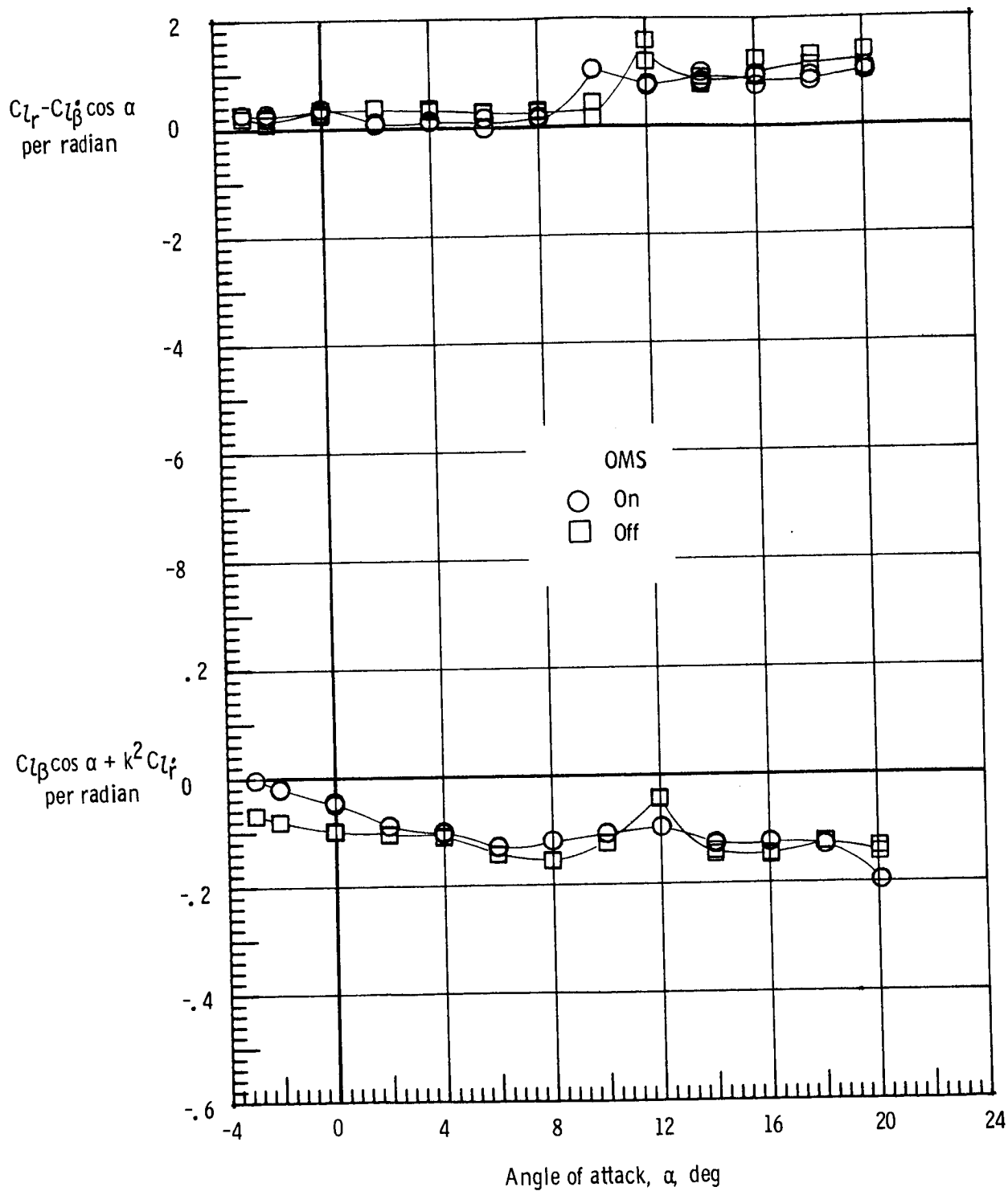
(c) M = 0.9.

Figure 26.- Continued.
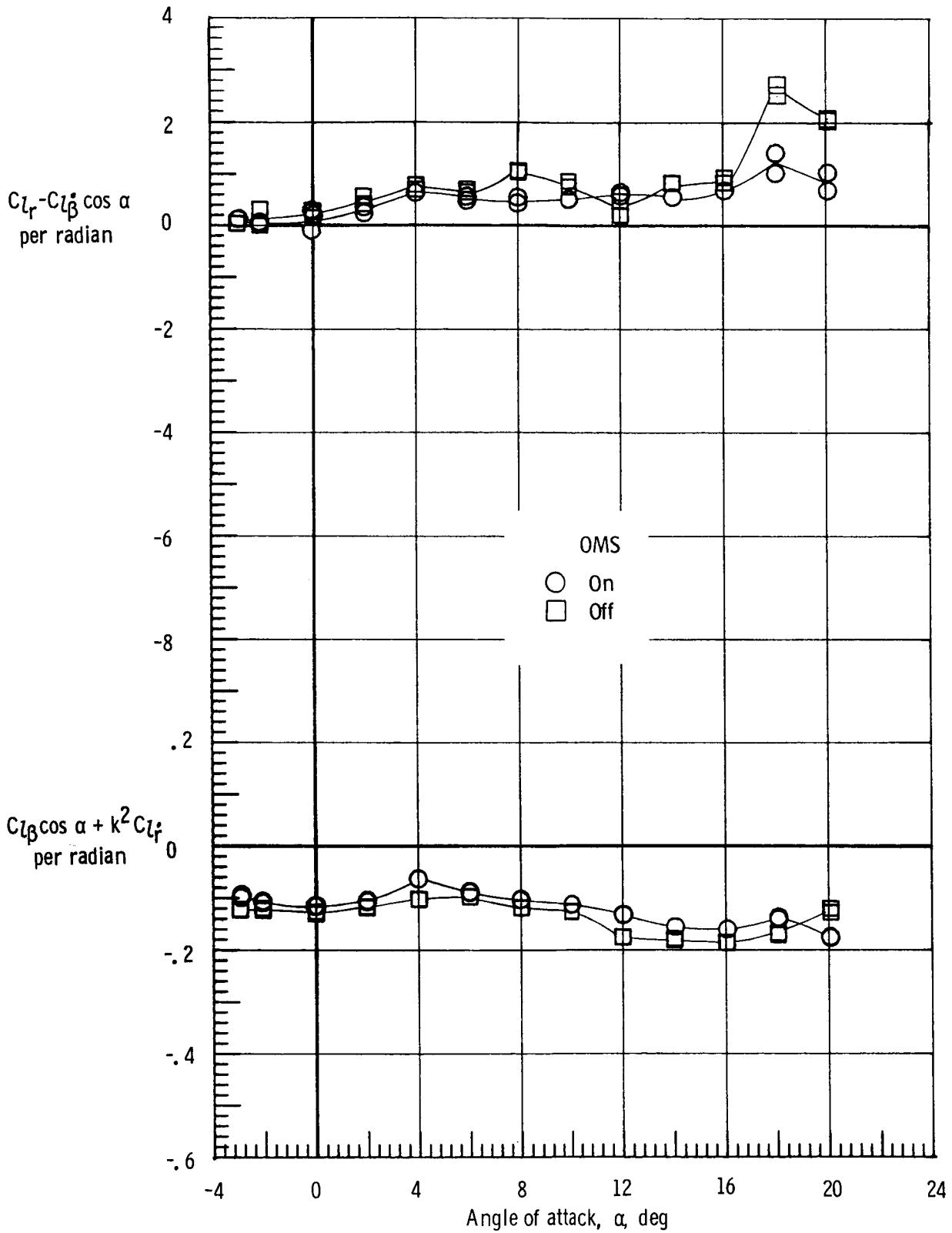
(d)   M = 0.98.

Figure 26.- Continued.
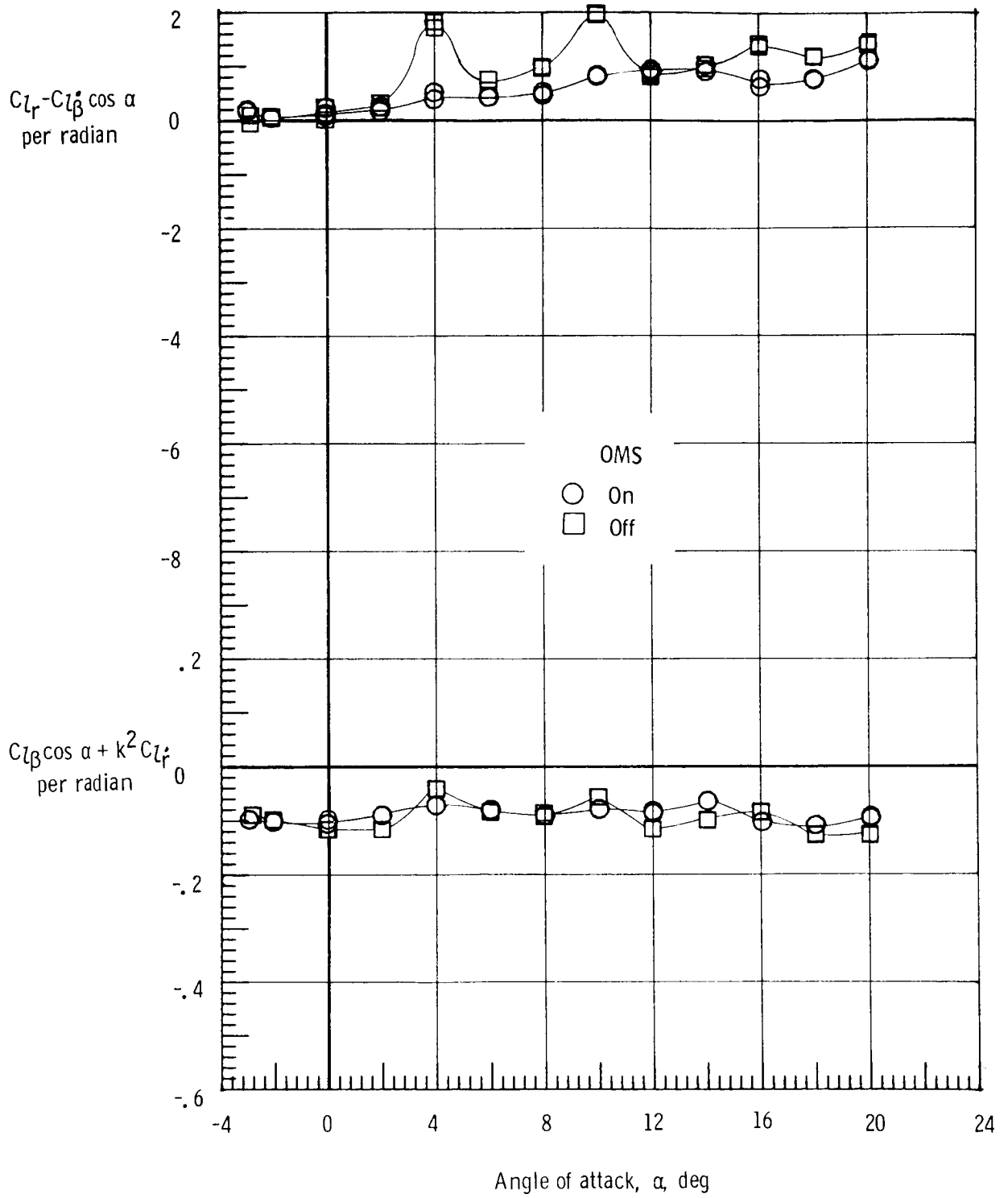
(e)   M = 1.2.

Figure 26.- Concluded.

$C_{l_p} + C_{l_{\dot\beta}} \sin \alpha$
per radian

Vertical tail

○   On

□   Off

----- On $(C_{l_\beta} \sin \alpha)$ static tests

$C_{l_\beta} \sin \alpha - k^2 C_{l_{\dot p}}$
per radian

Angle of attack, α, deg
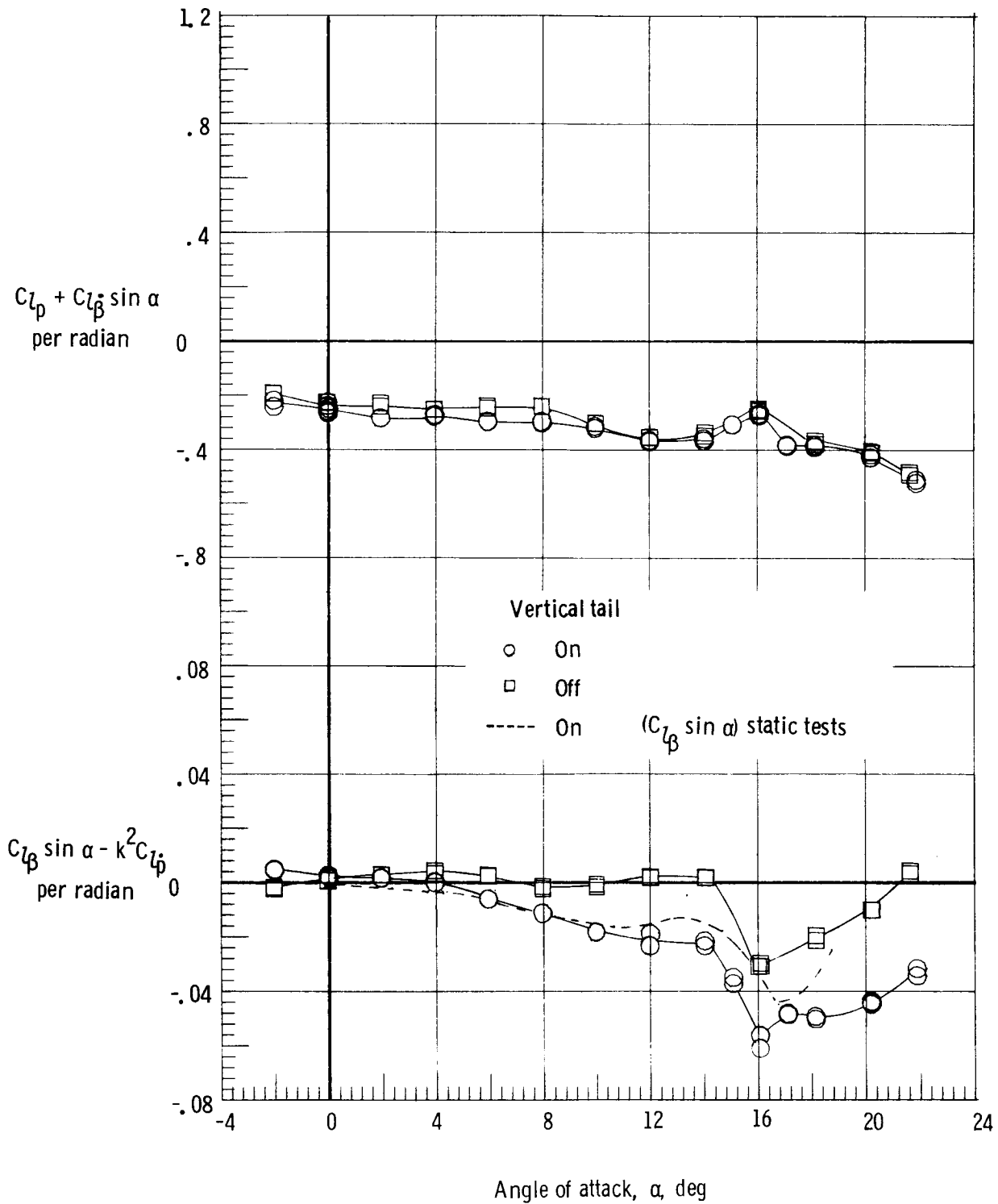
(a)   M = 0.3.

Figure 27.- Effect of vertical tail on the damping in roll parameter and on the rolling moment due to roll displacement parameter. Forward center of gravity; rudder flare, 10°; $\delta_{BF} = 0^{\circ}$.

133

(b)   M = 0.8.

Figure 27.- Continued.

$C_{l_p} + C_{l_{\dot{\beta}}} \sin \alpha$ per radian

$C_{l_\beta} \sin \alpha - k^2 C_{l_{\dot{p}}}$ per radian

Vertical tail

○   On

□   Off

----   On $(C_{l_\beta} \sin \alpha)$ static tests

Angle of attack, α, deg
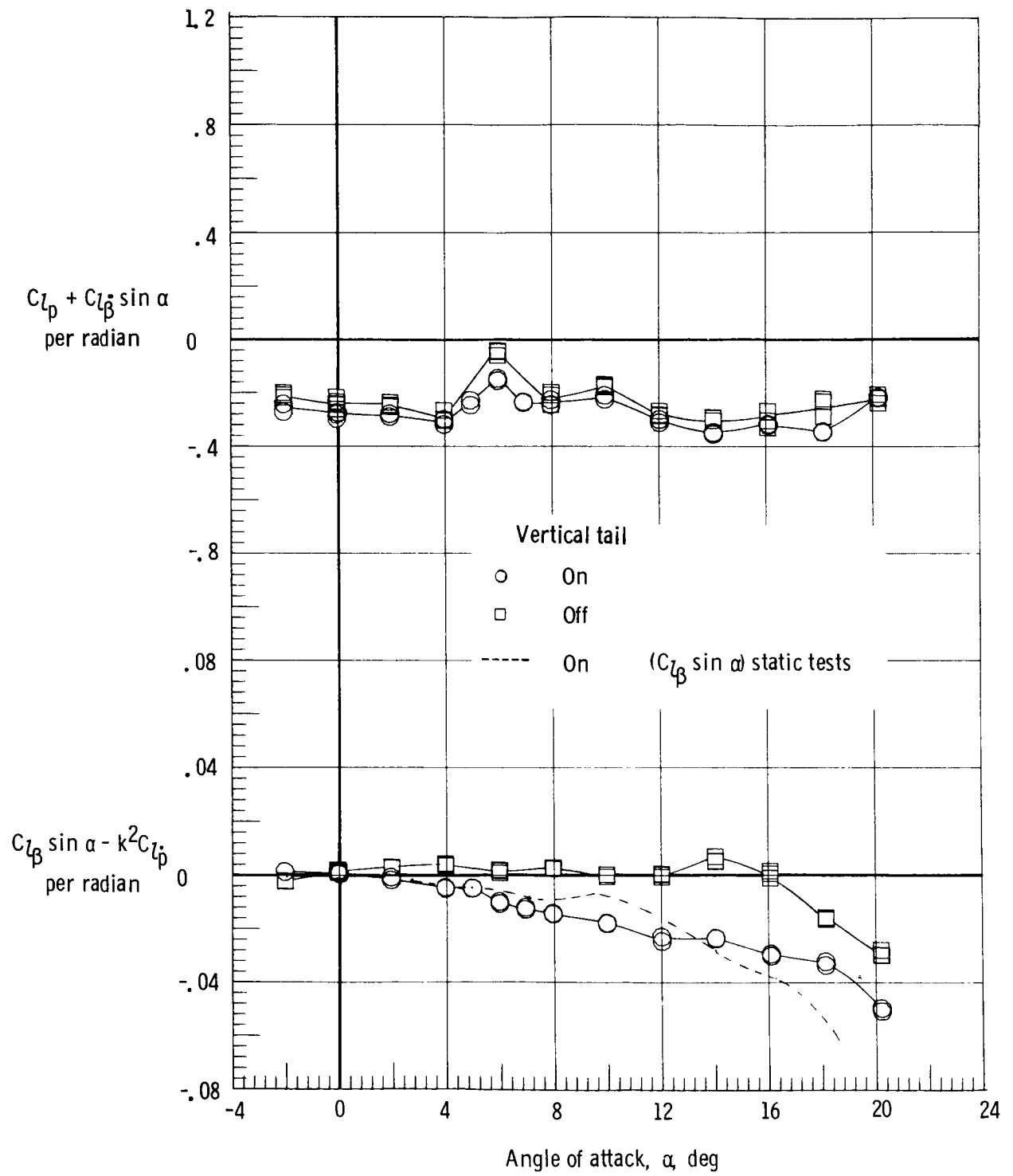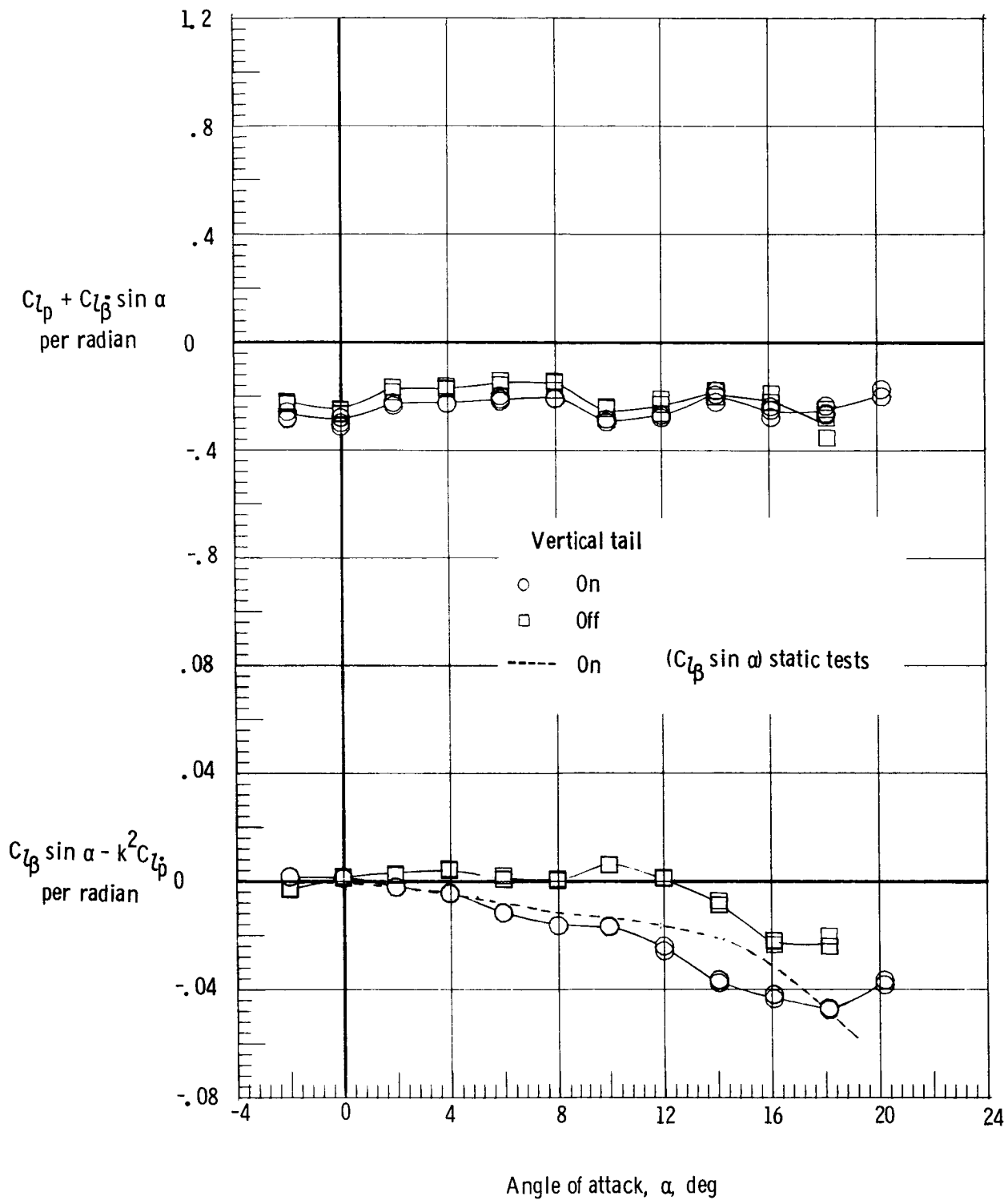
(c)   M = 0.9.

Figure 27.- Continued.
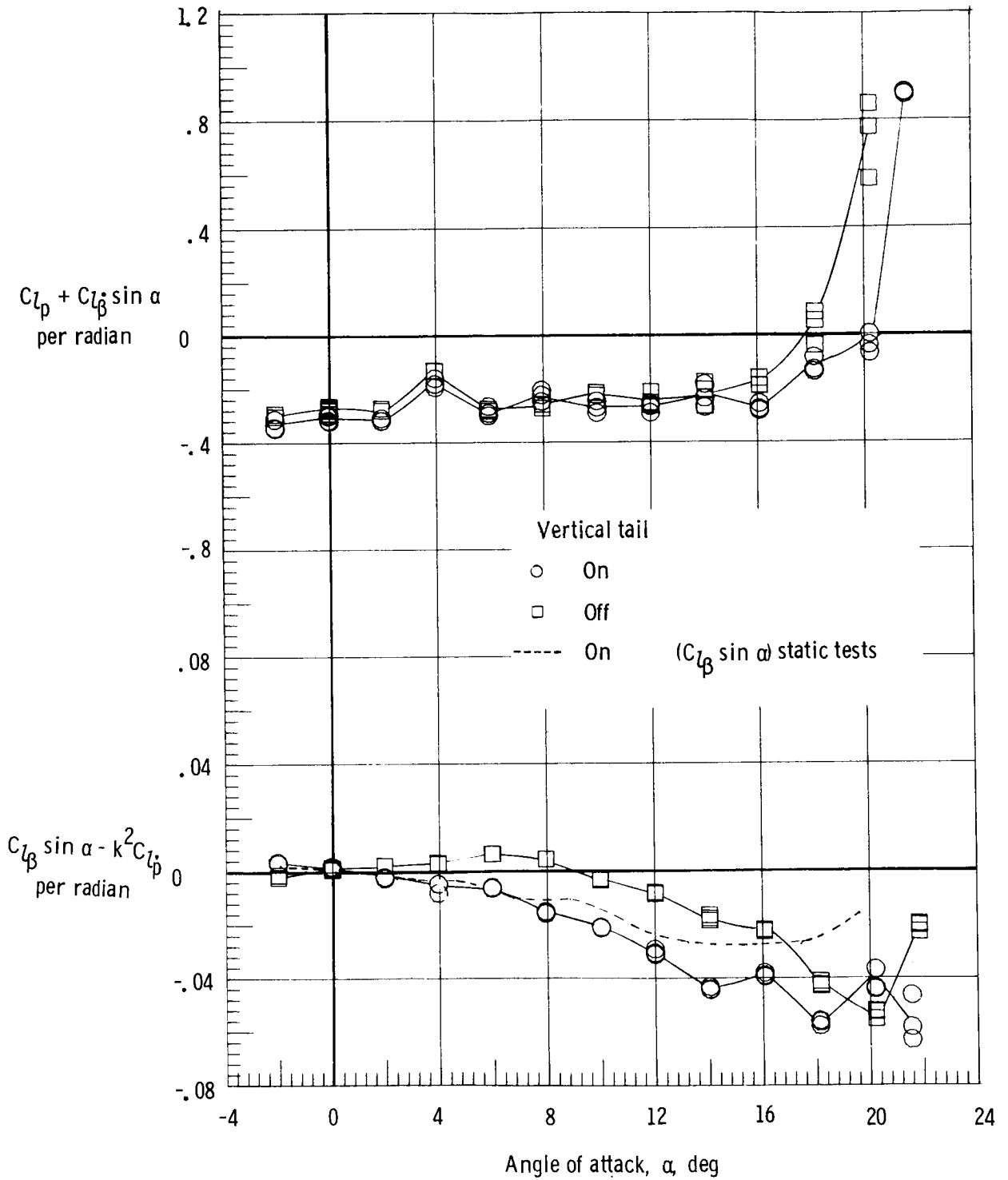
(d) M = 0.98.

Figure 27.– Continued.
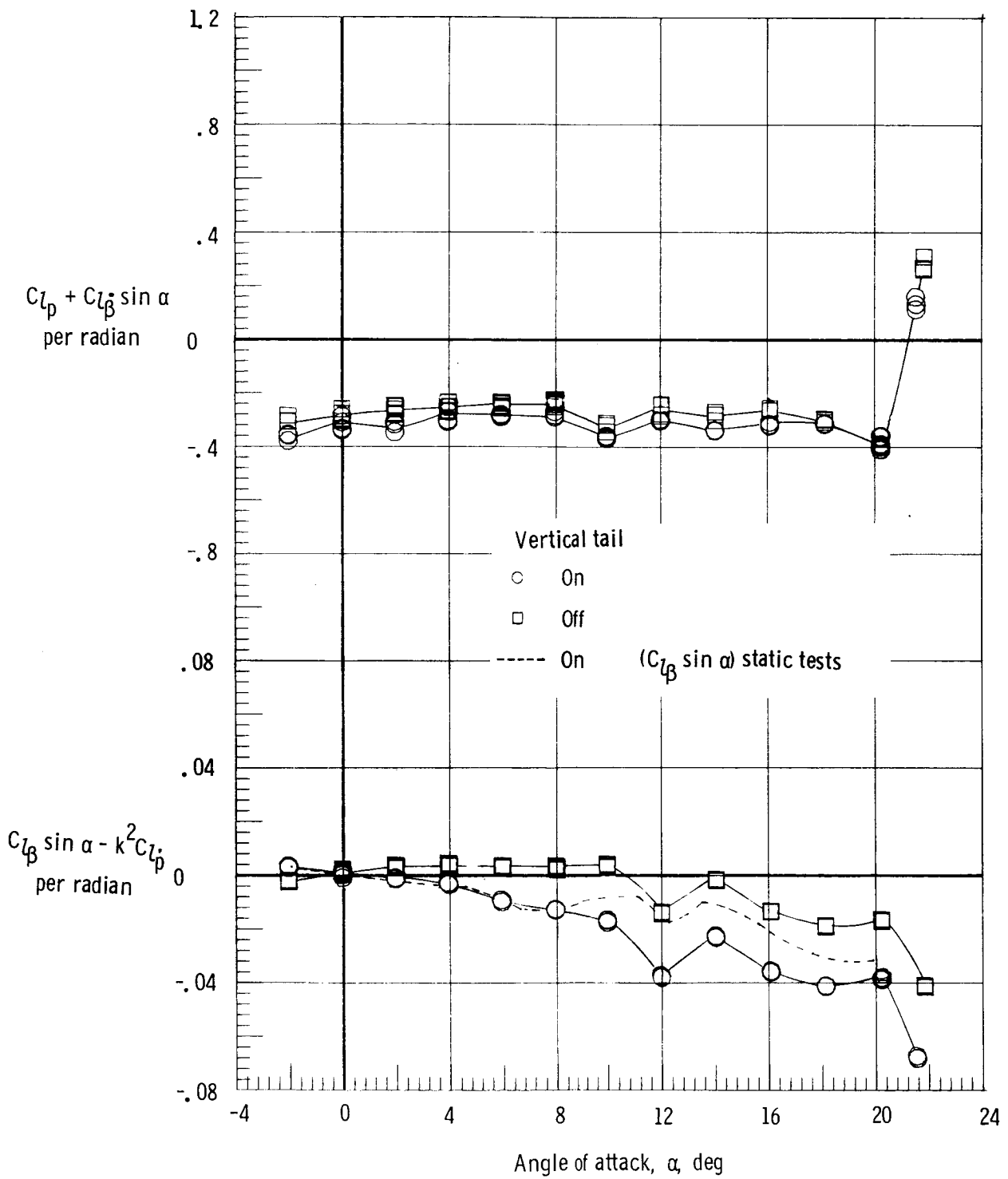
(e) M = 1.2.

Figure 27.- Concluded.
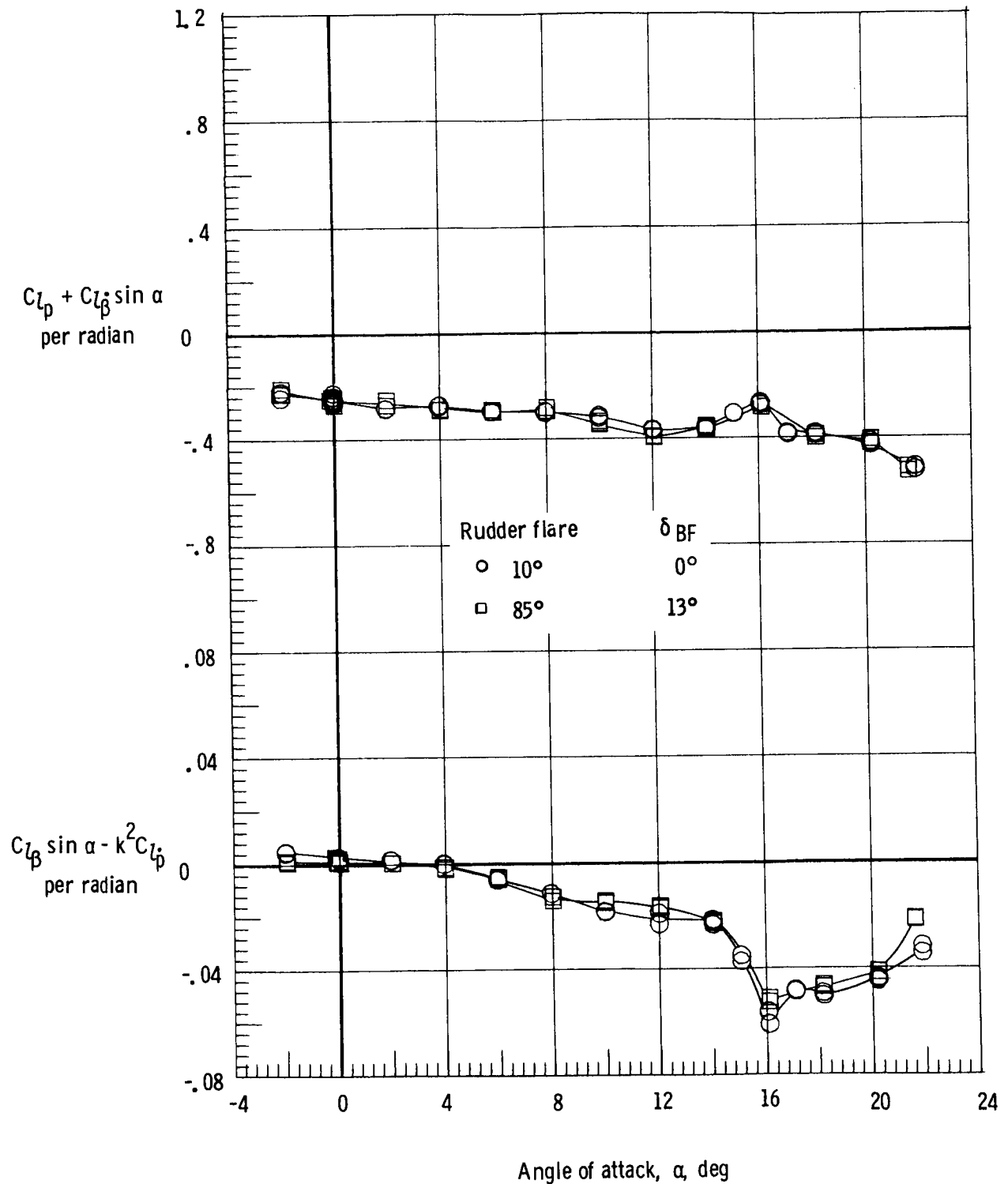
(a) M = 0.3.

Figure 28.- Effect of rudder flare and body flap deflection on the damping in roll
parameter and on the rolling moment due to roll displacement parameter.
Forward center of gravity.
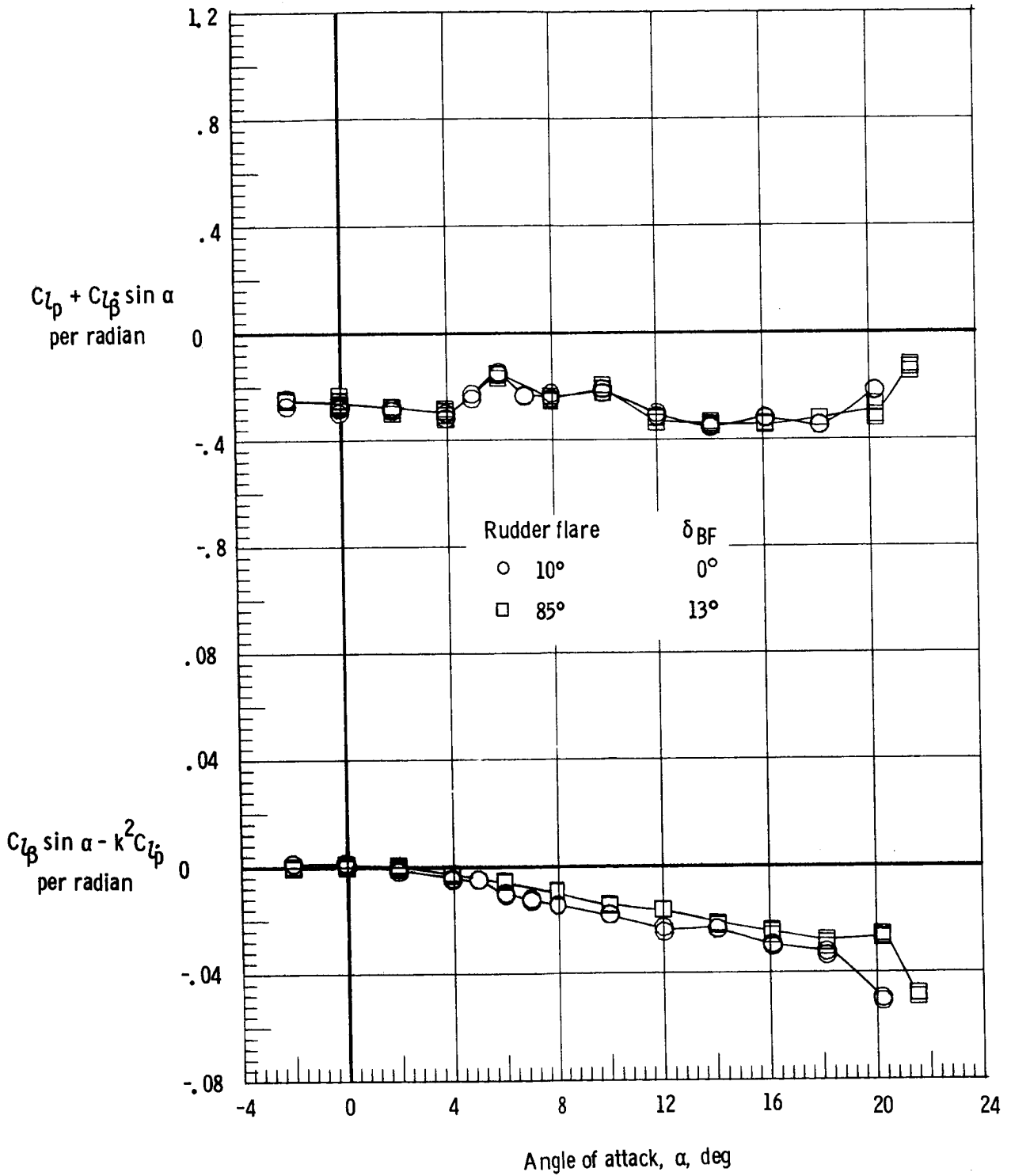
(b)   M = 0.8.

Figure 28.- Continued.
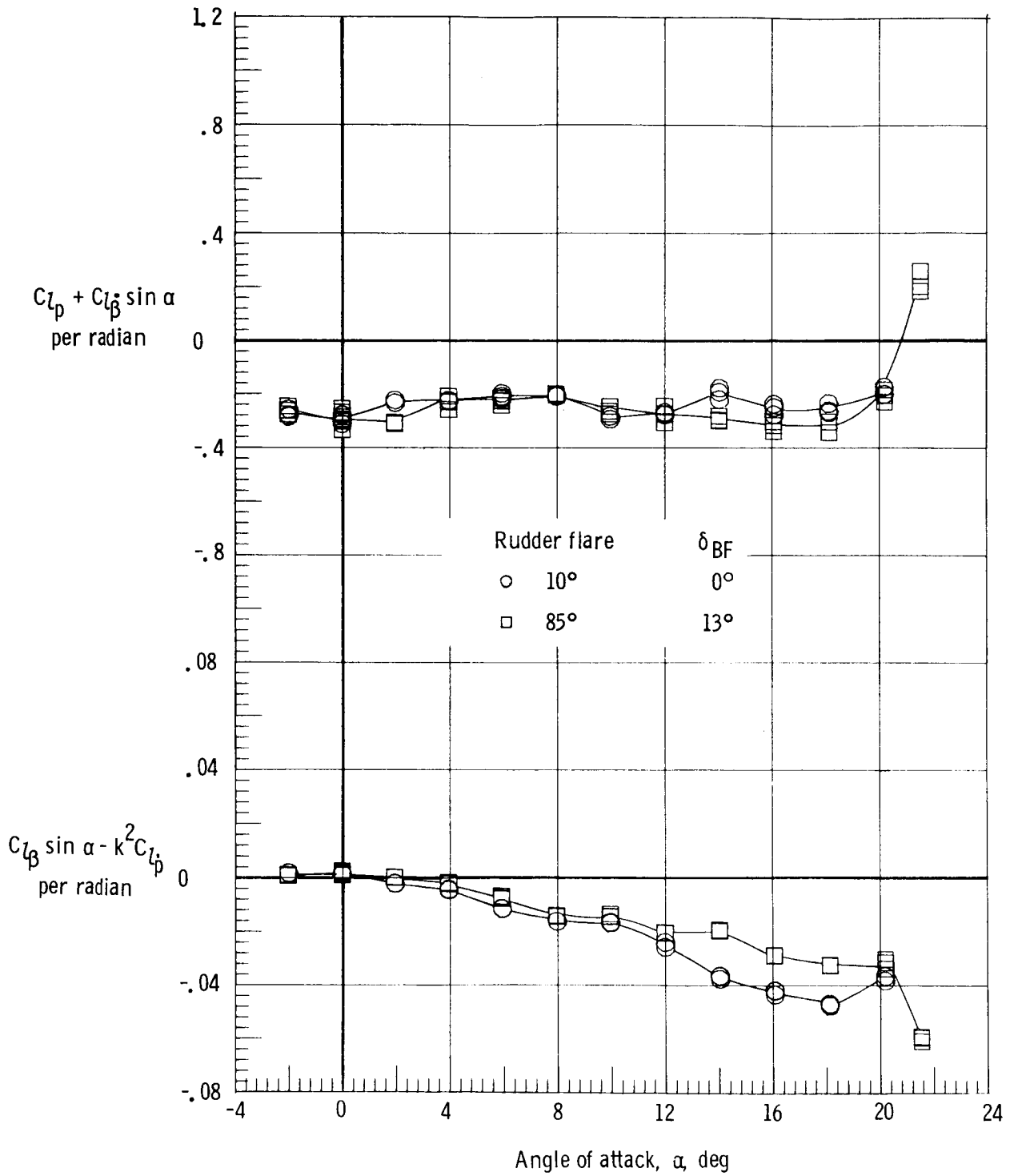
(c)   M = 0.9.

Figure 28.- Continued.
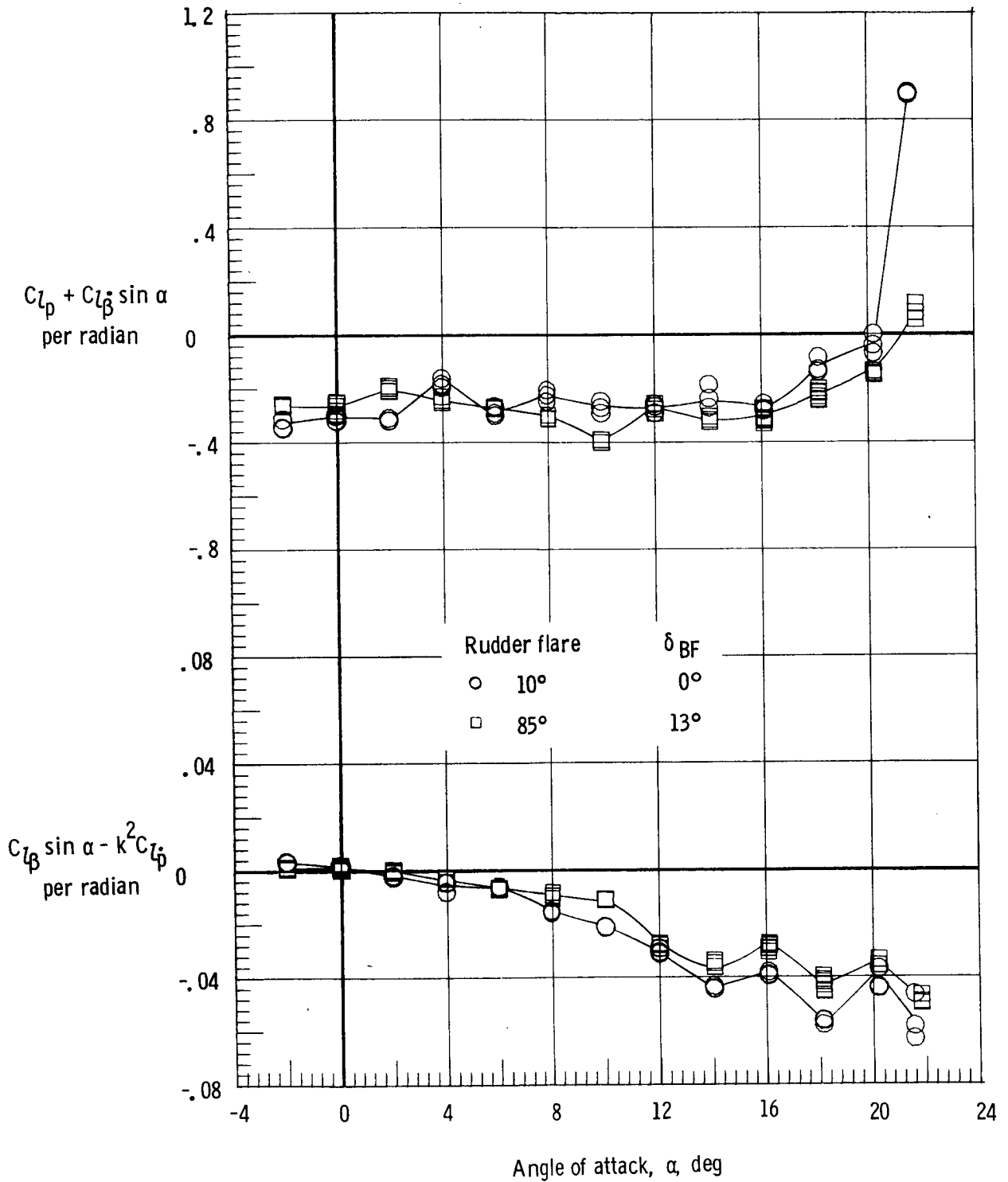
(d)   M = 0.98.

Figure 28.- Continued.
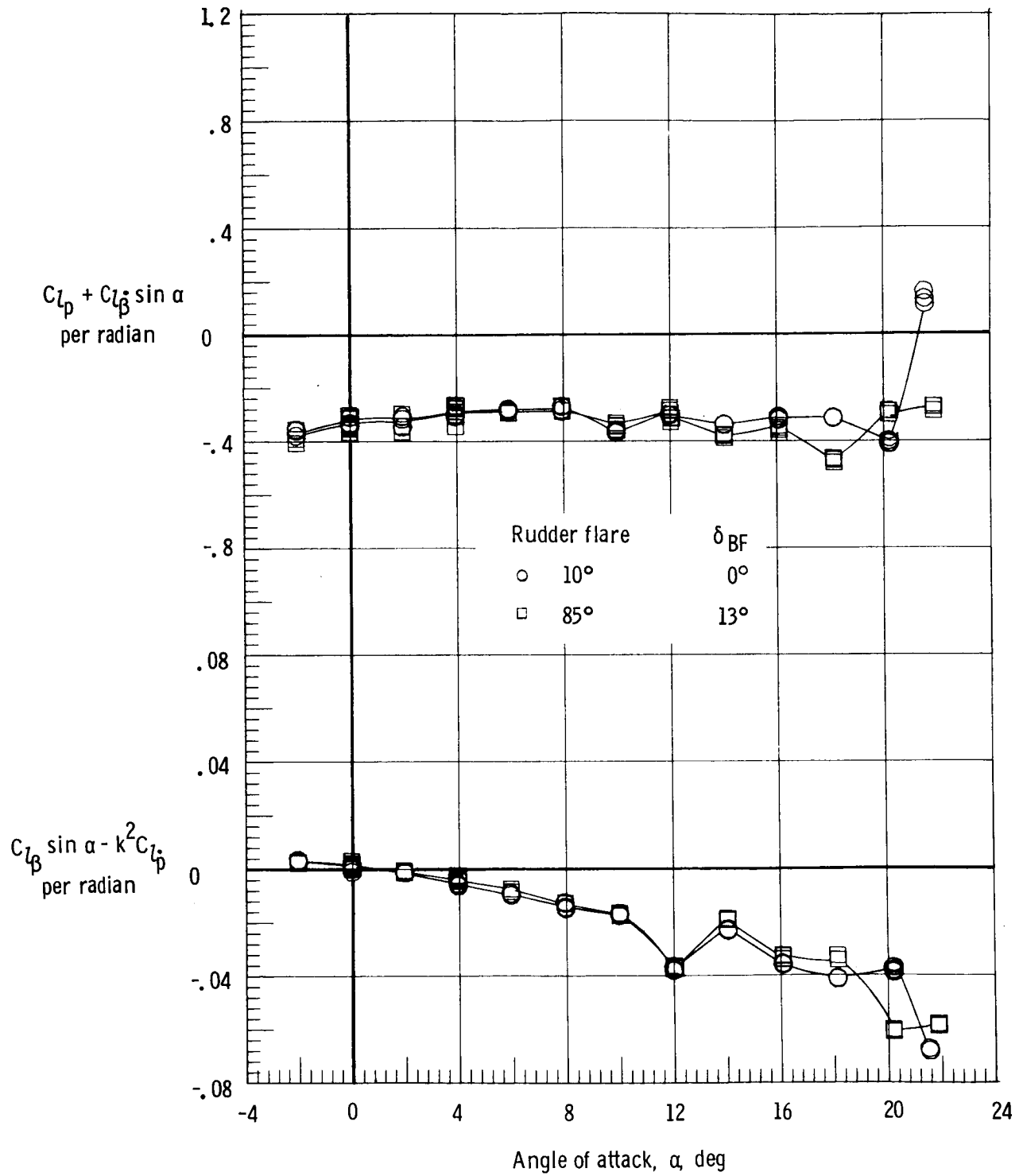
(e)   M = 1.2.

Figure 28.- Concluded.
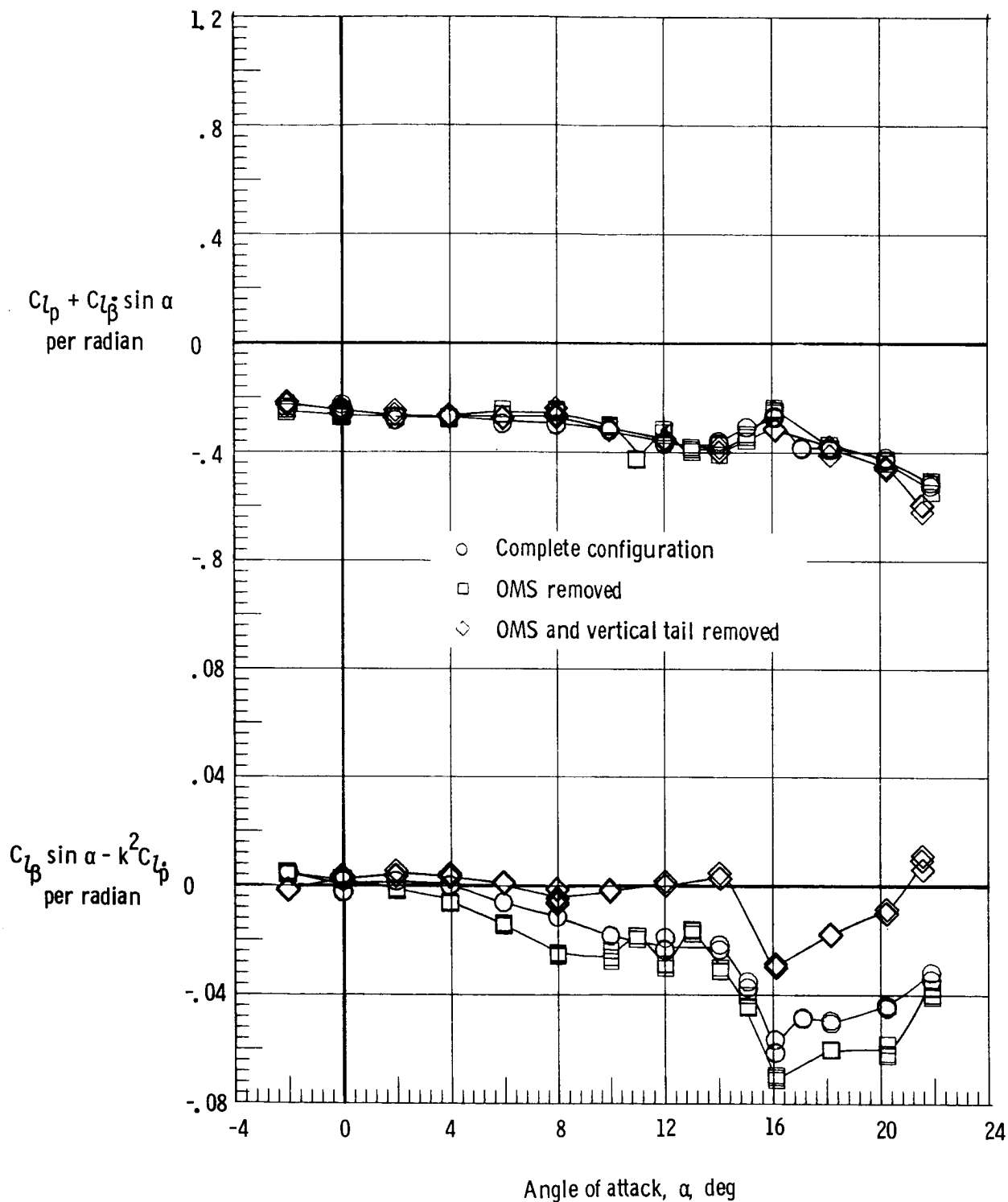
(a) M = 0.3.

Figure 29.- Effect of configuration components on the damping in roll parameter and on the rolling moment due to roll displacement parameter. Forward center of gravity; $\delta_{BF} = 0^O$.
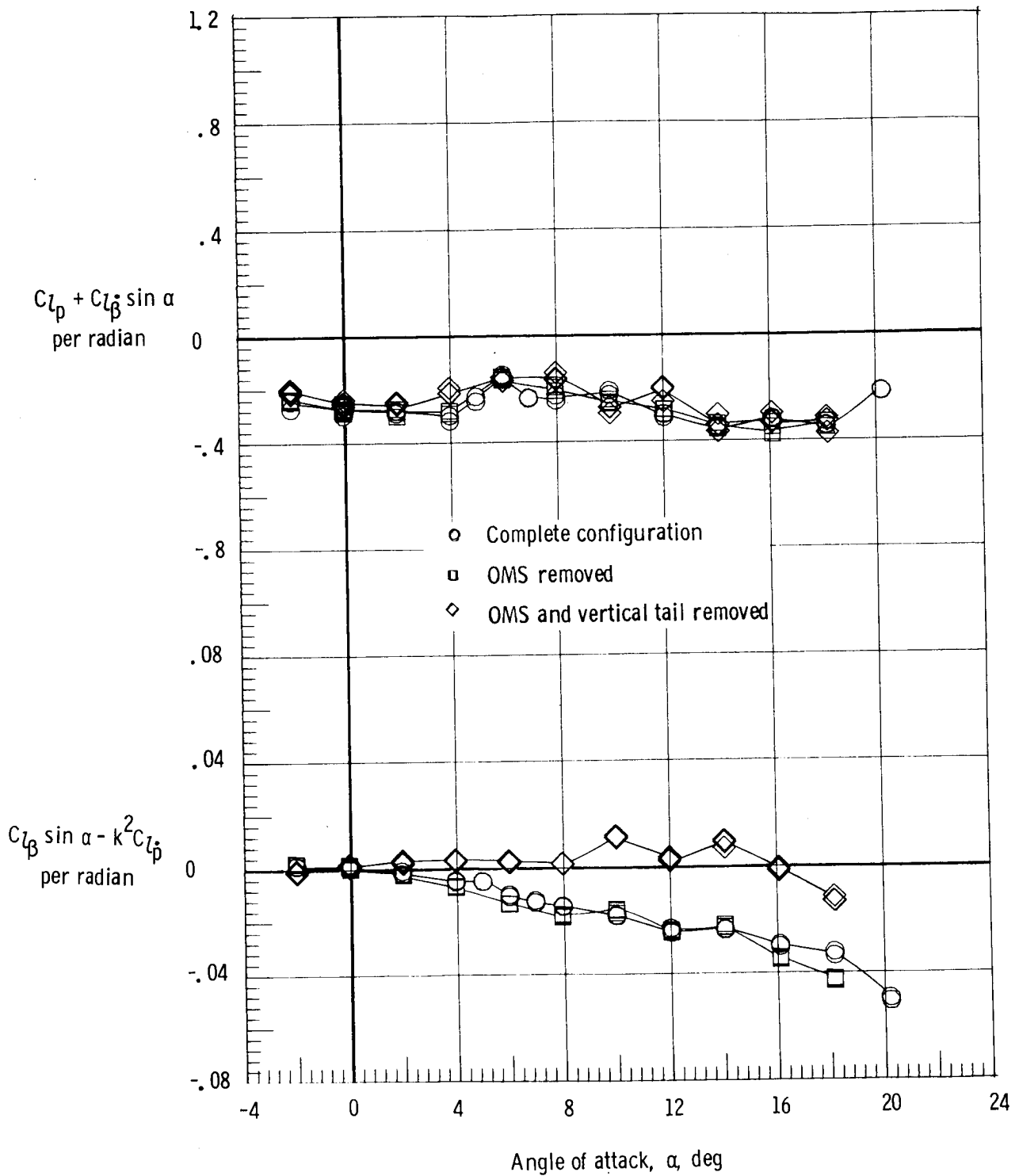
(b)   M = 0.8.

Figure 29.- Continued.

Angle of attack, α, deg
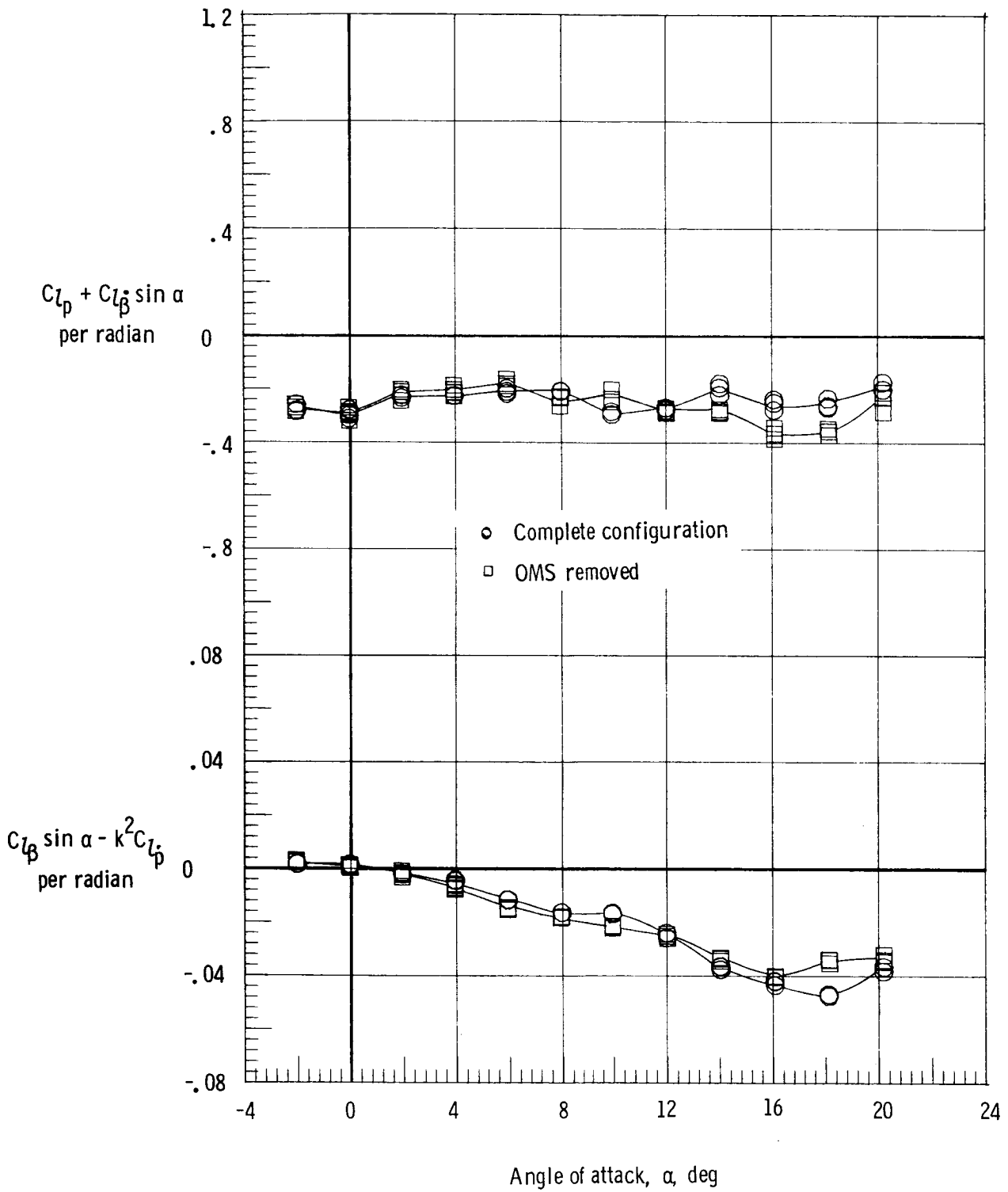
(c) M = 0.9.

Figure 29.- Continued.
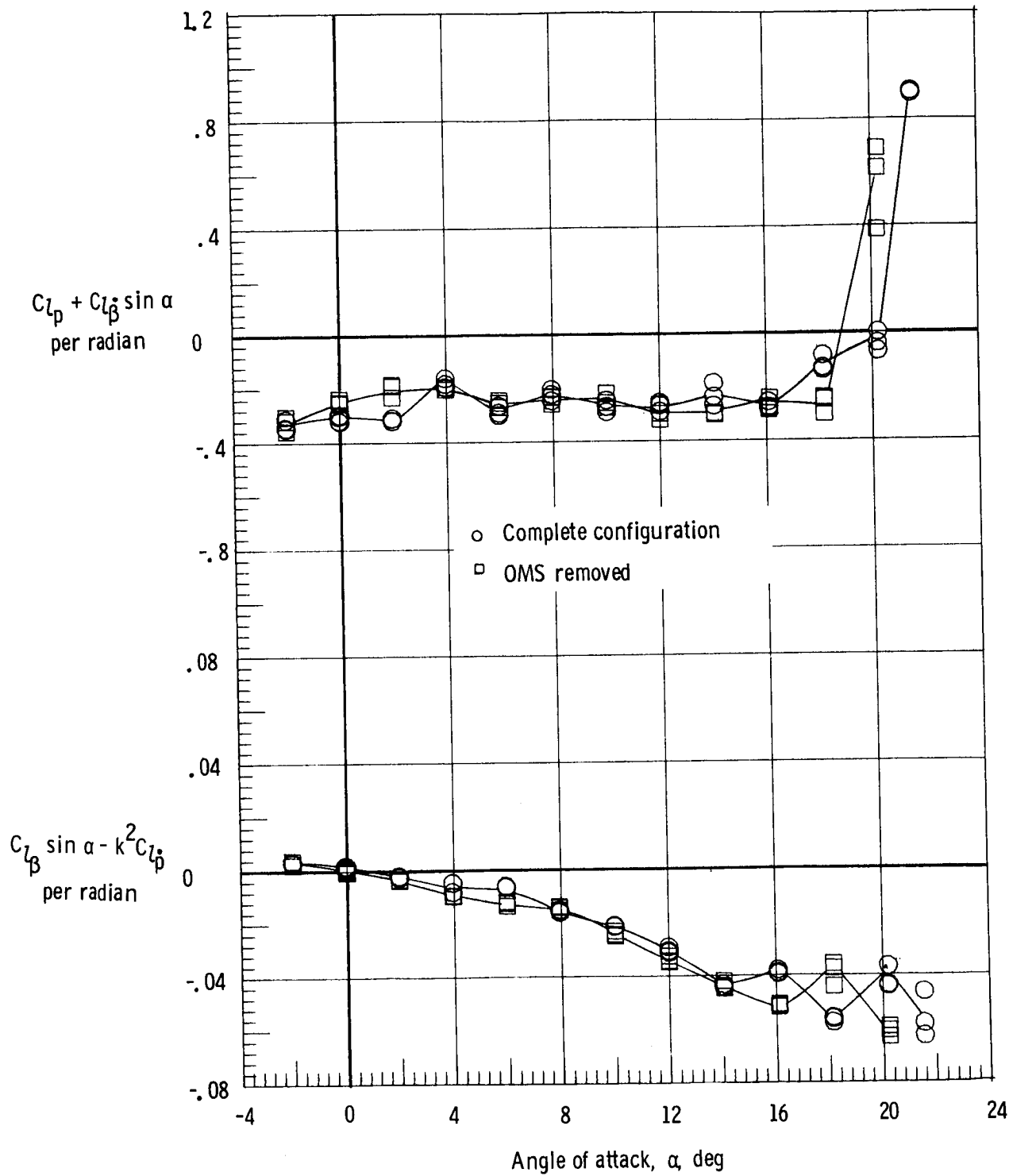
(d)   M = 0.98.

Figure 29.- Continued.

Angle of attack, α, deg
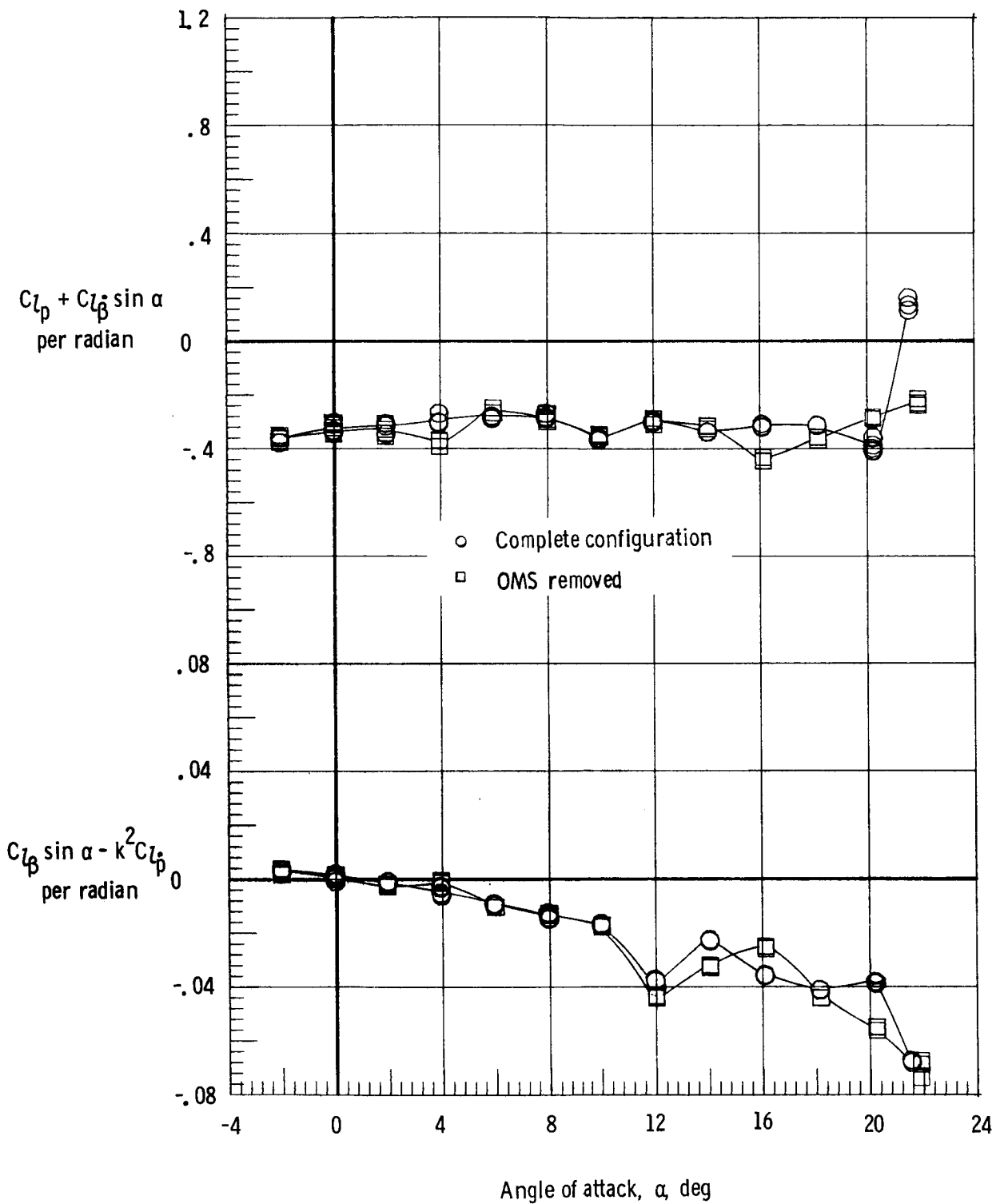
(e) M = 1.2.

Figure 29.- Concluded.
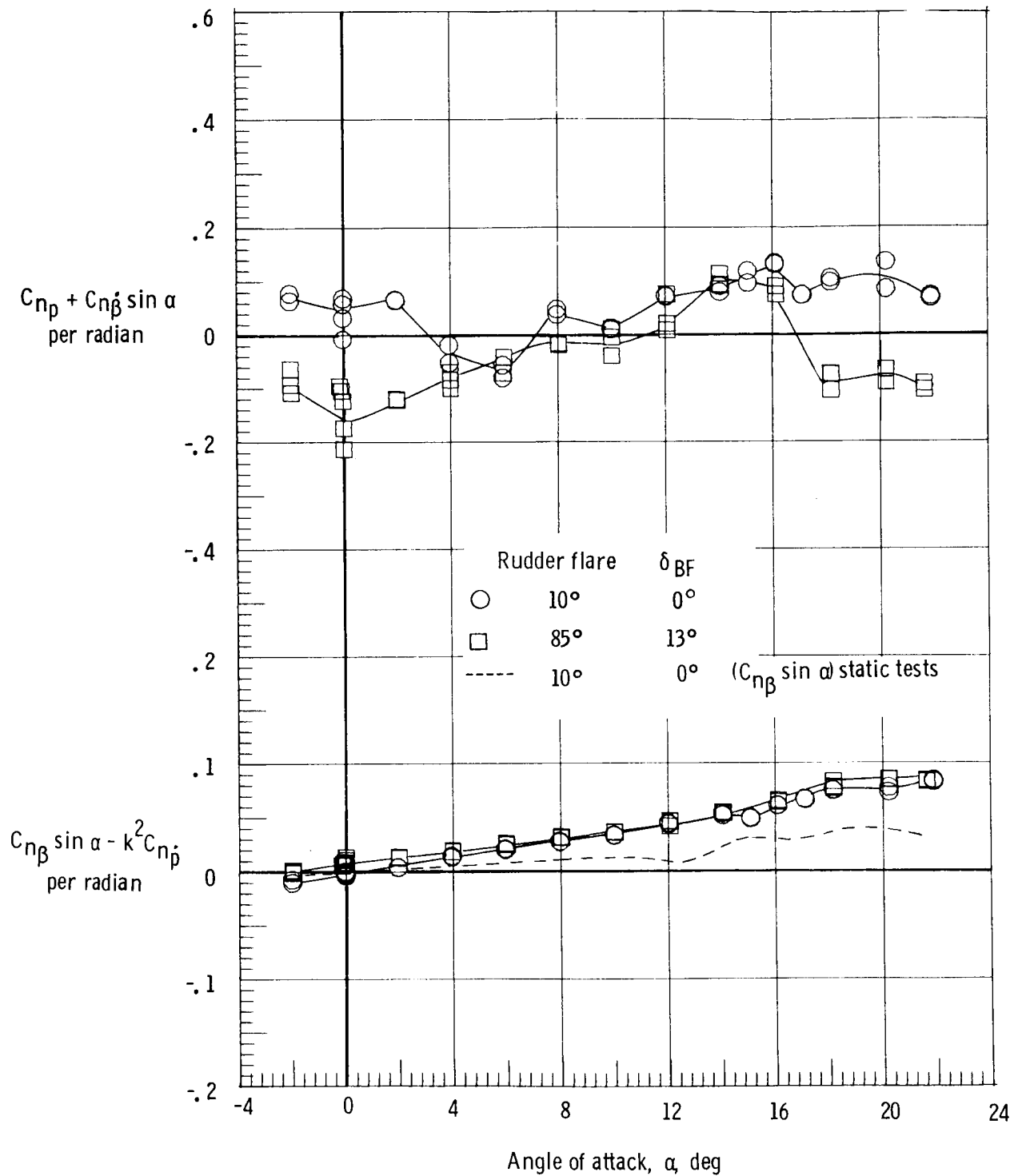
(a) M = 0.3.

Figure 30.- Effect of rudder flare and body flap deflection on yawing moment due to roll rate parameter and yawing moment due to roll displacement parameter. Forward center of gravity; $\delta_e = 0^o$.

(b) M = 0.8.

Figure 30.- Continued.

Figure caption area:

$C_{n_p} + C_{n_{\dot\beta}} \sin \alpha$ per radian

$C_{n_\beta} \sin \alpha - k^2 C_{n_{\dot p}}$ per radian

Rudder flare	δ_{BF}	
○	10°	0°
□	85°	13°
-----	10°	0° ($C_{n_\beta} \sin \alpha$) static tests

Angle of attack, α, deg
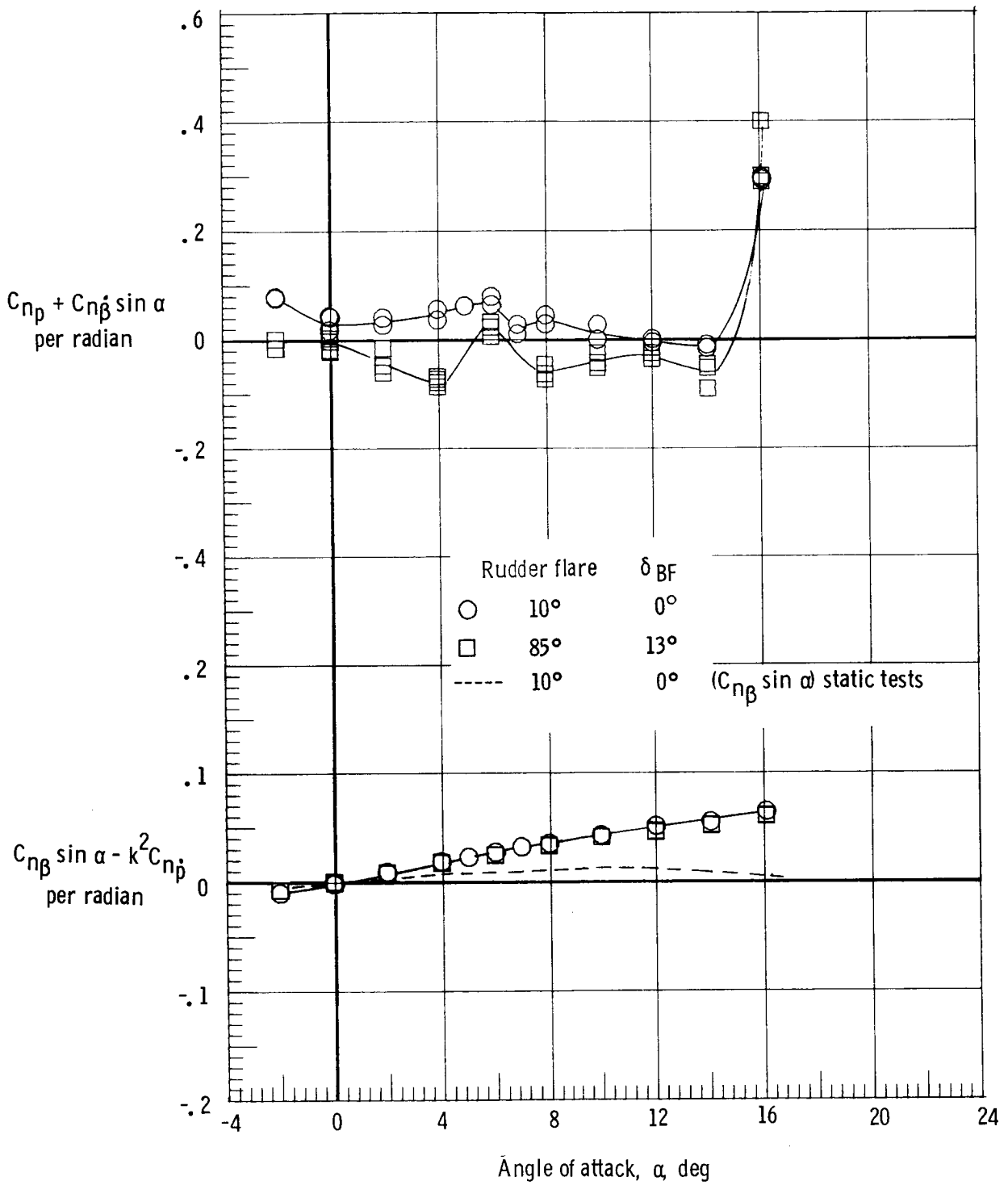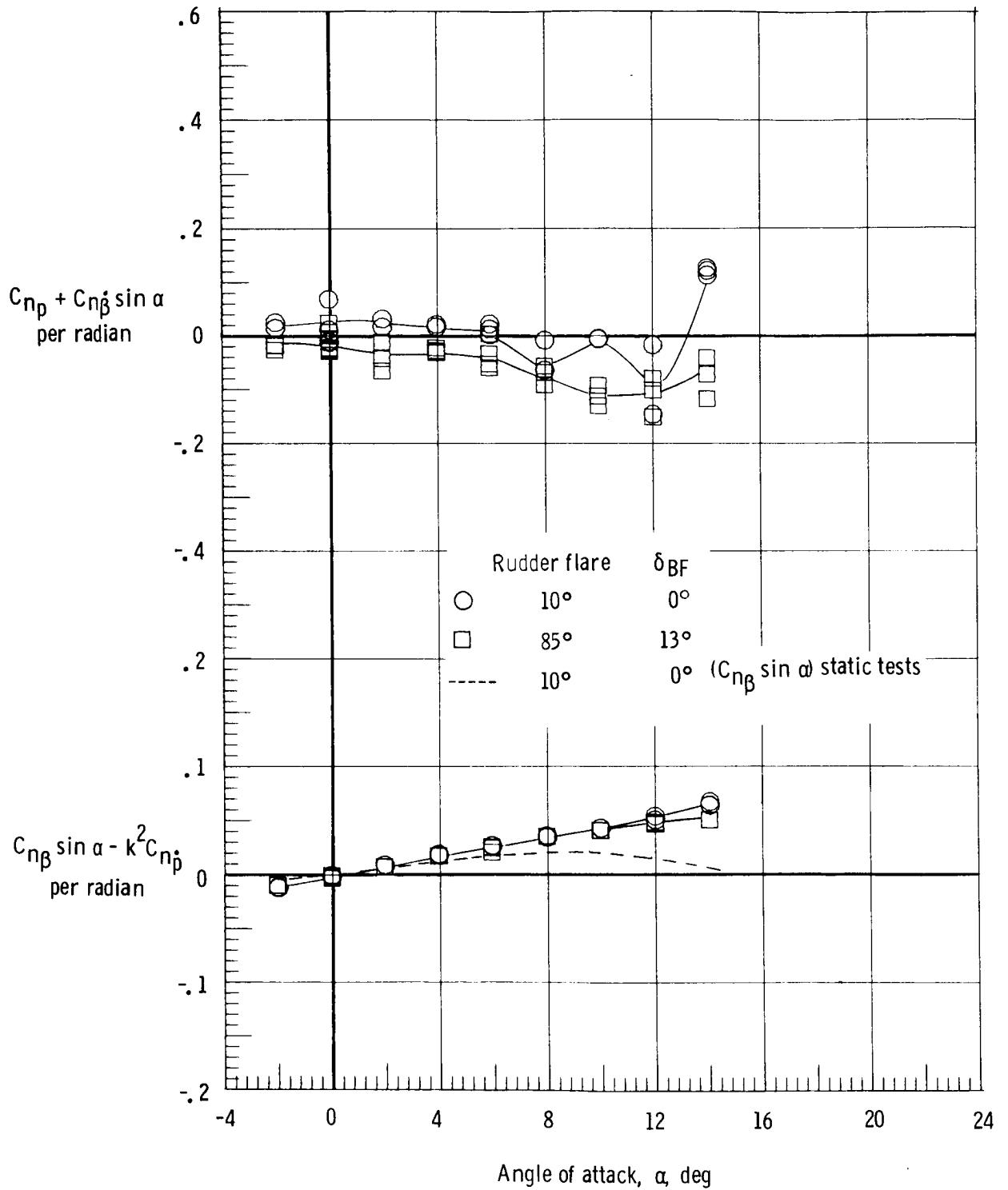
(c)   M = 0.9.

Figure 30.- Continued.
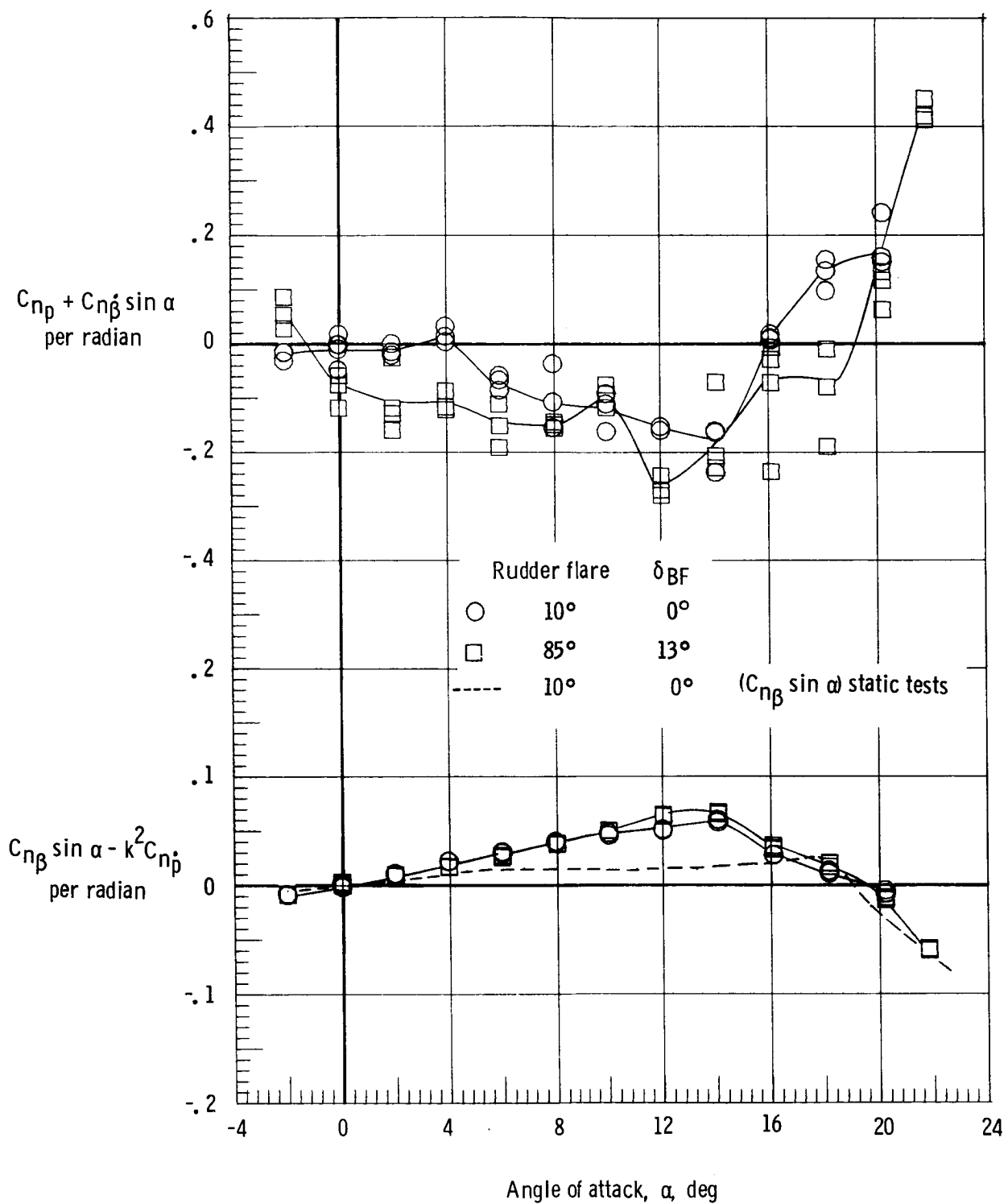
(d)   M = 0.98.

Figure 30.- Continued.
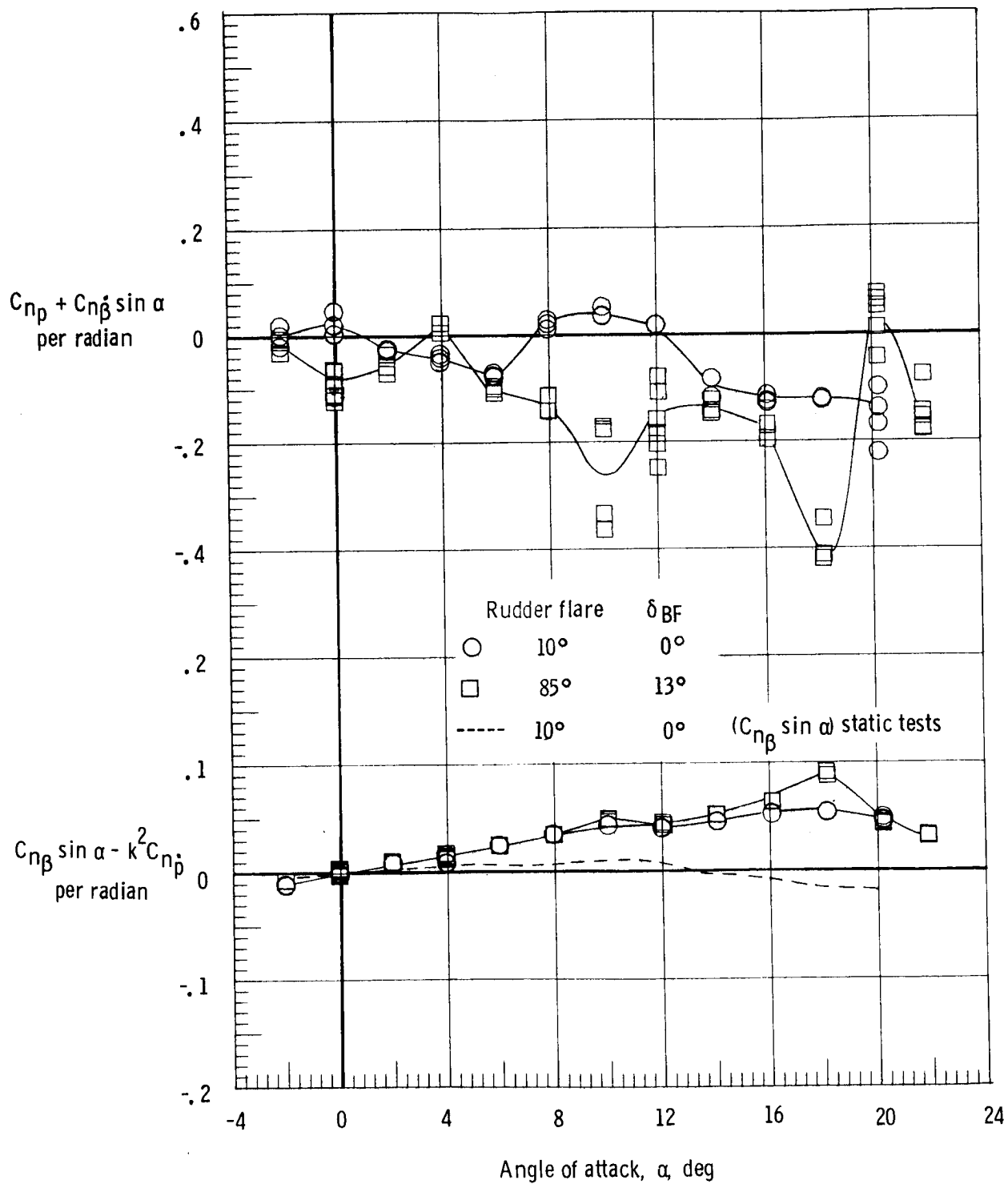
(e) M = 1.2.

Figure 30.- Concluded.
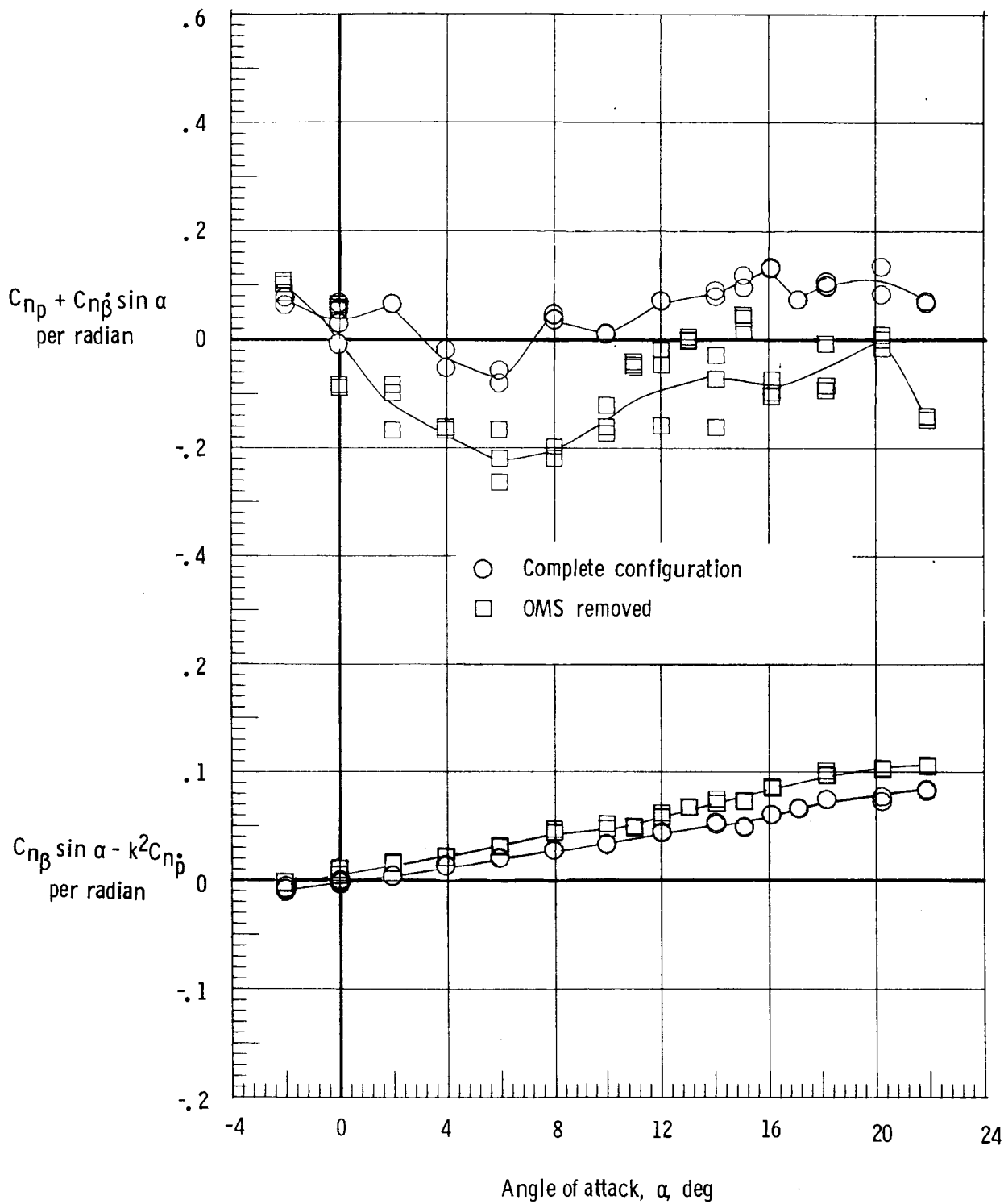
(a)   M = 0.3.

Figure 31.- Effect of configuration components on yawing moment due to roll rate
parameter and yawing moment due to roll displacement parameter.   Forward
center of gravity; $\delta_e = 0^O$, $\delta_{BF} = 0^O$.

Angle of attack, α, deg
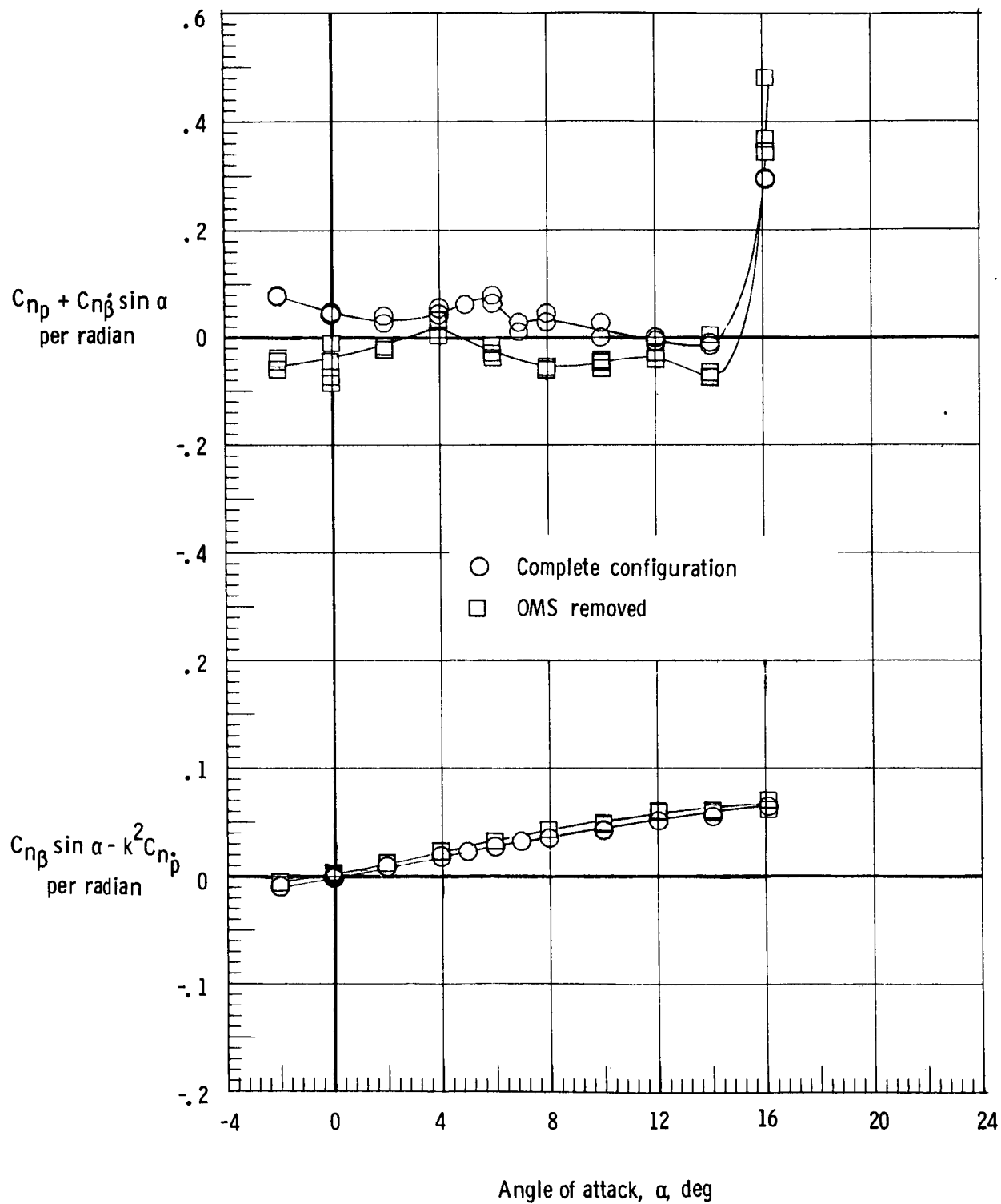
(b)   M = 0.8.

Figure 31.- Continued.

(c)   M = 0.9.

Figure 31.- Continued.

$C_{n_p} + C_{n_{\dot\beta}} \sin \alpha$
per radian

$C_{n_\beta} \sin \alpha - k^2 C_{n_{\dot p}}$
per radian

○ Complete configuration

□ OMS removed

Angle of attack, α, deg
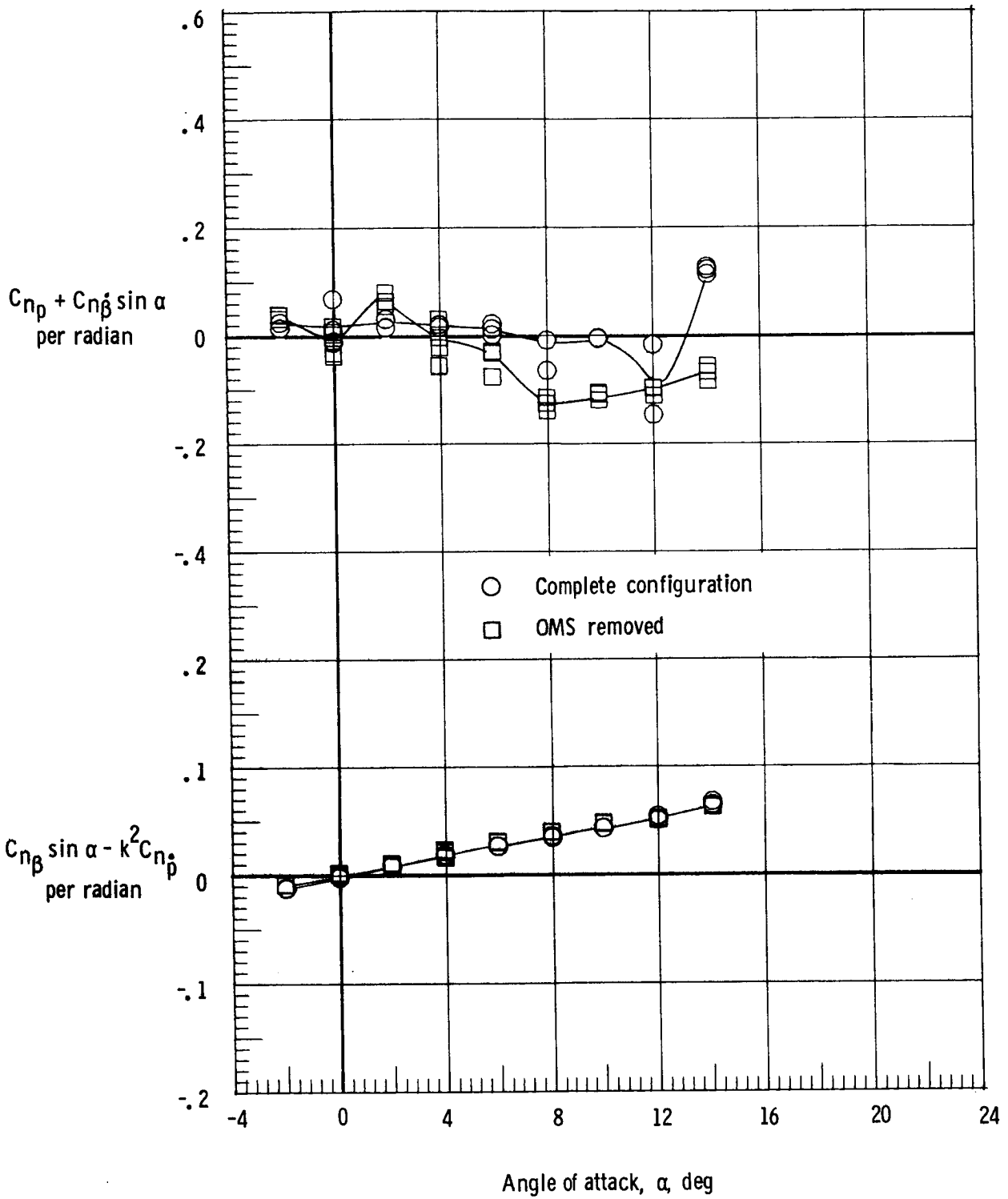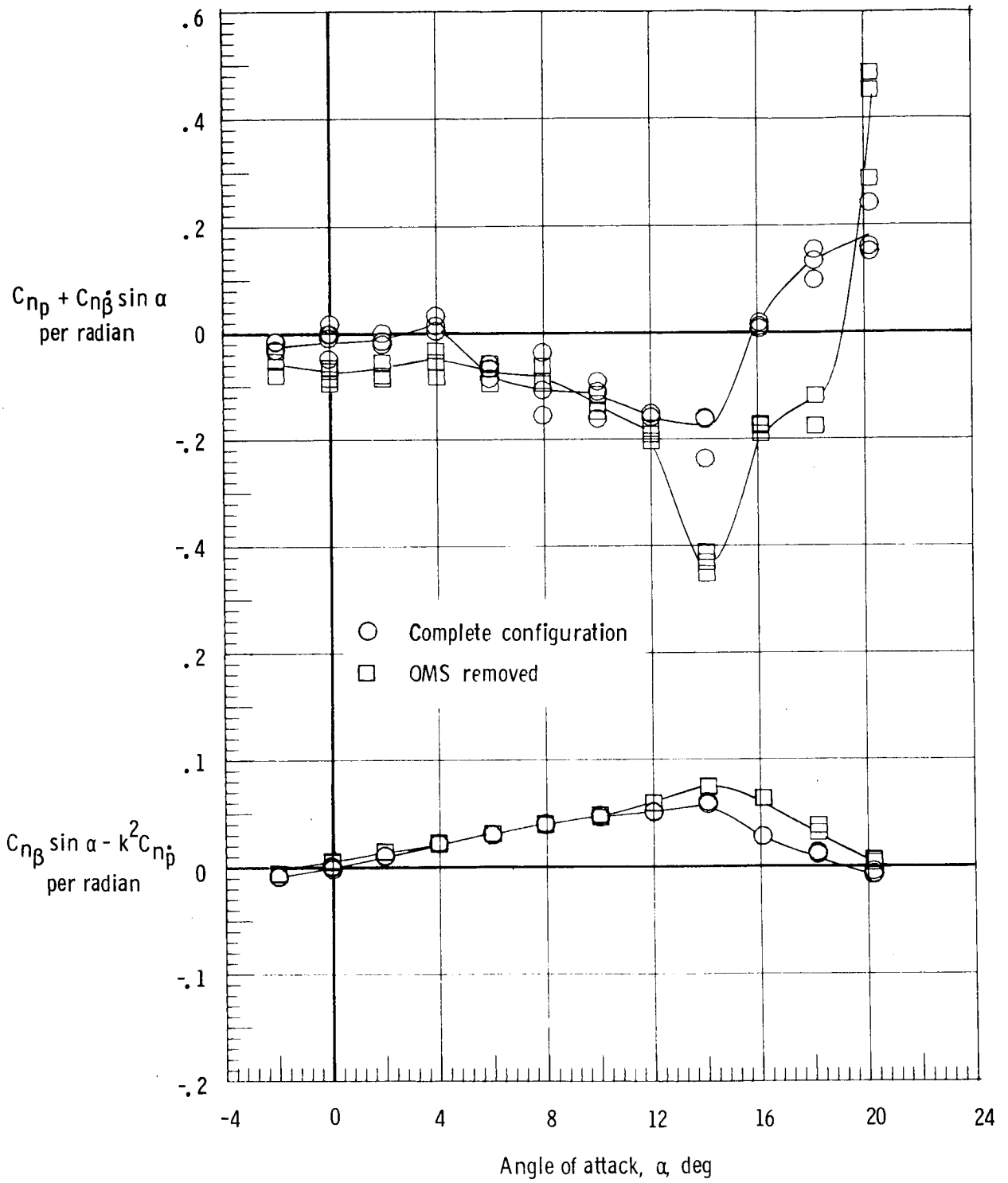
(d)   M = 0.98.

Figure 31.- Continued.

Angle of attack, α, deg
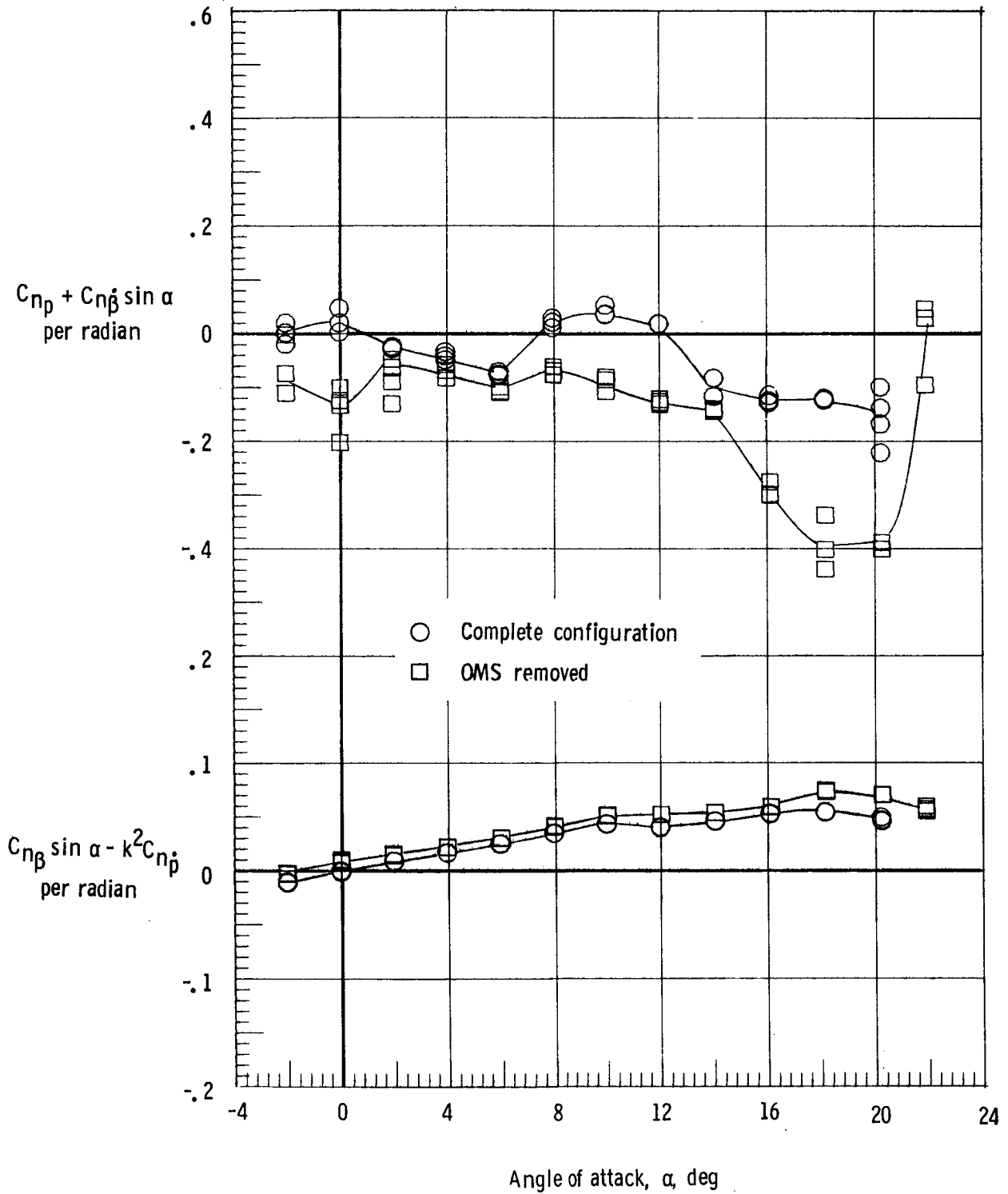
(e)   M = 1.2.

Figure 31.- Concluded.
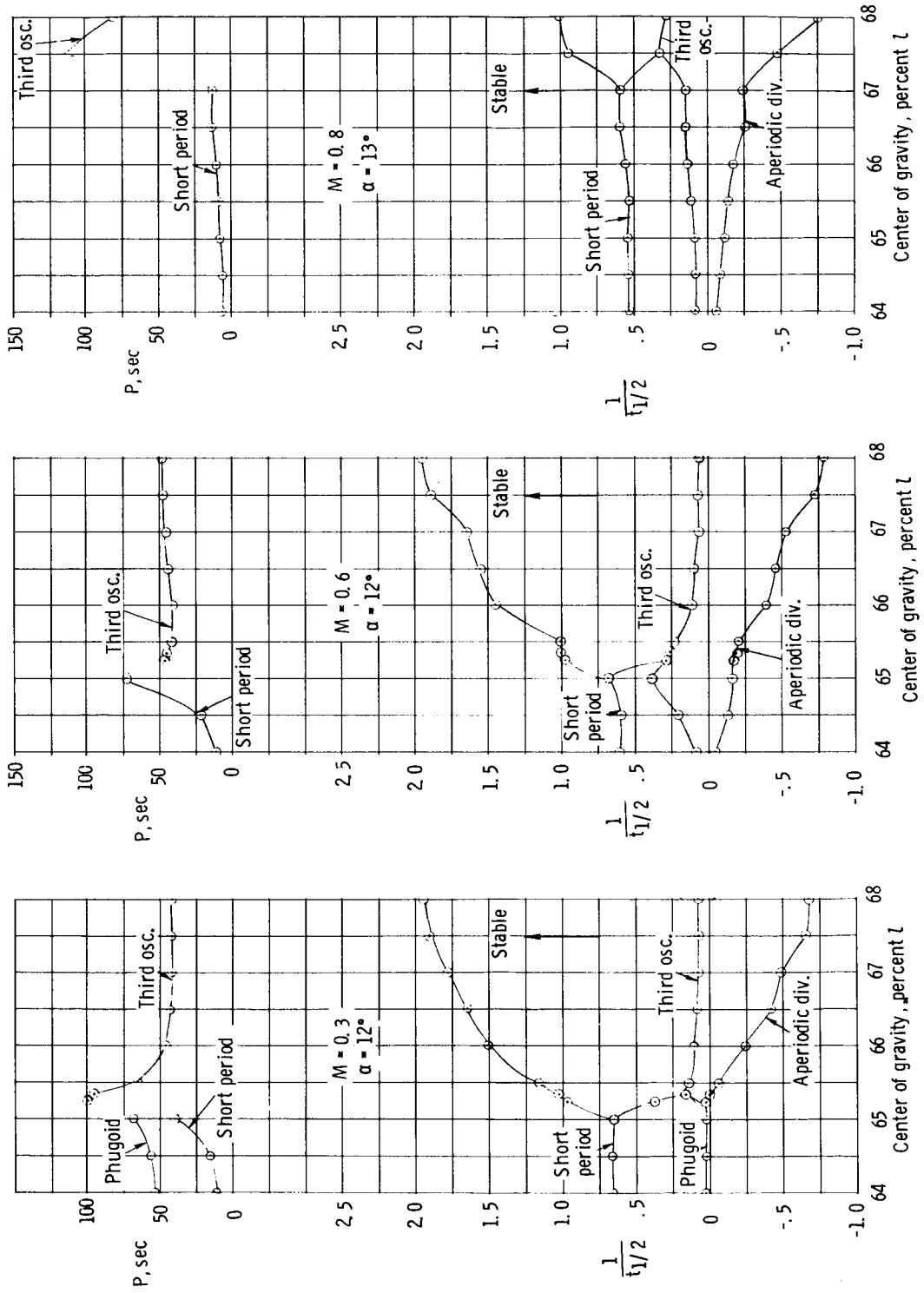
Figure 32.- Effect of center-of-gravity position on the computed vehicle damping and on the period of oscillation.

(a) M = 0.3, 0.6, and 0.8.
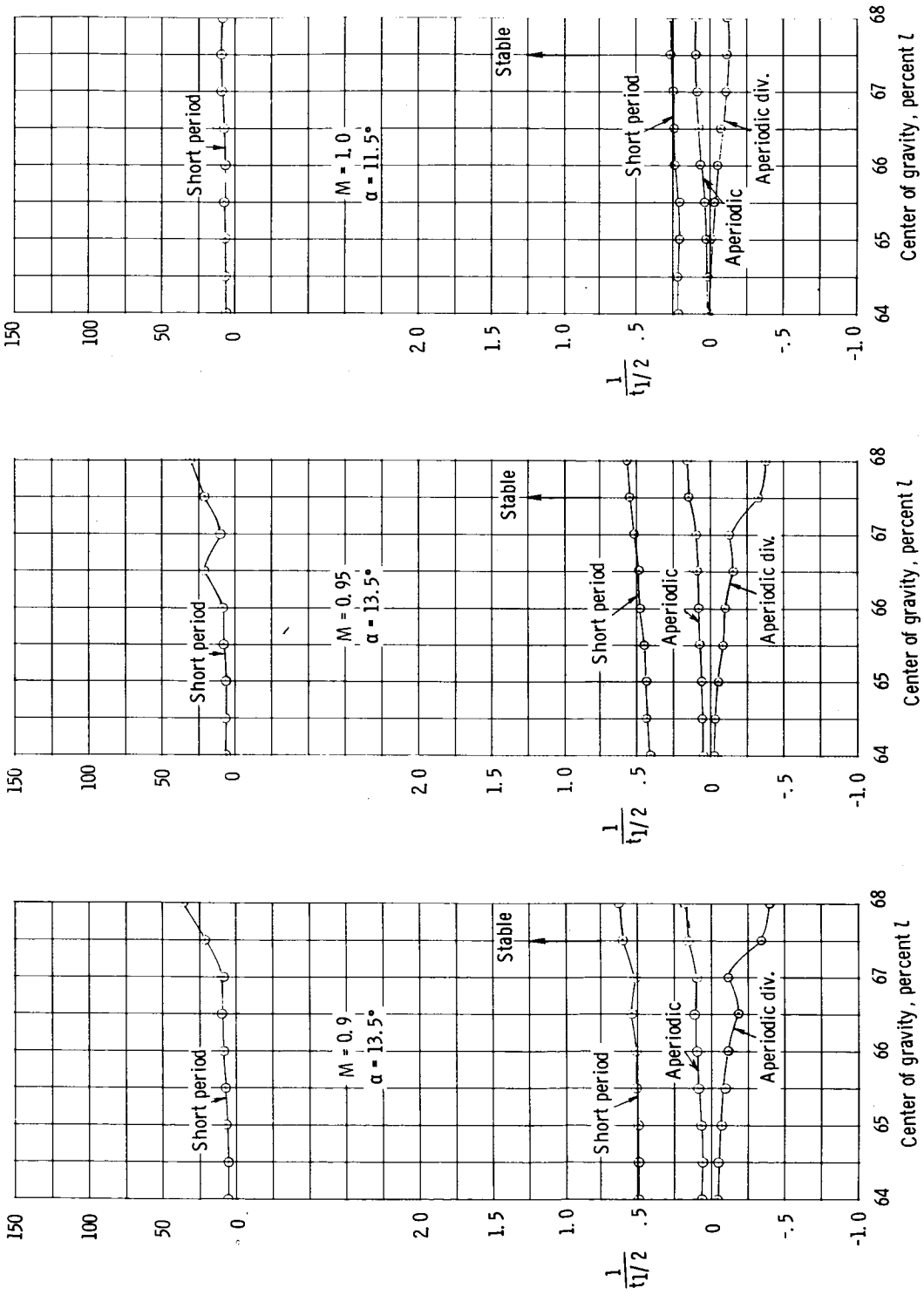
(b) M = 0.9, 0.95, and 1.0.

Figure 32.– Concluded.

159
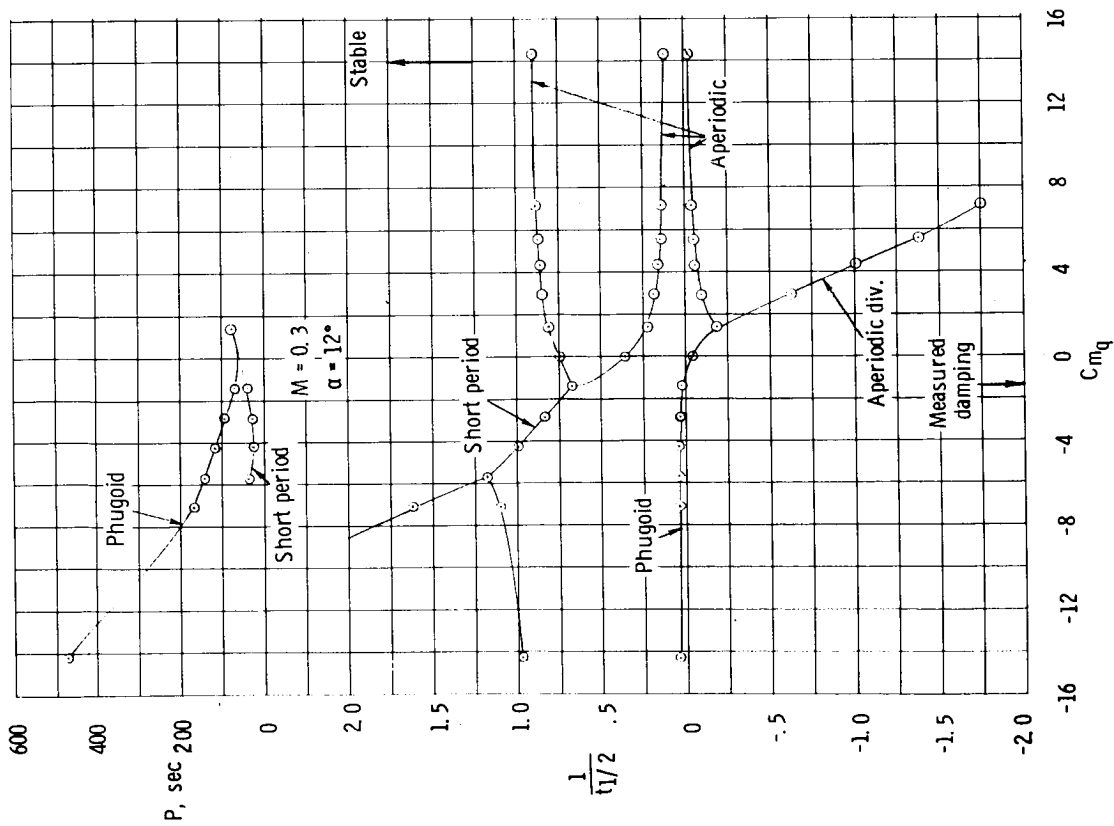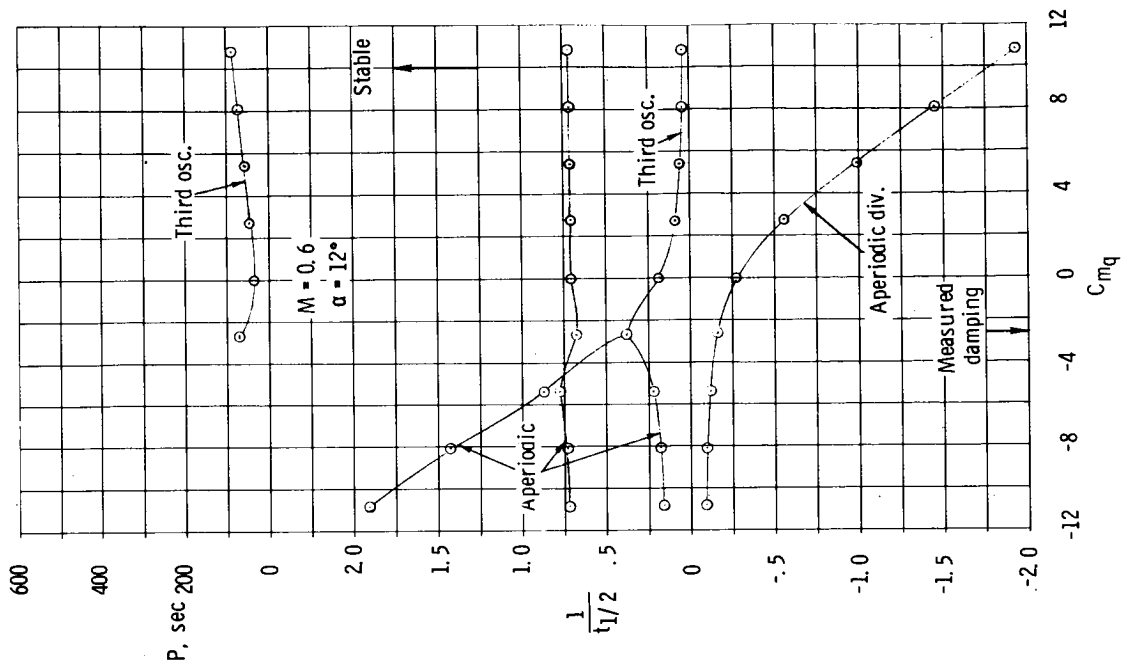
(a) M = 0.3 and 0.6.

Figure 33.- Effect of pitch damping on calculated vehicle damping. Forward center of gravity.
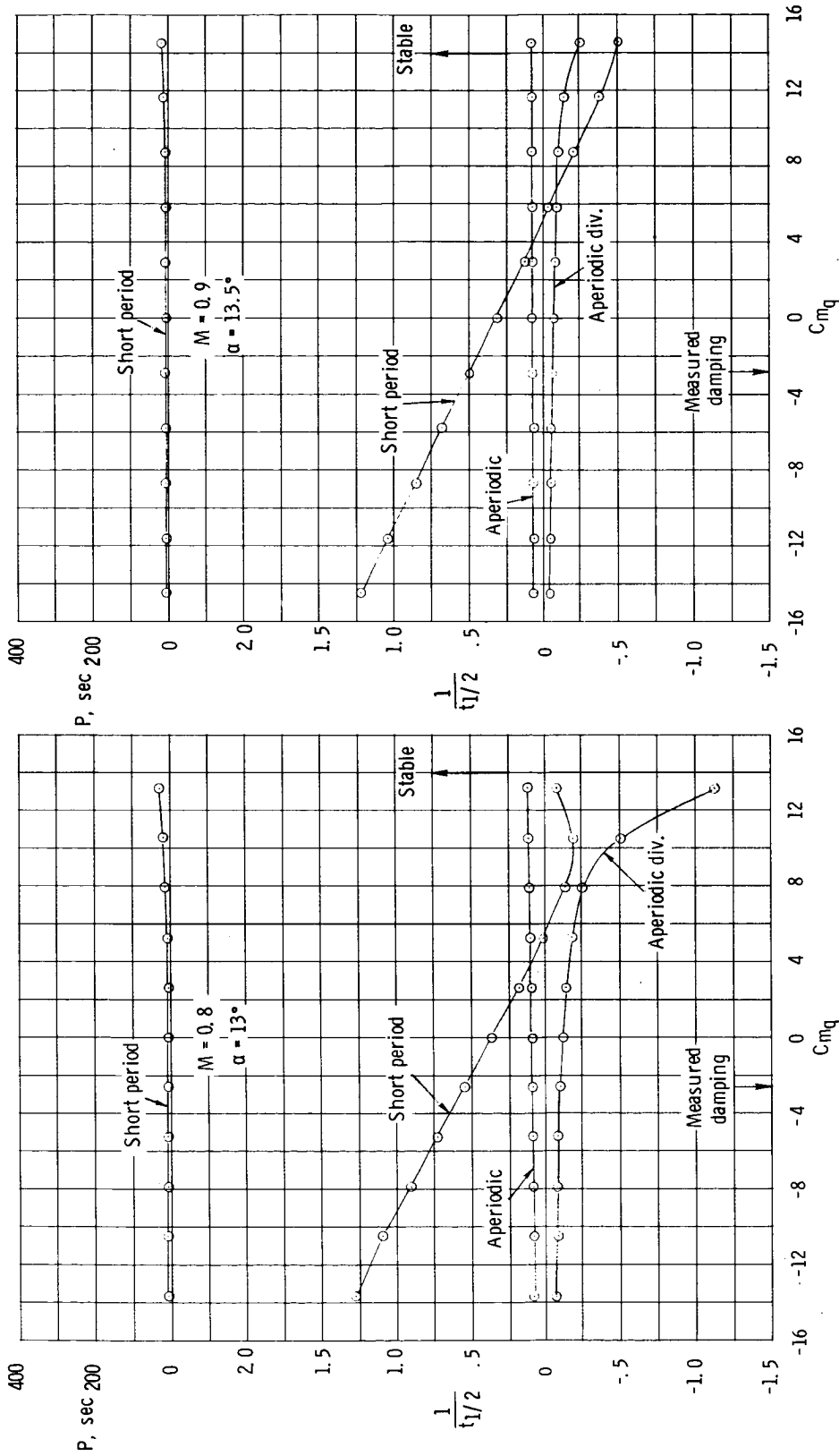
(b) M = 0.8 and 0.9.

Figure 33.- Continued.
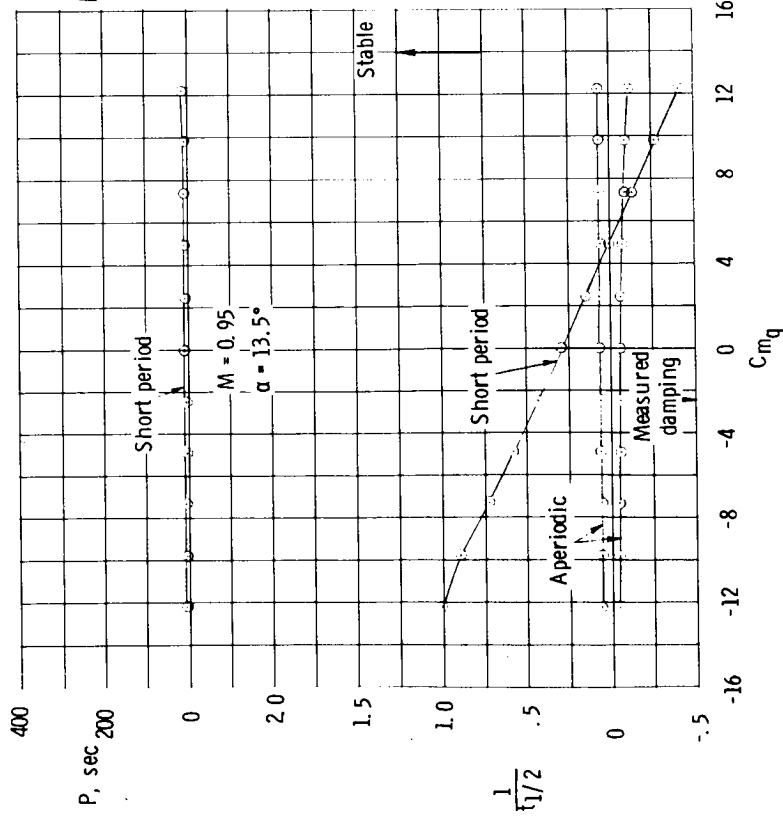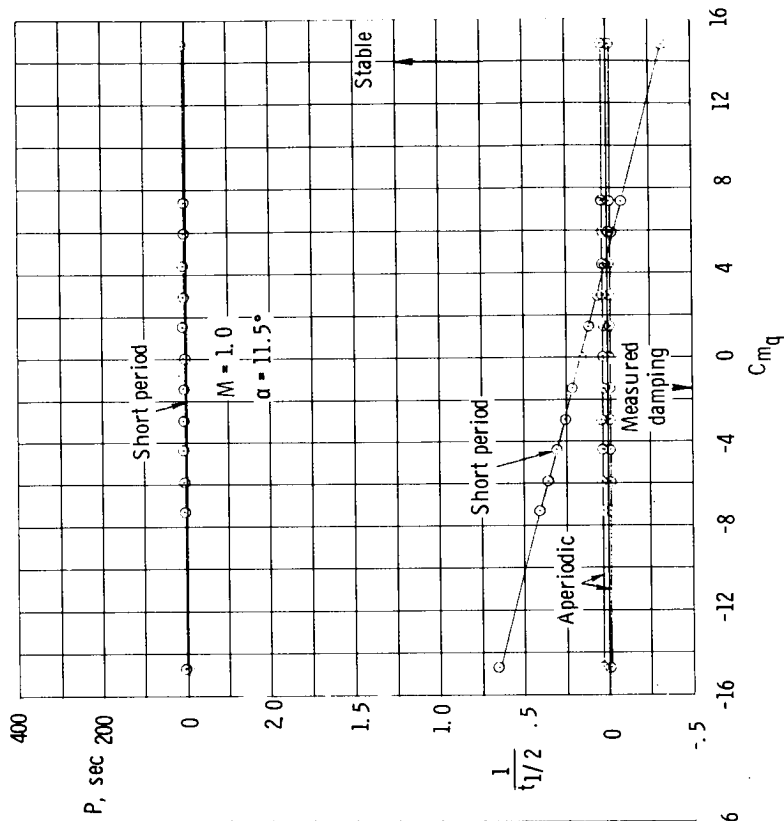
(c) M = 0.95 and 1.0.

Figure 33.- Concluded.
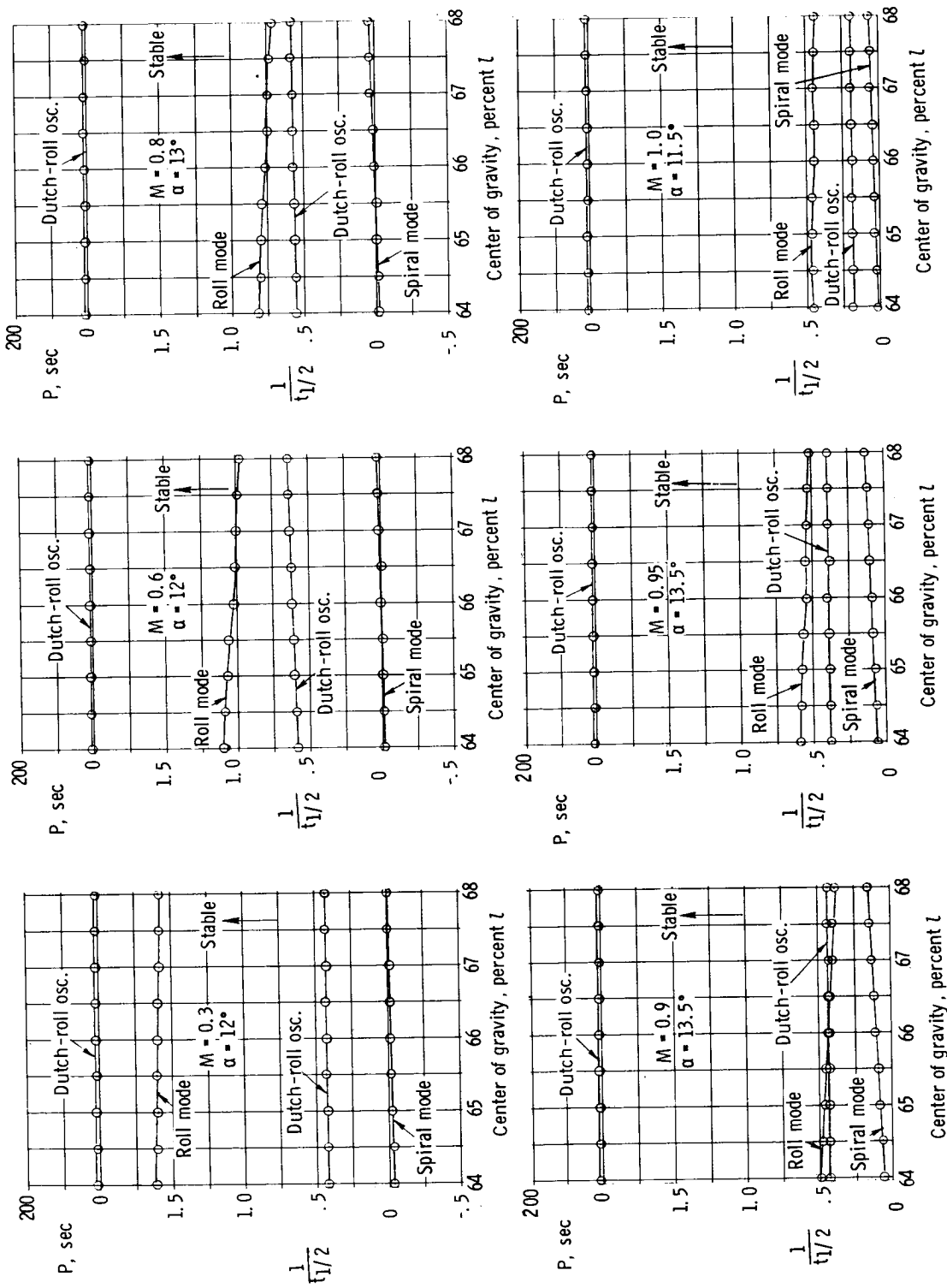
Figure 34.- Effect of center-of-gravity position on the computed vehicle lateral damping.

163
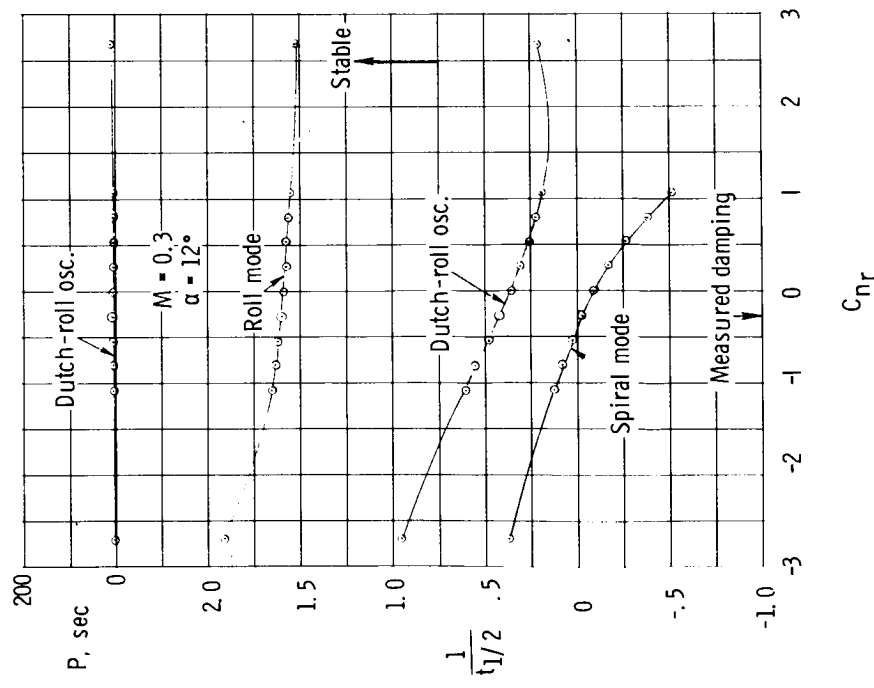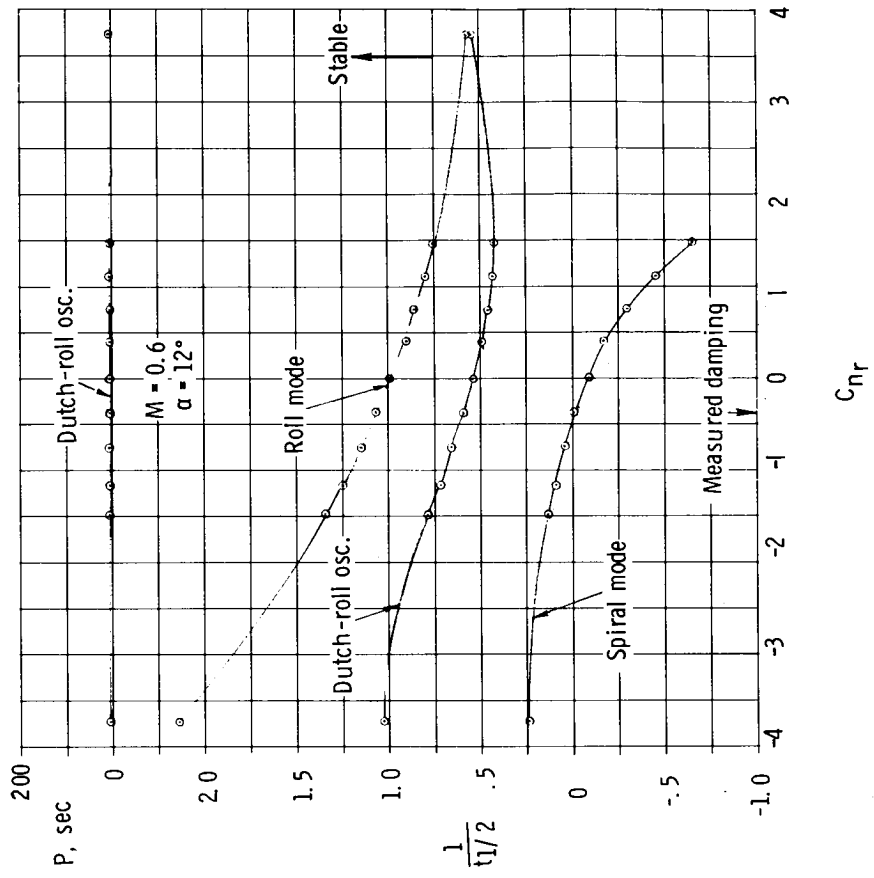
(a) M = 0.3 and 0.6.

Figure 35.– Effects of yaw damping on calculated vehicle damping.

(b) M = 0.8 and 0.9.

Figure 35.– Continued.
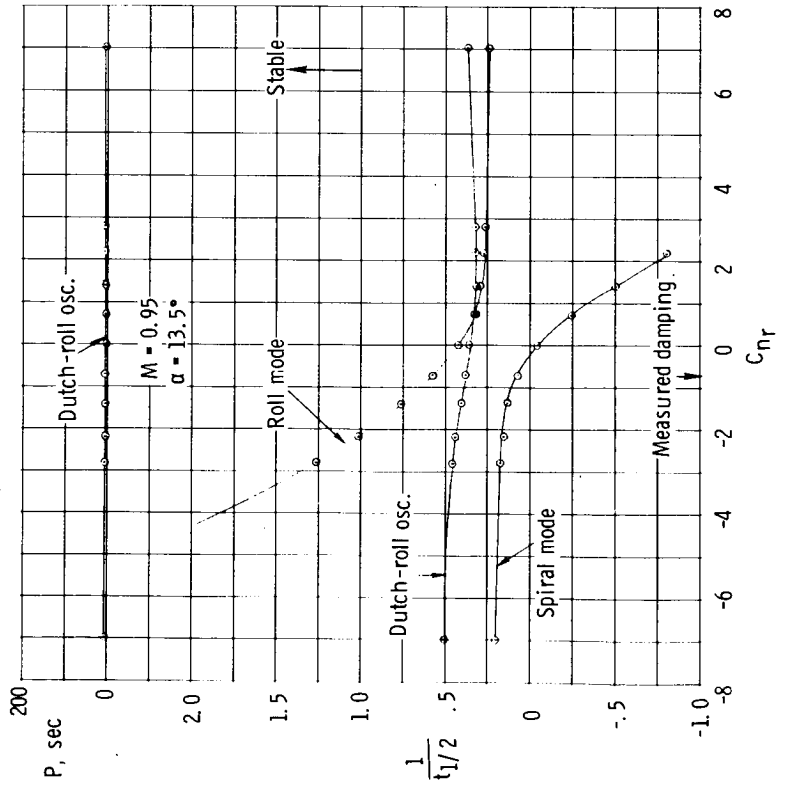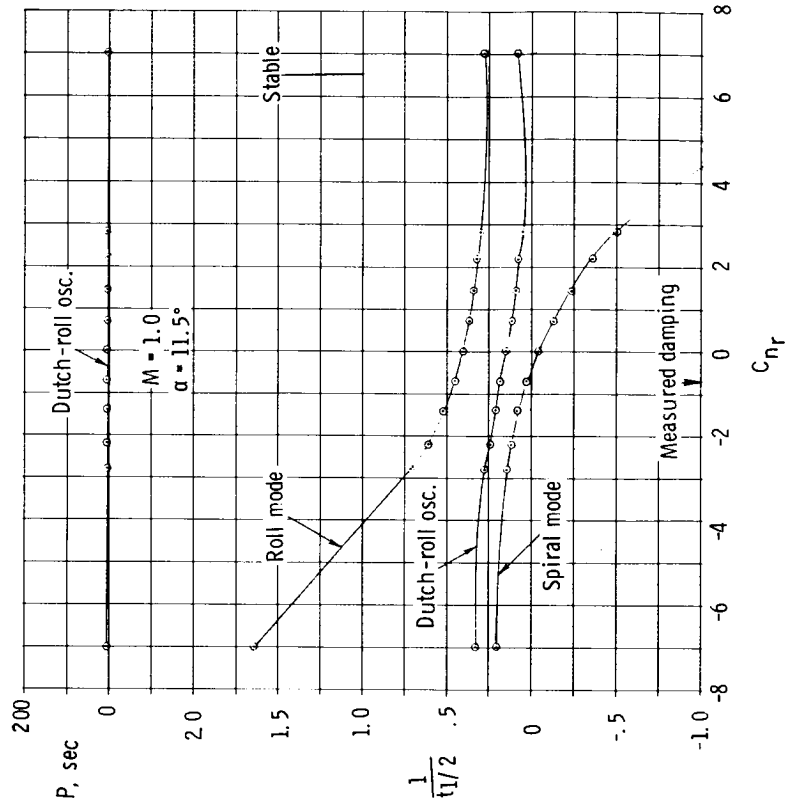
(c) M = 0.95 and 1.0.

Figure 35.- Concluded.
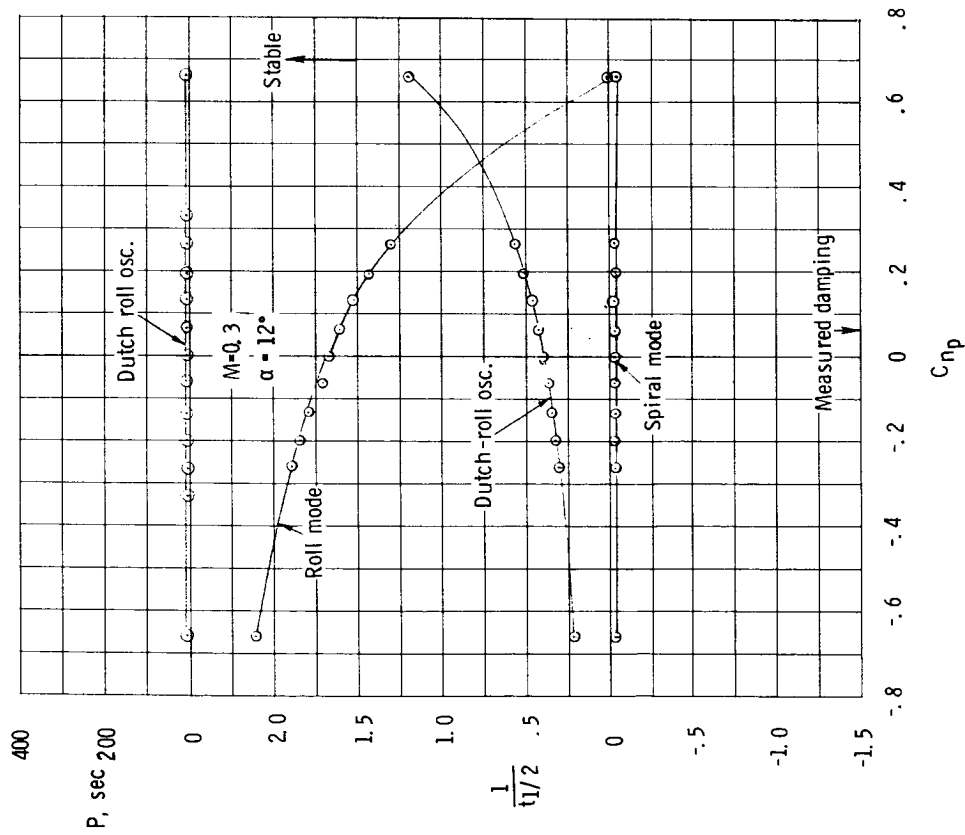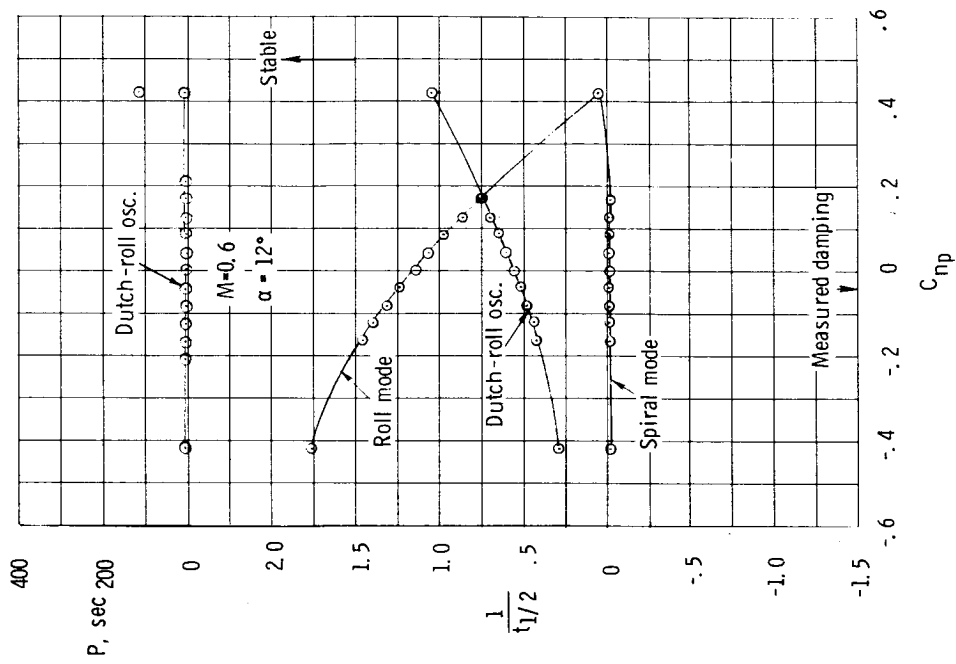
Figure 36.- Effect of yawing moment due to rolling velocity on calculated vehicle damping. Forward center of gravity.
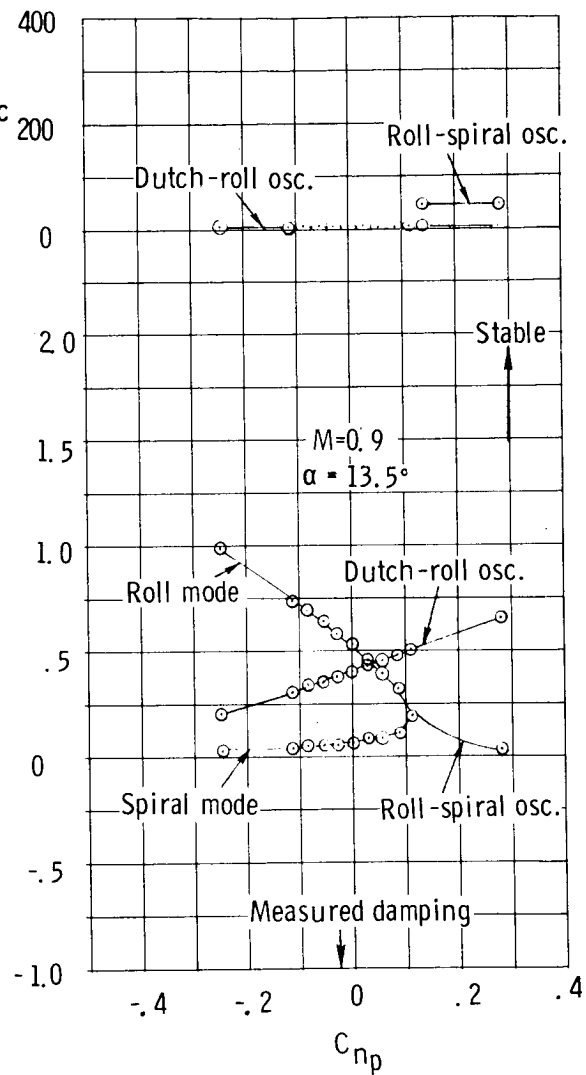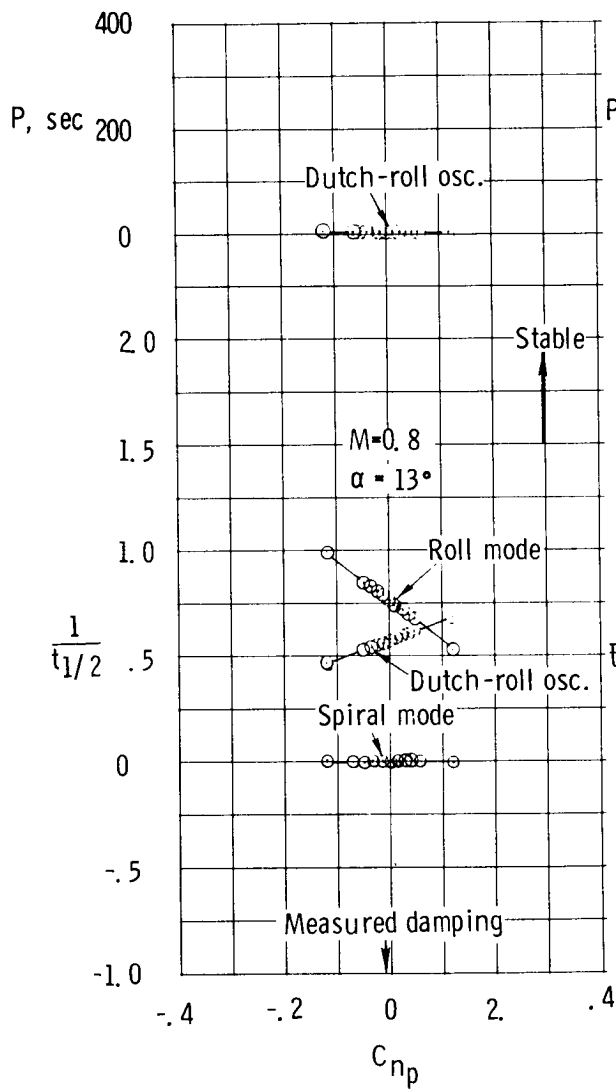
(a) M = 0.3 and 0.6.

(b)   M = 0.8 and 0.9.

Figure 36.- Continued.
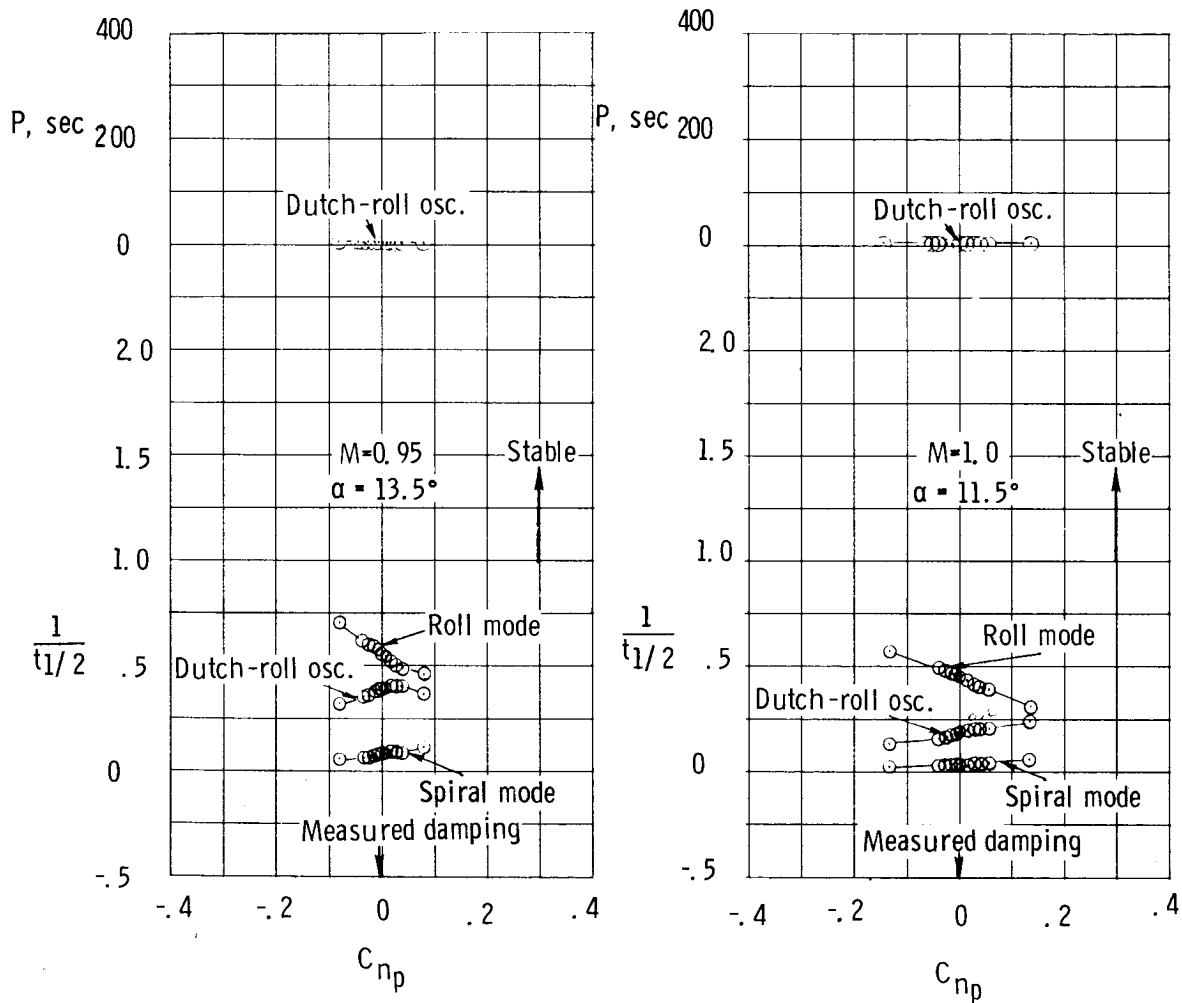
(c)   M = 0.95 and 1.0.

Figure 36.- Concluded.
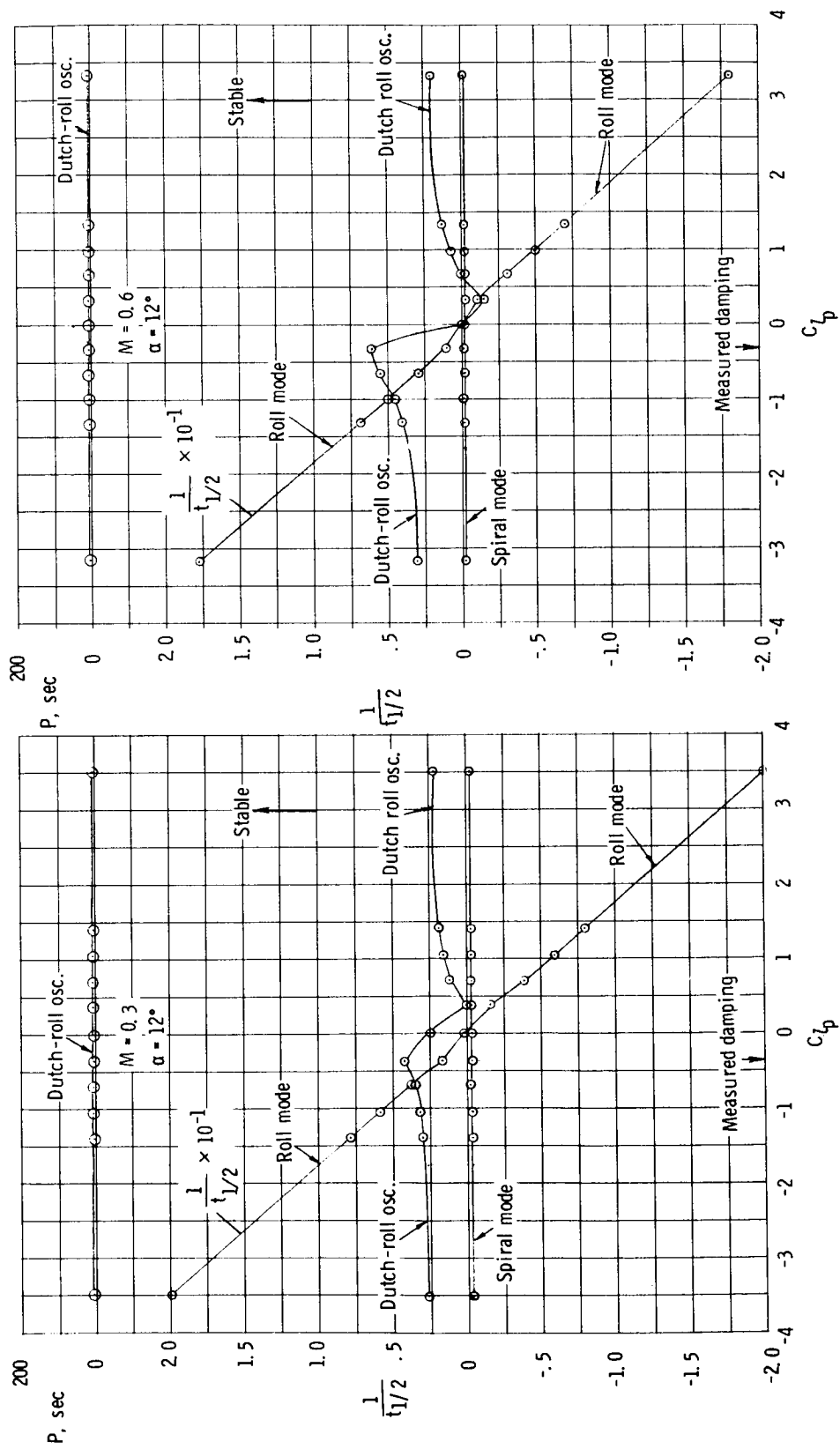
Figure 37.- Effect of roll damping on calculated vehicle damping. Forward center of gravity.
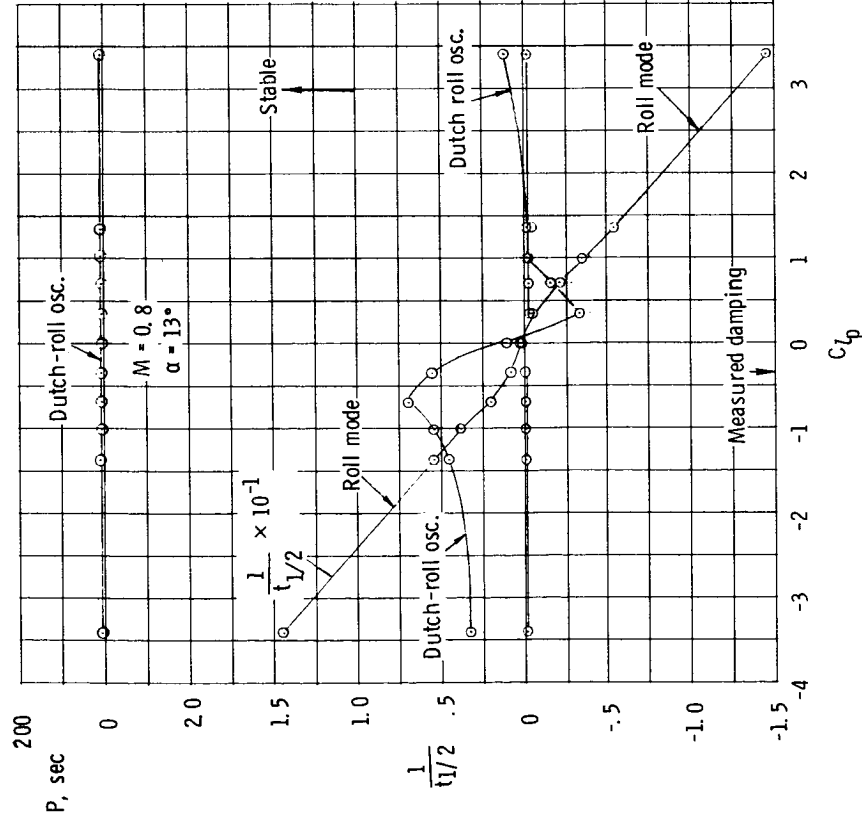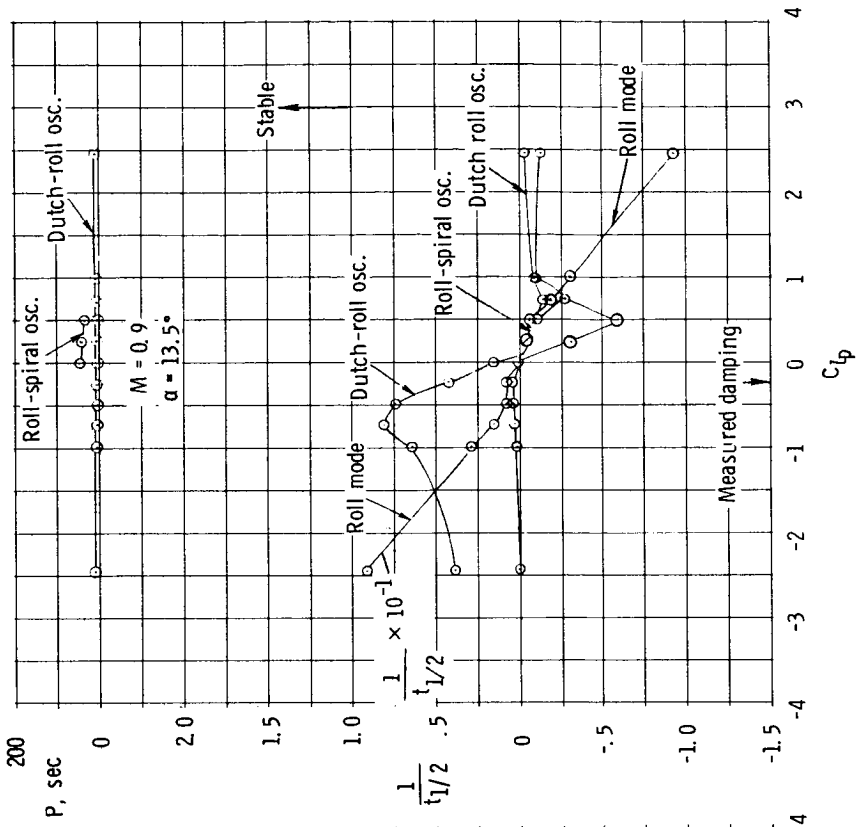
(a) M = 0.3 and 0.6.

(b) M = 0.8 and 0.9.

Figure 37.- Continued.
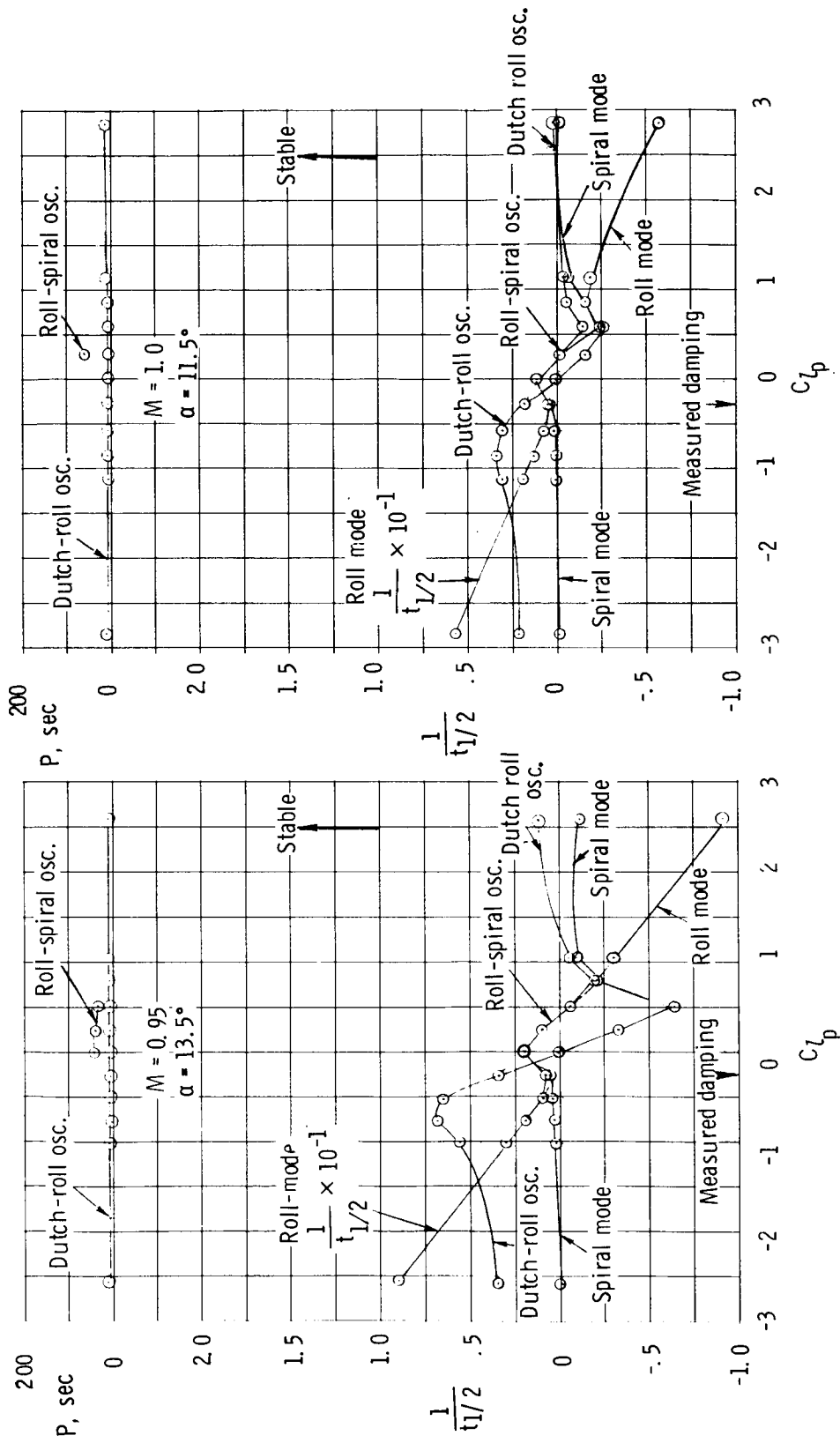
(c) M = 0.95 and 1.0.

Figure 37.- Concluded.
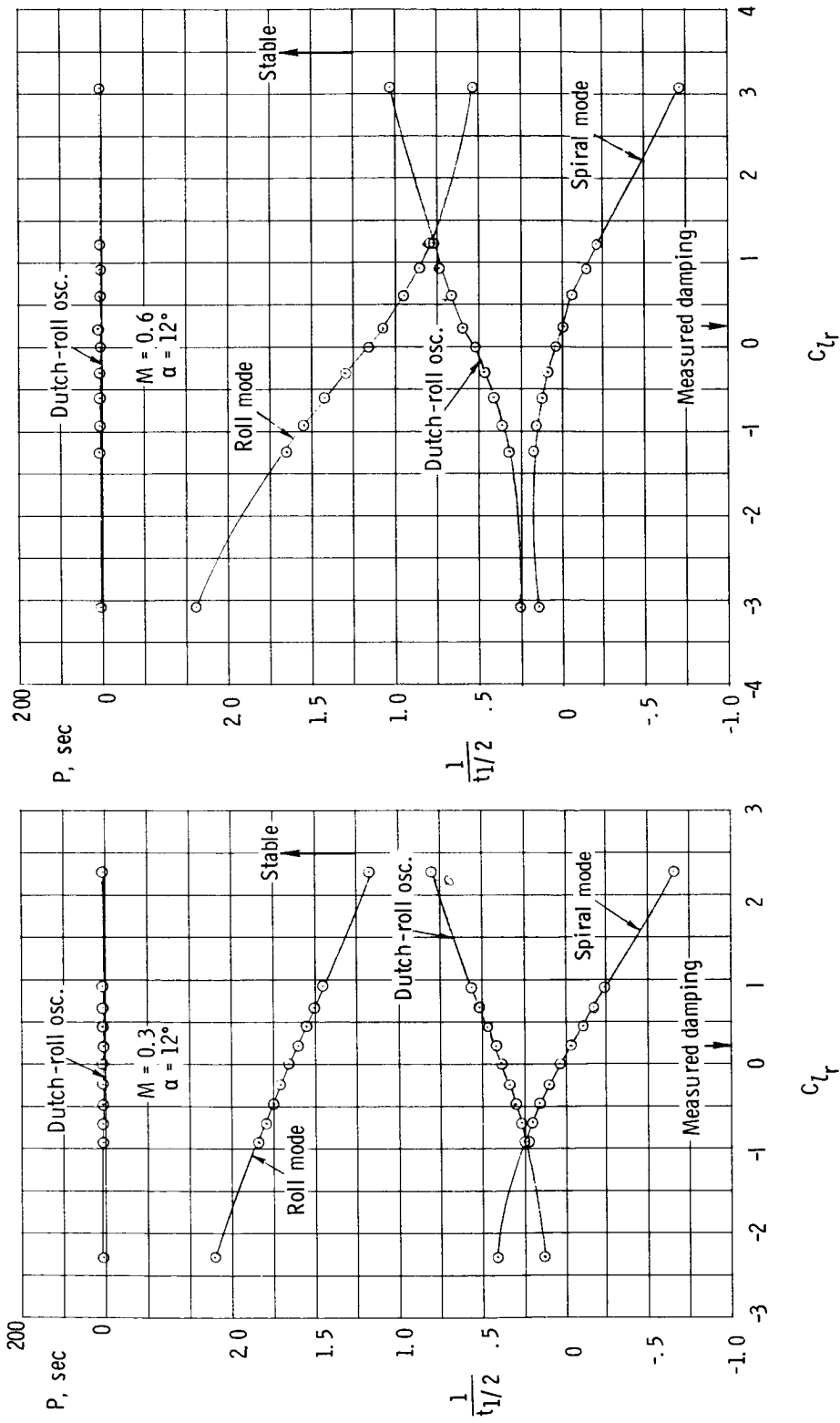
(a) M = 0.3 and 0.6.

Figure 38.- Effect of rolling moment due to yawing velocity on the calculated vehicle damping.
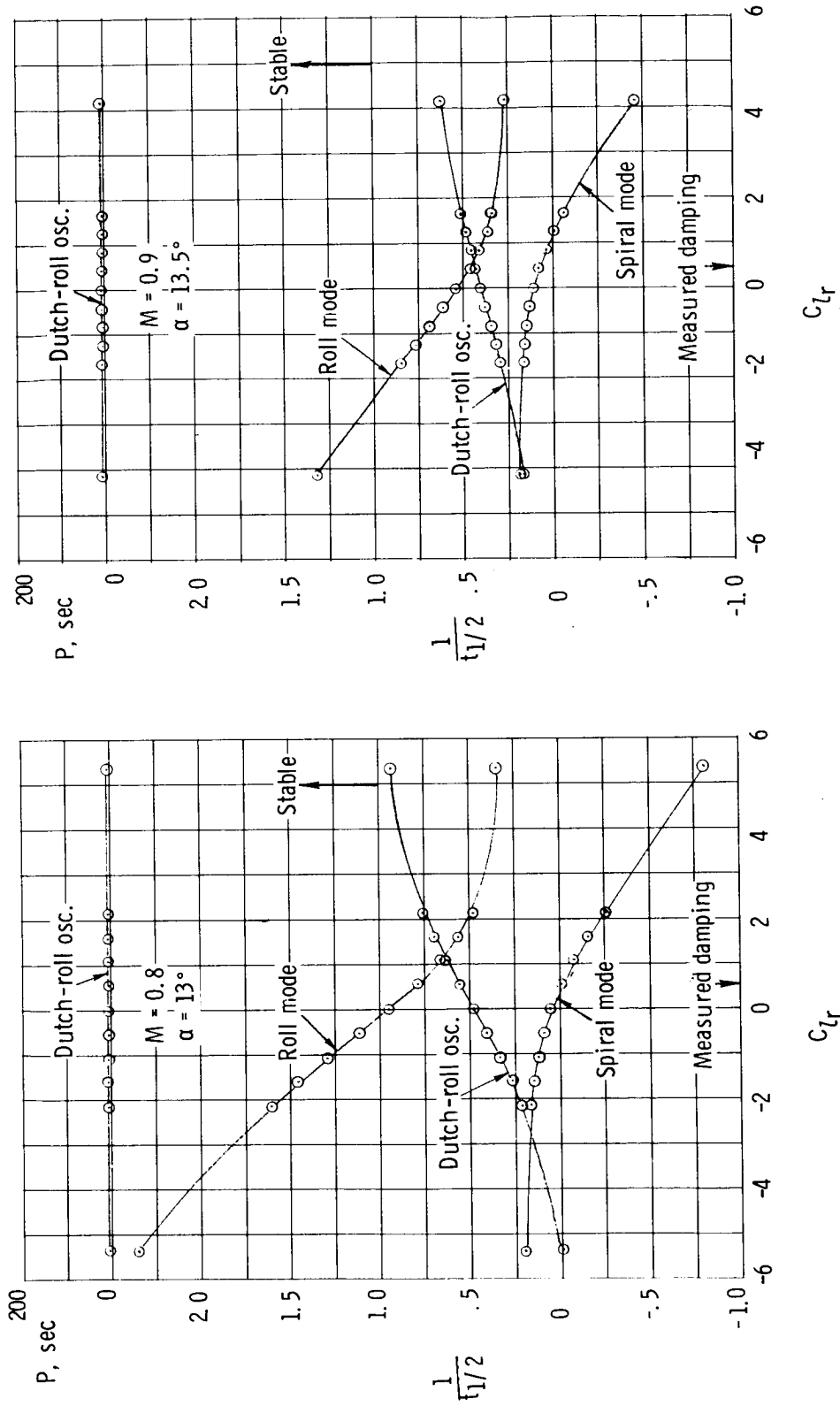
(b) M = 0.8 and 0.9.

Figure 38.- Continued.
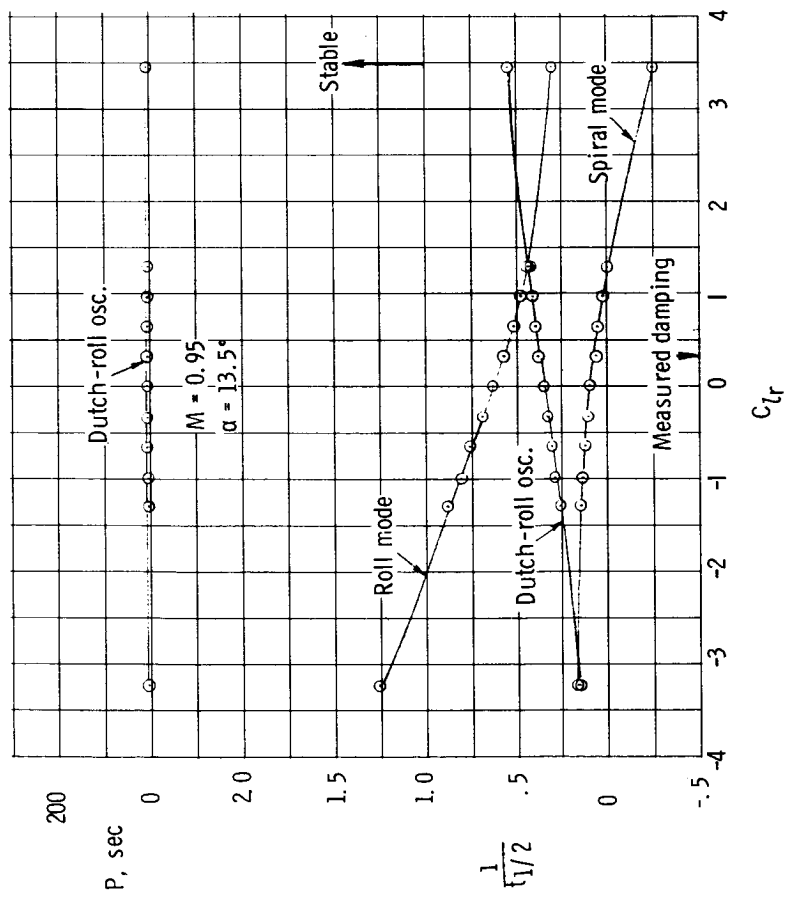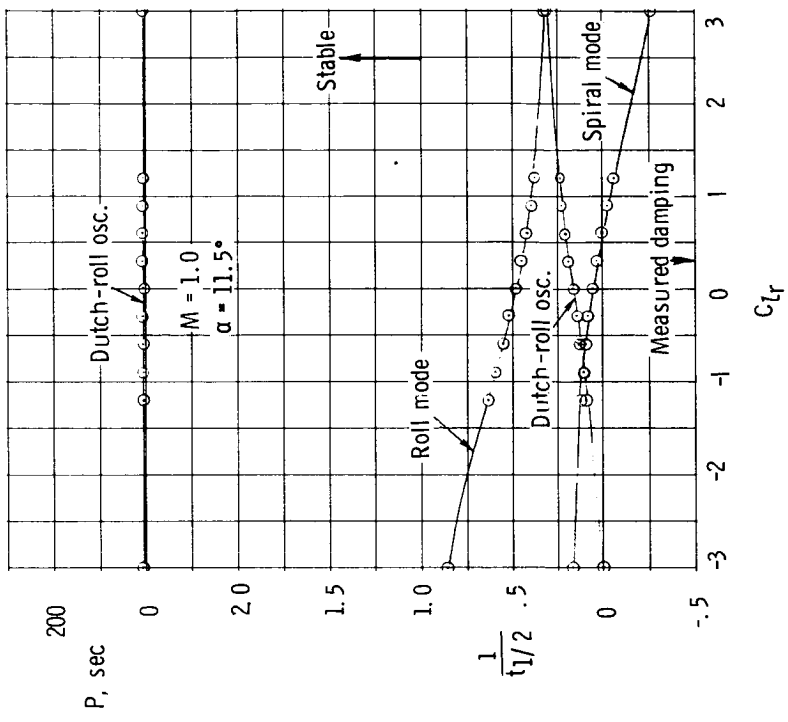
(c) M = 0.95 and 1.0.

Figure 38.- Concluded.

175

1. Report No. NASA TN D-8042	2. Government Accession No.	3. Recipient's Catalog No.
4. Title and Subtitle SUBSONIC AND TRANSONIC DYNAMIC STABILITY CHARACTERISTICS OF A SPACE SHUTTLE ORBITER		5. Report Date November 1975
		6. Performing Organization Code
7. Author(s) Richmond P. Boyden and Delma C. Freeman, Jr.		8. Performing Organization Report No. L-10304
9. Performing Organization Name and Address NASA Langley Research Center Hampton, Va. 23665		10. Work Unit No. 506-26-30-01
		11. Contract or Grant No.
12. Sponsoring Agency Name and Address National Aeronautics and Space Administration Washington, D.C. 20546		13. Type of Report and Period Covered Technical Note
		14. Sponsoring Agency Code

15. Supplementary Notes

16. Abstract
Subsonic and transonic forced oscillation tests of a 0.0165-scale model of a modified 089B Rockwell International space shuttle orbiter have been made in the Langley 8-foot transonic pressure tunnel. The period and damping of the basic unaugmented vehicle were calculated along the entry trajectory utilizing these measured dynamic data. Some parameter analyses were made with the measured dynamic derivatives.

17. Key Words (Suggested by Author(s)) Dynamic stability Shuttle orbiter Forced oscillations Aerodynamics	18. Distribution Statement Unclassified – Unlimited Subject Category 15

19. Security Classif. (of this report) Unclassified	20. Security Classif. (of this page) Unclassified	21. No. of Pages 175	22. Price* $6.25